Biomass Derived Laser-Induced Graphene with Embedded Catalysts: Towards Enhanced Oxygen Reduction Reaction Catalytic Performance

by

Tahani Rahil Aldhafeeri

A thesis

presented to the University of Waterloo

in fulfillment of the

thesis requirement for the degree of

Doctor of Philosophy

in

Chemical Engineering

Waterloo, Ontario, Canada, 2023

Examining Committee Membership

The following served on the Examining Committee for this thesis. The decision of the Examining Committee is by majority vote.

External Examiner Drew Higgins
Assistant Professor | Chemical Engineering | McMaster University

Supervisor Michael Pope
Associate Professor | Chemical Engineering | University of Waterloo

Internal Members Ali Elkamel
Professor | Chemical Engineering | University of Waterloo

Michael Fowler
Professor | Chemical Engineering | University of Waterloo

Internal-external Member Anh Pham
Associate Professor | Civil and Environmental Engineering | University of Waterloo

Author's Declaration

I hereby declare that I am the sole author of this thesis. This is a true copy of the thesis, including any required final revisions, as accepted by my examiners.

I understand that my thesis may be made electronically available to the public.

Abstract

Zinc-air batteries are viewed as one of the most promising energy storage technologies for consumer electronics, electric vehicles, and grid storage due to a number of benefits including relatively high theoretical specific energy density (1350 $Wh/kg_{active\ material}$) compared to lithium-ion batteries (1000 $Wh/kg_{active\ material}$), the abundance of zinc in the earth, and its inherent safety and ease of handling. Zinc-air batteries (ZAB) include an air-breathing cathode in addition to more standard battery components including a metal (zinc) anode, polymer separator, and alkaline electrolyte. This makes ZABs a unique technological advancement. Unlike other common battery systems like lithium-ion batteries, which store active material in the cathode, the air cathode of a ZAB uses gaseous oxygen molecules in the air as the fuel for an energy-generating process. The oxygen reduction reaction (ORR) and oxygen evolution reaction (OER) processes that take place during battery discharge and charge, respectively, largely control the overall energy efficiency of the ZAB system due to their inherently slow kinetics. Nevertheless, the most significant obstacles to the large-scale industrial deployment of ZABs are their low round-trip energy efficiency and performance deterioration. Both issues are directly connected to the poor activity and stability of the electrocatalysts used to catalyze the reactions at the air electrode and the reactions at the zinc electrode. In order to substitute precious metal catalysts, a variety of hybrid catalysts, transition metal-based catalysts, and metal free catalysts have been studied. However, the majority involve complex fabrication processes that demand special conditions and multiple, often energy intensive steps. This has hindered scale-up and can result in additional costs. Consequently, a straightforward technique for creating air electrodes with active catalysts is essential.

Laser induced carbonization has emerged as a promising, furnace-free approach to create carbon-based materials and electrodes in one step. However, little work has been carried out to determine whether precious and non-precious metal catalysts can also be formed during this rapid laser conversion process and whether such methods could result in high activity electrocatalysts for the air-cathode of a zinc-air battery. Thus, in this thesis, we sought to develop composites of carbon forming resins containing various precious and non-precious metal catalyst precursors that could be laser converted to high surface area carbon/catalyst composites.

We successfully designed a simple approach to prepare air cathodes consisting of laser biomass-induced graphene (LIG) decorated by different catalysts; platinum based, manganese oxides, and metal free catalysts. We used furfuryl alcohol (FA) as a LIG precursor and CO_2 laser to carbonize poly furfuryl alcohol instead of furnace in all the three projects. We demonstrate a facile approach to reduce platinum content to less than 2 wt.% by interfacing Pt with CoO_x as well-dispersed nanoparticles entrapped within a highly conductive laser-induced graphene (LIG) matrix as an air-cathode for ZABs. Furfuryl alcohol was used as the monomer of poly furfuryl alcohol (LIG precursor) and as a reducing agent. Laser-induced carbonization of polymerized furfural alcohol pre-loaded with Co, and Pt precursors resulted in the formation of a mixture of spherical nanoalloys and core-shell Pt-CoO_x structures with ultra-small size less than 2 nm. SEM, TEM and EDS analysis indicated excellent distribution of the nanoparticles consisting of core-shell (CoO_x-Pt) and mixed spherical nanoalloys throughout the three-dimensional LIG. Moreover, the onset potential of LIG-$PtCoO_x$ air cathode is ~ +20 mV (vs. Hg/HgO) in alkaline media which indicates fast ORR kinetics when compared to commercial Pt/C (-30 mV vs. Hg/HgO) with the same catalyst concentration. The half-wave potential is -150 mV (vs. Hg/HgO) which is 30 mV more positive than commercial Pt/C. ZAB cycling using LIG-$PtCoO_x$ as catalyst material showed improved stability and rechargeability compared to the commercial Pt/C electrode. A greater peak power density of 67.1 mW/cm^2 is also delivered by the LIG-$PtCoO_x$ cathode-assembled ZAB compared to the pricey Pt/C electrode (52.3 mW/cm^2). Moreover, commercial manganese oxide (MnO_2) was loaded in LIG via a facile one-pot polymerization reaction. Carbonization was accomplished by optimizing laser irradiation to produce a mixed-phase catalyst material supported by a highly conductive carbon matrix. Optimal loading of MnO/Mn_3O_4 vs LIG was determined via rotating ring disk electrode measurements where the samples that contained 10 wt.% MnO_2 catalyst precursor ($10Mn_xO_y$) had the best bifunctional performance towards ORR and OER and followed a four electron ORR pathway. While ZAB testing at 50 mA/cm^2 indicated a voltage gap was 1.72 and 1.47 for the $10Mn_xO_y$ composite and 20 wt.% Pt/C, respectively. The calculated power density showed peak powers at 48.3 and 69.0 mW/cm^2 for 10MnxOy and 20 wt.% Pt/C, respectively. Finally, the synthesis method to fabricate metal free catalysts was studied using precursors entirely derived from waste biomass. Nitrogen doping of the LIG was achieved using chitosan as a biomass-based nitrogen source and furfuryl alcohol as the carbon precursor. The resulting nitrogen-doped LIG (N-LIG) samples were tested towards ORR performance. Reducing the size of the chitosan by ball milling was found to be a necessary pretreatment step to improve the ORR performance. To the best of our

knowledge, this is the first work to utilize a nitrogen dopant in LIG for metal-free ORR electrocatalysis.

In summary, we demonstrated the feasibility of preparing high performance ORR catalysis by laser-induced carbonization and reduction of various one-pot synthesized composite resins based on the biomass-derived poly furfuryl alcohol system. Recipes for low Pt-content Pt-Co-based alloys, manganese oxides and nitrogen doped carbons were found to achieve performance comparable or exceeding many literature studies and will, hopefully, form the basis of future advancement for practical air cathodes recipes which hold promise for low-cost zinc-air batteries and related electrochemical systems.

Acknowledgements

“Be grateful for whoever comes, because each has been sent as a guide from beyond” Jalal ad-Din Rumi, 1207. During this transition I have many, many people to thank in long, long lists. The achievement of my PhD has been an extensive collaboration process. I could not have completed the journey without the help and encouragement of experienced mentors, supportive friends, and loving family.

First of all, I want to start by expressing my gratitude to my supervisor Professor Michael Pope, for his continuous support, mentoring, and encouragement throughout my Ph.D. studies. I am greatly impressed by his boundless enthusiasm and unquenchable thirst for academic research. Without his sincere guidance, I wouldn’t have been able to accomplish creating this PhD thesis.

I would like also to express my heartfelt appreciations to my Ph.D. thesis examining committee, including Professor Ali Elkamel, Professor Michael Fowler, Professor Anh Pham from the University of Waterloo, and Professor Drew Higgins as my external examiner from MacMaster University for the valuable time and contributions during this important process.

Special thanks go to Dr. Khalid Mahdi from Kuwait University for always giving me courage and for being my mentor with helpful advice for my graduate studies.

I also wish to thank my friends and colleagues, Mariam Gad, Dr. Marianna Uceda, and Dr. Manila Ozhukil for their encouragements and companionship in and outside of my school life.

Also, I am overwhelmed with gratitude for the immeasurable effect of my dearest friends; Mariam Ga, Marianna Uceda, Manila Ozhukil, Syeda, Gillian Hawes, Teri Sui, Mahshid Chekini, Nicholas Wilson, Nikolai Burton and Elizabeth Miller.

Most of all, my deepest gratitude goes to my parents, my sisters, and my kids for providing a tremendous wealth of unconditional love and sincere support as well as making my life enjoyable and delightful.

Finally, I would like to mention my gratitude to the University of Waterloo for their support. They provided excellent research opportunities during my Ph.D. and allowed me to stay focused on research.

Table of Contents

List of Figures

List of Tables

Chapter 1

Introduction

1.1 Scope and Challenges

Development of sustainable and clean energy resources is urgently needed due to the growing use of conventional fossil fuels and the resulting environmental pollution.[1,2] The energy demand by 2050 would triple that of today because the population would reach nine billion.[3] Reducing the requirement for conventional thermal power generation through the utilization of renewable energy sources could assist in reducing greenhouse gas emissions.[4] In response to the current rise in demand for more economical, sustainable, and renewable energy, several conversion devices are being developed with cutting-edge materials such as fuel cells and metal air batteries.

Zinc-air batteries have recently received a lot of interest due to their high theoretical energy density and low environmental impact. Zinc-air batteries (ZABs) are promising for application in large-scale, stationary energy storage. Because zinc has a greater reduction potential and a significant overpotential for hydrogen evolution, zinc-air batteries may be charged with a better current efficiency than Al/Mg equivalents. [5] Zinc is the 24th most prevalent element on the planet and is completely recyclable.[6] ZABs can provide a higher energy density (reach to 1350 Wh/kg)[7] than a Li-ion battery (reach to 1000 Wh/kg)[8,9] at half the price (90-120$ kW/h for ZAB).[10–12] Other advantages of the ZABs include safe operation and environmental friendliness because they do not contain flammable and hazardous organic electrolytes.

Both proton-exchange membrane (PEM) fuel cell and metal-air battery technologies rely on the oxygen reduction process (ORR), which is known for its sluggish kinetics. Therefore, to enable PEM fuel cells and metal-air batteries to be functional and feasible, ORR-active electrocatalysts must be utilized to speed up the electrochemical process. Therefore, over the last several decades, there has been a considerable increase in research on the synthesis and catalysis of catalysts for the oxygen reduction process (ORR) in electrochemical systems.[13,14] To date, platinum (Pt) and its alloys dispersed as nanoparticles on carbon black supports serve as the most efficient electrocatalyst for ORR, which favors the four-electron oxygen reduction reaction pathway to generate water. With only a modest quantity of hydrogen peroxide produced, platinum has the lowest overpotential and the maximum selectivity for the direct oxygen reduction.[15,16] However, platinum-based materials are costly, accounting for up to 50% of the total cost of a fuel cell and a metal-air battery.[15] Alternatively, several studies have been carried out on transition metals, metal oxides, and carbon-based materials as electrocatalysts for ORR due to their attractive physical and electrochemical characteristics.[17,18]

To develop new ORR catalysts, two strategies have been proposed and extensively researched: (1) using less platinum by alloying platinum with other transition metals; and (2) entirely switching out platinum-based catalysts for non-precious metal catalysts such as manganese oxide or doped carbon with heteroatoms such as nitrogen.

There are several advantages of platinum-transition metal alloy (Co, Ni, etc.) over pure platinum such as lower platinum content, lower price of the obtained catalyst, better catalytic activity, stability and durability under harsh electrochemical conditions relevant to fuel cell and metal air battery operations.[19–21] Polycrystalline Pt films alloyed with various transition metals were explored by Norskov *et al.* and Stamenkovi *et al.;* Pt_3Co was discovered to be the most active of those investigated, with a specific activity 3–4 times greater than Pt.[22,23] Despite their many advantages, platinum-transition metal alloys can present some challenges in their production and use. Such as; processing difficulties due to their high melting points and high reactivity with other materials, and specialized equipment and processes could be required to produce high-quality alloys. Generally, the difficulties posed by platinum-transition metal alloys could be manageable and handled with careful planning and specific methods. These alloys have special qualities and advantages that make them indispensable in a wide range of sectors and uses.

Alternatively, in terms of entirely moving to a non-Pt system, manganese oxides and oxyhydroxides offer an attractive replacement for the precious metal-based electrodes under basic conditions, due to their availability, low cost, and proven ability to catalyze both the oxygen reduction reaction (ORR) and the oxygen evolution reaction (OER) at high pH values.[24,25] When comparing manganese's abundance and price to that of platinum and iridium, manganese is about six orders of magnitude more abundant in the earth's crust and three to four orders of magnitude less expensive.[26] In summary, because of its low price, excellent stability, and availability, manganese dioxide (MnO_2) is a viable ORR catalyst for ZABs. Although there are still challenges with its low activity compared to platinum, research is constantly being done to improve its performance and make it more suitable for usage in energy storage applications.

It has been demonstrated that incorporating heteroatoms such nitrogen, oxygen, sulfur, phosphorous, and boron enhances the electroactivity of carbon-based materials. The nitrogen-doped graphene catalyst has recently been shown to have exceptional ORR catalytic activity that is comparable to Pt catalysts for ORR and has potential as an ORR catalyst due to its low cost, high stability, and high efficiency.[27] By pairing with the lone pair electrons from the N dopants, nitrogen atom doping in graphene can activate the carbon $\boldsymbol{\pi}$ electrons, reducing oxygen molecules on the positively charged carbon atoms nearest to them.[28] While nitrogen-doped carbon (N-C) catalysts for the oxygen reduction processes in ZABs appear to hold promise as alternatives to platinum-based catalysts, a number of obstacles need to be removed in order to enhance their functionality and make them widely available for commercial application. The key issues that researchers work to address are low activity, complicated synthesis, and nitrogen content optimization.[29–31]

As will be discussed in more detail in the upcoming sections, most of the ORR catalysts impose several limitations due to the complex fabrication methods that required special conditions, high catalysts precursor needed, low stability achievement, and poor ORR performance. Moreover, one of the serious challenges of embedding the catalyst in a carbon or graphene matrix as an ORR catalyst is the high temperature required in the furnace under inert gas. Using the laser induced graphene technique to carbonize the graphene precursor at ambient conditions instead of furnace under inert gas has been recently an interesting object for many researchers due the advantages of the laser induced graphene (LIG) technique that will be discussed in detail in the next chapters. However, using the LIG technique to fabricate air cathode was rarely explored due to the common casting method used to deposit the catalysts on the LIG. Casting the catalysts on the LIG caused limited stability, and aggregation/dissolution of the catalyst on/from the LIG substrate that cause a decrease in the device performance of the catalyst/LIG over time.

Therefore, the main goal of this research is the development of highly active nanostructured ORR catalysts decorated on a biomass derived three-dimensional LIG. This will be achieved by carbonization of carbon forming resins containing various precious and non-precious metal catalyst precursors that could be laser converted to high surface area carbon/catalyst composites. The research focuses on using a biomass-derived polymer which is poly furfuryl alcohol as a graphene precursor and entrapping the mentioned catalysts in the polymer matrix using a new and simple synthesis method under amber condition to improve the catalytic activity and stability forward ORR process . The specific objectives of my thesis are provided in the following section.

1.2 Thesis Objectives

This work will investigate the synthesis of different ORR catalysts using laser scribing of biomass polymer as graphene precursor with entrapped catalyst precursors. The main objectives are to:

1. Development of a furnace-free, ambient processed, laser scribing process for the synthesis of graphene embedded with ORR electrocatalyst.
2. Use a biomass polymer as LIG precursor instead of commonly used polyimide (Kapton) precursor.
3. Simultaneously incorporate ORR catalyst precursor in a carbon precursor resin filled that will be reduced during lasering leading to catalyst entrapped in LIG that would overcome the agglomeration/leaching issues caused by casting catalysts on the LIG.
4. Reduce the amount expensive Pt in LIG by alloying or replacing with inexpensive ORR active transition metal.
5. Understand the factors influencing how the catalyst structure evolves in LIG during laser scribing.
6. Provide insights on the effect of irradiation carbonization on the crystalline structure/phases of the embedded catalysts.
7. Simultaneously dope heteroatom in LIG (nitrogen) using biomass nitrogen source .
8. Test their electrocatalytic performance of LIG/catalysts for an air-cathode application in zinc air battery.

To achieve these goals, a series of catalyst design strategies that may boost the activity and durability performance of LIG/catalysts and nitrogen doped LIG materials toward ORR were explored as will mentioned in the next chapters.

Chapter 2

Background

2.1 Zinc-Air Battery (ZAB)

Metal-air batteries are an attractive electrochemical energy storage technology due to their high energy density and the fact that atmospheric oxygen is one of the reactants. The two metals that have drawn the most interest as anode materials are lithium and zinc, with zinc providing safety benefits over lithium over its highly reactive counterpart in addition to being abundant and totally recyclable. Moreover, when zinc is used as an anode metal in a metal-air battery, it offers benefits over other candidate metals in some of the following areas: production cost, polarization and stability, parasitic corrosion, uniformity dissolution, reactivity, tolerable rechargeability, practical handling, and safety.[32] Zinc-air battery (ZAB) storage presently costs \$90- \$120 per kWh, partly because zinc is less expensive than large-scale lithium ion energy storage, which costs around \$200 to \$250 per kWh.[33]

A ZAB typically consists of four components: a separator, an alkaline electrolyte, an air electrode with a gas diffusion layer (GDL) coated with catalyst, and a zinc electrode (**Figure 1.1**). As can be seen, through an external circuit, a negative Zn electrode is connected to a positive air electrode, and an ionically conductive electrolyte (typically an alkaline solution) serving as the electrochemical channel connecting the two electrodes. When the battery discharges, the Zn electrode oxidizes according to Equation 1.1, supplying a flow of electrons to the external circuit in the process.[34,35]

Oxygen reduction reaction occurs though two pathways as shown in Equations 1.4 and 1.5: either O2 reduced by 4 electrons pathway into H_2O or by two-electron pathway into H_2O_2. In an alkaline electrolyte, the four-electron ORR pathway is preferred. In the two-electron pathway, oxygen is reduced by two electrons to form superoxide radicals (O^{2-}), which react with water to form H_2O_2. Superoxide radicals are highly reactive and can cause degradation of the battery components, which is one of the main drawbacks of this pathway. The four-electron pathway is more efficient than the two-electron pathway in terms of energy conversion, as it requires a lower overpotential (i.e., the excess voltage needed to drive the reaction) to proceed. This means that the four-electron pathway can achieve a higher current density at a given voltage, leading to a higher power output. Moreover, the four-electron pathway produces only water as a byproduct, whereas the two-electron pathway produces hydrogen peroxide, which can build up and cause corrosion of the fuel cell and metal-air batteries components over time.[36] Finally, the four-electron pathway is more chemically stable than the two-electron pathway in an alkaline electrolyte. This means that the four-electron pathway is less susceptible to poisoning by contaminants, which can interfere with the reaction and reduce the efficiency of the battery or the fuel cell.[37,38] Overall, the four-electron pathway is a better option for ORR in an alkaline electrolyte as it is more efficient, produces only water as a byproduct, and is more chemically stable, leading to a longer-lasting and more reliable battery.

As shown in **Figure 2.1**, the oxygen reduction reaction (ORR), which oxygen is fueled by the ambient outside air, consumes the electrons once they travel the load in the external circuit and arrive at the air electrode according to Equation 1.4, 1.5 and 1.6. The diffusion of hydroxide (OH^-) ions created at the air electrode and consumed at the zinc (Zn) electrode maintains charge balance within the electrolyte (Equation 1.1,1.2, and 1.3). The overall chemical reaction yields a theoretical cell voltage of 1.65 V (Equation 1.6). During charge, by an external power source, the flow of electrons is reversed, and the processes described by Equations 1.1–1.7 take, releasing oxygen back into the environment.[39,40]

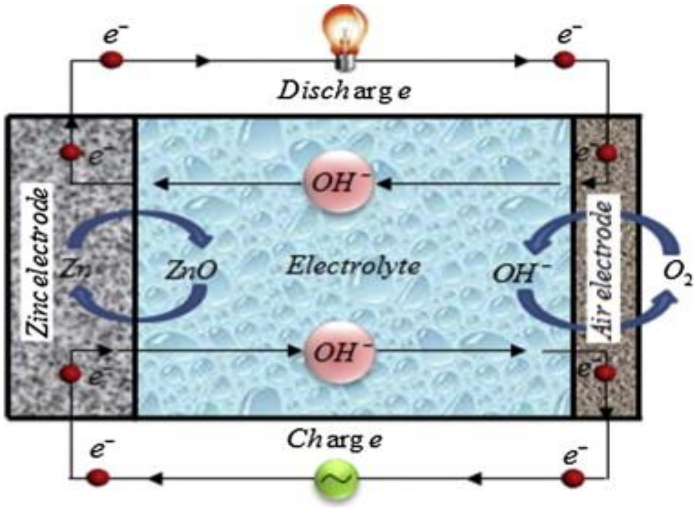

Figure 2-1 Bi-electrode-based zinc-air battery schematic view.[41]

Zn electrode reactions:

$Zn + 4OH - \Leftrightarrow Zn(OH)_4{}^{2-} + 2e^-$ (Equation 1.1)

$Zn(OH)_4{}^{2-} \Leftrightarrow ZnO + 2OH^- + H_2O$ (Equation 1.2)

Overall:

$Zn + 2OH^{-} \Leftrightarrow ZnO + H_2O + 2e^{-}$ (Equation 1.3)

Air electrode reaction:

4 electrons pathway: $O_2 + 2H_2O + 4e^{-} \Leftrightarrow 4OH^{-}$ (Equation 1.4)

2 electrons pathway: $O_2 + H_2O + 2e^{-} \Leftrightarrow 2HO_2^{-}$ (Equation 1.5)

$HO_2^{-} + H_2O + 2e^{-} \Leftrightarrow 3OH^{-}$ (Equation 1.6)

Overall cell reaction:

$2Zn + O_2 \Leftrightarrow 2ZnO, E^{\circ}_{cell} = 1.65 V$ (Equation 1.7)

Total energy efficiency and long-term cyclability of ZAB, which are currently less than a fifth of those of commercially available lithium-ion batteries, are the major impediments preventing them from being used in practical applications.[42] The air electrode is the crucial component that dictates the battery's performance, where the conversion of oxygen and metal hydroxide occurs. The primary causes of ZABs' high polarization and poor electrode reversibility are their inherently slow reaction kinetics (as mentioned above), which include oxygen evolution reaction (OER) during charging and oxygen reduction reaction (ORR) during discharging. Thus, the rational design of effective bifunctional oxygen catalysts has received a great deal of attention from researchers in an effort to improve battery performance by accelerating reaction kinetics and reducing discharge/charge overpotentials.[43]

While in principle ZABs show a lot of promise, several technological challenges from each component of the system face their own challenges and need still to be resolved. The challenges associated with air electrode, zinc electrode, and electrolyte are briefly discussed in the next sub-sections.

2.1.1 Anode Electrode Challenges:

In a zinc-air battery, there are four main phenomena that restrict the performance of a zinc electrode:[44]

- Dendrite expansion: At the anode, due to the high solubility of the zincate ions, it is difficult to reduce them on the zinc electrode surface, causing a morphology change on the surface of Zn electrode or dendrite growth during discharge-recharge cycling. Dendrites could lower the battery capacity and could cause a short circuit if penetrated through the separator.[45]
- Passivation and internal resistance: During the discharge process, ZnO that has been supersaturated in alkaline electrolytes can be deposited on the surface of the zinc electrode creating an insulating layer, blocking the electrode's surface and interfering with the electrode's subsequent reaction by hindering migration of the discharge product and/or OH^- ions. This process is known as passivation.[46] Passivation will reduce the Zn electrode's use, which will lead to a reduction in discharge capacity. In addition to raising the zinc electrode's internal resistance due to its nonconductive nature, ZnO also causes voltage losses during discharge and voltage gains while charging.
- Hydrogen evolution: the Zn/ZnO has a more negative standard reduction potential than the evolution of hydrogen gas, therefore, the zinc electrode at rest, will corrode over time and self-discharge because hydrogen evolution is thermodynamically favored. As a result of internal swelling caused by the created hydrogen, the battery's internal pressure will rise and cause damage.[47]

There are several factors can determine the best solutions and techniques for enhancing zinc-electrode performance such as:

- Increasing the surface area of the electrode could reduce the zinc-deposition overpotential, which could decrease the dendrite during charging. Parker et al. designed porous three-dimensional zinc anode with a high specific and volumetric capacity density. At high currents, this electrode proved capable of up to 90% zinc utilization and more than 80 charge-discharge cycles without any noticeable dendrite growth.[48] However, the rate of hydrogen evolution rises with exposed surface area, which is one drawback of utilizing a zinc electrode with a high surface area. Therefore, when researchers create zinc electrodes with greater and larger surface areas, attention to hydrogen-evolution reduction techniques must rise.

- Due to their conductivity and strong chemical resistance to alkaline conditions, carbon-based additions (most frequently carbon black) have been used to reduce the resistance of zinc electrodes. Masri et al added 2 wt.% carbon black to their porous zinc electrode which improved the specific discharge capacity, enhanced the zinc utilization (from 68% to 95%), and stabilized the voltage (1.4 V).[49]

- An effective way to reduce anode corrosion is modifying the Zn electrode's composition. Various heavy metal elements, including as Cd, In, Sn, Ti, Pb, and Bi (or their oxides), have been investigated as Zn electrode additions.[44] Moreover, these additives increase the conductivity and current distribution inside zinc electrodes. Aremu et al. fabricated a zinc electrode by mixing 30 wt.% Zn: 3 wt.% bismuth oxide: 10 wt.% potassium sulfide: 5 wt.% lead (II) oxide additives. The zinc electrode exhibited low dendrite growth, less corrosion rate, and excellent capacity.[50]

- The corrosion behaviour of Zn electrodes might be successfully changed by changing the electrolyte. Many investigators use a KOH electrolyte that is pre-saturated with $Zn(OH)_4^{2-}$ ions (usually by dissolving ZnO powder). Xiao et al. added organic additives like benzotriazole (BTA), thiourea (CH4N2S), and sodium dodecyl benzene sulfonate (SDBS) one at a time to the electrolyte in order to decrease the corrosion rate of zinc-air batteries and improve the charge and discharge performance of the zinc electrode. The zinc-air battery's cycle life and charge-discharge performance were both considerably enhanced, and the zinc electrode's corrosion inhibition effectiveness was 76.9%.[51]

- An additional technique to extend cycle life is to coat the surface of the zinc electrodes. Coating should prevent or significantly slow down $Zn(OH)_4^{2-}$ migration outward during the discharge process while permitting enough OH ion migration to facilitate the charge and discharge processes. Moreover, In order to prevent self-discharge and enhance the electrochemical performance of ZABs, Lee et al. coated a zinc electrode with a thin layer of aluminium oxide (Al_2O_3). This coating reduced the hydrogen evolution reaction and zinc-electrode corrosion and enhanced the stability of ZABs, while maintaining battery performance.[52]

However, many of the zinc-electrode improvement techniques discussed above need to be investigated for long testing periods to demonstrate that they qualify for a variety of battery applications.

2.1.2 Electrolyte Challenges

The electrolyte's role in the charge/discharge process is to provide fast ion conduction. The electrolyte controls the electrochemistry of ZABs because it is necessary for the transfer of active species, such as $Zn(OH)_4^{-2}$ and oxygen intermediates, which are essential for the output power density and energy density. The ideal electrolyte should have high ionic conductance, low electronic conductivity, robust chemical stability, and low cost. Aqueous alkaline electrolytes (e.g., aqueous potassium hydroxide (KOH) solutions) are often used as electrolytes for zinc-air batteries, primarily due to their superior ionic conductivity, greater oxygen diffusion coefficients low viscosity and interfacial characteristics than other acidic and neutral electrolytes. Alkaline electrolytes have a higher overpotential for HER compared to other electrolytes, making them more favorable for zinc-air batteries. The use of acidic electrolytes can accelerate the corrosion of the zinc electrode, leading to premature battery failure. Alkaline electrolytes, on the other hand, provide better protection against zinc corrosion due to their higher pH levels. Therefore, we used alkaline in the three project mentioned in chapter 3,4, and 5.

The ionic conductivity of a ZAB is greatly influenced by the alkaline content. Poor reaction activity and high ion-transfer impedance of the electrolyte would be seen when the alkaline concentration is relatively low, and large alkaline concentrations would also limit ion-transport because of the electrolyte's high viscosity.

However, carbon dioxide in the air readily dissolves in the electrolyte continuously reducing the pH and eventually precipitating carbonates. These can block pores within the gas diffusion layer (GDL), and hamper oxygen diffusion to the catalyst surface causing an increased polarization and shortening the life of the battery.[46,53]. For more details, the crystallization of carbonates in the porous air electrode follows the reactions below:

$CO_2 + OH^- \rightarrow CO_2^{-3} + H_2O$ (equation 1.8)

$CO_2 + KOH \rightarrow K_2CO_3 + H_2O$ (equation 1.9)

Because HCO_3/CO_2^{-2} has less mobility than OH does, the aqueous alkaline electrolyte's ionic conductivity decreases as a result of the carbonation process. It eventually damages the cathode, which results in performance degradation. Moreover, due to the development of carbonates, the OH^- content decreases, which has an impact on the conductivity and viscosity of the electrolyte. As a result, the electrolyte's viscosity becomes higher, and the oxygen transport becomes challenging, which degrades the bifunctional air cathode's oxygen reduction reaction (ORR).[54] Another electrolyte challenge is the high $Zn(OH)_4^{-2}$ solubility in alkaline electrolytes which cause zinc passivation and dendritic development on Zn anode during battery charge, lead to low battery performance. The development of electrolytes faces significant obstacles as well as possibilities due to the growing need for high-performance, flexible, durable, and rechargeable zinc-air batteries.[55]

2.1.3 Air Electrode Challenges:

For air electrode, low-cost, and efficient bifunctional electrocatalysts are needed to mediate the oxygen reduction and oxygen evolution reactions (ORR/OER). Since both the ORR and the OER exhibit significantly large overpotentials, the development of a highly bifunctionally active air electrode is rather difficult and strongly relies on an effective bifunctional electrocatalyst for successfully promoting both the ORR and the OER processes. Additionally, the electrode materials must be able to withstand both strong reducing conditions during oxygen reduction at high current rates and extremely oxidative situations during oxygen evolution. It has been suggested that using decoupled air electrodes for the appropriate ORR and OER will increase the battery cycle stability.[56] The critical GDL tasks are mass transport-related; oxygen diffuses to the catalyst layer with minimum resistance while preventing electrolyte from blocking the pores and flooding the cell. A relatively hydrophilic catalytic layer and a hydrophobic gas diffusion layer (GDL) are the basis construction of the bifunctional air electrode. In addition to providing conductive and physical support for the catalysts, the GDL also serves as a passageway for oxygen diffusion during charging and discharging, respectively. Since the oxygen reduction reaction (ORR), diffusion of ionic species, and conduction of electrons are all important modes of transport phenomena, the performance is greatly influenced by the characteristics of the porous air electrodes. The triple phase boundary (TPB), which marks the point of contact of the solid, liquid, and gas reaction phases, has a major effect on the kinetics of discharge and charge processes. Constructing appropriate electrode design to increase the TPB and creating active air catalysts to speed up ORR kinetics could both significantly improve battery discharge performance. In published work by Yu et al., they investigated how increasing the triple phase boundary can increase the cathode's rate of reaction. In their research, they used PTFE to treat one side of a carbon paper while growing a nickel iron layered double hydroxide catalyst on the other surface. They improved the TBP by creating 3D multiphase reactive interface by the asymmetric development of electrocatalysts inside the cathode, which significantly increased the number of functional active sites, sped up mass transfer, and improved interfacial stability.[57]

In addition, the flooding of the air electrode and loss of the triple phase boundary might result from the high OER potential that gradually oxidizes the electrocatalysts, porous conductive carbon, and the gas diffusion layer. The oxidative corrosion of the air electrode during the charging process is the main reason for the battery's performance degrading throughout cycle operations.

Studying deteriorated cathodes, where hindered mass transport results in a drop in cell performance, makes the importance of the mass transport features in zinc-air cathode performance apparent. The electrode structure which is designed for effective mass/charge transportation, is crucial to the performance of the zinc-air battery. In zinc-air batteries, mass transfer losses occur at the air cathode because oxygen must permeate through the cathode to cross TPB at active sites to participate in the reaction. Moreover, utilizing oxygen from air, while practical and economical, is a problem since the oxygen concentration is only about 20% and even lower if the air is fully humidified. This results in a low mass transfer driving force. The electrode's porosity and permeability affect the ease with which oxygen can penetrate the electrode structure. Higher porosity allows for increased gas flow and easier diffusion of oxygen which improves the mass transfer of oxygen to the catalyst. When a high concentration of KOH (> 7 M) used, more OH- is engaged in ORR kinetics and this increases the value of the exchange current density. Hhowever, the diffusion of O_2 to the TPB will be restricted, leading to increased concentration polarization losses. Therefore, optimizing the electrode structure, catalyst activity, electrolyte saturation, and operating conditions are key strategies to enhance oxygen mass transfer and improve the performance of zinc-air batteries.

Another important challenge facing the air cathode is the peroxide production during the 2 electrons ORR pathway. Because of its high oxidizability, the peroxide accumulation not only decreases the ORR catalysis's effectiveness but also contaminates the catalysts or carbon support materials. Therefore, a bifunctional catalyst with excellent selectivity may catalyze both oxygen reduction by using the four-electron transfer pathway to generate the needed OH specie and oxygen evolution by excluding CO_2 evolution (caused by carbon oxidation if the catalyst is carbon-based).

An ineffective catalyst with a tendency towards the two-electron route will result in a higher concentration of peroxide ions in the electrolyte. According to equation (1.10), the peroxide ions may move towards the zinc electrode during the discharge process with completely reduced hydroxide ions and then directly interact with the zinc electrode to cause self-discharge that reduce the specific capacity.

$Zn + HO_2^- \rightarrow ZnO + OH^-$ equation (1.10)

Carbon corrosion processes occur in alkaline air electrodes in two different ways. The first is an electrochemical carbon corrosion reaction, which arises from the fact that the air electrode reaction's (Eq. 1.11) potential is significantly larger than that of the carbon corrosion reaction equation (Eq. 1.12). The second is a chemical reaction that is brought on by hydrogen peroxide's (HO^{2-}) great oxidizability; it is a stable intermediate product of the oxygen reduction reaction (ORR) (Eq. 1.5).

$O_2 + 2H_2O + 4e^- \rightarrow 4OH^-$, E^o= 0.401 V vs. SHE equation (1.11)

$CO_3^{2-} + 3H_2O + 4e^- \rightarrow C + 6OH^-$, E^o = -0.584 V vs. SHE equation (1.12)

The two-electron ORR pathway caused peroxide to form, which then diffused into the electrolyte. The bonding between the catalyst particles, carbon, and other catalyst components is oxidized by the peroxide during this sluggish diffusion. This degradation, the main contributor in ZAB deterioration, blocked the pores, increased resistance, and decreased the ORR catalyst's active surface area.

The sluggish oxygen reduction reaction in the air cathode causes a large overpotential, which is the main reason for the decreased cell voltage (1.65 V) of ZAB, as shown in **Figure 2.2**. The practical voltage of the ZAB is less than 1.65 V because the electrochemical polarization at the air electrode is higher than the polarization at the Zn electrode. There are two types of electrode polarization: ohmic polarization, which is carried on by the electrode's electrical resistance, and electrochemical polarization of ORR. The catalysts, the substrate and the catalysts contact, could cause electrode resistance. While activity of the catalysts caused the electrochemical polarization.[58] Moreover, because the ZAB works as an open system, the impurities from air could poison the catalysts.

The slow oxygen reduction reaction (ORR) and the restricted reactant diffusion to the catalytic active sites on the cathode side have caused the cell to become highly polarized, which limits the maximum power the cell is capable of producing.

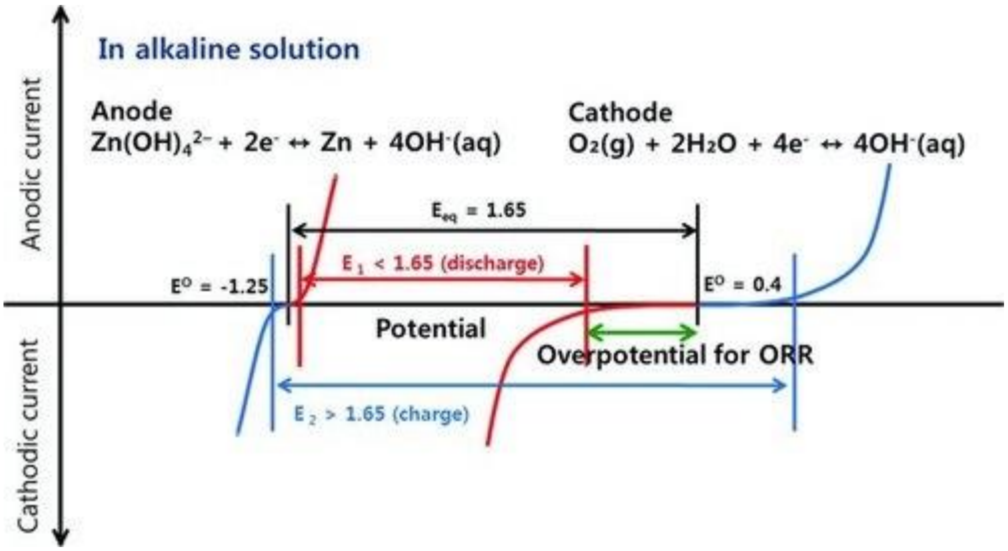

Figure 2-2 Schematic diagram the zinc-air cell's polarization curves. Although the zinc-air cell's equilibrium potential (black line) is 1.65 V, the practical voltage during discharge (red line) is less than 1.65 V as a result of the slow ORR. ZABs require a large potential, more than the equilibrium potential (blue line).[41,59]

2.2 Electrocatalysts for Air Electrode

ZAB's ability to be electrically recharged is made possible by fundamental electrochemical processes that reduce and evolve oxygen in alkaline conditions. Both oxygen reduction (ORR) and evolution (OER) reactions require four fundamental chemical steps; ORR involves first forming HOO* from adsorbed O_2, then reducing it to O* and HO*, whereas OER involves their backward reactions.[60,61] The sluggish kinetics of these reactions necessitates an active bifunctional oxygen electrocatalyst, with low overpotential to accelerate the rate of these reactions. Noble metals such as platinum, ruthenium, iridium and their oxides are regarded as the benchmark material for the ORR and OER electrocatalysis, respectively,[62,63] as these catalysts require low overpotentials (284 mV on Pt/C for ORR and 250mV on RuO_2 for OER in 0.1M KOH).[63–65] However, employing them for large-scale application is not viable due to high cost, limited bifunctionality and stability.[66,67]

In this research, we will focus on the air cathode catalysts because ORR is a limiting half-cell reaction for ZABs. ORR involves reduction of molecular oxygen during the discharging process. However, it is highly challenging to electrochemically break the O = O bond since it has a very high bond energy of 498 kJ mol^{-1}.[68] Currently, expensive carbon-supported platinum (Pt) nanoparticle based electrocatalysts (Pt/C, with Pt loading up to 60 wt.%) are employed to achieve acceptable rates for the electrochemical ORR.[69,70] Even though, Pt/C is a highly active catalyst for ORR, it often suffers from limited stability during charge/ discharge cycling, and the aggregation/dissolution of the Pt/C on/from the substrate causes a decrease in the device performance of the Pt/C over time.[71] Commercial Pt/C catalysts undergo degradation as a result of corrosion and dissolution during the demanding electrochemical process. Meanwhile, at high voltage, the carbon support is heavily oxidized, which causes the Pt nanoparticles to detach and (or) aggregate, losing the stability.[72] Furthermore, the high price of the Pt/C, scarcity, and susceptibility to poisoning limit its widespread application. For all these reasons, highly active, scalable, low-cost, stable and efficient bifunctional catalysts are essential for a ZAB.

Towards this direction, several research efforts have been reported. For example, Huang *et al*. summarized the strategies used to develop and improve the activity of Pt-based catalyst toward ORR as follows: [73]

1. Introduce transition metals such as Co, Fe, and Ni to form alloys to reduce the consumption of Pt and improve intrinsic activity and the stability.[74] The overall aim of Pt based alloy catalysts is to have nanoalloy PtM (M= Co, Ni, Fe) that form overlayers with catalytic activity and stability larger than of Pt and to lower the cost of the catalyst.[75,76] There are several explanations for the enhancement in the ORR electrocatalysis on PtM nanoalloys such as:[77]
    a. increasing in Pt surface area due to dissolution of non-noble element in Pt alloy.[78]
    b. more advantageous Pt-Pt interatomic distance.[79]
    c. greater Pt d-band vacancy.[80]

   Overall, the Pt nanoalloy technique shows promise for creating more effective and durable ORR catalysts, and further study in this area is required to fully realize the potential of this technology.

2. Increase the number of unsaturated active sites by improving the Pt-based catalyst's surface and morphology. For example, using nanoscale particles of Pt can increase the surface area and expose more active sites. Additionally, changing the shape of Pt nanoparticles to more open structures such as octahedra, cubes, or truncated octahedra can also expose more unsaturated sites and improve ORR performance.[81] By improving the surface and morphology of Pt-based catalysts, researchers hope to enhance their catalytic activity, reduce the amount of Pt required

for efficient ORR, and improve their durability and stability over long-term operation. This may have substantial effects for the advancement of more affordable and effective ZABs.

3. Enhance the graphitization degree of the carbon supports. The degree of graphitization, which can increase the conductivity and stability of the catalyst, describes how well the carbon support is structured in a crystalline structure resembling graphite.[82] Graphitized carbon materials have a more crystalline and organized structure than non-graphitized carbon materials, which can improve their mechanical and thermal stability as well and surface area. These characteristics may help the ORR catalyst function better and last longer. There are several ways to enhance the graphitization degree of carbon supports for Pt-based catalysts, including:
    a. Pyrolysis: heating the carbon support at high temperatures in an inert atmosphere can induce graphitization by removing the amorphous carbon and creating more ordered graphitic structures. The degree of graphitization can be controlled by adjusting the temperature and duration of the heat treatment.[83]
    b. Doping: Introducing dopants such as nitrogen, boron, or phosphorus into the carbon support can also enhance the graphitization degree. This is because the dopants can act as nucleation sites for the graphitic structure and promote the growth of ordered domains.[84]
    c. Templating: Using a template to direct the growth of the carbon support can also lead to higher graphitization degree. For example, using a hard template such as silica or alumina can create ordered channels in the carbon support, which can then be graphitized by pyrolysis.[85]

All of the above methods to improve the Pt-based catalyst are cost-effective and could enhance the ORR performance.

Developing an effective and stable catalyst for air cathodes in ZABs is a challenging task that necessitates careful consideration of many aspects such as; stability, activity, selectivity, cost, reproducible, and durability. Therefore, this thesis focuses on air cathode fabrication using a facile synthesis of platinum/cobalt oxides, manganese oxides, nitrogen doped graphene materials by using a laser-based technique to produce efficient cathode catalysts for rechargeable zinc-air batteries. Carbonization of biomass polymer that loaded with catalyst precursors by CO_2 laser at ambient conditions, instead of using furnace under inert gas and at high temperature, to produce laser induced graphene doped with catalysts in nanoparticle size, with excellent distribution, and in different controllable patterns. We developed a simple fabrication method to prepare platinum and cobalt oxides ($PtCoO_x$) nanoalloys and core shell nanoparticles loaded in biomass derived laser induced graphene (LIG) as ORR catalyst. The $PtCoO_x$ nanoalloy and core shell nanoparticles loaded in laser biomass-induced graphene with excellent distribution was accomplished and ORR/OER performance was investigated. Alternatively, manganese oxides as an ORR catalyst were developed and fabricated using one-pot synthesis method. Finally, doping the laser induced graphene with nitrogen was prepared by using biomass nitrogen precursor.

2.2.1 Platinum- based nanoalloy catalysts

Arguably, the most practical method to lower the Pt loading in ZAB cathodes is to make Pt more active by alloying it with other metals. Since Pt alloys were discovered at United Technologies Corp. as superior ORR fuel cell catalysts in the 1980s, they have gained a lot of interest and are now regarded as the second generation of fuel cell catalysts after pure Pt.[86–89] $PtNi_x$, $PtCo_x$, $PtFe_x$, and dealloyed $PtCu_x$ have all undergone comprehensive testing for the ORR in fuel cells.[90,91] These catalysts performed significant improvements in activity higher than pure Pt.

The higher ORR activity of Pt alloys has been attributed to a variety of factors as mentioned by Shoa *et al*.[92]. For instance, compressive strains resulting from shorter Pt–Pt bonds,[93,94] downshifting the Pt d-band center or changing the d-band vacancy owing to strain and ligand effects,[95,96] higher surface roughness brought on by the dissolution of the transition metal,[97] delayed oxide species formation,[98] all lead to better ORR activity.

To understand the activity of Pt alloys for ORR, the stability of the intermediates was investigated by many researchers.[99–103] The four electrons pathway ORR is a demanding reaction to catalyze because each oxygen molecule must receive a transfer of four electrons. OOH*, O*, and OH* are three of the intermediates that the catalyst must moderately bind to, in a 4-electrons ORR pathway. **Figure 2.3a** shows the measured activities of Pt alloys (Pt_3Ni, Pt_3Co, Pt_3Fe, Pt_3Ti, Pt_3Y, Pt/Pd) and pure Pt as a function of oxygen adsorption energy as a volcano-like plot . It demonstrates that a surface with an oxygen binding energy that is 0.0–0.4 eV less than that of Pt (111) should have higher ORR activity than Pt. This could be a guidance to improve Pt-based nanoalloy as ORR catalyst**.** Each intermediate's stability increases linearly as oxygen binding energy increases. On the weak binding side and the strong binding side of the “volcano” type relationship, OOH*, $* + O_2 + H^+ + e^- \rightarrow OOH*$, and OH*, $*OH + H^+ + e^- \rightarrow * + H_2O$, respectively are potential determining (* is the vacant active site). Note that, the oxygen binding energy was estimated from $\Delta E_O - \Delta E_O^{Pt} \approx 2(\Delta E_{OH} - \Delta E_{OH}^{Pt})$. As can be seen from the plot, at the volcano's peak, the ideal catalyst should have an oxygen binding energy that is about 0.2 eV weaker than pure Pt. Alloying Pt with another metals results a better activity compared to Pt due to their reduced contact with O. As a result, weakening the bonding of the intermediates to the surface atoms of Pt is the major result of alloying Pt with another metal. Theoretically, as shown in **Figure 2.3a,** Ni and Co are the two most promising elements for maximizing the binding free energy of adsorbed oxygen-containing species on Pt.[104] **Figure 2.3b** demonstrates that the Pt_3Co alloy catalyst is the optimum replacement for the traditional Pt/C catalyst. Furthermore, from the locations of Pt_3Ti and Pt_3V in the plot, it can be concluded that the d-band centre is too far from the Fermi level, the surface possesses lesser coverage of OH_{ad} and anions, while the binding energy of O_2 and the intermediates are too weak to enable a turnover rate of ORR.[105] Thus, it is crucial and effective to optimize the binding free energy of oxygen-containing species on surface-active sites when designing Pt-based catalysts in order to improve ORR performance.

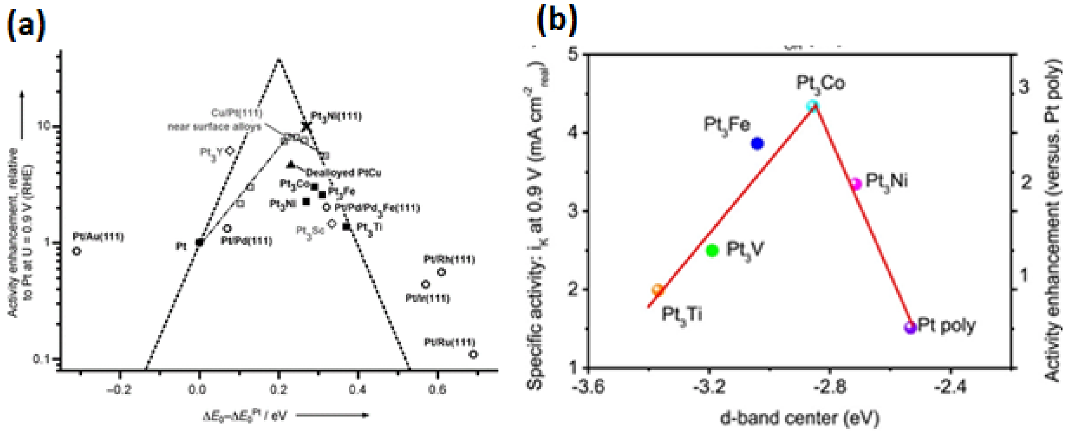

Figure 2-3 (a) Volcano plot for various catalysts with overlayers of Pt, demonstrating experimental ORR activity improvement in relation to oxygen binding energy EO and both in relation to pure Pt. All data point is at U=0.9 V. (RHE). [106] (b) Relationships between the various ORR activities that were determined experimentally on Pt3M surfaces in 0.1 M HClO4 at 333 K and the location of the d-band centre on the Pt-skin surface.[107]

There are numerous methods used to prepare PtM (M= Co, Ni, Fe) nanoalloys such as:

1. Electrodeposition: A substrate or glassy carbon is immersed in an electrolyte solution containing Co salt, and an electric current or voltage is applied to deposit Co on the substrate followed by electrodeposition of Pt using Pt precursor as shown in **Figure 2.4**.[108,109]

2. Seed-mediated growth: As shown in **Figure 2.5**, this method involves the formation of homogeneous nucleation by the growth and depositing the atom directly on performed seed.[110]

3. Gas-phase Synthesis: In this approach, the precursor materials are suspended in a gas phase, converting them to small clusters followed by imposing these clusters to grow to nanoparticles, then collecting the nanoparticles. [111]

4. Solvothermal Synthesis: This method involves a reduction reaction in a solvent at high temperature and pressure in a sealed vessel. Then the mixture allowed to cool down at ambient temperature before sonicating it with carbon support to minimize nanoparticle aggregation.[112,113]

5. Template-assisted synthesis: This method involves depositing Pt and other metal precursors onto the surface of the template. The template is fabricated with desired shape and size and made of solid such as silica, alumina , and polymer or a nonporous membrane. Then the reduction reaction is done by heat or reducing agent. Finally, the template is removed, leaving behind the Pt nanoalloys. This method controls the shape and size of the nanoalloys. [114]

6. Sol-gel: This process involves the reaction of metal precursors that dissolved in water or alcohol to form a gel-like material by heating or/and stirring. Then the gel is dried and calcined to produce the nanoalloy.[115]

7. Chemical Vapor Deposition (CVD): This method is widely used, where the gas or vapor precursors react with a substrate to produce the nanoalloy at high temperature and vacuum in chamber.[116]

8. Physical Vapor Deposition (PVD): This process is used to evaporate the metal elements in a vacuum chamber then deposit the evaporated elements on electrically conductive material or condense on a substrate to form the nanoalloy.[117]

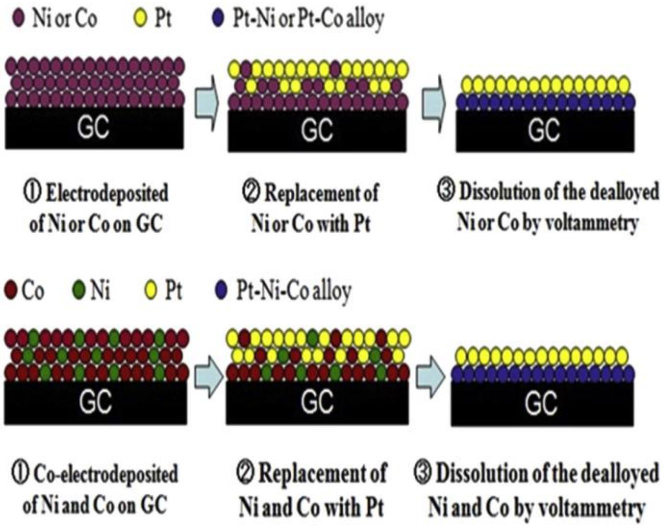

Figure 2-4. Steps of the electrodeposition method of different metals on the glassy carbon.[108]

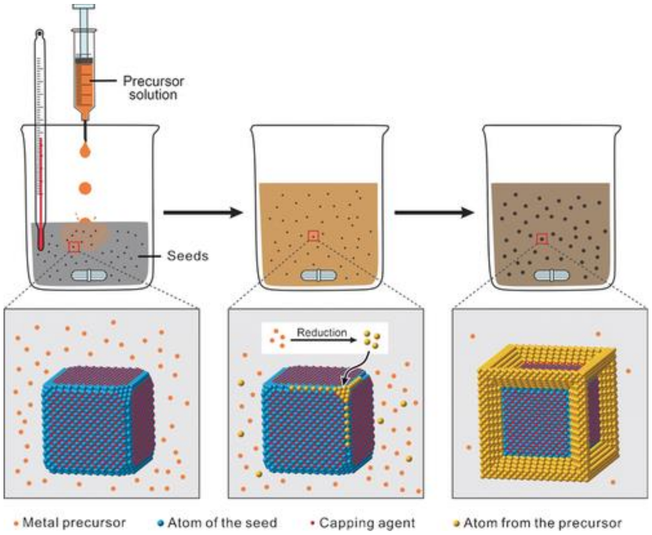

Figure 2-5 General approach to colloidal metal nanocrystal formation mediated by seeds. A vessel holding a combination of seeds, a reductant, a capping agent, and a colloidal stabilizer is injected with a precursor solution. The metal precursor is reduced (or destroyed), and these atoms then heterogeneously nucleate on the surface of the seeds. Well defined nanocrystals are created as a result of the seeds' continued growth along one of the many possible routes.[118]

Pt-based core-shell nanoparticles are among the most notable applicants of PtM (M=Co, Ni, and Fe) alloy catalysts.[119] In the last decade, PtM core-shell nanoparticles with a controlled size, structure, and composition have been synthesized using a wide range of techniques.[120–122] One of the most investigated Pt-based core-shell catalyst materials used in ORR applications is based on Co-Pt system. The improved ORR activity of Co-Pt core-shell catalyst originates from the Co core which persuades a strain in Pt-Pt interatomic distance.[120–123] In addition of the synthesis methods above; laser ablation could be used to synthesis core-shell Co-Pt nanoparticles. The Co-Pt core-shell nanoparticles prepared by ablation of Co shell target in already prepared Pt core nanoparticles colloidal solution.[124,125] Furthermore, sonication is a commonly used method to prepare core-shell Co-Pt nanoparticles. In this method, Co-Pt precursors are dispersed in a solvent and subjected to high-frequency ultrasonic energy for a certain time. Then, the mixture is subjected to thermal treatment in tube furnace under flowing inert or nitrogen gas, or surface modification, to form Co-Pt core-shell nanoparticles.[119,126] Overall, preparing core-shell and nanoalloy structures of platinum and cobalt can be challenging due to the complex interplay between the synthesis conditions, the materials properties, and the desired properties of the resulting nanoparticles. Therefore, the preparation of Pt-Co nanoalloys requires careful consideration of these factors to achieve the desired properties and ORR performance.

2.2.2 Metal oxide catalysts

Manganese oxides, a promising catalyst for ORR in alkaline electrolytes, have attracted great interest among the metal catalysts used for the ORR due to their availability, affordability, and tolerable catalytic activity due to their large surface area (reach to 254.1 m^2/g)[127] and number of active sites.[128,129] For example, doping MnO_x/C nanoparticles with nickel improved the oxygen reduction activity and performed mass activity (39.6 A/g) close to commercial 10% Pt/C (40.1 A/g).[130] The mass activity is the current density produced by the catalyst during the ORR divided by the mass of the catalyst used in the reaction. Furthermore, thin film of MnO_2, which was electrodeposited on a glassy carbon then calcined at 480 °C in air for 10 h, performed superior performance toward ORR in alkaline electrolyte with (E = 0.73 V vs. Ag/Agcl at -3 mA/cm^2) comparable to commercial 20% Pt/C (0.86 V vs. Ag/AgCl at -3 mA/cm^2).[131] Moreover, its potential for use in metal-air batteries and fuel cells was improved by their low toxicity and environmental friendliness.

A schematic summarizing various approaches to prepare MnO_2 based nanoparticles is shown in **Figure 2.6**. While there have been a lot of advancements in this regard, MnO_2 suffers from low electrical conductivity and agglomeration during ORR, which deteriorates the ORR catalytic activity. Therefore, anchoring MnO_2 over carbon support could improve the electrical conductivity, expand the electrochemically active sites for ORR (carbon could improve the dispersion of MnO_2 particles), and accelerate electron transfer rate by providing a conductive pathway for electron transfer between MnO_2 and the electrode.[132–134] There are several factors that could influence the ORR activity of MnO_2 such as particle size and morphology, surface defects, crystal structure, surface area, the concentration of the various phases composition, presence of other elements or impurities, pH of the solution , synthetic strategy used to obtain them presence of supporting material (such as carbon, graphene, graphene oxide, metal oxides), and electrode configuration.[135–137]. Defect engineering, [138,139] heteroatom doping, [140,141] surface modification, [142] and other material doping techniques might all be employed to increase the catalytic activity of MnO_2.[143]

MnO_2 can exist at different morphologies and structural characteristics. There are more than three different types of MnO_2 with various crystal structures, viz., α-MnO_2, β-MnO_2, γ-MnO_2 (1D chain structures), δ-MnO_2 (2D layered) and λ-MnO_2 (3D spinel structure),[144,145] which influences its functionality and catalytic activity.[146–149] The electron configuration of Mn is $3d^5 4s^2$, showing 5 unpaired electrons in d orbital, which easily promotes the electronic gain-and-loss process (variable oxidation state).[150] MnO_2's ORR catalytic activity in relation to various phases can be arranged as follows: $\beta < \lambda < \gamma < \alpha \approx \delta$-$MnO_2$, where α-MnO_2 exhibits the largest tunnel size.[151,152]

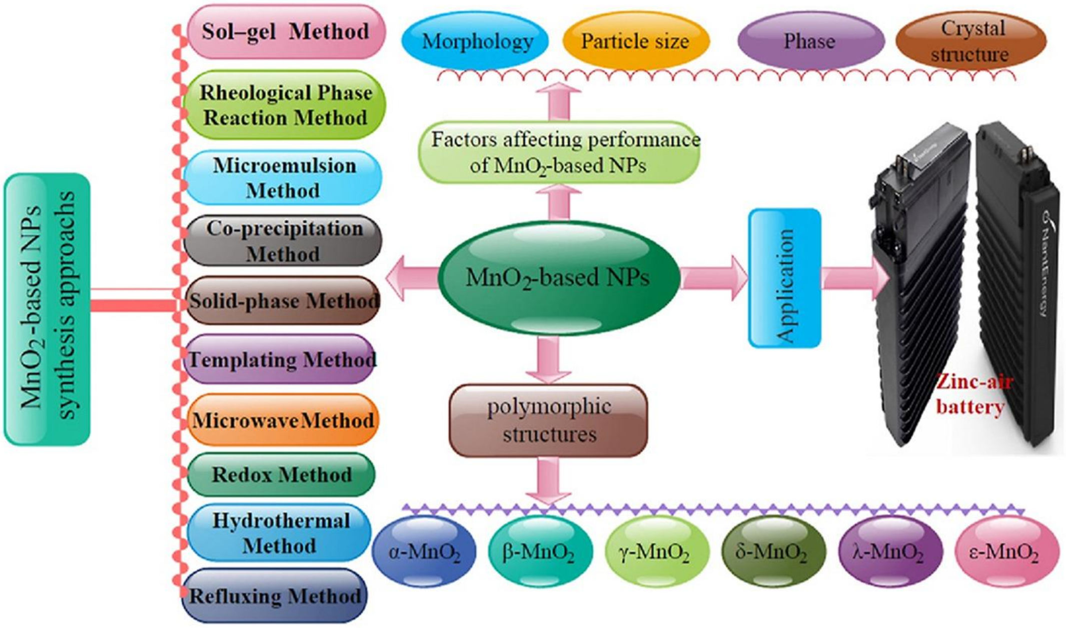

Figure 2-6 Schematic shows the various MnO_2 synthesis methods, highlights of the factors that affect the MnO_2's ORR performance, and the different polymorphic structures of MnO_2 that could be synthesized.[153]

Since α-MnO_2 shows promise for catalytic activity, extensive efforts have been devoted to preparing and testing α-MnO_2 for ORR. Recently, Shoa *et al.* prepared a rod-like structure α-MnO_2 by a hydrothermal method.[154] The α-MnO*2* performed excellent performance in alkaline electrolyte with onset potential 0.85 V vs. RHE and limiting current density 7.0 mA/cm^2. Defect engineering is a beneficial method to improve the catalytic performance because defects have a crucial function in regulating the surface electronic structures, altering catalysts adsorption behaviors, and optimizing the migration of intermediates.[155] Therefore, the defects can create vacancies in the crystal lattice of the catalysts, generate more active sites, and alter the electronic properties. A MnO_2 defect is a defect that exists in the crystal structure of the compound that can enhance its ORR performance. In particular, the defect might increase the MnO_2 catalyst's surface area of active sites, which can improve its capacity to catalyze the ORR. There are several types of MnO_2 defects that have been identified, including oxygen vacancies, surface defects, and substitutional defects.[156,157] There are several experimental techniques that can be used to identify defects in MnO_2 such as TEM, XRD, Raman spectroscopy and XPS. Liu *et al.* used plasma treatment at N_2 atmosphere to create defects on MnO*2* and N-doping.[158] XRD results showed that the crystal structure of MnO_2 remained stable during the plasma treatment, and it created defects. With a half-wave potential of 0.84 V vs.

RHE, a limiting current density of 6.7 mA/cm^2, and 3.9 transferred electrons, transition metal cation doping strategy was used by Selvakumar *et al.* to introduce Ni and Co atoms to α-MnO*2* using hydrothermal process, to enhance the bifunctional activity of the electrode.[159] They found that the α-MnO_2 crystal structure and morphology did not change after doping, while the crystal domain size was decreased. The Ni and Co dual doping caused an increase in the Mn^{3+} content in the sample, which led to superior OER and ORR catalytic performance (1.77 V at 10 mA/cm^2) and (onset potential (E_{onset}) = 0.9 V and half-wave potential ($E_{1/2}$ = 0.8 V) vs. RHE, respectively. Moreover, one dimensional reduced graphene oxide (rGO)-wrapped α-Mn_2O_3/α-MnO_2 nanowires ORR catalyst was prepared by hydrothermal and annealing technique.[160] The catalyst has a high surface area reached to 45.30 m^2/g and performs a positive onset potential +0.79 V vs. RHE. One of the reasons for the excellent performance of rGO/α-Mn_2O_3/α-MnO_2 is that Mn^{3+} and Mn^{4+} serve as oxygen acceptor/donor mediators. Moreover, the multivalent Mn accelerated the charge transfer process and improved the electron conduction. They also discovered that the rGO decreased aggregation and size reduction in addition to increasing the catalyst's surface area. As mentioned before, there are several factors affect the catalytic activity of the MnO_2 toward ORR such as morphology, crystallographic structure, defects, and surface area.[161,162] Overall, while MnO_2 is a commonly used catalyst in the air electrode of a zinc-air battery, its limitations must be taken into consideration in the design and operation of the battery to optimize its performance.

2.2.3 Metal-free heteroatom doped carbon-based catalyst

Carbon-based metal-free electrocatalysts show excellent electrical conductivity, robust resistance to acidic and alkaline conditions, and tunable molecular structures. The *sp2* carbon materials are promising catalysts for reactions requiring electrons, such as ORR, due to their abundance of free-flowing π electrons. However, these π electrons can't be utilized in ORR directly since they are too inert.[163]

Recent research has shown that the carbon π electrons can be activated by conjugating with the lone-pair electrons from nitrogen dopants. It is regarded as one of the best elements for chemically doping graphene among the many possible dopants since its atomic size is comparable to that of carbon, and it has five valence electrons that would form stable covalent bonds with nearby carbon atoms, making it simple to substitute with carbon atoms (lattice mismatch would be minimal).[164] Because of advantageous characteristics including superior conductivity, extremely large specific surface area, and distinctive electronic structure, nitrogen-doped graphene materials in particular have drawn great interest for use in electrochemical energy storage and conversion devices.[165,166] Zhao *et al.* discovered that notwithstanding if the dopants are electron-rich (like N) or electron deficient (like B), these materials will be transformed into active metal-free ORR electrocatalysts provided that the electroneutrality of the *sp2*-hybridized carbon atoms is broken and charged sites that favour O_2 adsorption are created.[167] N-doping can also improve the conductivity, which makes them a better electrode material with distinctive electronic structure.[168–170] The increased electron density on the carbon skeleton resulting from the N doping would be beneficial for the O_2 molecules to adsorb and then reduced on the positively charged C atoms next to N atoms.[171–176] An "activation area" on the graphitic structure is caused by doped-N atoms' that affects the electron density and charge distribution of the nearby carbon atoms.[177,178] These activated sites not only have the ability to participate directly in catalytic activities related to the oxygen reduction process (ORR), but they also have the ability to act as anchoring sites for metal nanoparticles with catalytic properties.[179] Strasser's group fabricated a sulfur-nitrogen co-doped functionalization ORR catalyst using ferric chloride as mediator that demonstrated greater activity and stability than commercial Pt/C catalyst in alkaline electrolyte. They reported that the role of the nitrogen presence is changing and improving the electronic structure of the carbon. They doped 1.51 wt.% N and 0.65 wt.% S using ionic liquid systems as nitrogen and sulfur precursor and 1.54 wt.% Fe from ferric chloride, and they got higher onset potential and limiting current density (0.88 V vs. RHE and -5.9 mA/cm^2) than 20 wt.% Pt/C (0.9 V vs. RHE and -5.5 mA/cm^2).[180]

Nitrogen doping of carbon materials such as graphene or carbon nanotubes can be achieved through different methods such as; chemical vapor deposition,[181,182] electrochemical doping,[183] thermal annealing,[184,185] and ion implantation.[186,187] Typically, N-doped carbon catalysts could also be prepared by pyrolyzing a combination of carbon and nitrogen-containing precursors, such as polypyrrole, polyaniline, metal-organic frameworks (MOFs), covalent organic frameworks (COFs), and urea.[188,189] On the other hand, using N-rich biomass as N-doped carbons precursors such as bamboo fungus, silk fibroin, fructose, and ginkgo leaves, have drawn a lot of attention since it is extremely abundant, renewable and inexpensive compared with traditional chemicals.[190–193] These biomass N-doped carbons have been used to prepare ORR electrocatalysts and exhibit the catalytic performance lightly below or comparable to Pt/C.[190–192,194,195]

2.2.3.1 Nitrogen doped carbon configurations

There are three main bonding configurations in N-doped carbon materials: pyridinic-N, pyrrolic-N, and graphitic-N as shown in **Figure 2.7a.**[196,197] Pyridinic-N and pyrrolic-N types of N exist along the layer's border, but they can also occur inside the layer by being linked to vacancies. Pyridinic-N is coupled with two C atoms to create a member of the hexagon, and pyrrolic-N forms a pentagon with two C atoms. By connecting to three C atoms in a *sp2* configuration on the interior of the layer, graphitic-N is acting as a substitute for the C atom in the graphene layer. A graphic representation of the nitrogen N1s XPS spectrum, with the subcomponents representing various nitrogen configurations in N-doped graphene is shown in **Figure 2.7b**. The content and types of N obtained in a N-doped carbonaceous catalyst is largely dependent on the synthesis approach adopted. For example, investigations done by Ruof and his co-workers showed how the choice of N precursors and annealing temperature affected the catalyst's effectiveness and the coordination of the nitrogen doped.[198] They found that annealing of polyaniline/reduced graphene and polypyrrole/reduced graphene tended to produce pyridinic-N and pyrrolic-N species, respectively, while annealing of graphene oxide with ammonia favored the formation of graphitic-N and pyridinic-N species. Depending on where in the carbon lattice they are located and the sort of nitrogen bonding they have, these various nitrogen species can have variable impacts on the ORR activity. Many papers reported that the pyridinic-N and graphitic-N are suitable dopants for rupturing the O_2 double bond and that the ORR activity depends more on the dopant configurations than the doping level.[197,199–202] We will explore in the next section the significance of various N functionalities in ORR catalytic activity as inferred from the wide range of literature reports.

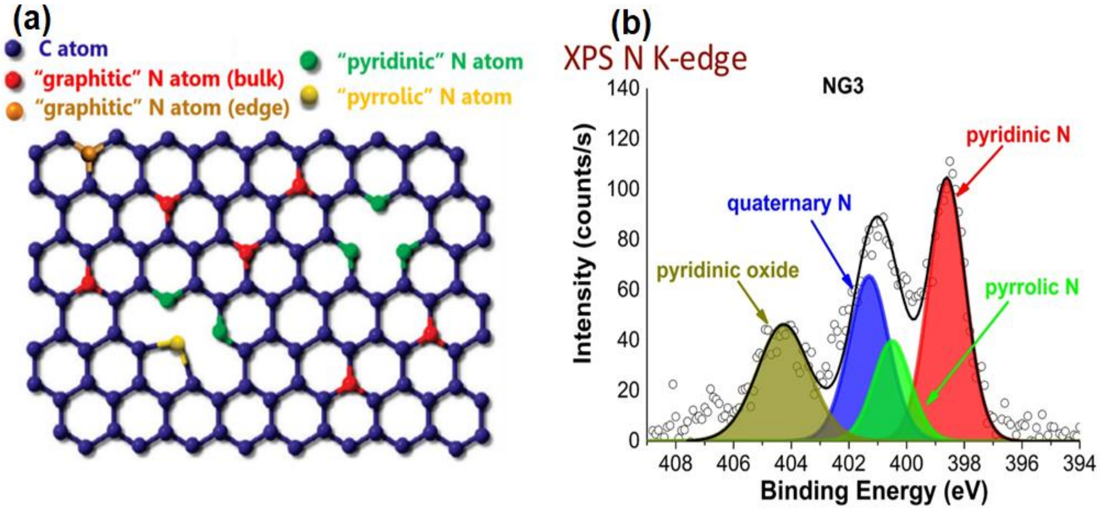

Figure 2-7 (a) Various configuration of nitrogen in nitrogen doped carbon.[203] (b) An example of N1s spectra of N-doped graphene [204]

2.2.3.2 Pyridinic nitrogen species

Pyridinic-N is a highly electronegative dopant that can act as an electron sink during ORR. Pyridinic-N and graphitic-N are more electronegative dopants compared to pyrrolic-N and pyridonic-N, as they are bonded to *sp2* hybridized carbon atoms, which have a higher electronegativity than *sp*3 hybridized carbon atoms.[205–207] The higher electronegativity of pyridinic-N and graphitic-N results in a stronger interaction with oxygen molecules, which facilitates the adsorption of oxygen on the graphene surface and the subsequent reduction of oxygen to water. In other words, pyridinic N can increase the catalyst's capability to donate electrons by donating one *p* electron to the aromatic system with a lone electron pair in the plane of the carbon matrix. Because of this, pyridinic N can enable the reduction of O_2 by weakening the O-O bond by bonding O with N or/and the nearby C atom.[82,208,209] There are several literatures investigated the effect of the pyridinic-N on ORR via both theoretical and experimental studies. Kim *et al.*, using density functional theory (DFT) calculations found that the ORR is catalyzed by pyridinic-N through a ring opening process.[210] Whereas other DFT reports showed that there occurs an enhancement of the oxygen adsorption energy on the surrounding carbon atoms due to the high electronegativity of nitrogen atom and resulting electron withdrawal effect.[211]

Wu *et al.*'s results on N-doped carbons showed that the most effective N-functional group to promote ORR at onset potential (0.97 V vs. RHE) which is comparable to commercial Pt/C (0.99

V vs RHE) in alkaline electrolyte by four electron pathway is the pyridinic N.[211] They achieved high N content up to 6.5 at.% (4.5 at.% pyridinic nitrogen coordinator) when their sample (graphene that doped with solid precursor g-C_3N_4) post doped at 800 °C. Lai *et al.* explored the configuration of nitrogen doped graphene-based catalysts effects on the ORR and they found that the graphitic N content determined the limiting current density while the pyridinic N species enhanced the ORR onset potential and can convert the ORR mechanism from 2 electrons pathway to 4 electrons pathway.[200] On the other hand, melamine and acetonitrile as nitrogen and carbon source were used recently by Zheng *et al.* to fabricate a pyridinic-N dominated carbon spheres by solvothermal pyrolysis conversion method as cathode material in ZABs.[212] They achieved very high nitrogen content in their sample (14.57 wt.%), which is mostly pyridinic-N. They also exhibited reasonable ORR catalytic activity ($E_{1/2}$=0.865 V vs. RHE) and high-power density (148 mW/cm^2) in ZAB test. Luo *et al.* employed zinc phthalocyanine as a precursor to reduce the loss of pyridinic -N during the pyrolysis process.[213] In contrast to 28% without zinc phthalocyanine, 86% of the pyridinic-N groups were maintained because of the strong Zn-N connection inherited from the zinc phthalocyanine precursor that protects them during pyrolysis. The catalyst works effectively as an electrocatalyst for ORR ($E_{1/2}$=0.88 V vs. RHE, $E_{1/2}$=0.9 after 8000 cycles) because of its high nitrogen content (2.285 at.% pyridinic-N) and porous carbon framework (NaCl elimination after pyrolysis).

All of these investigations demonstrate how important are the N-precursors and synthesis approaches in tuning the N content with pyridinic nitrogen as the main N type for ORR active electrocatalysts.

2.2.3.3 Pyrrolic nitrogen species

Pyrrolic N atoms are attached to two carbon atoms and included in five-membered heterocyclic rings. Due to the limited stability of pyrrolic species, which are uncommon in carbon materials, the concentration of this functionality is usually low following carbonization or heat treatment.[214,215] Moreover, the pyridinic coordination of nitrogen alone cannot provide efficient ORR activity, since graphene with pyridinic nitrogen follows a two-electron transfer pathway rather than the reaction's preferred four electron transfer.[216]

Even so several groups attempted to obtain N-doped carbons with high pyrrolic nitrogen content. For example, Unni *et al.* developed a simple synthesis method to fabricate nitrogen doped graphene with high pyrrolic-N coordinator by high temperature treatment under inert gas for graphene oxide and pyrrole monomer.[217] They achieved 53% pyrrolic nitrogen content, 4 electron ORR pathway in alkaline media, and excellent onset potential close to the commercial 40 wt. % Pt/C. In another work, the formation of pyrrolic-N coordinators was promoted in N-doped mesoporous carbon hollow sphere using 2-pyridinecarboxaldehyde and pyrrole.[218] also showing an excellent ORR performance with low peroxide formation (3.8%) and 4-electrons ORR pathway as shown in **Figure 2.8d,e**. High stability of these N-doped carbon after 3000 cycles was referred to modification of the nitrogen configurations during the potential cycling (graphitic-N to pyridinic, and pyrrolic to graphitic-N), as shown in **Figure 2.8a-c**.

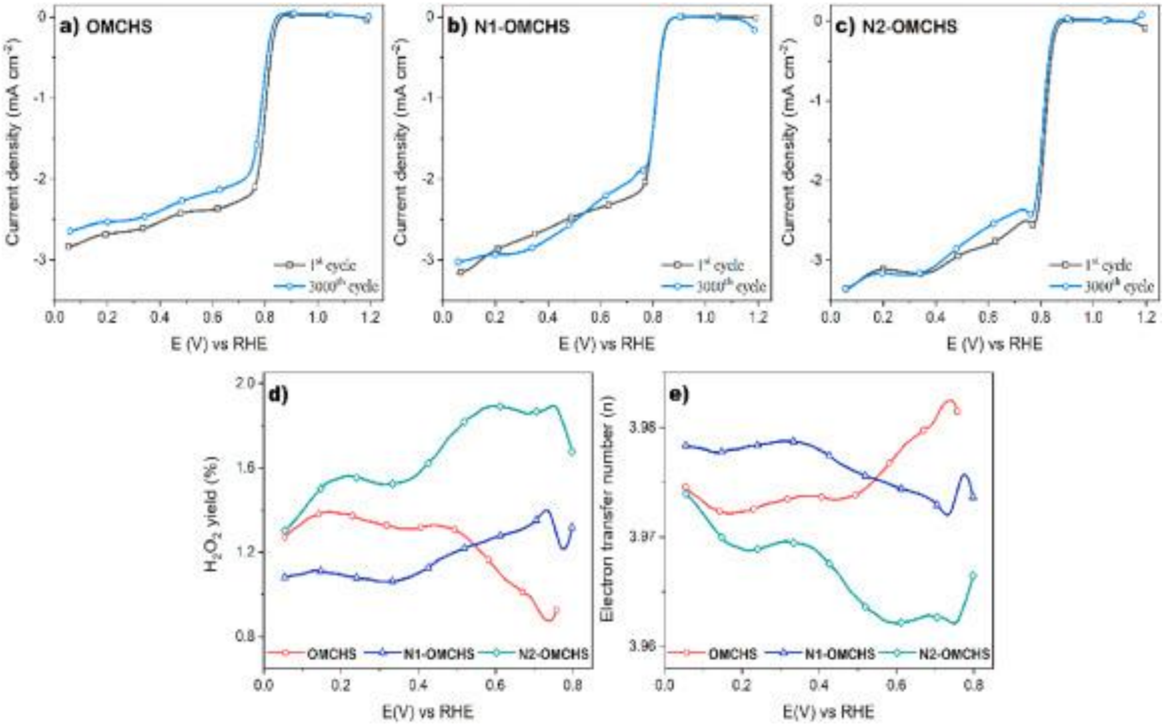

Figure 2-8. Linear sweep voltammetry (ORR) at 2000 rpm (1st and 3000th cycles) at N-doped mesoporous carbon hollow sphere using different nitrogen source a) non-doped b) pyridine carboxaldehyde source , c) pyrrole. Electrolyte: O2-saturated 0.5 M KOH, scan rate = 5 mV/s at 2000 rpm. d) %H_2O_2 and e) n plots at the 3000th cycle.

It should be mentioned that the majority of the researchers mostly view pyrrolic-N as inactive towards ORR. In comparison to pyridinic-N and graphitic-N structures, pyrrolic-N is less electronegative. Unlike pyridinic-N, which is connected to two adjacent carbon atoms, pyrrolic-N is attached to a nearby nitrogen atom and *sp3* hybridized carbon atom, resulting in a less polarized N-C connection. The N-C bond in pyrrolic-N is less efficient in attracting and facilitating the adsorption of oxygen molecules on the graphene surface as a result of its decreased polarity, which lowers ORR activity.[219–224]

2.2.3.4 Graphitic nitrogen species

As opposed to one electron per carbon atom, the replacement of electron-rich N in the form of graphitic-N (*sp2* hybridized nitrogen bonded with three *sp2* hybridized carbon neighbors) into the carbon system would add two electrons to the electron system. The additional electron could reach the π * state and have the effect of " π doping".[225] Therefore, graphitic N was recognized as an active site that produces optimal nitrogen-dopant characteristics. Because of their lower electron density on neighboring carbon nuclei, graphitic-N atoms' relative electronegativity aids in the transfer of electrons from those carbon nuclei to nitrogen atoms as well as the donation of electrons from nitrogen to nearby carbon p_z orbitals.[226] The donation and backdonation reactions aid in the formation of a strong chemical bond between oxygen and carbon as well as the O_2 dissociation on the nearby carbon atoms.[181] Moreover, due to the low energetic barrier of graphitic-N for donating electrons from surface to the π-conjugated system that leading to enhance oxygen adsorption for facilitating the formation of the OOH^* and O^* intermediates, graphitic-N sites could be responsible for ORR activity as investigated in this literature. [227]

Bermejo *et al.* prepared highly selective doping graphitic nitrogen species by heat treatment method of mixture of commercial carbon and urea as shown in **Figure 2.9**.[228] They achieved 8.9 at. % of nitrogen content in the samples that gave high surface area (3200 m^2/g) and excellent ORR performance. Also, the excellent ORR performance could be referred to the good balance between the graphitic-N content and the carbon properties such as the porosity and specific surface area as Liang and his co-workers reported.[229] In addition, rather than having either graphitic or pyridinic nitrogen exclusively, a combination of both are considered as more promising because of their distinct effects on promoting ORR.[221–223] For instance, Lai *et al.* found that the limiting current density is determined by the graphitic N content, whereas the pyridinic N content helps lower the onset potential.[230] Another report showed a rise in graphitic-N species (90 % graphitic N) and the disappearance of amines when PANI was treated at high temperatures of up to 1000 °C.[231] Interestingly, pyridine-N was also transformed to graphitic-N species as a result of condensation process. The catalyst exhibited a platinum-like ORR performance in alkaline electrolyte.

On the other hand, graphitic-N atoms, which have a three-dimensional structure, could be not active in the ORR as these literatures mentioned.[232,233] Thought to be primarily to blame for the poor catalysis is the low electrical conductivity of nitrogen doped carbon materials containing graphitic N atoms, which is caused by the 3D structure interrupting their π–π-conjugation.

Although different nitrogen sites (pyridinic, pyrrolic, and graphitic) have varying strengths, experimental investigation and theoretical simulations revealed that these sites can heavily adsorb and activate oxygen. The choice of nitrogen source and experiment conditions impact the most in discerning the nitrogen configurations in N-doped carbonaceous catalysts. The most commonly used nitrogen sources are mentioned in detail in the next section.

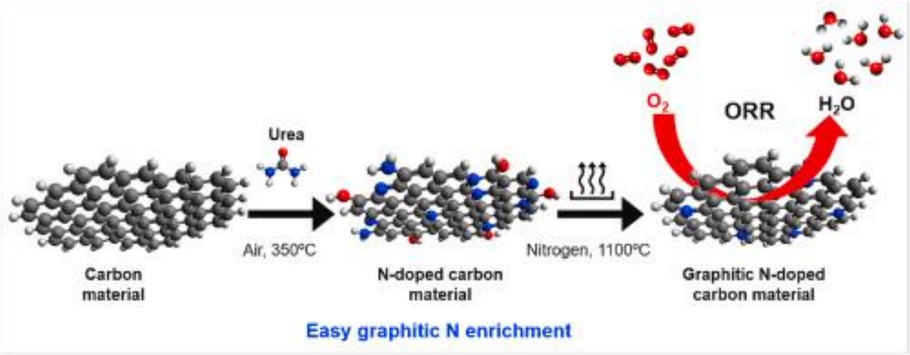

Figure 2-9. Synthesis method of selective graphitic nitrogen doped carbon.[228]

The deconvoluted high-resolution N 1s spectra are displayed in **Figure 2.10** as an illustration of the numbers of nitrogen configurations found in various samples with different atomic concentrations.[234] Pyridinic species has the highest at.% in samples shown in **Figure 2.10a,b,d**. While pyrrolic species has the highest at.% content in samples **Figure 2.10c,e,f**. Graphitic configuration has the highest atomic contents in samples that has been shown in **Figure 2.10g.**[235]

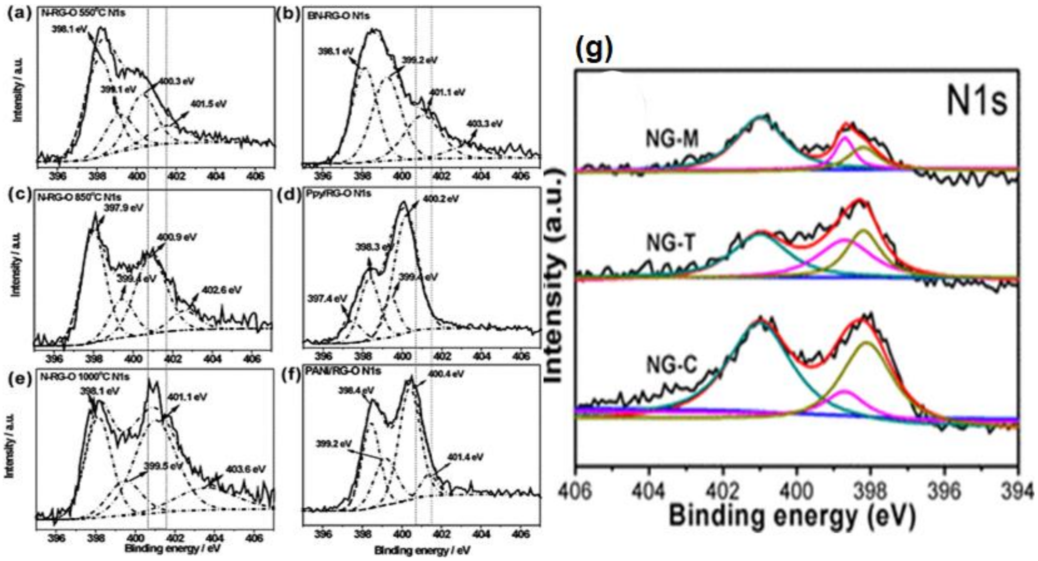

Figure 2-10. XPS spectra of N 1s of different samples where (398.1, 399- 400 eV , 401.1- 401.5 eV) peaks are corresponding to pyridinic, pyrrolic, and graphitic species, respectively.

2.2.3.5 Nitrogen precursors:

Nitrogen precursors play an important role in discerning the type and content of N in doped carbon and are largely dependent on the treatment and the content of nitrogen in the precursor. To date several nitrogen precursors have been reported such as dicyandiamide,[236] 1,8-diaminonaphthalene,[237] polyacrylonitrile,[238] urea,[239] melamine,[240] pyridine,[241] and N-containing ionic liquids.[242,243] In addition to above mentioned nitrogen precursors, there are several biomass-based conversion techniques to obtain N-doped carbons(less expensive and more eco-friendly). For example, Ginkgo leaves, Typha orientalis, and eggplant were used to obtain nitrogen doped porous carbons.[244–246] Alternatively, one can also employ nitrogen-containing gases, such as ammonia or nitrogen oxide, as the nitrogen source, which are then reacted with a carbon source under high-temperature conditions.[196]

Overall, for nitrogen-doped carbon ORR catalysts, the choice of nitrogen source relies on the required final material qualities and the particular synthesis technique employed. Potential nitrogen sources that might be employed to create high-performance nitrogen-doped carbon materials for ORR applications include melamine, urea, and chitosan, which are among the most commonly used nitrogen sources for nitrogen-doped carbon ORR catalysts. In the next sub-sections, we review the recent literatures used melamine, urea, and chitosan as nitrogen source for nitrogen doped carbon ORR catalyst.

Melamine

Melamine is a nitrogen-rich organic compound that has undergone substantial research as a nitrogen source for the production of carbon compounds with nitrogen doping.[247] It is a white, crystalline powder that is 66% nitrogen by weight and has the chemical formula $C_3H_6N_6$, and also a low-cost industrial material. Additionally, the high thermal stability of melamine enables the production of nitrogen-doped graphene at high temperatures without the nitrogen source decomposing.[248] In addition, melamine has been reported to be less harmful than other nitrogen sources like ammonia, which might endanger researchers' health and safety.[249] Melamine can be incorporated into carbon materials through various methods, including thermal treatment, chemical vapor deposition, and hydrothermal synthesis. The resulting nitrogen-doped carbon materials can exhibit different nitrogen functionalities depending on the synthesis conditions.[247,250–252] Sheng *et al.* prepared nitrogen doped graphene with 10.1% nitrogen content (graphitic-N) by thermal annealing approach using graphene oxide and melamine (as shown in **Figure 2.10).**[253] The resultant nitrogen doped graphene catalyzed ORR by 4-electron and performed excellent ORR process (E_{onset}= -0.1 V vs. Ag/AgCl). Ma *et al.* prepared porous nitrogen doped carbon by using salt template synthesis method using glucose, cellulose, lignin as biomass carbon precursor, and melamine as nitrogen source. They achieved 11.9 % of graphitic-N coordinator and high specific surface area of 1731 m^2/g.[254] Moreover, nitrogen doped carbon with large pores (as shown in **Figure 2.11**) and high surface area (1626 m^2/g) was fabricated using commercial melamine sponge as ORR catalyst.[255] The diffusion current density was notably comparable to that of the commercial Pt/C and the nitrogen doped carbon performed excellent durability after 10000 potential cycles (24 mV negative shift in $E_{1/2}$). The XPS analysis showed the presence of all types of nitrogen conjugations.

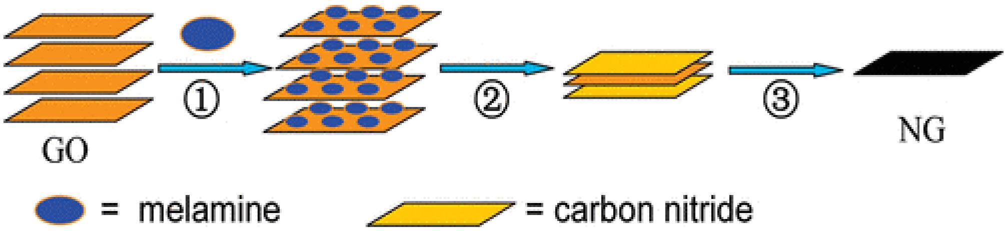

Figure 2-11. Illustration of the nitrogen doping of melamine into layers of graphene oxide (GO). (1) At a temperature of 300 °C, melamine adsorbed on the surfaces of GO. (2) When the temperature was below 600 °C, melamine condensed and produced carbon nitride. (3) As the temperature exceeds 600 °C, carbon nitride breaks down and is doped into graphene layers.

Urea

A popular nitrogen source for the production of nitrogen-doped carbon compounds is urea, which is rich (46 %) in nitrogen. It has the chemical formula $CO(NH_2)_2$ and is a solid that is tasteless and colorless. The use of urea as a nitrogen source has several advantages. First, urea is a water-soluble compound, which makes it easy to handle and mix with other materials. Second, the decomposition of urea at high temperature is a simple and effective method to introduce nitrogen into the carbon matrix. Finally, the use of urea as a nitrogen source is a cost-effective approach to prepare N-C materials. Ilnicka *et al.* prepared nitrogen doped porous carbon from chitosan and chitin as carbon and nitrogen precursors and urea as additional nitrogenation agent.[256] They studied the effects of urea on the specific surface area, nitrogen content and configuration, and ORR electrocatalytic activity. The specific surface area and the pore volume enhanced, nitrogen content increased, different nitrogen species performed (pyridinic-N, Pyrrolic-N, graphitic-N, and oxidized-N), and excellent ORR performance achieved (E_{onset}= 46 mV and $E_{@100mA/cm2}$=-100 mV vs. Hg/HgO). Three-dimensional honeycomb-like nitrogen doped carbon/graphene was synthesized by low cost and effective process as shown in **Figure 2.12**.[257] They found that the three-dimensional structure may substantially speed up the electrochemical reaction by preventing excessive restacking of graphene sheets as well as by providing a large accessible surface area, a multi-electron transport channel, and a short diffusion distance. Thus, the resultant nitrogen doped carbon has excellent ORR performance (E_{onset}= -70 mV vs. Ag/AgCl and current density = 4.64 mA/cm^2 at -0.7 V) close to the commercial Pt/C. Kong *et al.* achieved high pyridinic-N content by treating graphene oxide, oxidized carbon nanotubes and urea via hydrothermal reaction and annealing treatment.[258] The prepared nitrogen doped carbon exhibited effective ORR catalytic activity in alkaline electrolyte, and performed as ZAB cathode a high power density (149 mW/cm^2) and specific capacity (873 mAh/g$_{Zn}$). Urea and melamine, which are nitrogen precursors, were grinded by ball milling apparatus with carbon nanotubes, then thermally treated under inert gas to produce nitrogen doped carbon wit high pyridinic-N, pyrrolic-N, and graphic-N species.[259] They found that the as pyridinic-N to graphic-N ratio increased, the ORR electrocatalytic activity increased (less negative E$_{onset}$). In summary, using urea as a nitrogen source is a common and effective approach to prepare nitrogen-doped carbon materials for the ORR. It offers several advantages such as low cost, easy handling, and good performance, which makes it a promising method for the large-scale production of electrocatalysts for energy conversion systems.

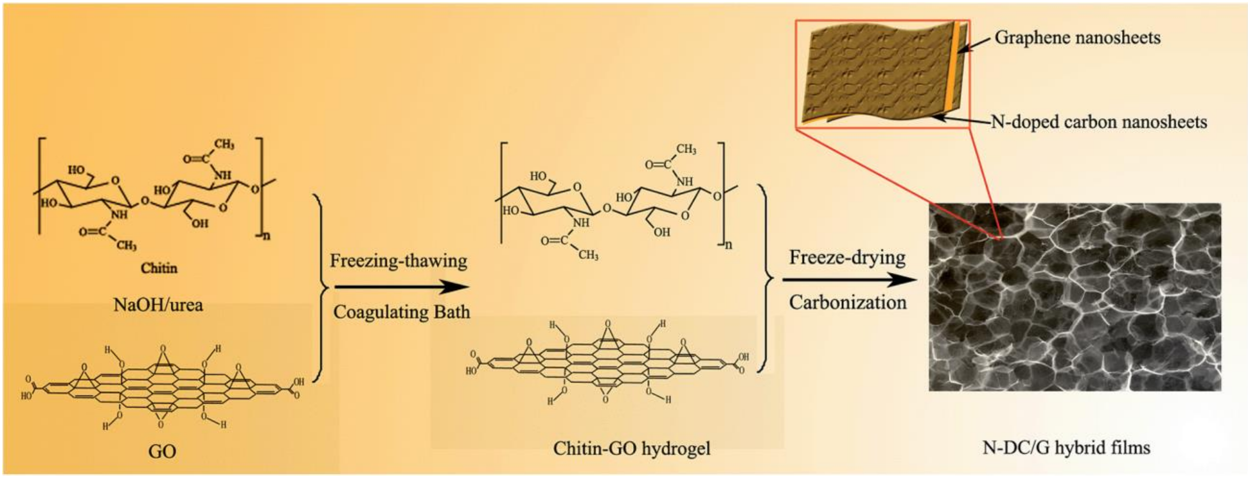

Figure 2-12. Schematic of the fabrication of nitrogen doped carbon/graphene (N-DC/G) that resemble honeycombs.

Chitosan

Chitosan, which is a low-cost biomass material, has a great capability to chelate metal ions, due to its abundance of amino and carboxyl groups. It is a linear polysaccharide with nitrogen content of about 7% (**Figure 2.11**).[178,260] It is the second most abundant and renewable biopolymer after cellulose, which is derived from the chitin in crustacean cells, insect exoskeletons, and fungus cell walls.[29] Primo *et al*. reported that the pyrolysis of chitosan under inert atmosphere at 800 °C produce high quality single layer of N-doped graphene.[261] Hoa *et al.* presented a fabrication method to produce porous graphene-based nitrogen using chitosan as raw material. This method controlled the ratio of the amorphous and graphene framework by the activation temperature.[262] Moreover, mesoporous structural biomass carbon material with high content of nitrogen (11.58%, where the pyridine N and pyridinium N are the major configurations) and ultrahigh surface area (1190 m^2/g) has been fabricated by mixing chitosan and ferric nitrate as a pore forming agent and pyrolysis the mixture at 800 °C under nitrogen atmosphere.[263] While Liu *et al*. developed a simple synthesis method, by mixing chitosan and urea, without involving any pore forming agent to produce highly porous N-doped carbon nanosheet with a high surface area reach to 1510 m^2/g that exhibited an excellent electrocatalytic activity toward ORR in alkaline electrolyte compared to commercial 20% Pt/C.[264] The prepared nitrogen doped carbon exhibited ratio of graphitic/pyridinic nitrogen structure (2.69 at. % graphitic N and 1.20 at. % pyridinic N). Guo *et al*. reported an excellent electrocatalytic activity of N-doped carbon nanoflowers toward ORR with half-wave potential of 0.84 V vs. RHE lower than by 20 mV than Pt/C.[265] They used silicon template method and chitosan as nitrogen and carbon precursor to produce thin carbon nanosheets doped with nitrogen with interconnected meso-porous channels, where graphitic-N and pyridinic-N contributed 75% of 7.8 wt.% N composition for the sample. Wittmar *et al.* developed a procedure to convert two biopolymers cellulose and chitosan (0.75:0.25) to electrocatalytic ORR nitrogen-doped carbon materials.[266] They demonstrated that the electrocatalytic activity could be modulated by the ratio between the two biopolymers as well as by the pyrolysis conditions, even though the electrocatalytic activity of the cellulose:chitosan blend does not rise to the ORR activity of similar materials reported. Moreover, nitrogen doped carbon nanosheet were fabricated thermal composition of chitosan and melamine under nitrogen atmosphere.[267] They demonstrated that the ORR activity is substantially influenced by the number of carbon "kinks" and/or surface roughness in addition to the total nitrogen content and the kind of nitrogen group (pyridinic or graphitic). The development of a method to anchor 30 wt.% platinum nanoparticles (PtNPs) onto a new hybrid chitosan derivative–carbon black support was reported.[268] The resulting catalyst's ORR performance was superior to that of commercial Pt/C as shown in **Figure 2.14.**

Overall, chitosan-based nitrogen-doped carbon materials have great potential as a cost-effective and environmentally friendly alternative to traditional platinum-based catalysts for ORR in energy conversion applications. **Chapter 5** focuses on the preparation of biomass derivative (chitosan-based) N-doped LIG materials to demonstrate the potential of using chitosan in ORR performance. We developed a facile simple method for synthesis of porous N-doped LIG that good ORR activity. This study provides a feasible synthesis approach for the scalable production of biomass derived high-performance carbon-based ORR catalysts.

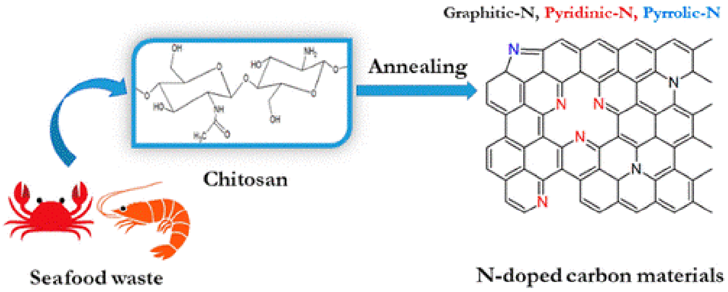

Figure 2-13 Schematic for the N-doped carbon from annealed chitosan and various possible configurations of doped nitrogen [147]

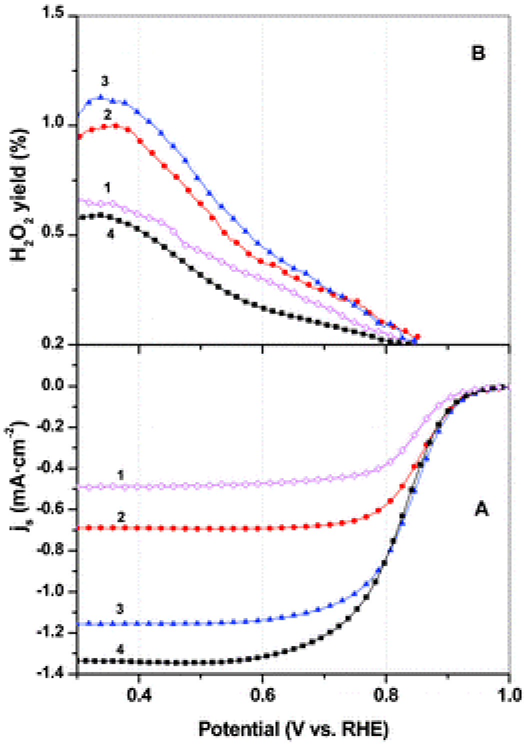

Figure 2-14. (A) linear sweep voltammetry curves on a glassy carbon rotating ring-disk electrode in 0.5 M H2SO4 at 2mV/s and (B) H_2O_2 yield of (1) 40 wt.% Pt/C, (2) 5 wt.% chitosan, (3)10 wt.% chitosan, and (4) 13 wt.% chitosan.

2.3 Manufacturing methods for patterning air cathode for ZABs

It is crucial and advantageous to include carbon with catalysts as catalyst support in the air cathodes of zinc-air batteries. The carbon support provides a large surface area and helps catalyst nanoparticles disperse, which increases the number of active sites for the oxygen reduction reaction

(ORR). Also, carbon or graphene may be added to materials to increase catalytic activity, possess excellent electrical conductivity, supports allows for easy access and diffusion of oxygen through the electrode structure due to the porous nature of carbon or graphene, could protect the catalyst nanoparticles from degradation, and improve the overall durability of the battery, and boost an air cathode's overall performance. Graphene is simply one atomic layer of graphite - a layer of sp2 bonded carbon atoms arranged in a hexagonal or honeycomb lattice. Graphite consists of multi-stacked layers of graphene (as shown in **Figure 2.15**). The catalysts developed in this thesis are supported by and distributed in graphene matrix.

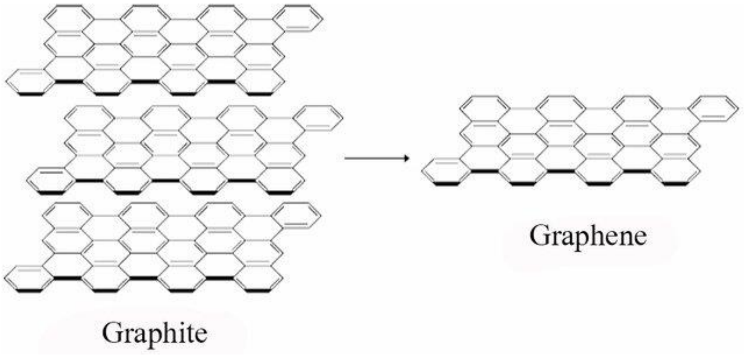

Figure 2-15 Structure of graphite and graphene

In order to incorporate PtCo nanoparticles, MnO_2, and nitrogen-doped carbon into air cathodes for ZABs, the manufacturing methods for patterning air cathodes are essential. Different approaches are to used deposit or fabricate a layer of carbon/catalysts onto the air cathode. The patterned layer can be optimized to maximize the electrocatalytic activity of the cathode, and the thickness of the layer can be controlled to ensure proper diffusion of oxygen to the active sites. In this section different air cathode patterning methods will be discussed.

While traditional electrodes are made by slurry casting electrochemically active materials, modern manufacturing techniques allow for the patterning of novel electrode architectures and the control of device geometries in real-time. The patterning of air electrode architectures and real-time design modifications are made possible by a number of manufacturing techniques, including inkjet printing, direct ink writing and laser-induced graphene. These techniques lead to electrodes with greater loading, enhanced electrochemical performance, and new functionality, such as flexibility and wearability.[56] Moreover, it allows to precisely regulate the structure of the electrodes and electrolytes in printed cathodes as well as their geometry (such as porosity, dimensioning, and morphology).[269] Nevertheless, not all these technologies and materials utilized in air cathodes are suitable for producing printed cathodes due to compatibility issues between preparation conditions, materials, and operational procedures.[270] The production of air cathodes via these techniques face several challenges that must be solved. In this section, we list the commonly adopted techniques used to fabricate air cathodes.

2.3.1 Inkjet Printing

The principle of inkjet printing involves a nozzle releasing droplets of ink that are loaded with active material, which are subsequently deposited onto a substrate to create a high-resolution pattern as shown in **Figure 2.16**. Inks with clearly specified viscosity, surface tension, and particle size must be used for inkjet printing.[271] This process is scalable for production over a broad area and enables additive manufacturing methods with changeable thickness and designs with high resolution deposition, at the same time it also decreases the material waste and costs.[272] Bassetto *et al.* combined the inkjet printing technique and photonic curing platform to fabricate ORR catalysts consisting of nitrogen doped graphene oxide and cobalt oxides.[273] A cobalt oxides/nitrogen doped graphene oxide ink prepared with stabilizers including ethyl cellulose and polyvinyl pyrrolidone (PVP) was completely described in order to achieve printability. The ink was treated by over curing to evaporate the solvents, eliminate the stabilizers, and produce good adhesive and catalytic active material. In another work, an air cathode was prepared via inkjet printing of a pattern of iron(III)p-toluenesulfonate as a solution in butanol onto paper.[274] The printed air cathode performed in ZAB 1.2 V open-circuit voltage and a discharge capacity of 0.5 mAh/cm^2.

While there are several advantages of inkjet printing, some of their main disadvantages are its slow printing speed and demanding ink formulation needs. The printing head is also less reliable and vulnerable to clogging and breakage. Moreover, inkjet printing produces electrodes that are less than 10 μm thick and loadings that are below 1 mg/cm^2, and frequently necessitates the printing of tens of layers to attain these thicknesses.[56,269]

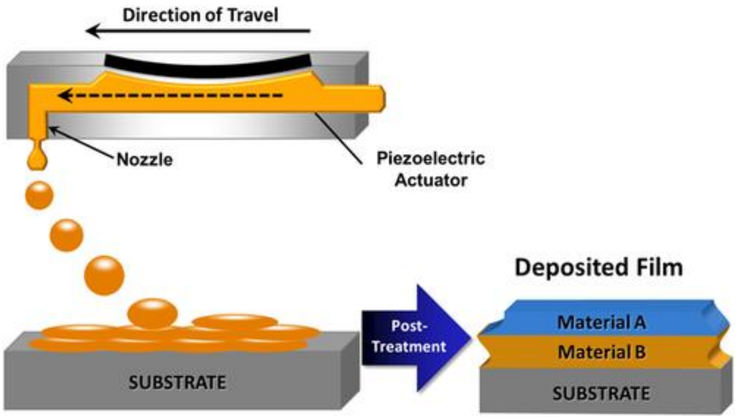

Figure 2-16. The fabrication of a multi-layer material via drop-on-demand printing is shown schematically. The tiny drops of ink combine to form wet layers. Dry layers are created when the solvent from the wet layer evaporates. The next material may be deposited on top of these dry layers called substrates. Once all layers have been deposited, post printing treatment may be employed to cross-link polymers or remove any remaining solvent or additives.[271]

2.3.2 Direct Ink Writing Technique

Direct ink writing is a form of 3D printing that uses the extrusion of liquid, gel, or paste-based inks with more active material loadings than inkjet printing. Due to its benefits of being inexpensive, simple to use, wide range of material, and solid modelling process, this has been the most popular 3D printing technique for producing battery electrodes. This technique could print individual layers that are thicker (between 1 and 100 µm) than produced from inkjet technique.[56] Gou and his co-workers designed and synthesized all the components of the ZAB by direct ink writing method as shown in **Figure 2.17**.[275] The air cathode was consisted of poly(vinylidene fluoride-co-hexafluoropropylene, PVDF), graphene, N,N-dimethylformamide, cobalt oxide and carbon black. The ZAB exhibited a high open-circuit voltage of 1.37 V, a large areal capacity of 71.1 mAh/cm^2 , and a good cycling stability of over 150 cycles at 4 mA/cm^2 for 50 h. Also, Ma *et al* synthesized fully printed ZAB; printed current collector on polyimide film, zinc electode, catalytic cathode, and gel electrolyte.[276] The obtained ZAB performed a high volumetric capacity 140 mAh/cm^3 and high areal capacity 2 mAh/cm^2. Zang *et al.* used direct ink writing technology to fabricate anode and cathode for ZAB.[277] The ink of the anode ink was zinc powder, carbon black, carbon nanofiber, and PVDF solution, while the cathode was reduced graphene oxide, carbon nanotubes and manganese oxide. The resulting ZAB performed high discharge capacity 670 mAh/g at 5mA/cm^2 and excellent stability.

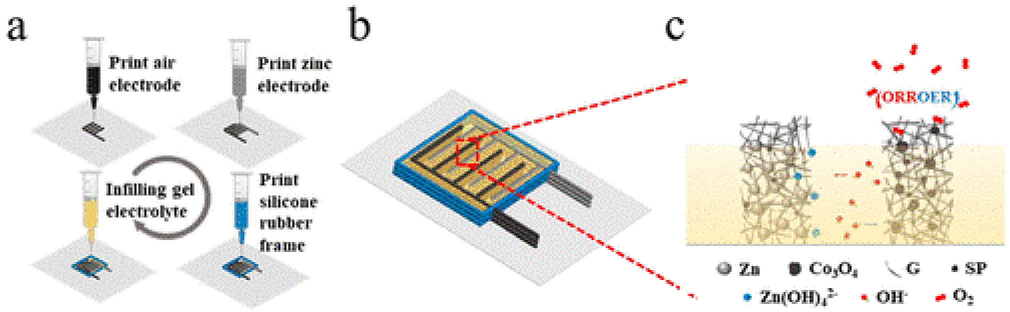

Figure 2-17. Solid-state ZAB creation and construction. (a) Diagram illustrating the printed manufacturing of ZAB using interdigital electrodes encapsulated in gel electrolyte. (b) Schematic showing the setup of the ZAB device. (c) Schematic illustration demonstrating how ZAB functions.

In terms of yield stress and storage modulus, the direct ink writing technique has strict standards for the gel-based viscoelastic inks. A significant issue that has to be resolved is the poor mechanical strength between the layers. Thus, further efforts must be made to enhance the direct ink writing technique's use in battery manufacture.

2.3.3 Laser Induced Graphene (LIG) Technique

For the bulk synthesis of electrochemical active materials, laser-based synthesis techniques, such as laser-based carbonization, have been widely used. Laser based patterning techniques, also known as direct laser writing, can also enable the simultaneous synthesis of active materials from a suitable precursor and the rapid patterning of electrodes.[56] Tour's group developed a one-step and facile technique to fabricate porous graphene from a polyimide (PI) sheet by thermal irradiation method using CO_2 infrared laser at ambient conditions.[278] This inexpensive CO_2 infrared laser system is commonly used in industry for engraving or cutting. The pulsed laser irradiation converted the sp^3 carbon atoms to sp^2 carbon atoms. This technique produces three-dimensional graphene called laser-induced graphene with excellent properties and has several advantages such as:

1. Produce high porosity LIG (as shown in **Figure 2.18**).
2. LIG has good electrical conductivity and high chemical stability.[279,280]
3. Cost effective and easy to produce
4. LIG can be patterned into various shapes and sizes and can be integrated into a wide range of applications.

5. Environmentally friendly
6. LIG produced has lightweight and flexible
7. Recently, this technique has been used to carbonize the carbonaceous precursors at ambient conditions for short time instead of using furnace at high temperature for long time and under inert gas atmosphere.

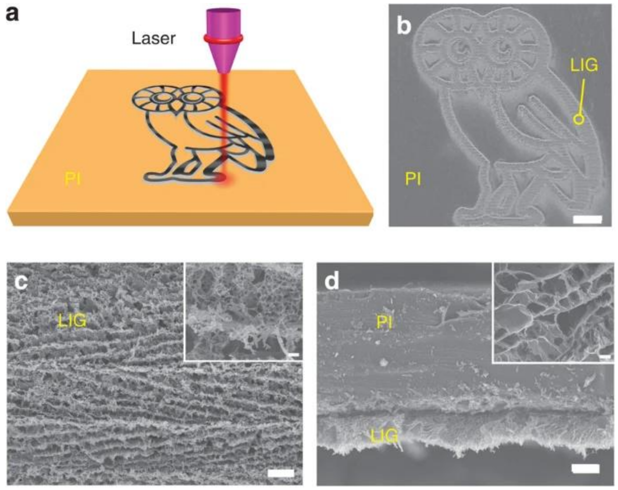

Figure 2-18. LIG schematic from PI. (b), a cross-sectional SEM picture of the LIG film on the PI substrate; (c), a SEM image of the LIG film circled in (b); and (d), a SEM image of a patterned LIG film. The SEM picture depicting the porous morphology of LIG is inset.

This technique has been widely applied to the fabrication of flexible and miniaturized devices for a variety of applications, such as:

1. Energy storage: LIG has been demonstrated as an effective electrode material for supercapacitors and batteries.[281,282]
2. Sensing: LIG has been used for the development of gas sensors, pressure sensors, and strain sensors. LIG can be formed in a variety of 3D shapes with a high surface-to-volume ratio, excellent thermal and electric conductivity of the LIG results in rapid response times for all studied gases.[283] There are various types of LIG sensors based on different sensing mechanisms such as electrochemical,[284] thermoacoustic,[285] chemiresistive,[286] photoelectric.[287]
3. Water purification: as LIG composite membrane because LIG's antifouling and antibacterial capabilities may be aa feasible option for water treatment technology.[288,289]

The properties and applications of LIG are strongly influenced by the choice of precursor material. By selecting the appropriate precursor, LIG can be tailored to meet specific requirements for various applications. The different LIG precursors mixed with ORR catalysts to prepare an air cathode are discussed below.

2.3.3.1 LIG precursors:

LIG preparation is currently restricted to a few polymeric precursors, most notably the polyimide (PI) known, whose precursors, 4,4′-oxydianiline and pyromellitic dianhydride. Other polymers that have been reported to be appropriate for LIG synthesis include sulfonated poly(ether ether ketone), polysulfone, and polyethersulfone, which have structures comparable to polyimide or polyetherimide.[290,291] These materials are expensive, poisonous, and generated from petroleum or coal. Recent efforts have also been made to produce LIG from other carbon-based including thermoplastic polymers, phenolic resins, biopolymers such as lignin, and even textiles, cellulose, wood, cork, or even food (e.g., potato skins, bread, and coconut shells).[292–295]

While most of the polymeric precursors used are toxic, poly (furfural alcohol) (PFA) is a sustainable and green polymer which is usually used as adhesives, binders, and carbon precursors. Furfural alcohol, which is the monomer of PFA, is manufactured by hydrogenation of furfural that is produced from biomass waste by-products, such as corncobs, oat, wheat bran, or sugar cane bagasse.[296] PFA is synthesized by the cationic condensation of furfural alcohol (FA) leading to a highly cross-linked structure with aromatic rings.[297] This chemical structure is similar to several laser induced graphene (LIG) precursors such as phenol-formaldehyde resins that formed LIG based supercapacitors.[298,299] Since the polymerization process of furfural alcohol can be implemented at different temperatures and using various catalysts, carbon yield when pyrolyzing can be controlled and organic and inorganic materials can be combined.[300,301] In addition, the different preparation methods of PFA can change the morphology, thermal, and mechanical properties of the carbon resulted from pyrolyzing PFA.[302–307] Furthermore, because PFA is appropriate with a wide range of materials, it can be used to create polymer nanocomposites for a variety of applications such as adsorbents, separation membranes, catalysts, and electrodes of fuel cells, and electric double-layer capacitors, etc.[304] Hawes *et al*. achieved for the first time the laser-induced carbonization of PFA by doping PFA films with graphene oxide (GO) as a carbonization aid at loading (1 wt.% GO).[308] This allowed for the formation of a highly porous LIG with low resistance and a relatively higher carbon yield. The supercapacitor achieved a high specific areal capacity that yielded capacitances of 16.0 mF/cm^2 at 0.05 mA/cm^2 when compared to the undoped material. For the first time, we developed CoO_x-Pt core shell and spherical nanoalloy structures, MnO_2 and metal-free catalysts loaded in laser induced graphene. Theses catalysts fabricated using a simple synthesis method, a small quantity of catalyst precursors, and laser induced pattering under ambient conditions, without using GO as a pseudocatalyst or furnace for the PFA carbonization process (as will described in chapter 2, 3 and 4).

2.3.3.2 Catalysts doped LIG as air cathode for ZAB:

Introducing catalysts on to the air cathode is very critical for the performance of ZAB. There are several approaches to incorporate catalysts on to the cathode matrix. For example, Tour's team developed LIG that was decorated with catalysts as air cathode for ZAB by drop-casting the catalysts' precursor solution onto the LIG that had been treated by O_2 plasma and laser it again. [309,310] Ni/Fe/Mn/LIG as air cathode for ZAB performed high durability through charge and discharge cycles >200 h and high-power density reach to 98.9 mW/cm^2. They reported the reason of the good performance could be the interconnection between LIG and the anchor nanoparticles that provide high active area and the optimum ratio of the catalyst.[311] While, the Co_3O_4/LIG air cathode exhibited a good durability reach to more than 66 h.[309]

Electrodeposition of metal nanoparticles (Pt, Pd, Cu, Au) is widely used to decorate LIG with metal nanoparticles. But the applications mostly were sensors.[312–315] On the other hand, MnO_2 decorated LIG by different methods to fabricate supercapacitors; hydrothermal method (immersing LIG in MnO_2 precursor solution then laser it or apply high temperature),[316,317] and electrochemical deposition.[318,319] Han *et al.* demonstrated a simple synthesis method to produce LIG embedded with different metal nanocrystals (Cu, Co, Ni, Fe, NiFe) from biodegradable cedar wood. By using CO_2 laser, the cedar wood was converted to graphene and the metal salts were reduced to metals (as shown in **Figure 2.19**).[320] The cedar LIG/NiFE electrode was tested toward OER, and it performed a superior activity with low overpotential 296 mV at current density 10 mA/cm^2 and a 50 mV/dec Tafel slope.

In all these catalysts incorporation strategies, the metal or metal oxide gets simply deposited on the LIG surface and embedded within the pore-space surrounding it, but not well-anchored to the carbon. Casting the catalysts on the graphene, on the other hand, involves depositing the catalyst particles onto the surface of the graphene material. This method can result in a heterogeneous distribution of catalyst particles on the graphene surface, which can lead to lower catalytic activity and stability due to particle aggregation or deactivation. While encapsulating or anchoring the catalysts in a graphene matrix involves embedding the catalyst particles within the graphene structure, forming a composite material. This approach provides a high degree of control over the catalyst's dispersion and size distribution. The catalysts are protected from aggregation and deactivation, leading to improved catalytic performance and stability. This method also provides a large surface area for catalytic reactions to occur, enhancing the reaction rate. Fewer studies have focused on incorporating the metal or metal oxide catalyst directly into the carbon precursor itself. To our knowledge, Zhang *et al.* was the first to incorporate a Pt precursor into the monomer solution prior to the polycondensation reaction used to form the polyimide (PI) film.[321] Laser-scribing under H_2/Ar atmosphere with a CO_2 laser led to uniformly dispersed Pt nanoparticles with a size of about 5 nm embedded within the carbon at a loading of 5 wt.%. The system was not tested for ORR but the overpotentials needed to reach 10 and 100 mA/cm^2 for the hydrogen evolution reaction (HER) were 107 and 256 mV, respectively. Instead of using a PI precursor, Zou *et al.* laser converted a cobalt containing metal organic framework (MOF, ZIF-67) into a nitrogen-doped carbon with Co embedded in the carbon structure.[322] However, the size of these particles was fairly large, ranging from 70 to 250 nm. Despite this, the OER performance was good and when the electrode acted as anode used as the cathode for a ZAB, the stability was significantly enhanced. These electrodes with the embedded Co enabled cycling for over 220 h compared to conventional Pt/C electrodes which failed after only 20 h.

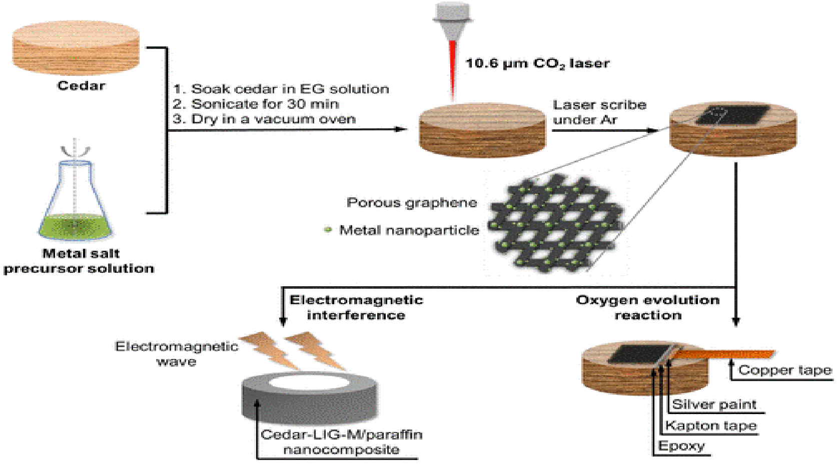

Figure 2-19. Cedar-LIG-M in situ formation is depicted schematically. In an ethylene glycol (EG) solution containing metal nitrate salts, cedar wood was immersed and then sonicated in the bath. The modified cedar monolith was scribed by a 10.6 m CO2 laser in Ar atmosphere after the solvent had been vaporized in a vacuum oven. Next, a device was made for OER, and paraffin nanocomposite preparation was done for EMI shielding.

As mentioned above, entrapped the catalysts nanoparticles in biomass derived LIG as air-cathode for ZAB was rarely investigated. Therefore, this research focuses on combining novel ideas; LIG technique, biomass carbon precursor, biomass nitrogen precursor, simple synthesis method, and low quantity of catalysts precursors to achieved ultra-small nanoparticles (< 2 nm) distributed in LIG matrix, good ORR performance and high stable air cathode for ZAB.

2.4 Summary of Challenges and Thesis Layout

As it was briefly mentioned in Section 1, ZABs are a promising electrochemical energy storage technology. However, to promote widespread adoption of this technology, improvements to their air-breathing cathodes are needed that address challenges as the high cost of platinum (Pt) catalyst used to boost the kinetics of the oxygen reduction reaction (ORR) as well as the stability of Pt/C interfaces over long-term cycling. Therefore, the main challenge in research associated with air cathode is to improve the ORR activity and stability during charging and discharging process. Improving the ORR activity requires an increase in electrode’s catalysts, optimize the catalyst such as tuning the particle size and shape of the catalyst, or/and add functional atoms. As mentioned above, entrapping the catalysts nanoparticles in LIG matrix as air-cathode for ZAB by carbonizing carbon forming resins containing various precious and non-precious metal catalyst precursors could enhance the insufficient stability and improve the ORR activity. Therefore, this research focuses on combining novel ideas; using LIG technique instead of furnace, nano-alloying platinum/cobalt oxides, using biomass carbon precursor and biomass nitrogen precursor, designing facile simple synthesis method, and using low quantity of catalysts precursors to achieve ultra-small nanoparticles (< 2 nm) distributed in LIG matrix with good ORR performance and high stable air cathode for ZAB.

Chapter 2 of the thesis contains a brief description of zinc-air batteries. A brief review of the mechanism of the oxygen reduction reaction in alkaline conditions. The catalysts used as air cathode such as platinum, platinum and transition metal, manganese oxides and nitrogen doped carbon. Moreover, the role of using the laser induced graphene technique to carbonized graphene precursors is elaborated along with the advantages of using the biomass polymer (poly furfural alcohol) as a carbon precursor. **Chapter 3** of the thesis introduces and investigates the designing of the platinum/cobalt oxide/laser induced graphene catalyst synthesis method and discusses the catalyst's performance toward oxygen reduction reaction. **Chapter 4** of the thesis explores the manganese oxides incorporation with LIG as air cathode and evaluates the ORR performance in different tests. **Chapter 5** of this thesis discusses the nitrogen doped graphene fabrication and the determines the ORR performance. Finally, **Chapter 6** of this thesis discusses the lessons from the work completed, summarizes and proposes future directions that can be taken.

Chapter 3

Embedded Platinum-Cobalt Nanoalloys in Biomass-Derived, Laser Induced Graphene as Stable, Air-Breathing Cathodes for Zinc-Air Batteries

Fuel cells and metal–air batteries hold significant promise to help decarbonize transportation and the electricity grid. To encourage widespread adoption of these technologies, improvements to their air-breathing cathodes are required, which address problems such as the high cost of platinum (Pt) catalysts used to boost the kinetics of the oxygen reduction reaction (ORR) as well as the stability of Pt/C interfaces over long-term cycling. In this paper, we demonstrate a facile approach to reduce Pt content to less than 2 wt % by interfacing Pt with CoO_x as well-dispersed nanoparticles entrapped within a highly conductive laser-induced graphene (LIG) matrix. Laser-induced carbonization of polymerized furfural alcohol preloaded with Co and Pt precursors resulted in the formation of a mixture of spherical nanoalloys $PtCoO_x$ and core (CoO_x)–shell (Pt) structures. This LIG-$PtCoO_x$ electrode exhibited a low onset and half-wave potential in alkaline media, which closely approached a benchmark Pt/C. The effectiveness of LIG-$PtCoO_x$ was demonstrated by its performance in rotating disk and rotating ring disk electrode studies versus commercial Pt/C with the same concentration of the catalyst, which resulted in 4-fold greater mass activity and more than 6-fold higher specific activity, which are reflected in a high turnover frequency (TOF). The resulting material was tested as an air–cathode for zinc (Zn)–air batteries leading to improved stability (118 h of operation) and rechargeability (0.75 V voltage gap), exhibiting a higher peak power density compared to batteries assembled with the commercial benchmark Pt/C cathodes with similar composition.

Contributions

The result of this chapter has been accepted in ACS Applied Nanomaterials Journal as: Embedded Platinum-Cobalt Nanoalloys in Biomass-Derived Laser Induced Graphene as Stable, Air-Breathing Cathodes for Zinc-Air Batteries,[323] and the authors in order are Tahani Aldhafeeri, Marianna Uceda, Angad Singh, Manila Ozhukil Valappil, Prof. Michael W. Fowler, and Prof. Michael Pope

I designed the experiments in consultation with Dr. Michael Pope. The experiments were performed entirely by myself with the assistance of an undergraduate co-op student Angad Singh .

I also wrote the manuscript for publication and Dr. Marianna Uceda, Dr. Manila Ozhukil Valappil and Dr. Pope helped with organization and editing of the manuscript for publication and responding the reviewer's comments.

Funding Acknowledgements

This project was funded by Natural Sciences & Engineering Council of Canada's Alliance Program, the Ontario Centre for Innovation, the University of Hafr Al Batin though the Saudi Arabian Cultural Bureau in Canada, and in collaboration with e-Zinc company (Mississauga, ON)

3.1 Introduction

Improving the efficiency, stability and cost of electrocatalysts for the oxygen reduction reaction (ORR) and oxygen evolution reaction (OER) are essential for enabling the wide-spread use energy storage and conversion devices such as fuel cells and metal-air batteries.[324] A major efficiency bottleneck in these devices is the sluggish ORR kinetics at the cathode which causes high cathodic overpotentials and low overall battery efficiency. Platinum (Pt), supported on a high surface area conductive carbon scaffold, is extensively used as the electrocatalyst for ORR, but poses a barrier to commercialization due to its high cost, poisoning sensitivity, poor long-term stability, and low efficiency due to high overvoltage between ORR and OER.[325] Strategies to improve the activity and stability of ORR while potentially decreasing costs include lowering Pt content,[326] use of non-precious metal catalysts,[327–331] including heteroatom doped carbon,[332] and combinations of these strategies.[333–335] To reduce Pt content, significant progress has been made in terms of reducing the size of Pt nanoparticles and to improve their distribution on and within the carbon supports.[326] The Pt content within these nanoparticles can also be reduced by mixing Pt with less expensive transition metals (M), such as cobalt (M = Co) or nickel (M = Ni), via the fabrication of PtM_x alloys or metal oxide Pt-(MO_x) core-shell structures.[328–331,333,336] One of the most investigated Pt-based catalyst used in ORR applications is based on PtCo system. The synergistic effect of Pt and Co in PtCo catalysts is believed to arise from the electronic interactions between the two elements. Specifically, the electronic structure of Pt is perturbed by Co, which can enhance the Pt activity.[337,338] In addition, Co can induce structural changes in the Pt lattice, leading to the formation of more active sites. An effective four-electron ORR process is produced by the PtCo double site, which encourages the fixing of OOH* intermediates and the dissociation of OH* intermediates.[339] Huang *et al.* and Salgado *et al.* summarized the factors that cause an improvement in the ORR electrocatalysis on

PtCo alloys; the shortening of Pt-Pt interatomic distance, surface roughening due the dissolution of the more oxidizable alloying component, and electronic considerations due to an increase in Pt d-band vacancy.[340,341]

However, even with these designs, significant challenges remain in terms of stability. Nanoparticles are typically only physiosorbed to a surface and can easily agglomerate.[342,343] Metal catalyst dissolution and particle coalescence cause coarsening over time which reduces the number of active sites available for catalysis.[344] Carbon corrosion and oxide formation at high potentials can also enhance coarsening or cause catalyst detachment from the support.[345–347] Thus, recent work has focused on the development of strategies to more strongly anchor M-Pt or MO_x-Pt nanoparticles to the support. For example, Co-Pt alloys have been attached to carbon surfaces using weaker surface interactions such as metal-Pi interactions or chelating effects.[338,348]

Furthermore, Jung *et al.* developed an approach to create a PtCo intermetallic within a N-doped carbon shell on top of a graphitized carbon support.[336] When tested as the cathode for a polyelectrolyte membrane (PEM) fuel cell, this catalyst showed minimal loss in voltage and power over 30,000 cycles. While promising, further improvements to stability and reducing the number and time of the various processing steps are required to make such methods commercially attractive.

Laser-based methods have recently demonstrated promise to form both the conductive carbon support and electrocatalysts used to decorate these supports. By avoiding the typically slow heat treatment step, the oven-free method of using a laser spot or line to convert carbon and catalyst precursors photothermally or photochemically has the potential to be higher throughput and more energy efficient.[349] For example, Tour's group first demonstrated that porous, high surface area, graphene-like traces could be scribed onto commercial polymers like Kapton using an inexpensive CO_2 laser often used in industry for cutting and marking.[350] Later, it was demonstrated that a catalyst precursor salt could be cast onto this so-called laser-induced graphene (LIG) and lasing repeated to decompose the salt into a metal oxide.[351] Various oxide-based electrocatalysts such as Co_3O_4 and MnO_x were deposited on the LIG surface in this way.[352,353] These, and more recently, mixed metal oxides containing Ni, Co and Fe have demonstrated high ORR and OER activity and stability when used as air cathodes in zinc-air and lithium (Li)-air batteries.[354] The same strategy has been used to deposit Cu-Sn alloys for CO_2 conversion.[355] In these strategies, the metal or metal oxide sits on the LIG surface and are embedded within the pore-space surrounding the LIG but not within the carbon itself. Similarly, in other works, Pt, Co, Ni or Fe have been electrodeposited onto the pre-formed LIG and used either as electrocatalysts for sensors or for water splitting.[312,313,356] The use of more rapid laser treatment compared to slow thermal annealing is also thought to prevent coarsening – leading to smaller nanoparticle sizes.[357]

Fewer studies have focused on incorporating the metal or metal oxide catalyst directly into the carbon precursor itself. Zhang *et al.* were the first and, as far as we know, only to incorporate a Pt precursor into the monomer solution prior to the polycondensation reaction used to form the polyimide (PI) film. Laser-scribing under H_2/Ar atmosphere with a CO_2 laser led to uniformly dispersed Pt nanoparticles with a size of about 5 nm embedded within the carbon at a loading of 5 wt.%.[356] The system was not tested for ORR but the overpotentials needed to reach 10 and 100 mA/cm^2 for the hydrogen evolution reaction (HER) were 107 and 256 mV, respectively. Instead of using a PI precursor, Zou *et al.* used laser to convert a cobalt containing metal organic framework (MOF, ZIF-67) into a nitrogen-doped carbon with Co embedded in the carbon structure.[358] However, the size of these particles was fairly large, ranging from 70 to 250 nm. Despite this, the electrode exhibited impressive performance as a Zn-air battery, with significantly enhanced stability. These electrodes with the embedded Co enabled cycling for over 220 h compared to a conventional Pt/C electrode which failed after only 20 h.

In this work, we aim to further explore the idea of incorporating catalyst directly within the carbon support by in situ laser conversion to develop air-cathode for Zn-air batteries. To reduce the Pt content, we explore the use of a dual Pt/Co precursor to generate a Pt-Co or Pt-CoO_x alloy upon photothermal conversion. Instead of PI (e.g., Kapton™), we use the biomass-derived poly furfuryl alcohol (PFA) resin, which is a commodity chemical often used in adhesives, binders, and as a carbon precursor.[359] PFA is synthesized by a simple, acid catalyzed, self-condensation polymerization of liquid furfural alcohol (FA).[359] This simple and versatile chemistry leads to a mechanically robust, cross-linked resin which has been well-studied over the last few decades as a precursor to hard carbons. For example, we were inspired by early work carried out by Foley's group who embedded platinum nanoparticles into PFA and pyrolyzed this Pt-filled resin in a furnace to achieve a composite with 6.4 wt.% Pt^0.[303,360] The material exhibited remarkable thermal stability upon high temperature (800 °C) treatment and kinetic stability during hydrogenation of long chain and bulkier alkenes in liquid phase. Our group has recently demonstrated the use of PFA as a promising precursor to LIG which can often outcompete LIG derived from PI in terms of conductivity and electrode capacitance.[308] However, the incorporation of catalyst within the PFA and how it impacts the resulting LIG, has yet to be explored.

Herein, we investigate the laser-induced conversion of PFA with embedded CoO_x-Pt catalysts for Zn-air battery applications. Our approach, described in Scheme 1, involves a simple one-pot synthesis method under ambient conditions using a CO_2 laser for carbonization. To improve the stability of the noble metal and reduce the amount of the platinum precursor used, cobalt precursor was appended. The nanoparticle size was effectively controlled via optimization of Triton X-100 (TX) as a surfactant. The material produced was < 2 nm nanoparticles with a unique structure consisting of core-shell and nanoalloy $PtCoO_x$ entrapped within a 3D-LIG conductive matrix. The electrocatalytic performance of the resulting materials are investigated as ORR catalysts. Finally, the performance within a Zn-air battery cell was tested which yielded an excellent peak power density of 67.1 mW/cm^2 and a high specific capacity based on consumed zinc electrode at discharging current density 20 mA/cm^2 . This was comparable to the commercially available Pt/C material at the similar composition (52.3 mW/cm^2).

Scheme 1

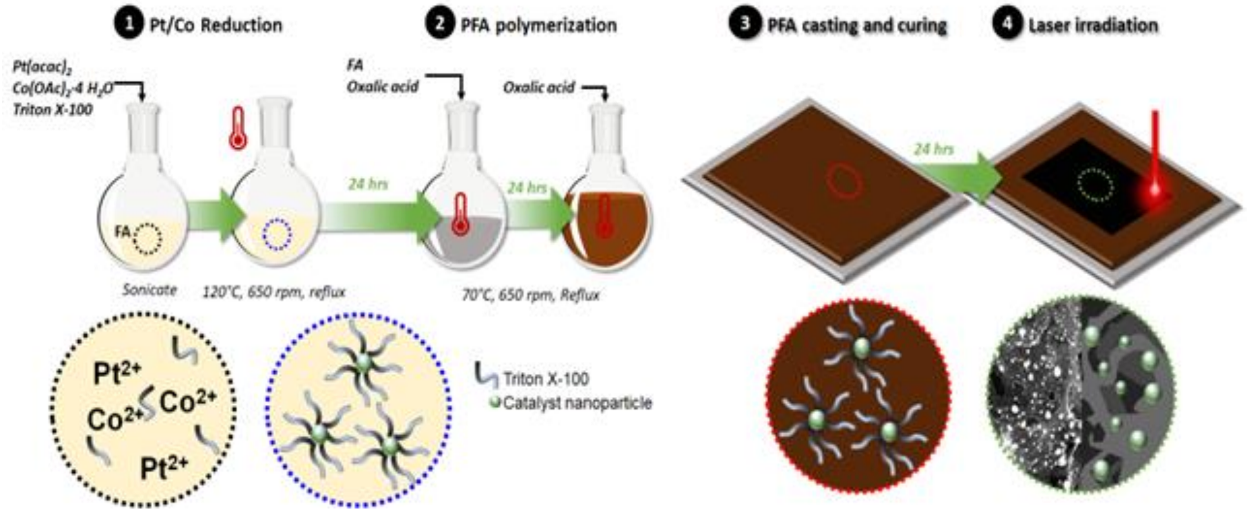

Figure 3-1. Material and synthesis procedure to prepare LIG-$PtCoO_x$ samples: (1) Step1; the reduction reaction of the catalysts salts in the reflux process, (2) Polymerization step by mixing the monomer FA with the acidic catalyst (oxalic acid), (3) Casting the viscous material on a foil by doctor blade and curing it in the oven, and (4) Step 4 which is the photothermal carbonization of the sample by the CO_2 laser machine at specific conditions.

3.2 Experimental Methods

3.2.1 Synthesis of loaded LIG (CoO_x/Pt/graphene)

To form the polymer precursor with embedded electrocatalyst, 48 mg of platinum (II) acetylacetonate ($Pt(acac)_2$, 48.0 wt.% Pt, Alfa Aesar) and 98 mg of anhydrous cobalt (II) acetate ($Co(OAc)_2 \cdot 4\ H_2O$, Alfa Aesar, 98%), were added to 2 g of the liquid monomer, furfuryl alcohol (FA, Thermo ScientificTM, Acros Organics, 98%). In this step, FA acts as a reducing agent. FA and similar alcohols are known to act as reducing agents for metal ions. Varying amounts of the non-ionic surfactant, Triton X-100 (TX, Millipore Sigma), were used to aid in the dispersion of the Pt and Co salts in the FA. The TX:FA ratio (wt./wt.) was varied to determine the impact on catalyst dispersion and the ability to carbonize the catalyst loaded polymer with the laser. These precursors were mixed in the FA by tip ultrasonication with a 10 s pulse and at 60% power (BioLogics, Inc. Model 150 V/T ultrasonic homogenizer, 150 W) for 15 min. The resulting dispersion was then heated to 120 ˚C and stirred at 650 rpm under reflux conditions for 24 h in a single neck round bottom flask. An additional 4 g of FA was then added along with 68 mg of oxalic acid dihydrate (EMD, 99.5%) as the initiator to catalyze FA polymerization. The polymerization of FA was carried out at 70 ˚C for an additional 24 h under reflux. A further 68 mg of oxalic acid was added, and the condenser was removed. Once the FA polymerized sufficiently to produce a dispersion with suitable viscosity for doctor blading, the dispersion was cast onto an aluminum foil substrate using a wet gap of 1 mm. The coating was then cured in an oven at 80 ˚C for 24 h. As a benchmark, PFA-based formulations were compared to diluted commercial cathode mixtures (3.39 wt.% Pt/C) prepared by mixing carbon black (Super C45, MTI Corp.) with commercial 20 wt.% Pt/C (Sigma-Aldrich).

3.2.2 Laser-Induced Carbonization and Electrode Assembly

Once the loaded PFA had finished curing, the aluminum foil was peeled off. The free-standing PFA film was then irradiated with a CO_2 laser engraver (Boss Laser 1416L, 50W) in order to convert the surface of the dense, electrically insulating PFA to a porous, high surface area, conductive scaffold for the embedded electrocatalysts. Electrodes of $1 \times 1\ cm^2$ were patterned in the films using approximately 10.2% power (5.1 W) for the carbonization and the scan speed was 10 mm/s. The sheet resistance at various powers was measured before each sample and the power yielding the maximum conductivity was chosen to account for variations in laser alignment/focus with time.

Four samples with varying TX weight ratios were prepared and referred as: LIG-PtCoO$_x$-0, LIG-PtCoO$_x$-1, LIG-PtCoO$_x$-2, and LIG-PtCoO$_x$-3, with TX to FA weight ratios of 0:1, 0.5:1, 1:1, and 1.5:1, respectively. Also, the “Commercial Pt/C” that mentioned in the figures is the commercial 3.39 wt.% of Pt/C.

3.2.3 Material Characterization

The morphology, size, and distribution of the catalysts were imaged by scanning electron microscopy (SEM, Zeiss Leo 1530) with energy dispersive X-ray spectroscopy (EDS, Oxford) operating at 20 kV acceleration voltage. The count number was 3000 counts per second (cps). The scanning transmission electron microscopy (STEM) and EDS experiments were performed using a Thermo Fisher Scientific Talos 200X operated at 200 kV. High-angle annular dark-field (HAADF) was performed with a spot size less than 1 nm and a convergence semi-angle of 10.5 mrad. The EDS data were analysed using Velox program from Thermo Fisher Scientific. The high-resolution transmission electron microscopy (HRTEM) experiments were performed using a Titan 80-300 equipped with an imaging lens aberration corrector FEI microscope operated at 300 kV. For imaging, powders scraped off the laser-irradiated areas were dispersed in water, sonicated and the solution spread on a holey carbon, Cu supported TEM grid.

X-ray diffraction (XRD, Rigaku Miniflex II) was carried out using a scan rate of 2°/minute, from 2θ values of 10-100 operated at 15 kV at 10 mA. X-ray photoelectron spectroscopy (XPS, Thermal Scientific KAlpha XPS spectrometer, 150 eV) was used to analyze the surface functional groups. The XPS spectra were fitted using CasaXPS software.

To investigate the effect of the surfactant on the polymerization of the PFA, attenuated total reflectance Fourier transform infrared (ATR-FTIR) spectroscopy of the samples was done prior to scribing using a Bruker Tensor FTIR equipped with a Pike attenuated total reflectance (ATR) adapter and a ZnSe crystal. The samples PFA-PtCoO$_x$-0, PFA-PtCoO$_x$-1 and PFA-PtCoO$_x$-2 are cured PFA samples (before lasering) that contained 0:1, 0.5:1, 0:2 of TX to FA weight ratio, respectively. In this study, TGA was used to obtain the total platinum and cobalt contents of the synthesized catalysts. A temperature ramp of 5 $^{\circ}$C/min was used, and the maximum temperature was 100 $^{\circ}$C. The experiment was conducted under flowing air to burn the carbon support and determine the weight of the remaining compound which was platinum and cobalt. TGA profiles were collected on a TA instrument Q50 TGA Thermogravimetric Analyzer.

Finally, ultraviolet-visible (UV-vis) absorption spectra were recorded by a Thermo Scientific Evolution 300UV-VIS spectrophotometer using 1 nm resolution, and 240 nm/min scan speed with samples placed in quartz cuvettes with a 1 cm path length. UV-vis spectroscopy was used to follow the reduction reaction of the metal salt using distilled water as solvent.

3.2.4 Electrochemical measurements

To test the electrocatalytic response towards the oxygen reduction reaction (ORR), electrochemical tests were conducted using a Biologic SP-300 potentiostat, under ambient conditions, using a three-electrode cell with a rotating ring disk electrode (RRDE) system (Pine Research Instrumentation, USA). The cell consisted of a glassy-carbon-based working electrode (GC, 0.196 cm^2), a Pt-wire counter electrode, and a Hg/HgO (1 M KOH solution) reference electrode (RE-61AP, ALS). An LIG ink prepared by scraping off some of the LIG sample and dispersing with 40 vol% isopropanol (≥ 99%) in deionized water (< 8 µS/cm) at 5 g/L LIG composite and 0.002 mL of 5 wt.% Nafion (Sigma-Aldrich) as a binder was used to modify a glass carbon electrode. Prior to casting, the ink was bath ultrasonicated for 1 h in an ice bath by 4-gal Digital Sonic Cavitation Machine, 360W. A 5 µL volume of ink was drop cast every 15 minutes until a total of 20 µL ink was loaded onto a 5 mm diameter glassy carbon disk (Pine Research). The ink and glassy carbon solids loading were kept the same for all samples. After the ink dried, the tip was installed onto the rotating shaft of a WaveVortex Rotator (Pine Research). The tip was then carefully lowered into 60 mL of 0.1 M potassium hydroxide (KOH) within a 5-neck glass cell (Pine Research). The rotation rate was set at 1600 rpm. Prior to any experiments, the current was stabilized by performing 50 cycles of cyclic voltammetry at 20 mV/s between 0.1 V and -0.8 V vs. Hg/HgO reference electrode under oxygen (Linde, 99.999% O_2) or nitrogen purging. After stabilization, CVs and ohmic drop compensation (80% at 1kHz) were followed by linear sweep voltammetry at 5 mV/s between 0.1 V to -0.8 V vs. Hg/HgO under oxygen or nitrogen purging. The final LSVs under oxygen were normalized with respect to the LSV acquired under nitrogen purging. The number of electrons (n) transferred via the ORR half-cell reaction under different electrode potentials was estimated by the Koutecky-Levich (K-L) equations 2 and 3:

$$\frac{1}{j} = \frac{1}{j_{\mathrm{L}}} + \frac{1}{j_{\mathrm{K}}} = \frac{1}{B\omega^{\frac{1}{2}}} + \frac{1}{j_{\mathrm{K}}}, \tag{1}$$

$$B = 0.62\, nFC_0(D_0)^{\frac{2}{3}}(v)^{-\frac{1}{6}}, \tag{2}$$

where j is the measured current density, j_K is the kinetic limiting current density (A/cm^2), j_L is the diffusion-limited current density (A/cm^2), B is the corresponding K-L slope value, ω is the electrode rotation rate (rad/s), F is the Faraday constant (96485.31 C/mol), C_0 is the bulk concentration of O_2 in 0.1 M KOH solution (1.26×10^{-6} mol/cm^3), D_0 is the diffusion coefficient of O_2 in 0.1 M KOH solution (1.93×10^{-5} cm^2/s), and v is the kinematic viscosity of the electrolyte (v = 0.01 cm^2/s in 0.1 M KOH solution). The Koutecký–Levich analysis was conducted by performing the LSV test at varying rotation rates (200, 600, 900, 1600, and 2200 rpm). Peroxide formation was analyzed by setting the RRDE at 0.333 V vs. Hg/HgO on a separate channel during the LSV at 1600 rpm in 0.1 M KOH electrolyte saturated with O_2 conducted to the RRDE. The H_2O_2 yield and the n were calculated by equations 4 and 5:

$$H_2O_2\,\% = 200\left(\frac{\frac{J_\mathrm{r}}{N}}{J_\mathrm{d}+\left(\frac{J_\mathrm{r}}{N}\right)}\right), \tag{3}$$

$$n = 4J_\mathrm{d}/(J_\mathrm{d} + (J_\mathrm{r}/N)\,), \tag{4}$$

where J_d is the disk current (A/cm^2) , J_r is the ring current (A/cm^2), and N is the collection efficiency (0.27) reported by the manufacturer.

Information related to the rate-determining process of the ORR mechanism is provided via the Tafel equation:

$$\eta = a + b\log(j_\mathrm{k}), \tag{5}$$

where η is the overpotential, a and b are the intercept and the Tafel slope, respectively, and j_k is the kinetic current density.

Electrochemical active surface area (ECSA) was evaluated by integrating the hydrogen adsorption-desorption regions in the CV curves using:

$$ECSA = \frac{A}{vC}\frac{1}{m_\mathrm{pt\ loaded}}\,, \tag{6}$$

where A is the peak area (mA.V), v is the scan rate (V/s), C is the charge required to reduce the proton monolayer of the active platinum (0.21 mC/cm^2), and $m_{\text{pt loaded}}$ is the platinum load in the catalysts (mg). The electrolyte is 0.1 M H_2SO_4 saturated with N_2 for at least 1 h prior to the experiment. A Pt wire was used as CE, Ag/AgCl (1 M) reference electrode, a 3 mm diameter glassy carbon (GC) disk was used as the WE, and 2µL of ink was cast onto the GC. Mass and specific activities were established at -0.1 V vs. Hg/HgO, at room temperature. The turnover frequency (TOF) value can be calculated using the following relation: [361]

$$TOF = \frac{j_{\mathrm{k}} A}{(\ n\ e\ N_{\mathrm{s}})} \tag{7}$$

where j_{k} is the kinetic current density, A is the electrode surface area (cm^2), n is the number of electrons transferred during ORR (n = 4), e is the charge of an electron (1.6×10^{19} C), N_s is the number of active sites on the catalyst surface. In this case we assumed only Pt atoms are active. The electrode materials were tested in Zn-air batteries by air-spraying (ABEST, CA-TJ-186ACF4K) the ink onto a gas diffusion layer. The ink is prepared using the same process as the ink for RRDE. However, the concentration is lowered to 1 mg/cm^2 to prevent blockage in the air-sprayer nozzle. Approximately 0.56 mL of ink was sprayed onto a 1.5 × 1.5 cm carbon paper -(Toray 120 with a microporous layer, 0.43 mm thick) to produce 1 mg$_{(\mathrm{LIG/catalyst})}$ /cm^2 loading. The loaded carbon paper was allowed to dry on a hotplate at 60 °C overnight. It was then assembled into a homemade cell composed of 5/16" acrylic sheets with 1/16" thick ethylene propylene diene monomer rubber (EPDM) rubber gaskets. Electrical contact with the carbon paper is made with a Monel mesh (200 × 200 mesh size). The anode is a zinc plate (0.02-" Zinc Sheet EN 988 Shiny, 99.99% min purity), and the electrolyte is 6 M KOH and 0.2 M zinc acetate ($Zn(CH_3COO)_2 \cdot 2H_2O$, Sigma). The assembled Zn-air battery was allowed to rest for 6 h prior to any measurements. All measurements were carried out on an Arbin battery tester (BT2000, Arbin Instruments, USA). Galvanostatic cycling was carried out at 10 mA/cm^2 for 150 s in charge and 150 s of discharge and then by using galvanodynamic charge/discharging by applying a current density from 0-100 mA/cm^2 at 1 mA/s scan rate.

Specific capacity was tested using chronopotentiometry. Discharge at 30 mA/cm^2 was performed for a long time until the zinc plate that contacts the electrolyte fully react. After the reaction, the zinc plate was ultrasonicated with distilled water until the zinc oxide layer was completely removed. The specific capacity was calculated using the following equation

$$specific\ capacity = (i_{\mathrm{discharge}} \times t_{\mathrm{reaction}})/(m_{\mathrm{Zn1}} - m_{\mathrm{Zn2}}) \tag{8}$$

where $i_{\mathrm{discharge}}$ = 20 mA/cm^2 , t_{reaction} is the time when reaction stops, m_{Zn1} is the weight of the polished zinc plate before test, and m_{Zn2} i the weight of the zinc plate after the reaction.[362]

3.3 Results and Discussion

3.3.1 PFA polymerization and production of LIG-PtCoO$_x$ via CO$_2$ laser.

As shown in **Figure 3.2a,** the simple, one-pot, and oxalic acid-catalyzed polymerization of FA monomer with dispersed metal catalysts, yields a free-standing 2000 ± 310 μm thick film after casting. The films appear black and are relatively flexible and mechanically robust. Polymerization of FA was slower with the added catalyst and surfactant, taking 12 h longer to cure/solidify compared to polymerization of FA alone (**Figure 3.2b**). Laser irradiating these films with an industrial CO$_2$ laser at powers between 4.85-5.25 W converts the material into a shiny, gray/metallic film as shown in **Figure 3.2c**. The electrical sheet resistance (**Table 3.1)** of these films was the lowest when 10.2% power was used. In general, the addition of TX to the PFA increased the resistance of the film by a factor of four to five (from ~10 to ~ 40-50 Ω/sq). There was no consistent difference in sheet resistance between TX:FA weight ratios of 0.5:1 (LIG-PtCoO$_x$-1) and 1:1 (LIG-PtCoO$_x$-2). The increased resistance is likely due to residual, non-conductive TX in the sample after laser treatment. Note that LIG-PtCoO$_x$-0 is referred to as the sample that does not contain TX and LIG-PtCoO$_x$-3 is referred to 1.5:1 ratio of TX to FA.

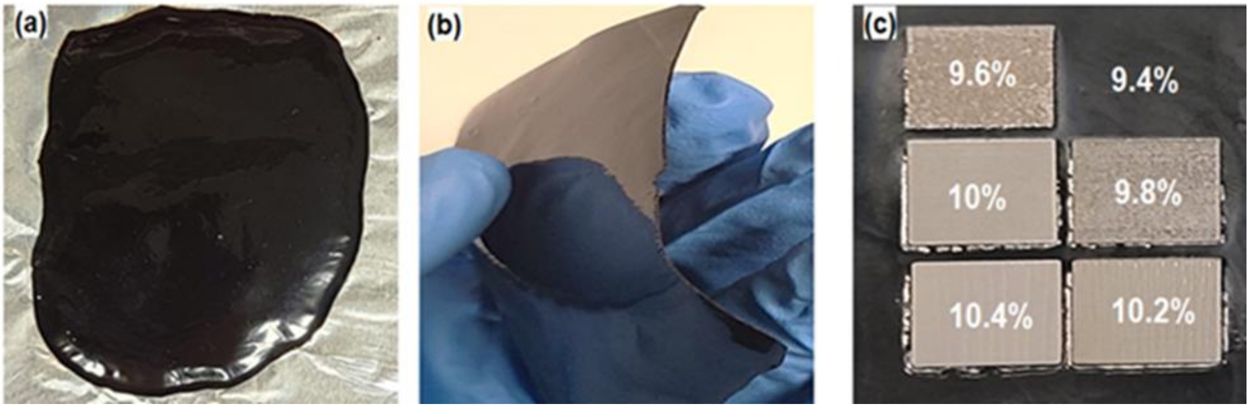

Figure 3-2. Images of PFA in different steps (a) PFA that cast onto foil after curing, (b) Free-standing PFA film after being peeled off the foil, and (c) Square 1 x 1 cm^2 LIG with different scribing power at scan speed 10 mm/s.

Table 3-1. Sheet Resistance (Ω/Sq) as a function of laser power for samples prepared with different TX to FA ratios.

Power / Samples	Sheet Resistance (Ω/Sq) at different scribing power %			
	9.80 %	10.0 %	10.2 %	10.4 %
LIG from neat PFA (without catalysts)	N/A	12.8 ± 4.8	12.0 ± 4.7	11.6 ± 1.6
LIG-PTCoO$_x$-0	N/A	6.6 ± 2.3	5.7 ± 1.7	3.5 ± 0.7
LIG-PTCoO$_x$-1	42.4 x 10^3 ± 1 x 10^3	26.9 ± 6.5	23.7 ± 7.9	47.2 ± 14.1
LIG-PTCoO$_x$-2	338.9 ± 105.3	51.6 ± 10.2	37.1 ± 9.2	48.2 ± 11.4

To determine the impact of metal salt reduction and loading on the extent of polymerization, ATR-FTIR was performed (**Figure 3.3a**). Full polymerization is evidenced by the elimination of the (OH-) stretching peak present in the FA monomer between 3750-3328 cm^{-1}.[363] The FTIR spectrum for the FA monomer exhibits the hydroxyl (OH) stretching peak at ~3325 cm^{-1}. This disappeared after polymerization of the neat FA resin and indicates full conversion to polymer. There is also a significant decrease in the intensity of the 1005 and 1150 cm^{-1} peaks in PFA attributed to C-O stretches in the FA monomer. Furthermore, there are weak peaks presented around 1660−1670 cm^{-1} attributed to ring stretching of 2,3-bisubstituted furan rings, ∼1548 cm^{-1} resulting from the conjugated C=C stretching bonds or ring vibrations, 1350 cm^{-1} assigned as the C−H ring deformation, 1215−1180 and ∼1015 cm^{-1} arising from =C−O−C asymmetric and symmetric stretching, and 815 cm^{-1} from the vibration of C-O of furan rings. When Pt(acac)$_2$ and Co(OAc)$_2$ salts are first added to the FA, some of the FA itself oxidizes to furfural. This can be observed in the FTIR spectra shown for the dispersion immediately after the reduction reaction (step1) compared to the neat FA where peaks are associated with 1713 and 1735 cm^{-1} (**Figure 3.3b**).[364] These peaks occur in conjugated unsaturated aldehydes and not ketone group. Moreover, the presence of a peak between 2845 and 2960 cm^{-1} is attributed to the aldehyde group and aliphatic C-H stretches (**Figure 3.3c**).[365] This is why additional FA was added in Step 2, to compensate for oxidized FA. As shown in **Figure 3.3d**, the strong OH and CH$_2$ stretching vibrations are seen in the spectra of pure TX at 3480 cm^{-1}, 2948 cm^{-1} (asymmetrical stretch), and 2869 cm^{-1} (symmetrical stretch), respectively. At 1642, 1610, 1581, and 1511 cm^{-1}, four distinct aromatic absorption bands are seen:

C-H bending vibrations are responsible for bands at 1456 cm^{-1} and 1364 cm^{-1}; C-O stretching vibrations produce bands between 1096 cm^{-1} and 1300 cm^{-1}. It is observed from the FTIR spectrum of FA/TX-catalysts (after reduction reaction) that the intensity of peaks assigned to C-O bond of TX is decreased on interaction with catalyst salts. This suggests that the hydrophilic polyoxymethylene group effectively caps the Pt^{2+} and Co^{3+} ions while the oxygen of the C-O bond interacts with Pt^{2+} or Co^{2+} ions.[366] **Figure 3.3d**, also shows the FTIR spectra for samples containing varying TX:FA ratios. The results suggest that all samples do not have the OH stretching vibration peak between 3750- 3328 cm^{-1} except for the sample with LIG-PtCoO$_x$-3; this is due to TX remaining in LIG, despite the sample being irradiated by the CO$_2$ laser. This sample was also found to be non-conducting after laser carbonization and the color of the irradiated area was not gray and shiny as the other samples. Therefore, only lower TX contents were considered in further characterization.

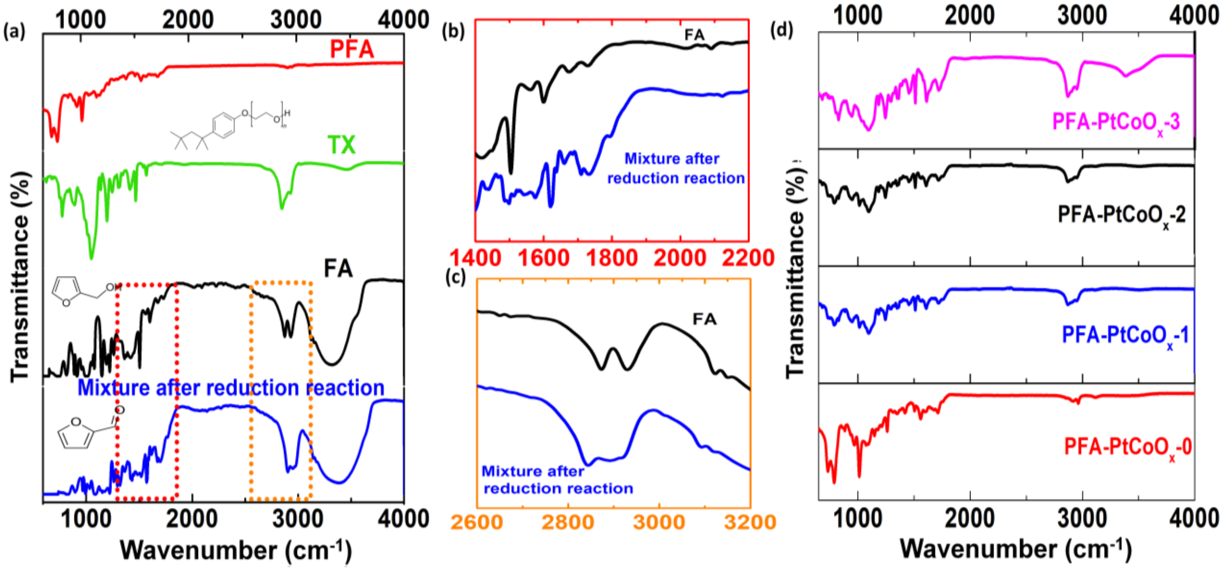

Figure 3-3.Fourier transform infrared (FTIR) spectra of various samples: a) FA monomer, TX, mixture after the reduction reaction step1, and neat PFA after cured in oven, (b) FA monomer and mixture after reduction reaction in wavenumber range 1400-2200 cm^{-1}, (c) FA monomer and mixture in the wavenumber range 2600-3200 cm^{-1}, and (d) Cured PFA resins with different weight ratio of TX to FA (before scribing by laser) used for laser-scribing.

As shown in **Figure 3.4a**, UV-vis was carried out to follow the reduction of the Pt(acac)$_2$ to Pt metal following step1 and step4. The Pt(acac)$_2$ graph exhibited absorption at 227, 253, 285 and 350 nm, which are the signatures of the Pt complexes.[367] These peaks are diminished after the reduction reaction and accompanied by the appearance of the typical absorption bands of the aldehydic and furan functional groups (at ~ 278 and 218 nm), respectively, and confirms the oxidation of FA to furfural during step1 (**Figure 3.4b**).[368] A characteristic absorption peak of graphene in LIG (from neat PFA) has been observed at 266 nm. The incorporation of catalysts with LIG leads to a shift in the graphene absorbance peak to shorter wavelengths (**Figure 3.4c**). It has been observed that the absorption peak position of graphene for LIG-catalysts changes to 255 nm, a blue shift of 10 nm as compared to LIG without catalysts dispersion.[369,370] The blue shift may be the result of a charge transfer interaction between graphene and catalyst nanoparticles. In addition, the absorption peak located at 225 nm in LIG-catalysts curve could be related to the Pt nanoparticles present in the sample.[371] Note that, this peak could not be observed in the mixture after the reduction reaction due to the large peak of the furan functional group (200 to 239 nm).

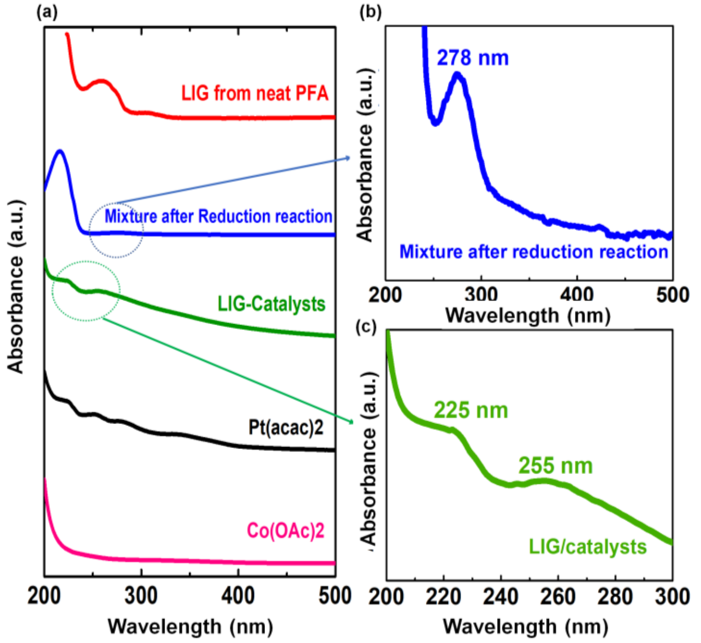

Figure 3-4.UV-vis spectrum for (a) cobalt, platinum precursors, LIG-catalysts, mixture after step 1 (reduction reaction), and LIG from neat PFA (without TX and without catalysts), (b) maximize the graph area from 200 to 500 nm of the sample after reduction reaction, and (c) maximize the area from 200 to 300 nm of the LIG-catalysts sample.

3.3.2 Catalyst identification and oxidation state

The irradiated material was analyzed using XRD to probe the crystal structure of the prepared samples and to confirm the presence of platinum metal and cobalt oxides (**Figure 3.5a**). For all samples, there is a broad reflection at 2θ=25.9^o, associated with the (002) plane of graphite which is indicative of a disordered carbon structure. A broad (100) reflection at 2θ=42.9^o is also observed and overlaps with reflections associated with Pt metal and cobalt oxides between 40^o and 47^o. The peaks indexed at 2θ=40.5^o and 46.8^o are attributed to (111) and (200) facets of FCC Pt (PDF# 1-087-0647) and are apparent in all samples with various amounts of TX. The diffraction peaks at 2θ = 43.1 and 36.5^o are attributed to the (200) and (111) reflections of CoO (PDF# 00-002-1217). The diffraction peak at 2θ=36.8^o corresponding to (311) reflections of Co_3O_4 (PDF# 00-042-1467). The position of the (222) reflection of the platinum oxide (PtO) is 2θ = 50.1^o (PDF# 03-065-6984), while the position of (110) and (020) reflections of PtO_2 are in 2θ= 35.0^o and 39.9^o (PDF#153-7412). The XRD results did not show any diffraction peaks for metallic Co and most of the diffraction peaks for cobalt oxides are weak as shown in **Figure 3.5a** and this may be attributed to the Pt-CoO_x alloy formed when CoO_x dissolved into the Pt lattice, or they are present as an amorphous phase.[372]

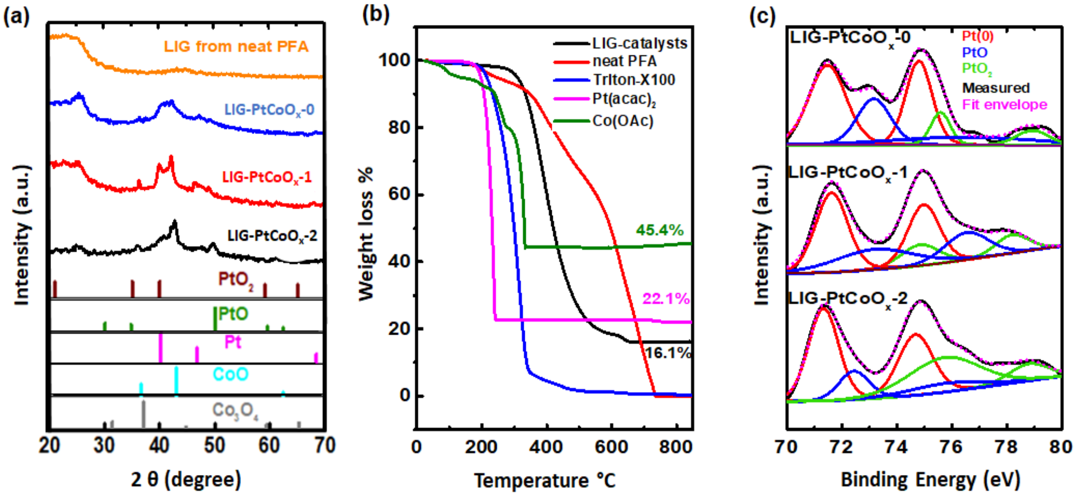

Figure 3-5. Characterization of catalyst structure. (a) XRD patterns for PFA, and LIG-PtCoO_x-1, (b) Thermogravimetric analysis (TGA) in air atmosphere for PFA,TX, $Co(OAc)_2$, $Pt(acac)_2$, and LIG-PtCoO_x-1, and (c) High resolution XPS spectra of the Pt 4f region for samples prepared with various amounts of TX.

TGA was used to determine the content of catalyst present in the samples before and after laser irradiation. As shown in **Figure 3.5b**, after heating in air $Co(OAc)_2$, $Pt(acac)_2$, TX, PFA, PFA-catalyst and LIG-catalysts all exhibited weight loss between 200 $^{\circ}$C and 710 $^{\circ}$C. For the $Pt(acac)_2$

samples, 22.4 wt.% remains after heating which we attribute to Pt metal. After heating to 1000 ˚C, the $Co(OAc)_2$ sample retained 41.1 wt.% which is attributed to Co^0 and CoO content in $Co(OAc)_2$ (the boiling points of Co, CoO, and Co_3O_4 are 2927 ˚C, 1933˚C, and 900 ˚C). A decomposition study of TX alone showed thermal degradation started around 380 ˚C and lost its entire mass around 500 ˚C. The neat PFA is completely oxidized at ~735 ˚C. Burning off the carbon in the LIG-$PtCoO_x$ powder indicates that the sample contains 16.1 wt.% catalysts (Co, CoO_x and Pt). Since this gives no information about the ratio of components and there are unknown mass loss/gains by reduction of platinum oxides and oxidation of cobalt species, we analyze the composition further by XPS and hydrogen underpotential deposition as discussed below.

The elemental chemical states and compositions of the catalyst were probed via XPS. The survey spectra are given in **Figures 3.6a**, which show the existence of Pt, O, and C in different samples. Cobalt was only apparent in the LIG-$PtCoO_x$-1 sample. The oxygen content increased with the concentration of the TX, supporting the hypothesis that some residual TX remained in the sample after laser treatment. As shown in **Figure 3.6b**, the C 1s spectrum was deconvoluted into C=C (284.4 ± 0.35 eV) and C-C (284.9 ± 0.3 eV) components. The curve at the O1s core level in **Figure 3.6c** was fitted with three components, referring to O-C=O (534.1 eV), C-O (533 eV) and metal oxide (531.2). The highest area% (~at. %) of the metal oxide was for the LIG-$PtCoO_x$-2. The high-resolution spectrum for Pt 4f is shown in **Figure 3.5c**. The Pt 4f is distinguished by doublet peaks Pt $4f_{7/2}$ and Pt $4f_{5/2}$ for Pt^0, Pt^{2+}, and Pt^{4+}, respectively. The presence of Pt^{2+} and Pt^{4+} indicates the incomplete reduction of the Pt salt during the synthesis process, leaving behind PtO, and PtO_2. The Pt 4f spectrum was deconvoluted into three species with binding energies (71.4, 71.5 eV), (73.0, 72.5 eV) and (75.6, 75.7 eV), which correspond to Pt^0, Pt^{2+}, and Pt^{4+} respectively for samples LIG-$PtCoO_x$-0, LIG-$PtCoO_x$-2. While for sample LIG-$PtCoO_x$-1, the Pt 4f binding energies for metallic Pt, Pt^{2+}, and Pt^{4+} were at (71.8, 73.2, and 74.9 eV). The Pt 4f peaks are red shifted for the LIG-PtCoOx-1 sample which indicates electron transfer from the 5d electron in Pt-based alloys to the CoO_x. These observations are in overall agreement with literature report.[373]

Based on peak integration, the composition of Pt^0, Pt^{2+}, and Pt^{4+} was calculated to be (51.9%, 34.9%, 13.2%), (62.2%, 27,2%, 10.5%), and (44.8%, 23.8%, 31.4%) for samples LIG-$PtCoO_x$-0, LIG-$PtCoO_x$-1, and LIG-$PtCoO_x$-2, respectively. The total of Pt^{2+}, and Pt^{4+} in sample LIG-$PtCoO_x$-2 samples was the highest and this result agrees with the result from the O 1s spectra analysis.

Moreover, we observed from the XPS Pt 4f results that as the TX weight ratio increases, the PtO atomic percentage decreases. **Figure 3.6d** displays the high-resolution Co 2p XPS spectra for all samples, signifying three chemical states of cobalt: Co at binding energy (778.4 eV), Co^{2+} (781.2 eV), and Co^{3+} (779.3 eV) for the LIG-PtCoO$_x$-1 sample. For the other samples, Co 2p was not able to be detected by XPS. As we will show later, this may be due to Co being buried in the core of a platinum shell. Integration of the deconvoluted peaks indicates that the LIG-PtCoO$_x$-1sample is composed of 49.8% Co^{2+}, 5.1% Co^{3+} and 13.5% metallic Co. **Table 3.2** lists the atomic percentage, full width at half maximum (FWHM), and the position of each element in the spectra.

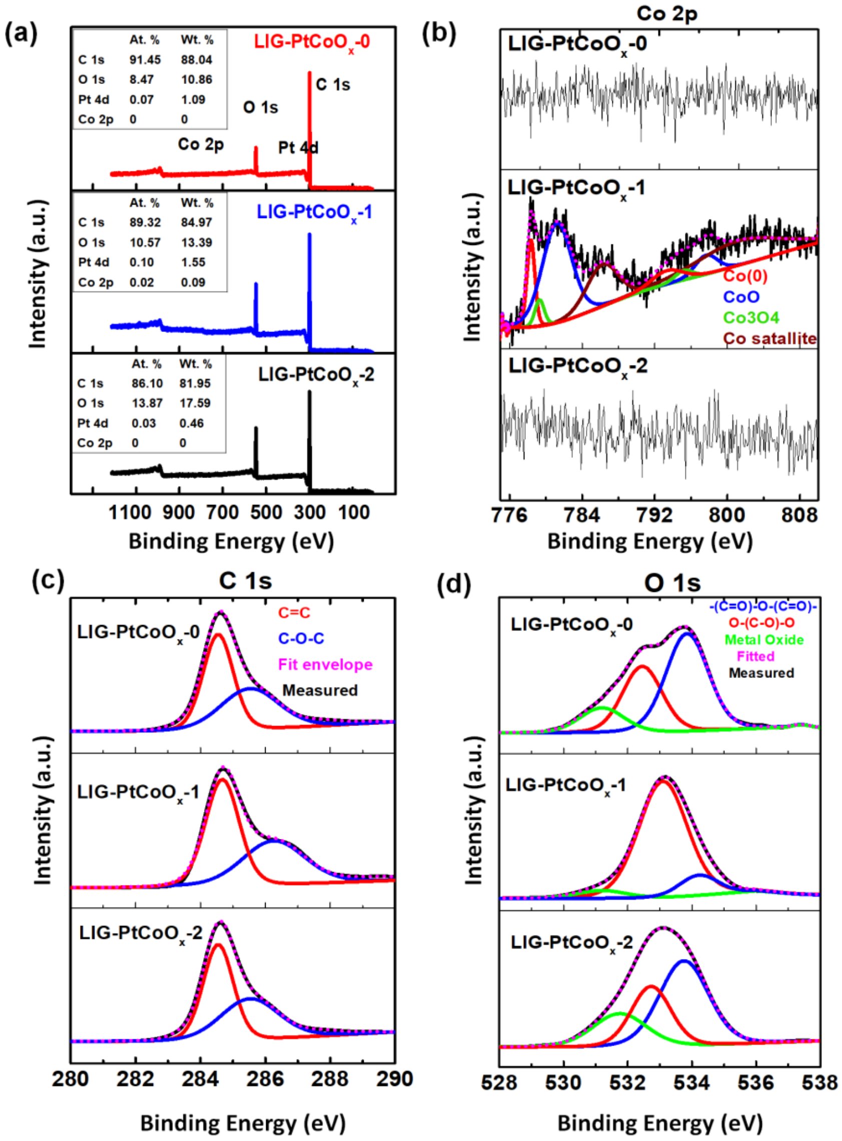

LIG-PtCoO$_x$-0

	At. %	Wt. %
C 1s	91.45	88.04
O 1s	8.47	10.86
Pt 4d	0.07	1.09
Co 2p	0	0

LIG-PtCoO$_x$-1

	At. %	Wt. %
C 1s	89.32	84.97
O 1s	10.57	13.39
Pt 4d	0.10	1.55
Co 2p	0.02	0.09

LIG-PtCoO$_x$-2

	At. %	Wt. %
C 1s	86.10	81.95
O 1s	13.87	17.59
Pt 4d	0.03	0.46
Co 2p	0	0

Figure 3-6. XPS results; (a) surveys for different samples with various amount of surfactant LIG-PtCoOx-0, LIG-PtCoOx-1, and LIG-PtCoOx-2, (b) cobalt region (Co 2p), (c) High resolution XPS spectra of the carbon region (C 1s), and (d) oxygen region O 1s for different samples.

Table 3-2.XPS analysis details for each sample (TX to FA weight ratio); position, FWMH, and the atomic concentration percentage (%area) using Casa software (a) LIG-PtCoO$_x$-0, (b) LIG-PtCoO$_x$-1, and (c) LIG-PtCoO$_x$-2.

(a)

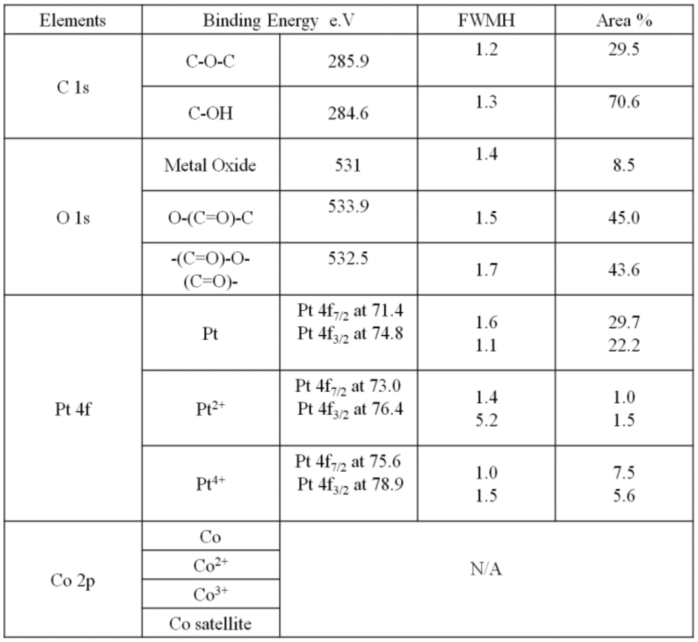

Elements	Binding Energy e.V		FWMH	Area %
C 1s	C-O-C	285.9	1.2	29.5
	C-OH	284.6	1.3	70.6
O 1s	Metal Oxide	531	1.4	8.5
	O-(C=O)-C	533.9	1.5	45.0
	-(C=O)-O-(C=O)-	532.5	1.7	43.6
Pt 4f	Pt	Pt $4f_{7/2}$ at 71.4 Pt $4f_{3/2}$ at 74.8	1.6 1.1	29.7 22.2
	Pt^{2+}	Pt $4f_{7/2}$ at 73.0 Pt $4f_{3/2}$ at 76.4	1.4 5.2	1.0 1.5
	Pt^{4+}	Pt $4f_{7/2}$ at 75.6 Pt $4f_{3/2}$ at 78.9	1.0 1.5	7.5 5.6
Co 2p	Co	N/A		
	Co^{2+}			
	Co^{3+}			
	Co satellite			

(b)

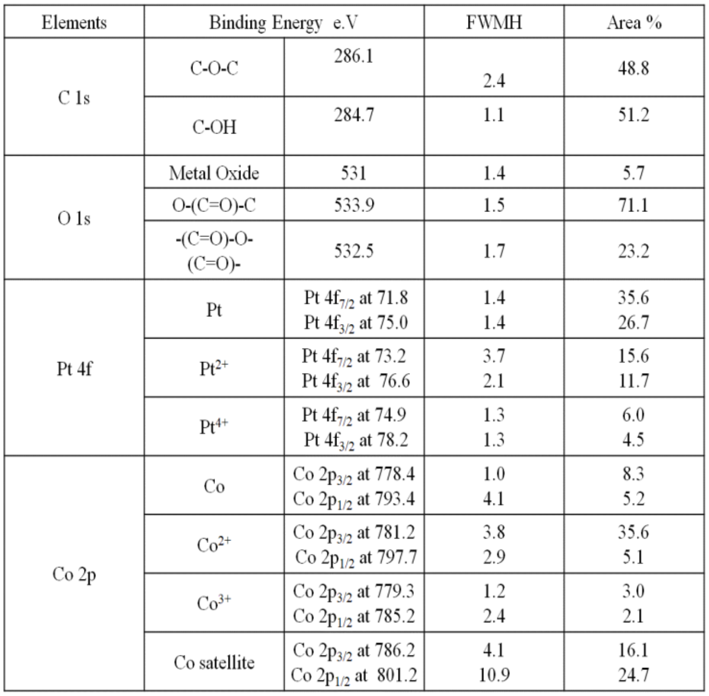

Elements	Binding Energy e.V		FWMH	Area %
C 1s	C-O-C	286.1	2.4	48.8
	C-OH	284.7	1.1	51.2
O 1s	Metal Oxide	531	1.4	5.7
	O-(C=O)-C	533.9	1.5	71.1
	-(C=O)-O-(C=O)-	532.5	1.7	23.2
Pt 4f	Pt	Pt $4f_{7/2}$ at 71.8 Pt $4f_{3/2}$ at 75.0	1.4 1.4	35.6 26.7
	Pt^{2+}	Pt $4f_{7/2}$ at 73.2 Pt $4f_{3/2}$ at 76.6	3.7 2.1	15.6 11.7
	Pt^{4+}	Pt $4f_{7/2}$ at 74.9 Pt $4f_{3/2}$ at 78.2	1.3 1.3	6.0 4.5
Co 2p	Co	Co $2p_{3/2}$ at 778.4 Co $2p_{1/2}$ at 793.4	1.0 4.1	8.3 5.2
	Co^{2+}	Co $2p_{3/2}$ at 781.2 Co $2p_{1/2}$ at 797.7	3.8 2.9	35.6 5.1
	Co^{3+}	Co $2p_{3/2}$ at 779.3 Co $2p_{1/2}$ at 785.2	1.2 2.4	3.0 2.1
	Co satellite	Co $2p_{3/2}$ at 786.2 Co $2p_{1/2}$ at 801.2	4.1 10.9	16.1 24.7

(c)

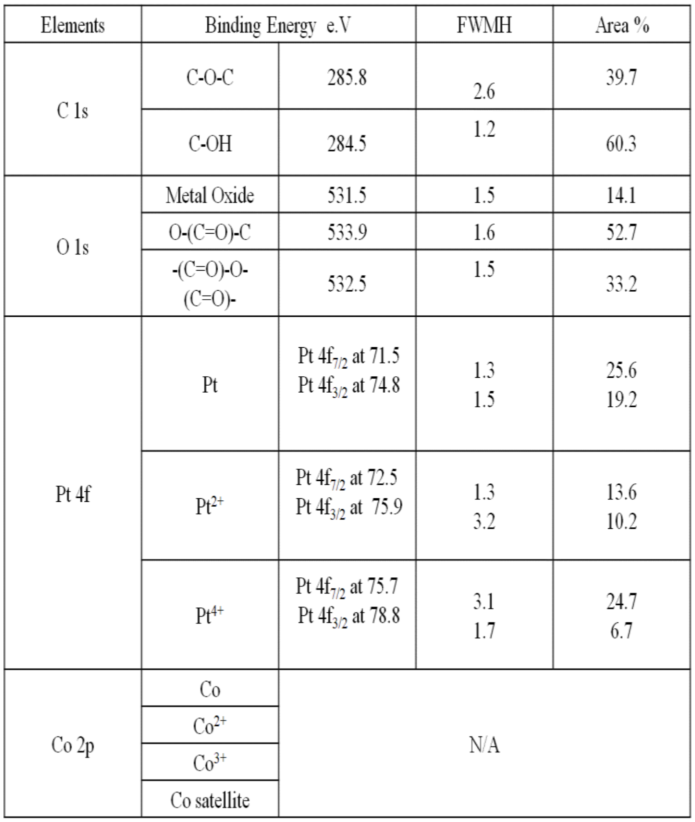

Elements	Binding Energy e.V		FWMH	Area %
C 1s	C-O-C	285.8	2.6	39.7
	C-OH	284.5	1.2	60.3
O 1s	Metal Oxide	531.5	1.5	14.1
	O-(C=O)-C	533.9	1.6	52.7
	-(C=O)-O-(C=O)-	532.5	1.5	33.2
Pt 4f	Pt	Pt 4$f_{7/2}$ at 71.5 Pt 4$f_{3/2}$ at 74.8	1.3 1.5	25.6 19.2
	Pt^{2+}	Pt 4$f_{7/2}$ at 72.5 Pt 4$f_{3/2}$ at 75.9	1.3 3.2	13.6 10.2
	Pt^{4+}	Pt 4$f_{7/2}$ at 75.7 Pt 4$f_{3/2}$ at 78.8	3.1 1.7	24.7 6.7
Co 2p	Co	N/A		
	Co^{2+}			
	Co^{3+}			
	Co satellite			

3.3.3 Catalyst microstructure and LIG composition

SEM images of LIG-PtCoO_x produced with varying amounts of TX revealed that the size of the catalyst nanoparticles was impacted by the quantity of TX. The control sample LIG-PtCoO_x-0 contains larger (~2 µm) catalyst particles than other samples as shown in **Figure 3.7a,d** . In fact, without TX, the catalyst dispersion was observed to agglomerate and quickly settle in the FA during processing (**Figure 3.84a,b**). On the other hand, using TX as a dispersant led to a more homogeneous distribution of smaller sized particles as shown in **Figure 3.7b,c,e,f.** TX can act as dispersant in the FA where the hydrophobic part has affinity towards FA and the hydrophilic head groups of TX has high affinity towards catalysts surface.

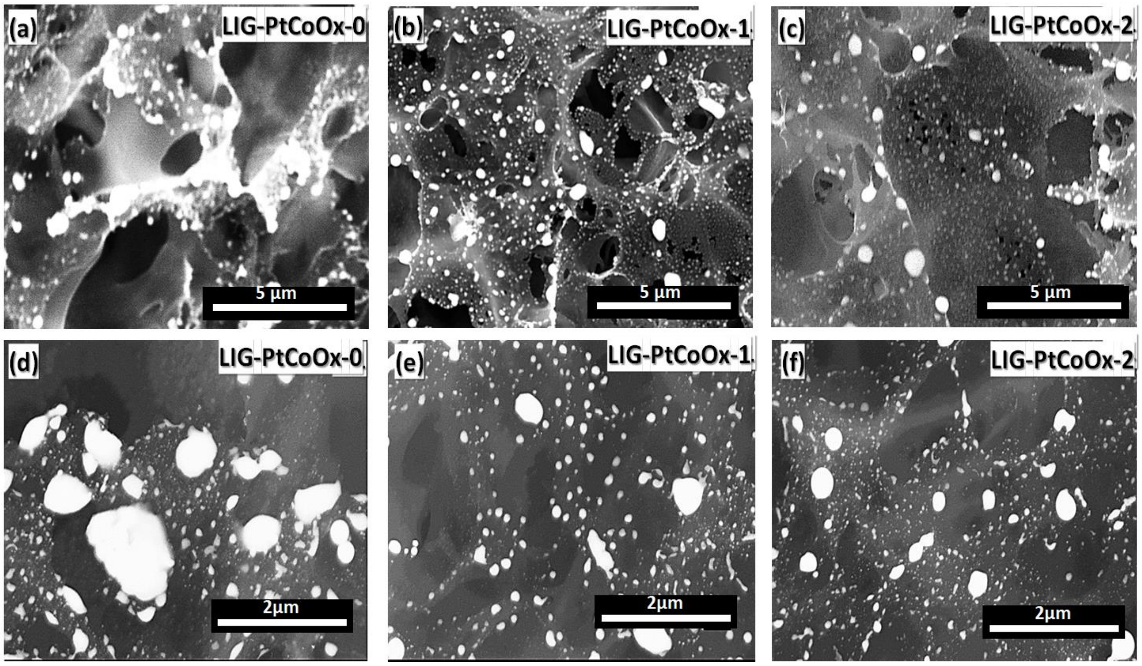

Figure 3-7. SEM images of samples with varying amounts of TX: (a and d) LIG-PtCoO$_x$-0 (b and e) LIG-Pt-CoO$_x$-1, and (c and f) LIG-PtCoO$_x$-2. All images were collected with the secondary electron (SE) detector.

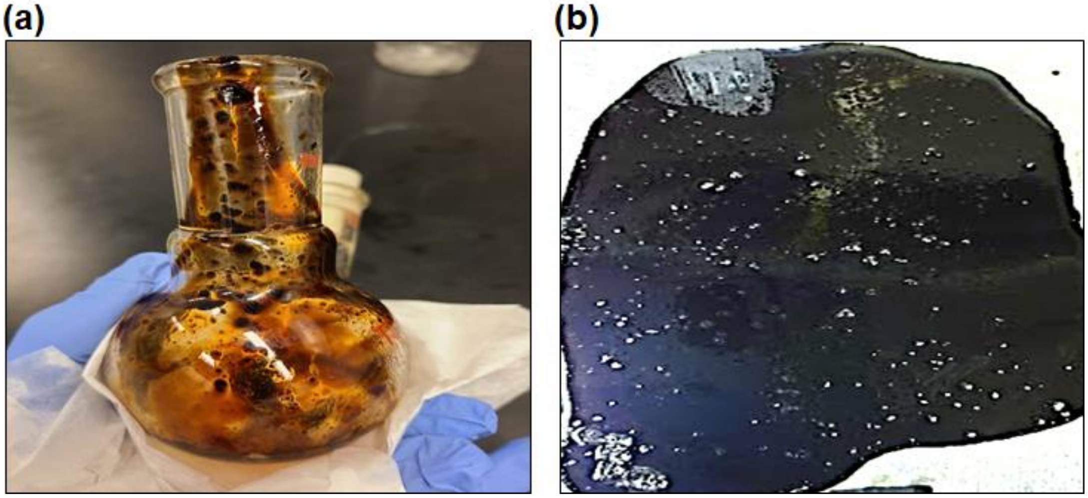

Figure 3-8. Images of LIG-PtCoO$_x$-0; (a) the bottom flask that contains agglomerated catalyst, and (b) after cured the sample in the oven, large particles were presented in the sample.

EDS data (**Figure 3.9**) acquired on various samples indicate the presence of Co, Pt, O, and C with different weight percentages. The EDS results (taken from different spots on the sample) show that as the TX concentration increases in the sample, the oxygen weight percentage increases. This is likely due to the presence of some TX in LIG after carbonization by the CO_2 laser.

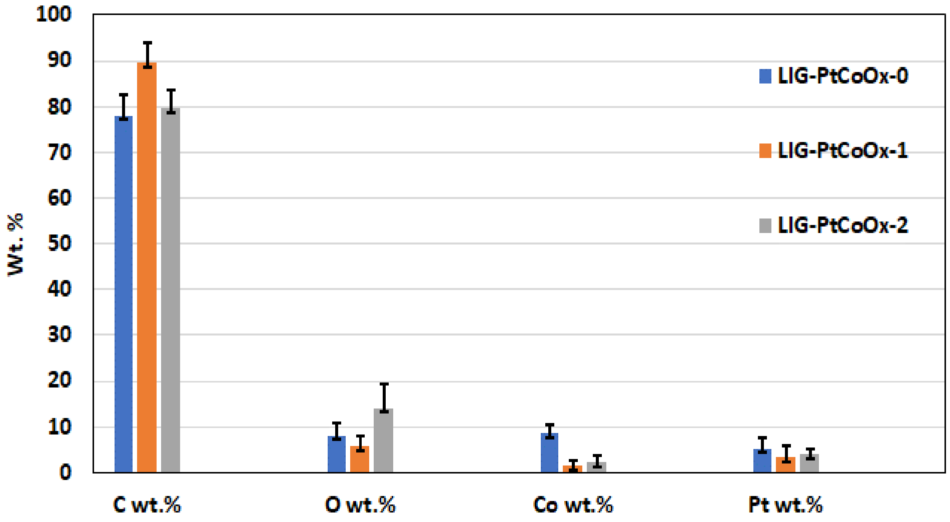

Figure 3-9. Weight percentage for C, O, Co and Pt from EDS analysis for different sample.

Figures 3.10 show the HRTEM images at different magnifications for the LIG-$PtCoO_x$ catalysts. The most remarkable observations from the investigation of the HRTEM images (**Figure 3.10a** and **Figure 3.11a**) are the limited size of the spherical nanoparticles (~1.7 – 5.5 nm) and how well-dispersed the $PtCoO_x$ is throughout the carbon network. The histogram from the TEM image showed a homogeneous PtCoOx size distribution (~ 1.7- 6.0 nm), as shown in the top inset of **Figure 3.10a**. The mean particle diameter is analyzed as 3.0 ± 0.90 nm (N=143). Note that the discrete count as a function of exact size conforms well with a Gaussian distribution.

Based on the HRTEM images (**Figure 3.**10b**),** a core-shell structure of $PtCoO_x$ is observed where the CoO_x core diameter is ~2.3 nm. The corresponding HRTEM image **(Figure 3.10c**) clearly shows that there are 3-4 atomic layers of Pt shell on the surface and the lattice spacing of Pt shell is 0.228 nm. Moreover, the $PtCoO_x$ nanoparticles are surrounded by carbon, which can be clearly seen at the edges (demarcated by a yellow dotted line on **Figure 3.11b-d**). The size of the nanoparticles of different TEM images was determined with ImageJ software as shown in **Figure 3.11e,f**. The typical results of HAADF-STEM imaging and energy dispersive X-ray spectroscopy (EDS) for

LIG-$PtCoO_x$-1 sample are shown in **Figures 3.10d-i**, **Figures 3.12a-f** and **Figures 3.13a-f.** As illustrated by these images a spherical structure of mixed $PtCoO_x$ nanoalloys is observed. In addition, O appears to be enriched in areas where Co is present which suggests the existence of CoO_x (the yellow arrows in **Figure 3.10f,i**, **Figure 3.12e** and **Figure 3.13e**). Core-shell and nanoalloy structures may form for the following reasons. $Co(OAc)_2$ is a volatile organic compound while $Pt(acac)_2$ is practically non-volatile.[374] Volatile $Co(Oac)_2$ could selectively vaporize and accumulated in the bubbles formed by the action of the mixing the reaction in the tip ultrasonicator and/or the reduction reaction in the reflux process and are decomposed to cobalt oxides atoms through the reaction with FA. Pt may then heterogeneously nucleate on and/or alloy with these cobalt oxide particles during the thermal irradiation by CO_2 laser.[375] Another possibility is that during the refluxing process (step 1 in Scheme1), $Pt(acac)_2$ molecules could undergo a galvanic displacement reaction with cobalt oxide nanoparticles when they diffuse into the solution leading to a nanoalloy formation or a CoO_x core covered with a Pt shell.[376] However, as shown in the HRTEM images , the mixed spherical nanoalloy structure of $PtCoO_x$ is more numerous than the core-shell nanoparticles structure.

Since XPS is only able to provide compositional information 1 to 10 nm deep into the material, the cobalt in samples LIG-$PtCoO_x$-0 and LIG-$PtCoO_x$-1 were not detected. On the other hand, EDS probe microns into the samples and estimates larger percentages of Co as it can probe material within the core-shell structure and can identify Pt and Co buried in the LIG network.

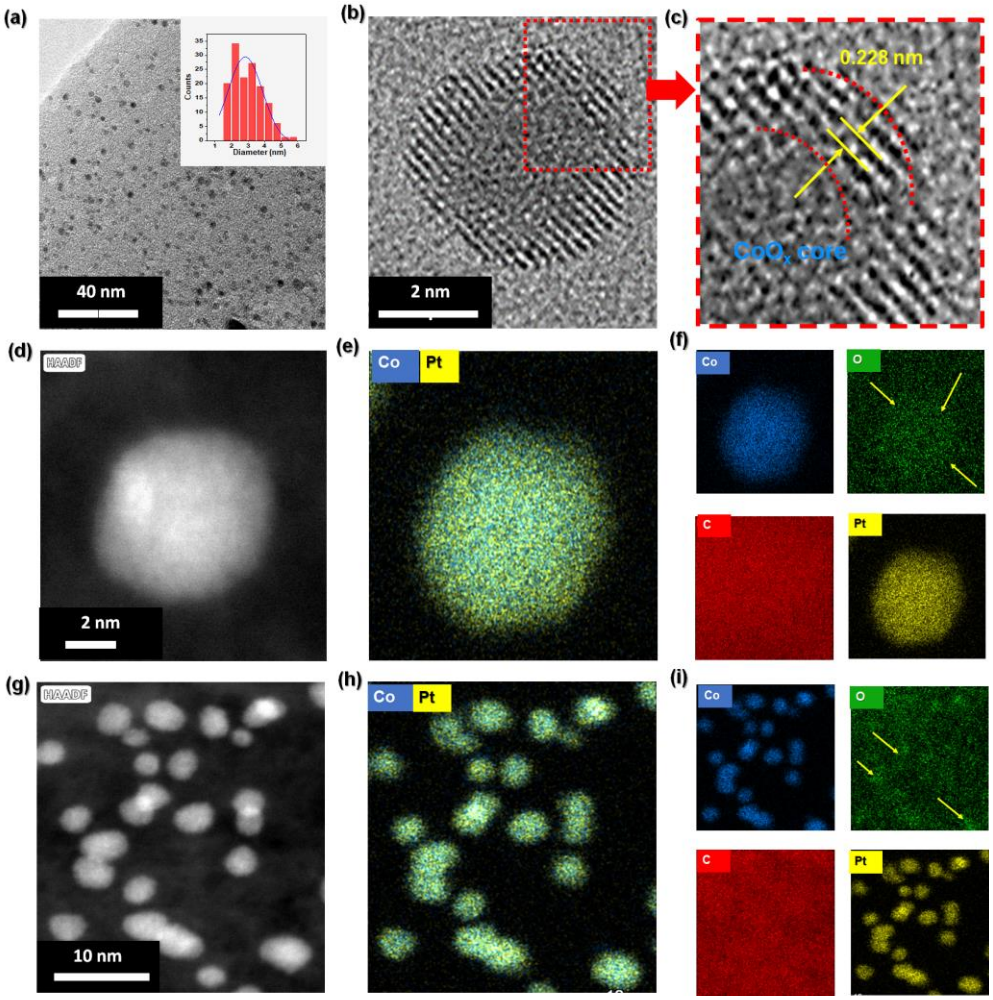

Figure 3-10. Transmission electron microscopy and elemental mapping of LIG-PtCoO$_x$-1 samples. (a) HRTEM image of LIG/ PtCoO$_x$-1. The inset shows the particle size distribution histogram based on the TEM image in (a) with N = 143 determined with ImageJ software, (b) HRTEM of core-shell particle, (c) Higher magnification HRTEM image of core-shell nanostructures from (b) showing lattice spacing of shell corresponding to Pt, (d) and (g) HAADF images, (e, f) and (h, i) EDS elemental maps for Co, O, C, and Pt illustrating the mixing of Pt and Co in the more frequent nanoalloy structures. No examples could be found of solely Pt or solely Co-based nanoparticles.

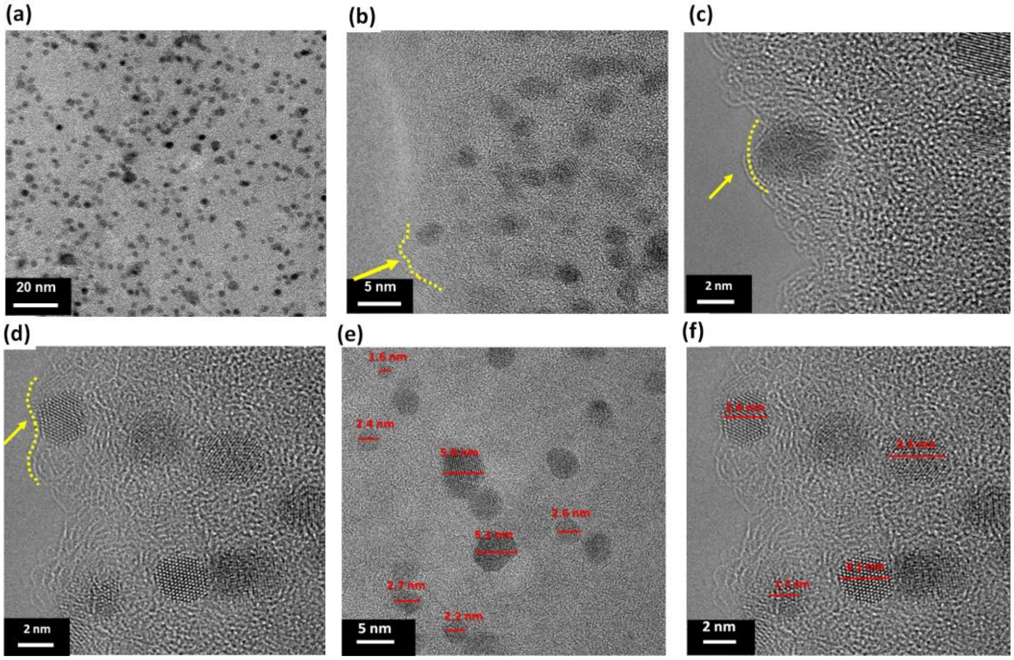

Figure 3-11. HRTEM images (a) show catalysts are distributed uniformly in sample, (b-d) catalysts are surrounded by the carbon matrix (yellow dottes line and arrow) and (e)(f) show the size of the nanoparticles using ImageJ software.

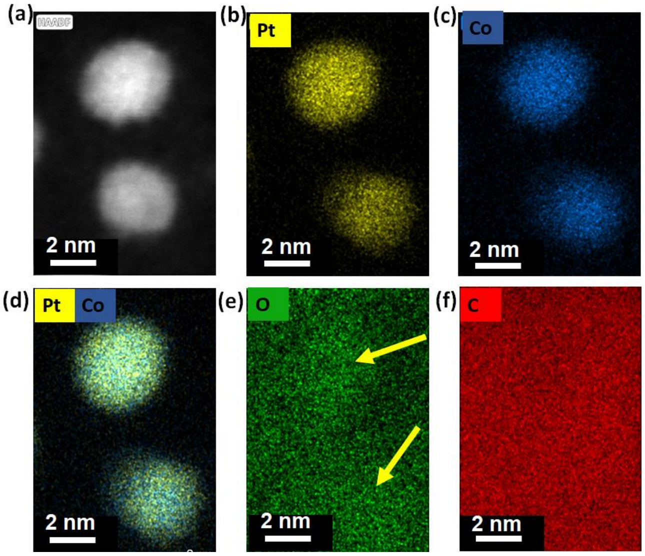

Figure 3-12. EDS elemental maps of LIG-PtCoO$_x$-1 where (a) HAADF image, for (b) Pt, (c) Co, (d) mixed Pt and Co, (e), O, and (f) C elements.

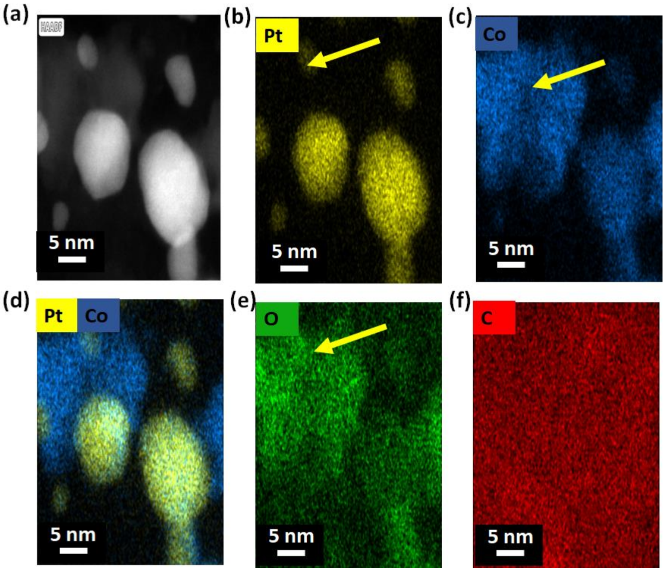

Figure 3-13. EDS elemental maps of (a)HAADF image for (b) Pt, (c) Co, (d) mixed Pt and Co, (e), O, and (f) C elements.

3.3.4 Catalyst performance towards oxygen reduction reaction

Figure 3.14a displays the LSV curves at 1600 rpm in 0.1 M KOH vs. Hg/HgO for different samples. The LIG-PtCoO$_x$-1 sample exhibited an onset potential for ORR of ~ +0.02 V vs. Hg/HgO as shown in **Figure 3.15a**. This was significantly lower than the commercial Pt/C (3.39 wt.% Pt) (~-0.03 V vs. Hg/HgO) benchmark. The fact that the onset potential of LIG-PtCoO$_x$-1 was markedly more positive than that of commercial Pt/C (with the same catalyst concentration) signifies the important role of the TX concentration that affected the ECSA and the spherical nanoalloy PtCoO$_x$ structure in enhancing the ORR activity (**Table 3.3**). The LIG-PtCoO$_x$-1 sample shows a large positive shift in half wave potential ($E_{1/2}$) compared to the other samples and has a limiting current density of 3.29 mA/cm^2 at -0.80 V vs. Hg/HgO, which is comparable to that of the commercial Pt/C with the similar composition (3.70 mA/cm^2). At a voltage of -0.1 V, the current density was - 1 mA/cm^2 for the LIG-PtCoO$_x$-1 which is comparable to the value (-0.85 mA/cm^2) in literature[377] where the sample contained a higher concentration of catalyst (20 wt.% Pt and 20 wt.% Co) dispersed on carbon.

The ECSA was used to estimate the real active surface area of the electrocatalysts (**Eq.6**). As shown in **Figure 3.14b,** the area of the hydrogen desorption peak for commercial 3.39 wt.% Pt/C, and LIG-PtCoO$_x$-1 decreases with decreasing Pt weight percentage and the corresponding ECSA values are 22.57, and 13.60 m^2/g, respectively. Due the low weight percentage of platinum in LIG-$PtCoO_x$-1 and the presence of CoO_x in the sample that decreases the number of active Pt sites, the ECSA value of LIG-$PtCoO_x$-1 is less than commercial 3.39 wt.% Pt/C samples.[378] There were less defined peaks in the hydrogen underpotential (H_{UPD}) region for LIG-$PtCoO_x$-1 relative to other commercial Pt/C, likely due to the presence of CoO_x in the LIG-$PtCoO_x$ sample which cannot be quantified by H_{UPD}.

Furthermore, LIG-$PtCoO_x$-1 and the commercial 3.39 wt.% Pt/C were evaluated for their activity by dividing their mass activity by their mass loading and specific activity normalized to ECSA. We demonstrate that, compared with the commercial 3.39 wt.% Pt/C catalyst, the $PtCoO_x$ catalyst in LIG-$PtCoO_x$-1 achieves fourfold higher mass activity (119.33 $mA/mg_{(PtCoOx)}$ vs. 30.07 mA/mg_{pt}) and more than six times higher specific activity (0.86 mA/cm^2 vs. 0.13 mA/cm^2) at -0.1 V vs. Hg/HgO as shown in **Figure 3.15b**, showing the effectiveness of our LIG-$PtCoO_x$-1. Further, this is reflected in a higher turnover frequency (TOF) at -0.1 V vs. Hg/HgO which was found to be 0.356 s^{-1} and higher than the commercial benchmark (0.054 s^{-1}). The TOF is of similar magnitude to those reported for similar systems such as reported in literature.[339].

The exchange current density estimated from the Tafel region for LIG-CoO_x-1 was estimated to be 0.64 mA/cm^2_{pt} and is higher than the exchange current density of the commercial 3.39 wt.% Pt/C (0.23 mA/cm^2_{pt}). Also, the Pt utilization of the samples was calculated by dividing the Pt mass from the ECSA by the Pt mass from the catalysts mass in the ink used while RRDE/RDE tests. The Pt utilization of the LIG-PtCoOx-1 is close to the value for commercial 3.39 wt.% Pt/C (29.0% vs. 28.2%, respectively), despite the mass from ECSA and from ink used of the Pt in LIG-$PtCoO_x$-1 being lower than the commercial 3.39 wt.% Pt/C (0.58 µg, 1.99 µg) and (0.96 µg and 3.39 µg), respectively. All these results indicate that the LIG-CoO_x-1 electrode with low platinum content achieves higher ORR performance compared to the commercial Pt/C with similar composition. These results are attributed to the platinum and cobalt oxides compositions and the core-shell and nanoalloys morphology which is crucial to promote ORR activity.

These results demonstrate that the optimized Pt content modified in the CoO_x core and with CoO_x as nanoalloys are more advantageous than the Pt distributed in carbon as in commercial Pt/C for promoting the ORR activity. The most noticeable feature here is that even though the ECSA of the commercial 3.39 wt.% Pt/C is higher than LIG-$PtCoO_x$-1, the specific activity of the catalysts in LIG-PtCoO$_x$-1 is significantly higher than in the commercial 3.39 wt.% Pt/C (six times), increasing the overall mass activity.

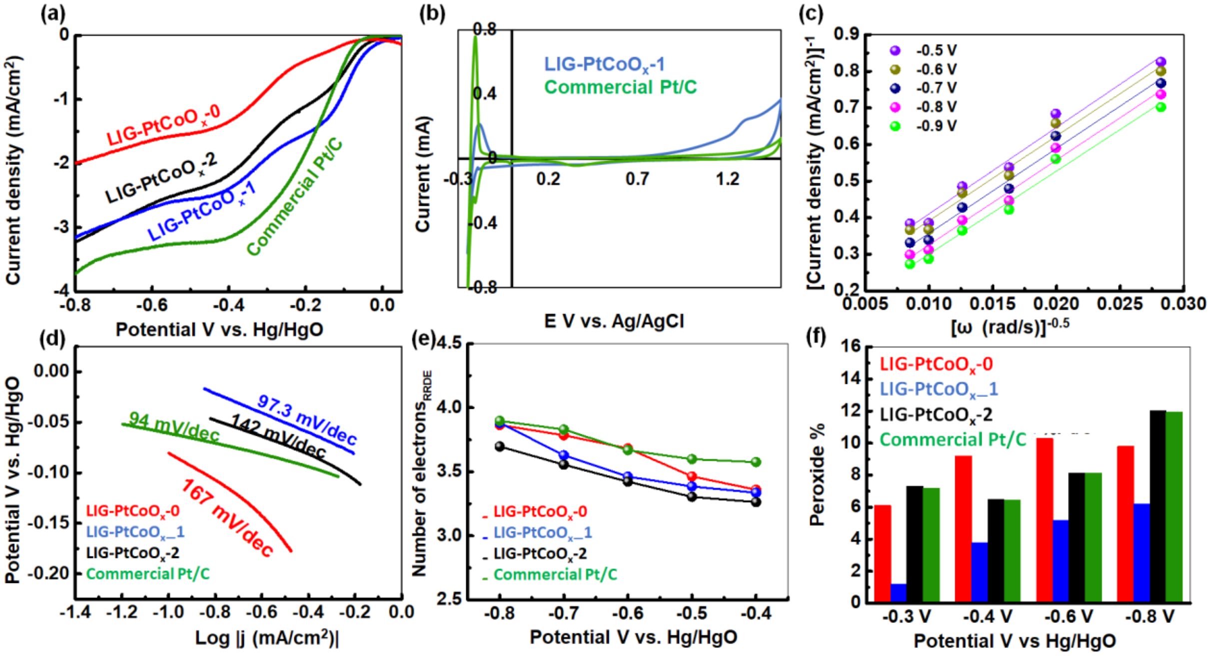

Figure 3-14. Oxygen reduction reaction (ORR) activity tests for various amount of TX samples and the commercial 3.39 wt.% Pt/C; a) LSV curves of LIG-PtCoO$_x$ and commercial 3.39 wt.% Pt/C samples in the ORR region in O_2-saturated 0.1 M KOH, b) cycle voltammetry for hydrogen underpotential desorption test in 0.1 M H_2SO_4 saturated with N_2 for 3.39 wt.% Pt/C, and LIG-PtCoO$_x$-1 samples, c) K-L plot for LIG-PtCoO$_x$-1 sample, d) Tafel plot for various samples and Pt/C, e) number of electron calculated for different samples calculated from **eq.4**, and f) H_2O_2 yields for the different LIG-PtCoO$_x$ and the commercial 3.39 wt.% Pt/C samples.

Table 3-3. Onset potential, half wave potential, and current density values from LSV graphs for TX to FA weight ratio samples and the commercial 3.39 wt. % Pt/C toward ORR using RDE at 1600 rpm, 0.1M KOH as electrolyte, and vs. Hg/HgO.

Sample	**Onset Potential (V vs. Hg/HgO)**	**Half wave potential (V vs. Hg/HgO)**	**Current density (mA/cm²) at -0.75 V vs. Hg/HgO**
LIG-PtCoO$_x$-0	**-0.06 V**	**-0.29 V**	**1.46 mA/cm²**
LIG-PtCoO$_x$-1	**+0.02 V**	**-0.15 V**	**3.15 mA/cm²**
LIG-PtCoO$_x$-2	**-0.01 V**	**-0.24 V**	**2.40 mA/cm²**
Commercial Pt/C	**-0.03 V**	**-0.18 V**	**3.42 mA/cm²**

Figure 3.14c shows the Koutecky-Levich (K-L) plots at different potentials in the region of -0.5 V to -0.9 V vs. Hg/HgO for the LIG-PtCoO$_x$-1 sample (other TX ratios are shown in **Figure 3.16a,b**). The LIG-PtCoO$_x$-1 electrode catalyzes the ORR with *n* = 3.32-3.84, which suggests that the four-electron process is favored, similar to the commercial 3.39 wt.% Pt/C catalyst benchmark (*n* = 3.55-3.85) (see **Figure 3.16c).**

Figure 3.14d shows the Tafel plots for the electrocatalysts. The excellent activity towards ORR of the LIG-PtCoO$_x$-1 is also confirmed by its low Tafel slope (97.3 mV/dec) in the kinetically controlled region (at 0 to 0.2 V vs. Hg/HgO). This was significantly lower than that of the LIG-PtCoO$_x$-0 (167 mV/dec) and the LIG-PtCoO$_x$-2 (142 mV/dec) and comparable to that of the 3.39 wt.% Pt/C (94 mV/dec), revealing much faster reaction kinetics than other samples, helping to achieve the limiting current density with a minimum potential. The high electrochemically active surface area of the LIG structure that is decorated with PtCoO$_x$ nanoalloys and core-shell nanoparticles in the sample LIG-PtCoO$_x$-1 enhances the surface concentration and diffusion ability of oxygen and provides favorable ORR kinetics, and thus reduces the Tafel slope of the sample with a LIG-PtCoO$_x$-1 close to that of the commercial Pt/C catalyst with the similar composition.

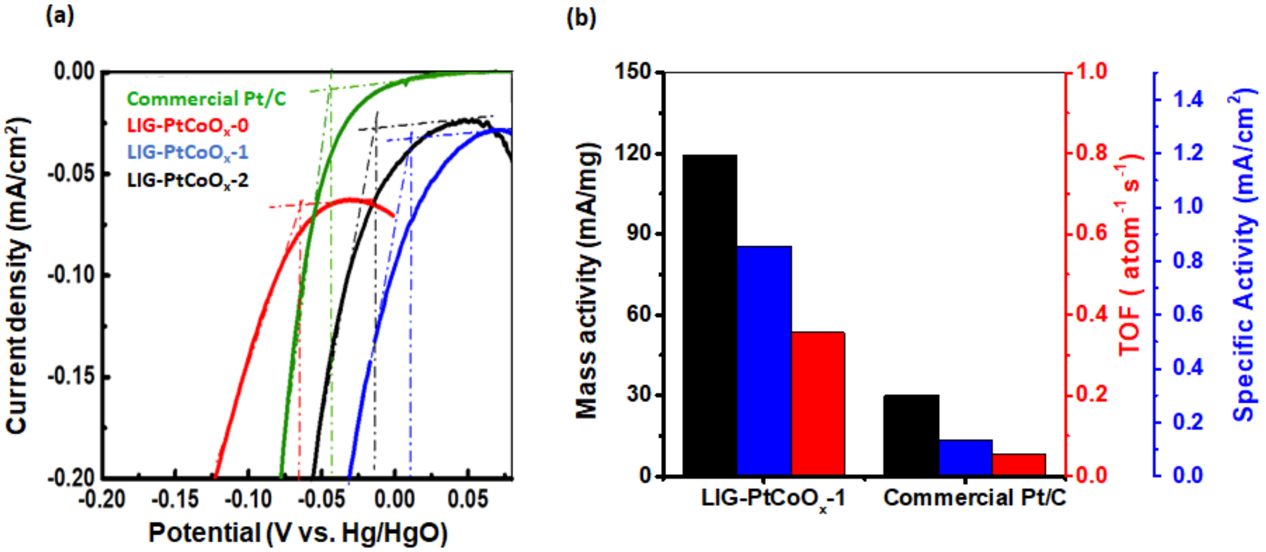

Figure 3-15. ORR performance (a) Onset potential (dash lines) from LSV graph where the 0.1 M KOH is the electrolyte and 1600 rpm used for testing different samples, and (b) mass and specific activity and TOF of the LIG-PtCoO$_x$-1 and commercial 3.39 wt.% Pt/C samples at -0.1 V vs. Hg/HgO.

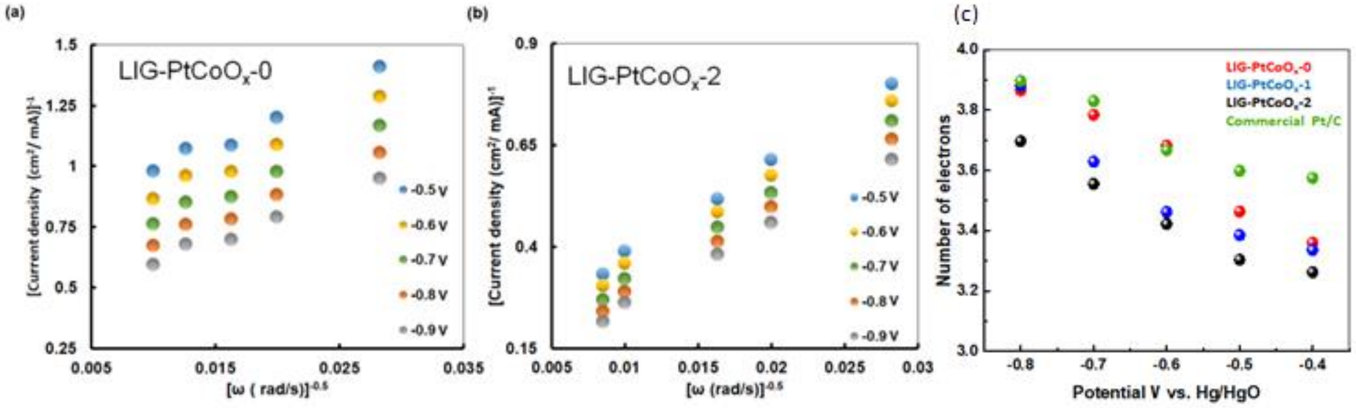

Figure 3-16. Koutecky-Levich (K-L) plot for (a) LIG-PtCoO$_x$-0, and (b) LIG-PtCoO$_x$-2 at different rotation speed and at different potential vs. Hg/HgO, and (c) Number of electrons calculated by K-L equation 2 from different samples with different weight ration of TX and the commercial 3.39 wt. % Pt/C.

RRDE was used to monitor the generation of peroxide species generated by the ORR process and to quantify the ORR catalytic pathway of the samples. The corresponding electron transfer number (*n*) was calculated by **eq.4** for the different samples as shown in **Figure 3.15e**, indicating that all the samples exhibit a dominating four-electron oxygen reduction reaction pathway. This is consistent with the result gleaned from Koutecky–Levich plots based on RDE measurements (**Figure 3.16c**). The highest peroxide yield was for the LIG-PtCoO$_x$-0 sample at potential region (-0.3- -0.6 V vs. Hg/HgO), which was expected given that this sample had the largest carbon weight percentage compared to other samples, as shown in **Figure 3.14f.**

The electrochemical performance of LIG-PtCoO$_x$ nanoalloy catalyst is compared with that of Pt/Co nanoalloy catalysts previously reported (**Table 3.4**) and indicates that LIG-PtCoO$_x$ catalysts possess competitive performance without post-synthesis treatment, nitrogen doping, furnace usage, or gas (Ar, N_2, or He) flashing. The magnitude of the current density was lower for our study – likely due to some of our PtCoO$_x$ being buried in the carbon matrix. However, the LIG-PtCoO$_x$-1 onset potential has a comparative value to other papers although the concentration in our work has the lowest catalyst concentration (10.14 $\mu g_{pt}/cm^2$, 7.13 $\mu g_{CoOx}/cm^2$). While we attempted to increase the loading of catalyst precursors into the FA precursor, there was a clear precipitation post curing. This resulted in poor polymerization as shown in **Figure 3.17a-d** and inactive films upon laser scribing. This could be because the FA is too weak a reducing agent. For example, when others use alcohols as reducing agents for synthesizing noble metal nanoparticles, they produced less than 1 or 2 wt.% of the metal.[379,380]

Table 3-4. Comparison of compositions, and ORR activities for different PtCo alloy catalysts in 0.1M KOH at 1600 rpm and vs. RHE.

Air catalysts	Carbon precursor	Wt% Catalysts	Onset potential V (vs. RHE)	Current density (mA/cm^2) at 0.8 V vs RHE	References
Pt/Co @NMC	Nitrogen-doped mesoporous carb	15.6% Pt 4.34% Co 4.69% N	1.04 V	5.0 mA/cm^2	[381]
PtPdCo NRS	carbon (Vulcan XC-72	12% Co %Pt and %Pd N/A	1.04 V	5.7 mA/cm^2	[382]
Pt-Co6Mo6C2/gC	macroporous acrylic-type anion-exchange resin (D314)	40% Pt	1.06 V	4.8 mA/cm^2	[383]
Pt/FeCo OMPC	mesoporous porphyrinic carbons	5%Pt	0.95 V	5.5 mA/cm^2	[384]
Co-Pd-Pt /CNT	CNT powders	2.4 Pt	0.94 V	5.7 mA/cm^2	[385]
$PtCoO_x$	PFA	1.99% Pt 1.40% CoO	0.95 V	3.5 mA/cm^2	In this work

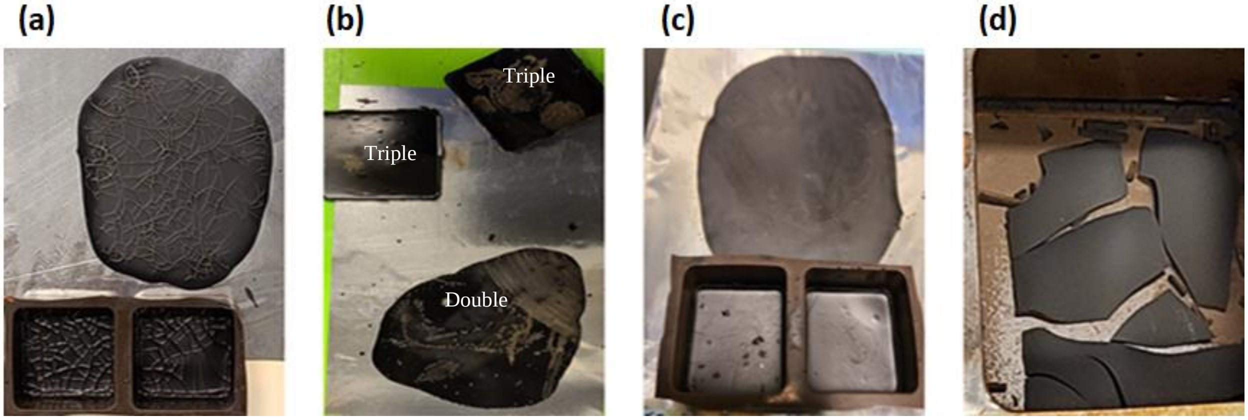

Figure 3-17.Samples with high concentration of Pt and/or Co precursors after curing in oven. (a) Triple (2.52 wt. %Pt(acac)$_2$, 4.98 wt. % Co(OAc)$_2$) precursors, (b) triple and double Pt(acac)$_2$, (c) double (1.68%Pt(acac)$_2$ and 3.32%Co(Ac)$_2$), and (d) double Co(OAc)$_2$.

Mass loss calculation and explanation of LIG-PtCoO$_x$-1 sample was studied. The total weight percentage of the reactants used in this study were 0.84 wt.% of Pt(acac)$_2$, 1.66 wt.% Co(OAc)$_2$, 82.76 wt.% FA, 0.74 wt.% oxalic acid and 14 wt.% TX LIG-PtCoO$_x$-1 sample. We measured the weight of the sample, and we found that total weight loss percentage before scribing was 44.8 ± 2.3 wt.% which could be related to the evaporation of acetate (boiling point = 118 ^{o}C) and acetylacetonate (boiling point = 140 ^{o}C) groups during the reduction reaction and evaporation of water during the polycondensation reaction for FA to PFA. After thermal carbonization by laser, the calculated final mass loss was ~95 ± 3.1 wt.% due to the evaporation of TX (boiling point = 200 ^{o}C), most of CoO$_x$ (boiling point of Co_3O_4 is 900 ^{o}C and boiling point of CoO is 1933^{o}C, the CO_2 laser temperature is 2226.85^{o}C to 2726.85^{o}C),[386i] and the carbonization of the PFA. From XPS results, ~ 62.2 wt.% of the platinum in the Pt(acac)$_2$ reduced to Pt^0. From EDS ratio, we have 3.2 wt.% Pt^{n+} and 1.4 wt.% Co^{n+} in LIG and from XPS 62.2% of the Pt^{n+} presented on the surface is Pt^0, therefore 1.99 wt.% Pt^0 and 1.40 wt.% (CoO_x + Co^0) are presented on the surface of the LIG-PtCoO$_x$-1.

3.3.5 Zinc–Air Battery Performance

To further test the performance of our laser-scribed electrodes, we evaluated their performance as Zn–air batteries. During charge-discharge cycling tests carried out at 10 mA cm^{-2} (**Figure 3.18**), the Zn-air battery with the LIG-PtCoO$_x$-1 cathode shows the highest round-trip efficiency (54.3% at the first cycle, 48.8% at the 240th cycle) when compared with the commercial 3.39 wt.% Pt/C cathode (round-trip efficiency = 47.9% at the first cycle and 43.1% at the 240th cycle) at the same loading, which can be accounted for by the high density of catalytically active sites in LIG-$PtCoO_x$-1 and the unhindered mass transfer through the abundance of pores in the LIG-$PtCoO_x$-1. After ~-20 h, the changes in the charge and discharge voltage plateaus are 1.17% and 2.48%, respectfully while using the LIG-$PtCoO_x$-1 air cathode. The LIG-$PtCoO_x$-1 shows improved cycle stability compared to the commercial 3.39 wt.% Pt/C sample where the potential change after 20 h was 2.85% and 8.96% for ORR and OER voltage plateaus, respectively. The OER result was investigated by RDE at 1600 rpm at 0.1M KOH electrolyte that saturated with O_2 as shown in **Figure 3.19** and it showed that LIG-$PtCoO_x$-1 catalyzed OER with lower potential (0.63 V) than the commercial 3.39 wt.% Pt/C (0.80 V). Wange *et al.* reported that the overpotential of the commercial RuO_2/C (14 µg/cm^2) was 780 mV, which is comparable to our result (950 mV) with lower platinum content in LIG-$PtCoO_x$-1 (10.14 µg/cm^2) in 0.1 M KOH, 1600 rpm, and at scan rate 5 mV/s.[387] Moreover, Selvakumar *et al.* mentioned that the E_{OER} for the benchmark RuO_2 (20.4 µg/cm^2) at 10 mA/cm^2 was 1.0 V vs. Hg/HgO which is close to the result achieved with LIG-$PtCoO_x$-1 (1.1 V vs. Hg/HgO) with a lower loading of Pt (10.14 µg/cm^2) in 0.1 M KOH, 1600 rpm, and at scan rate 5 mV/s.[388]

Generally, the considerable deactivation of the Pt/C-based batteries was often due to the accumulation of precious-metal nanoparticles and/or their subsequent separation from the carbon substrate. Thus, it was proven that the core-shell nanoparticles and the mixed spherical nanoalloys structure of $PtCoO_x$ that entrapped within 3D-LIG not only decreased the aggregation of the catalyst particles or loss of contact to the carbon support, but also it maintains continuous electron/mass transport channels for the ORR and OER processes. The LIG-$PtCoO_x$-1 air cathode resulted in a significant increase in the Zn-air battery's performance compared to the commercial Pt/C with the same catalyst concentration and suggested a wide range of possible applications for rechargeable batteries. To further assess the stability of LIG-$PtCoO_x$-1 air cathode, the cycling performance was recorded for a total time of about 120 h, as seen in **Figure 3.20a**. The LIG-$PtCoO_x$-1 based Zn-air battery exhibited stable charge and discharge for 118 h at 10 mA/cm^2. After 118 h, the discharge voltage and charge voltage were 0.54 and 2.26 V, respectively, with a difference of only 0.57 V and 0.11 V, and the round-trip efficiency of charge and discharge decreased only to 24.90 %. Moreover, LIG-$PtCoO_x$-1 -based Zn-air battery showed good charging and discharging stability compared to batteries cycled with the commercial catalyst with the similar composition.

The specific capacity was normalized to the mass of the consumed zinc plate for LIG-PtCoO$_x$-1 and commercial 3.39 wt.% Pt/C (using eq. 8) . The specific capacity was 739 mA h/g$_{\mathrm{Zn}}$ at discharging current (20 mA/cm^2), exceeding that of the commercial Pt/C battery (specific capacity = 605 mA h/g$_{\mathrm{zn}}$) compared with the theoretical specific capacity (820 mA h/g$_{\mathrm{Zn}}$),[44] 20 wt.% Pt/C and IrO$_2$ based Zn-air battery (761 mAh/g$_{\mathrm{Zn}}$),[389] and a majority of the published Pt based electrocatalysts.[390,391] Further discharge stability tests show that LIG-PtCoO$_x$-1 maintains a constant voltage output of 1.03 V at 20 mA/cm^2, which only decrease 63.4 mV in 9 h (**Figure 3.20b**). These results demonstrate that optimization of both mass transfer and charge transfer through PtCoO$_x$ configuration in LIG-PtCoO$_x$-1 as very essential for application in practical electrochemical energy storage devices.

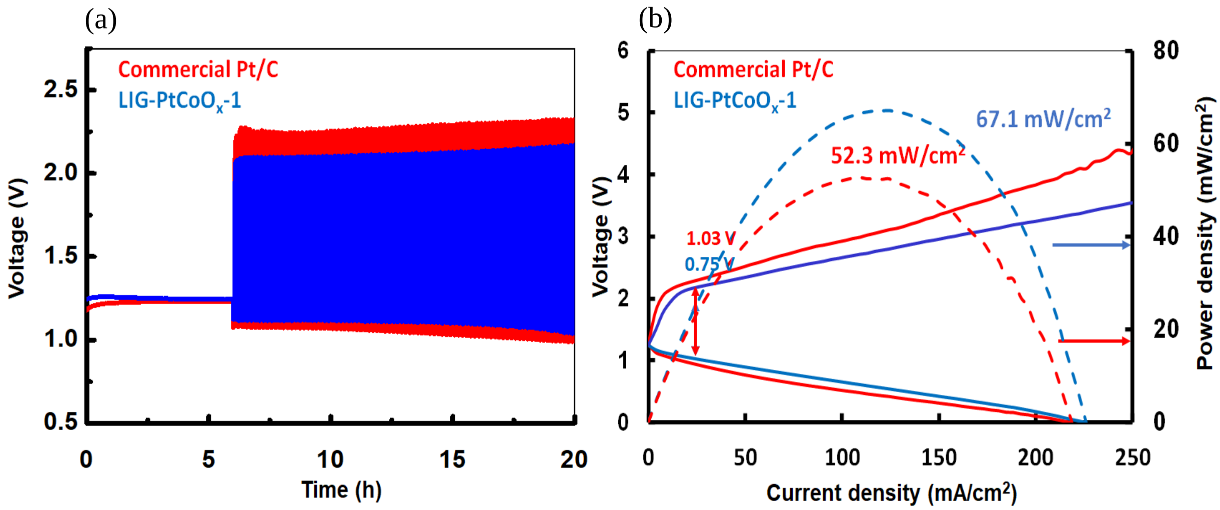

Figure 3-18. Sample performance as an air-cathode using carbon cloth coated with catalysts and zinc sheet as anode in (6 M KOH + 0.2 M Zn acetate) electrolyte: a) Charge−discharge cycling performance of rechargeable Zn−air batteries at a constant charge−discharge current density of 10 mA/cm2, b) Performance of Zn-air batter with LIG-PtCoOx-1 and commercial 3.39 wt.% Pt/C air electrodes; charge−discharge curves and power density curves (a current density from 0-100 mA/cm2 at 1 mA/s scan rate) where the dash line are the power curves.

The open-circuit potential (OCP) of the Zn–air battery employing LIG-PtCoO$_x$-1 was up to 1.32 V for LIG-PtCoO$_x$-1 which is close to OCP of the commercial Pt/C sample with the same concentration of catalyst (1.23 V). For the galvanodynamic charge-discharge polarization profile (**Figure 3.18b**), the LIG-PtCoO$_x$-1 catalyzed battery enables the voltage gap of 0.75 V at 10 mA/cm^2 which is better than for Pt/C formed battery 1.03 V implying and confirming the better rechargeability of the LIG-PtCoO$_x$-1 catalysts towards both ORR and OER. Moreover, LIG-PtCoO$_x$-1 cathode assembled Zn-air battery delivers a higher peak power density of 67.1 mW/cm^2 than that of the precious Pt/C electrode (52.3 mW/cm^2). To ensure a fair comparison, we have to state that the power density of the Zn-air battery is greatly influenced by a number of parameters such as zinc electrode type, cell design parameters, membrane, distance between the anode and cathode, size of the anode and cathode, and the presence of channel flow on the air side.[392–394] Therefore, the most crucial step in analyzing the Zn-air battery performance of the various samples is to compare the power density of the LIG-PtCoO$_x$-1 to the commercial Pt/C (with the same catalyst concentration) based Zn-air batteries that are produced using the same Zn-air battery design and under the same operating circumstances.

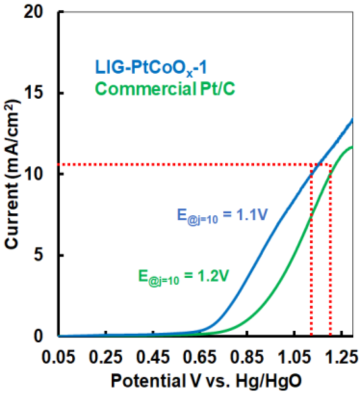

Figure 3-19. OER performances of the commercial 3.39 wt. % Pt/C and LIG-PtCoO$_x$-1 (LSV curves measured at a rotation speed of 1600 rpm with a scan rate of 5 mV s^{-1} in 0.1 M KOH electrolyte)

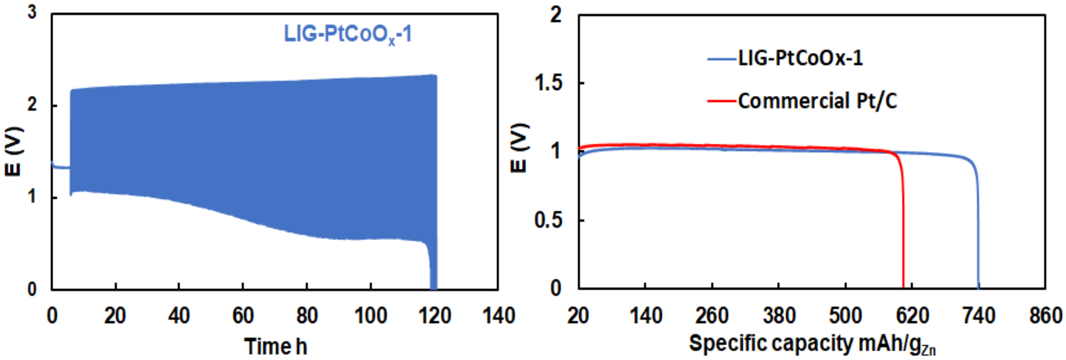

Figure 3-20. ZAB performance at different tests for LIG-PtCoO$_x$-1. a) Galvanostatic charge–discharge profile of the ZAB equipped with LIG-PtCoO$_x$-1 at a current density of 10 mA/cm^2, b) The specific capacity normalized to the mass of consumed zinc plate at discharging current density 20 mA/cm^2.

Finally, despite the low concentration of the catalysts loaded in LIG-PtCoO$_x$-1, the excellent performance and stability of the Zn-air battery based on the LIG-PtCoO$_x$-1 catalyst are comparable to, even better than, many reported LIG relevant works (**Table 3.5**).

Table 3-5. A comparison of ZAB performance of this work with relevant literatures that used LIG/catalyst as air cathode and (6 M KOH+0.2M Zn acetate) as electrolyte.

Air cathode	Graphene precursor	Wt% catalysts	Voltage gap at 10 mA/cm^2	Peak power density (mW/cm^2)	Cycling stability	Ref.
MnNiFe/LIG	Kapton PI film	2 x 2 cm^2 LIG With 1M(23%Fe+20%Ni+57%Mn)	0.88 V	98.9	200 h	[322]
Co_3O_4/LIG	Kapton PI film	4.20 wt% Co_3O_4	0.96 V	84.2	~ 67 h	[309]
Ni/Fe/LIG	polybenzimidazole (PBI) (5 wt. %) and DMAC (95 wt. %) cast on carbon paper	19.40% Ni 6.02% Fe	0.80 V	163.0	1800 h	[395]
Co N-LIG	2-methylimidazole and triethylamine	65.10% Co-N$_x$	0.80 V	80.0	220 h	[311]
LIG-PtCoO$_x$	PFA	1.99% Pt 1.40% CoO$_x$	~0.75 V	67.1	118 hr	**This work**

3.4 Conclusion:

Spherical, mixed PtCoOx nanoalloys and core-shell nanoparticle catalysts entrapped within a LIG matrix have been introduced as efficient, bifunctional air catalysts for Zn-air batteries. Using biomass carbon precursor and low concentrations of catalyst precursors, and laser induced graphene technology, a simple synthesis method was demonstrated to prepare nanoparticles which are significantly smaller (< 2 nm) than most other reports and that are enmeshed within the carbon matrix – the combination of which led to high catalyst activity and stability. The resulting LIG-PtCoO$_x$-1 not only contains a small amount of Pt (1.99 wt.%) and CoO$_x$ (1.40 wt.%), but also shows excellent activity for ORR that are comparable to commercial Pt/C with similar composition (3.39 wt. % Pt). Furthermore, in a home-made Zn-air battery, the LIG-PtCoO$_x$-1 cathode delivers a high open circuit voltage of 1.23 V, high power density 67.1 mW/cm^2, high specific capacity based on consumed Zn, and excellent long-term stability of up to 118 h with a low overvoltage between charging and discharging. Therefore, this hybrid catalyst not only has the potential to lower the price of commercial catalysts, but also demonstrates a generic design principle for second-generation high performance electrocatalysts.

Chapter 4

Laser induced graphene supported mixed-phase MnO/Mn_3O_4 composite materials for Zinc-Air Batteries

In this study, laser induced graphene supported manganese oxide with a composite of Mn_3O_4 and MnO (LIG-MnO/Mn_3O_4), as an air cathode, was successfully synthesized via a facile one-pot synthesis method under ambient conditions. Using low-cost CO_2 infrared laser system, simultaneous carbonization of poly furfuryl alcohol (PFA), a waste biomass-derived polymer, and incorporation manganese oxides were achieved. Since the partially polymerized PFA that can hold the mixed manganese oxide particles in suspension as it cures and carbonizes, a homogenous dispersion of mixed manganese oxide catalyst was observed. Most significantly, we demonstrated how the oxygen reduction reaction (ORR) of the LIG-MnO/Mn_3O_4 cathode could be tuned based on the quantity of manganese oxide precursor that was employed, i.e.,less than 10 wt.% MnO_2 precursor tends to follow a 2e- ORR pathway, while high concentration (≥10wt. % MnO_2 precursor) tends to 4e- ORR pathway. In comparison to the other concentrations, the LIG/MnO/Mn_3O_4 catalyst that included 10 wt.% manganese oxide precursor (LIG-10Mn_xO_y) had the highest catalytic activity toward ORR. The LIG-10Mn_xO_y catalyst had comparable performance when tested as an air cathode in a zinc-air battery (ZAB) to the conventional benchmark Pt/C (20 wt.%).

Contributions

The results of this chapter are ready for submission as: Laser induced graphene supported mixed-phase MnO/Mn_3O_4 composite materials for Zinc-Air Batteries, and the authors in order are Tahani Aldhafeeri and Marianna Uceda (as first authors), Manila Ozhukil Valappil, Jessi Wan, Weixuan Li, Hao Yu Zhang , Angad Singh, and Prof. Michael Pope.

Funding Acknowledgements

For this project, I and Dr. Marianna Uceda designed the experiments in consultation with Dr. Michael Pope and all experiments were entirely conducted by myself and Dr. Marianna Uceda with the assistance of the following undergraduate co-ops Jessi Wan, Weixuan Li, Hao Yu Zhang, and Angad Singh. BET measurements and analysis was performed by Dr. Manila Ozhukil Valappil . I and Dr. Marianna Uceda prepared the manuscript and Dr. Manila Ozhukil Valappil, and Dr. Michael Pope helped in editing of the manuscript.

This project was funded by Natural Sciences & Engineering Council of Canada's Alliance Program, the Ontario Centre for Innovation, the University of Hafr Al Batin though the Saudi Arabian Cultural Bureau in Canada, and in collaboration with e-Zinc company (Mississauga, ON)

4.1 Introduction:

The oxygen reduction reaction (ORR) serves as the essential and the vital cathodic reaction for both metal-air batteries and fuel cells. Depending on whether the $4e^-$ or $2e^-$ ORR pathways, molecular oxygen (O_2) is electrochemically reduced to H_2O or H_2O_2.[396] The former is crucial for maximizing the efficiency of chemical energy conversion in fuel cells and metal-air batteries,[397,398] while the latter is an environmentally friendly way to produce hydrogen peroxide on-site.[399,400] As a consequence, uncomplicated ORR reaction pathway tuning is significantly required for fundamental studies and various application scenarios.[401]

Platinum, which is the preferred catalyst for metal-air battery, presents a challenge to commercialization due to its high cost, poisoning sensitivity, poor long-term stability, and low efficiency due to high overvoltage between ORR and OER.[402,403] On the other hand, peroxide produced from the $2e^-$ ORR pathway is formed by highly energy consuming process in many applications such as water treatment and paper production. Therefore, the $2e^-$ ORR pathway is presently under investigation by researchers.[404–406]

In spite of the fact that Pt-based electrocatalysts have historically been used to catalyze the ORR with great efficiency, manganese oxides have shown considerable ORR activity in the comprehensive investigations on non-platinum catalysts.[407,408] Manganese oxides has high catalytic activity, high availability, high stability, low cost, and absence of environmental concerns.[409,410] However, there are still challenges in using manganese oxides as an effective ORR catalyst because manganese oxides have a low intrinsic electrical conductivity. Mixing manganese oxides with conducting carbon materials increase the electrical conductivity of the catalysts and potentially can have carbon-oxide interaction; though a portion of the oxide is left electrochemically inactive.[411] Feng *et al.* demonstrated that the growth of manganese oxide nanoparticles on graphene generated strong carbon-oxide interactions. [412] This feature enhanced the ORR activity and stability in alkaline solutions.

Wet chemistry and thermal pyrolysis are the main foundations of the current synthetic approaches to produce the catalysts, such as high-temperature carbonization of precursors, hydrothermal reactions, and wet chemistry combined with thermal treatment methods.[413,414] To avoid the complexity and high cost of the catalyst's precursors or/and the synthesis method, a simple and straightforward procedure would be beneficial. Direct laser writing over relevant materials (e.g. paper, wood, lignin, thermoplastic polymers) has attracted a significant attention since it can be used to simultaneously pattern electrodes, synthesize three-dimensional graphene in one step, and induce the nucleation of metal ions. [310,350] Tour's group demonstrated a solid-phase synthesized bifunctional catalyst MnO_2/LIG as cathode catalyst for Li-O_2 battery. [415] They treated the LIG by oxygen plasma before dropping the $MnSO_4$ solution, then the soaked LIG lasered again. Later in 2015, they fabricated a flexible micro-supercapacitor by electrodeposited MnO_2 on LIG as a pseudocapacitive material.[279] Goa *et al.* prepared a microsupercapacitors with a specific area 32.45 m^2/g by drop casting a mixture of GO/$MnSO_4$ onto PET substrate and laser it to get LIG that doped with manganese oxides and sulfur (S).[416] The specific area of the catalysts was much lower than of the LIG from GO without manganese oxide (174.76 m^2/g). It is important to mention that most of the laser induced graphene that doped with manganese oxides are used for supercapacitor.[316,317,417–419]

Herein, we used poly furfuryl alcohol as carbon precursor for the same reasons as mentioned in **Chapter 2** and **3**. The utilization of PFA as a promising precursor to LIG, which can frequently outperform LIG generated from PI in terms of conductivity and electrode capacitance, has recently been proven by our group. [308] However, air cathodes based on laser-induced carbonization of biomass-derived polymers with non-platinum catalysts such as MnO_x has not been investigated yet in any energy storage applications. Accordingly, we have developed a never-reported, single- step synthesis of mixed-phase MnO/Mn_3O_4/laser induced graphene hybrid materials by direct laser writing technique of PFA that mixed with MnO_2 precursor to produce efficient air cathode catalysts (LIG-MnO/Mn_3O_4) for zinc-air batteries. Interesting electrochemical studies show that ORR pathways of these catalysts are dependent on MnO_x content As the MnO_x content increases up to 10 wt.%, the catalyst has a high affinity towards the 2e^- pathway forming H2O2, while 15% lean towards a direct 4e^- pathway. Further investigation of the LIG-MnO/Mn_3O_4 catalyst in a zinc-air battery (ZAB) reveals that the maximum peak power density of the catalyst was comparable to the commercial Pt/C (20%).

4.2 Experimental Methods

4.2.1 Preparation of catalyst loaded PFA

The loaded polymer is prepared by mixing 4 mL of the monomer furfuryl alcohol (FA, Thermo Scientific^{TM}, Acros Organics, 98%), 332 mg of anhydrous citric acid as acidic initiator (Fischer Chemical^{TM}), and 0-20 wt% of electrolytic manganese dioxide (EMD, MnO_2, Tosoh). This mixture is then tip sonicated for 10 minutes with an amplitude of 40% (Sonics CV334, 750W) in an ice bath. The monomer suspension is then placed in an oil bath at 85°C under 350 rpm stirring. Depending on the quantity of MnO_2 added, the suspension is allowed to polymerize for 4.5-6.5 h. This produces a partially polymerized and viscous suspension (see **Figure 4.1a-c**) which is removed from the oil bath and doctor bladed onto aluminum foil (Fisherbrand, 18 µm thick) at a wet gap of 1500 µm using an adjustable film applicator (MTI corp.). The coating is placed in an oven at 85°C and allowed to cure for 24 hours.

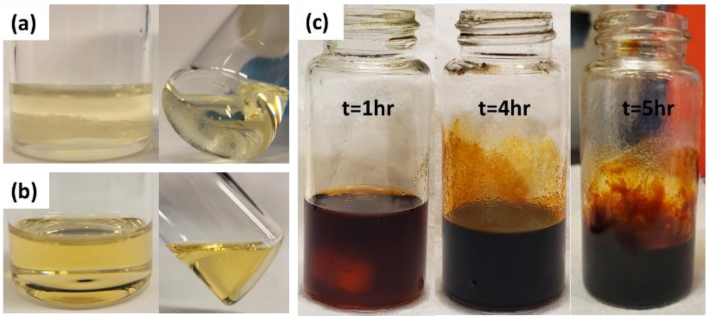

Figure 4-1. A mixture of the FA monomer with citric acid (a) before and (b) after tip sonication. (c) the change in color and viscosity during polymerization after 1, 4, and 5 h on the hot bath.

4.2.2 Laser-induced carbonization

After polymerization is completed, the aluminum foil is peeled off to reveal the smooth PFA surface. This polymer layer is then placed in a CO_2 laser (BossLaser 1416L, 50W, and a laser spot diameter of 60 µm) to selectively irradiate the surface of the PFA. LIG powder samples for RRDE inks, TGA, XPS, and XRD are made by irradiating a 3 cm × 5 cm square with the laser unilateral mode along the x-axis, a laser interval of 0.1 mm, a scan rate of 10 mm/s, and varying laser power.

4.2.3 Material characterization

Fourier-transform infrared spectroscopy (ATR-FTIR) of the materials is performed using a Bruker Tensor 27 Fourier-transform infrared spectrometer with Pike attenuated total reflectance (ATR) attachment possessing a ZnSe crystal. The liquid FA monomer is analyzed by placing a drop onto the ZnSe crystal, whereas the polymerized resins are pressed onto the crystal. Scanning electron microscopy and energy dispersive spectroscopy (SEM-EDS) is performed using a Zeiss Leo 1530. The resins were gold coated and the powders were pressed into a pellet for EDS analysis. The latter is performed at an accelerating voltage of 20 kV. Sheet resistance measurements were performed with a 4-point probe (Ossila). The thickness of the irradiated areas was then taken from cross-sectional SEM imaging to calculate the conductivity when needed. Raman spectroscopy of the irradiated material was performed using a Horiba Jobin-Yvon HR800 Raman system equipped with an Olympus BX 41 microscope with a 50 mW, 532 nm laser operating at 25% laser power. The D, G, and 2D peaks of the Raman spectra were determined using Lorentzian modeling on OriginPro. X-ray Diffraction (XRD) of the irradiated materials is performed using a Rigaku Miniflex II at a scan rate of 1 degrees/minute, from 2θ values of 10-90. Rietveld refinement is performed using GSAS-ii. Thermogravimetric analysis of the irradiated powder was performed using a TA Instruments Q500 at a 10 °C/min ramp rate from 30 °C to 900 °C, under nitrogen and air atmosphere. The Brunauer-Emmet-Teller (BET) surface area was estimated using a Micromeritics Gemini VII 2390 with nitrogen as the gaseous adsorbate. The powders were degassed under nitrogen at 300 °C for 12 h beforehand. For the pristine LIG samples (made with unloaded PFA) and the pristine MnO_2, the partial pressure of nitrogen (p) was varied in the range $p/p_{\text{sat}} = 0.05\text{-}0.3$. XPS was performed on the composite powders with a Thermal Scientific Kα XPS spectrometer, 150 eV, and spectra were fitted using CasaXPS software.

4.2.4 Electrochemical characterization

The conditions for ORR performance and ZAB testing are same as mentioned in section 3.3.4 of Chapter 3

Conversion between Hg/HgO reference the RHE reference is given by Eq. 1:[420]

$$E_{\text{RHE}} = E_{\text{Hg/HgO}} + 0.0591pH + E^{o}_{\text{Hg/HgO}}, \qquad \textbf{Eq. 1}$$

where $E^{o}_{\mathrm{Hg/HgO}} = 0.098V$ vs NHE at T=25 °C. For a solution of 0.1 M KOH, the equation is further simplified to give the formal potential as:

$$E_{\mathrm{RHE}} = E_{\mathrm{Hg/HgO}} + 0.866, \qquad \text{Eq. 2}$$

The ring collection efficiency was acquired by adding 10 mM of ferricyanide to 0.1M KOH in an O_2-free environment, the disk underwent a linear sweep from 0.5 to -0.5V vs Hg/HgO and the ring was set at 0.653V vs Hg/HgO as shown in **Figure 4.2a**. The collection efficiency, N, is then taken from the slope of the ring vs disk current graph.[421,422] For this setup, the collection efficiency was found to be ~0.27 (as shown in **Figure 4.2b**).

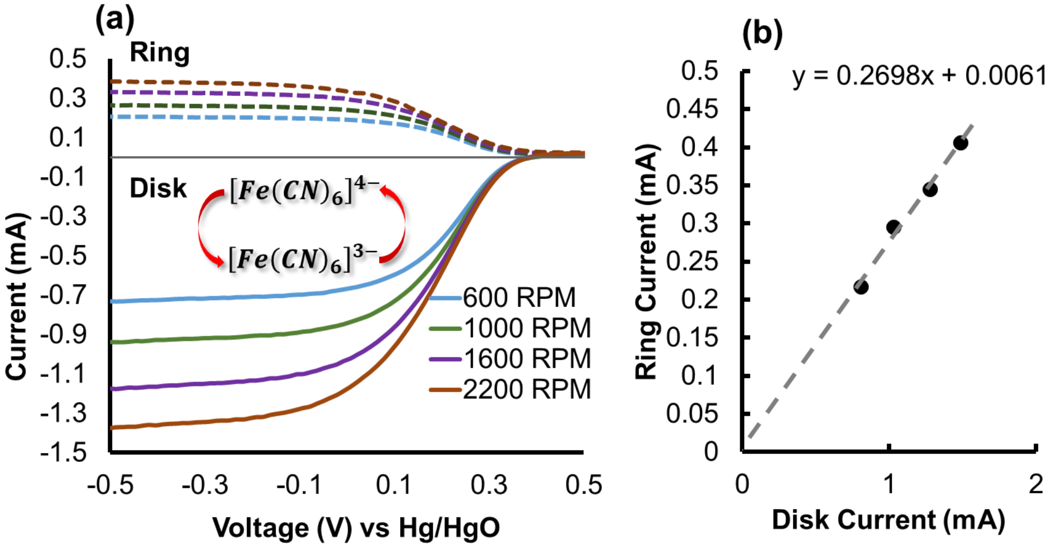

Figure 4-2. The collection efficiency, N, is then taken from the slope of the ring vs disk current graph (a) ring and disk current for 10 mM ferricyanide in 0.1M KOH at different rotation rates. (b) Plot of ring current vs disk current.

The kinetic current i_K may also be approximated by a mass transport correction of the RRDE data using Eq. 3:[423–425]

$$i_K = \frac{i \times i_L}{i_L - i} \qquad \text{Eq. 3}$$

where i is the measured current density (mA/cm^2) and i_L is the diffusion-limiting current density.

4.2.5 Zinc-air battery tests

The conditions for ZAB testing are same as mentioned in section 3.3.4 of Chapter 3

The ZAB setup used is a homemade cell composed of 5/16” acrylic sheets with 1/16” thick EPDM rubber gaskets (see Figure 4.3). Electrical contact with the GDL is accomplished by using a monel sheet with 1.3 cm diameter hole exposing the coated GDL. A zinc plate is used as the anode and the electrolyte is composed of 6 M KOH and 0.2 M zinc acetate. The assembled cell is connected to an Arbin battery cycler (CYCLER MODEL), allowed to rest for 6 h to measure the OCV followed by galvanostatic charge/discharge (performed at 10 mA/cm^2 for 2.5 min charge and 2.5 min discharge yielding a 5 min cycle) or galvanodynamic polarization tests (performed by applying a current density from 0-100 mA/cm^2 at a rate of 1 mA/s).

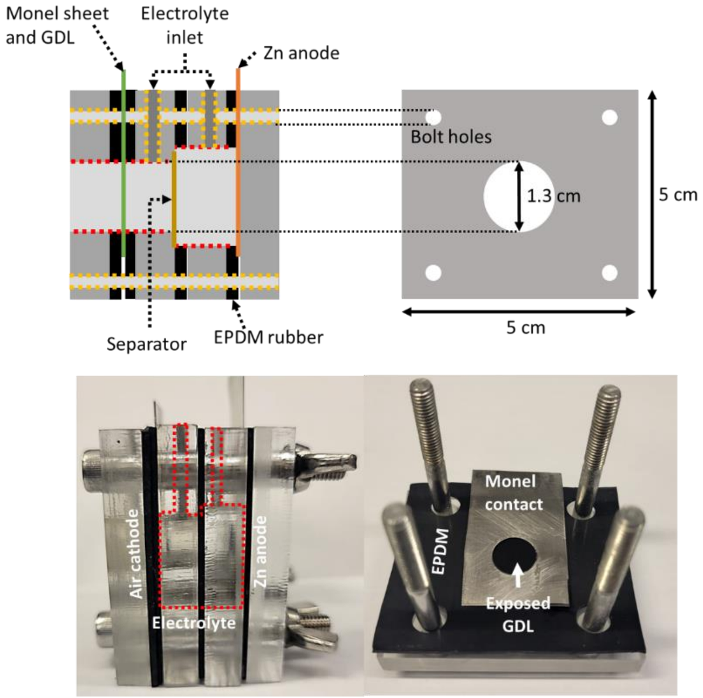

Figure 4-3. Homemade ZAB setup made from acrylic, EPDM rubber, and stainless steel 316 socket head screws, washers, and wingnuts

4.3 Results and Discussion

4.3.1 PFA composite and irradiation conditions

A schematic showing the synthesis of the composite PFA is shown in **Scheme 4.1**. This is a 3-step process consisting of 1) mixing of the FA monomer, citric acid initiator, and MnO_2 catalyst at high temperature to produce a viscous, partially polymerized suspension; 2) the viscous suspension is then cast onto aluminum foil using a film applicator and allowed to cure overnight, this produces a hardened resin; 3) Finally, the resin is carbonized via direct laser writing carbonization (DLWC) at 10 mm/s and a power of 5.3 W.

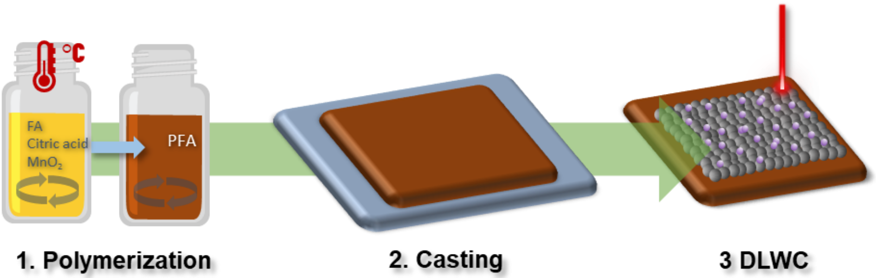

Scheme 4.1: Schematic showing the 3-step process involving 1) mixing of MnO_2 and polymer precursors followed by high temperature acid-catalyzed polymerization; 2) casting of the partially polymerized suspension followed by overnight curing; and 3) direct laser-writing carbonization to produce catalyst loaded laser-induced graphene.

FTIR, shown in **Figure 4.4a** and inset in (**b**), was used to confirm the polymerization of PFA with and without MnO_2 loading. Pristine FA is a colourless liquid monomer which exhibits a wide band at ~3320 cm^{-1} attributed to the stretching band for hydroxyl groups characteristic to the monomer.[300,308,426] This band is lacking in the polymerized resins without MnO_2 (referred to as “0MnO2”) and with MnO_2 (referred to as “10MnO_2” and “20MnO_2”) loading due to the intermolecular dehydration required to begin the linear polymerization. This indicates the addition of MnO_2 does not interfere with the polymerization pathway. However, it should be noted that, whilst a hardened resin is produced, loading beyond 25% MnO_2 with reference to FA leads to formation of cracks within the resins (see **Figure 4.5**). This indicates the MnO_2 may be physically interfering with the cross-linking process. Thus, the system was tested with 5-20% MnO_2 added. For PFA systems loaded with MnO_2, characteristic peaks are located at 1716 cm^{-1} which is attributed to carbonyl groups suggesting the occurrence of ring opening processes;[300,427] 1505 and 1560 cm^{-1} attributed to ring vibrations; peaks such as 787, 1420 cm^{-1} are assigned to 2,5-disubstittued furan rings, 2,3-disubstituted furan rings; and a peak in 2920 cm^{-1} which is attributed to methyl groups. These occurrences support the formation of branched species resulting in a cross-linked resin.

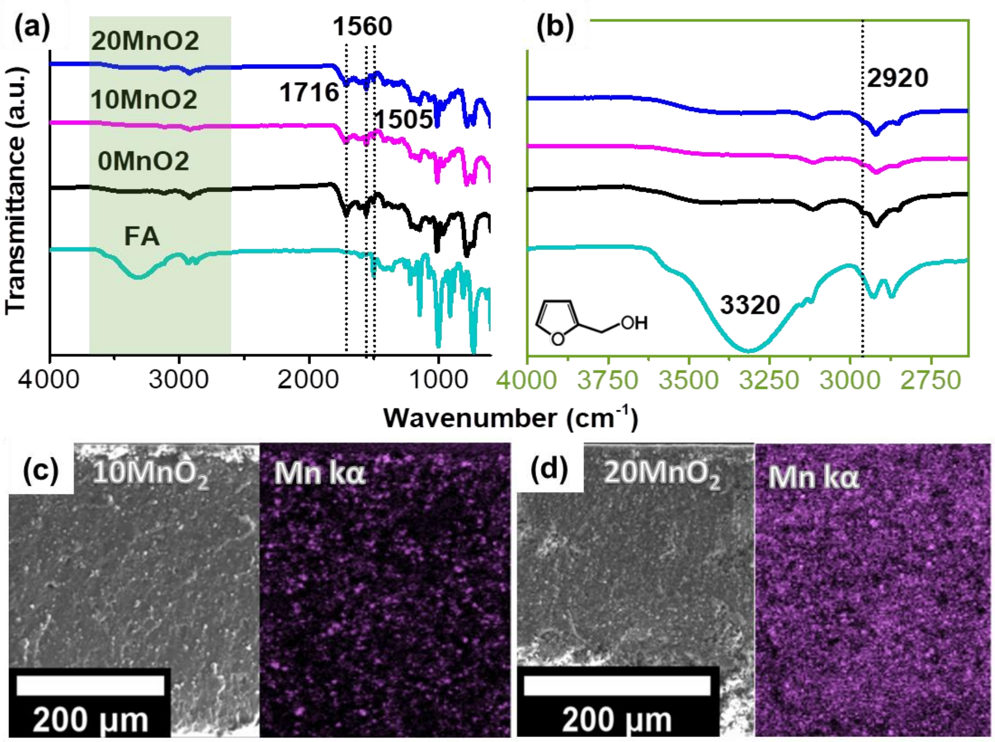

Figure 4-4. Successful production of loaded polymer resins. Cross-linking and resin formation can be seen by comparing (a) FTIR of the FA monomer, pristine PFA ("0MnO2"), and loaded PFA resins containing 10 and 20 wt% MnO_2 relative to FA added ("10MnO2" and "20MnO2"). (b) Closeup of the 2600-3800 cm^{-1} band region in FTIR. Cross-section SE image and corresponding Mn Kα EDS map of (c) 10MnO_2 and (d) 20MnO_2.

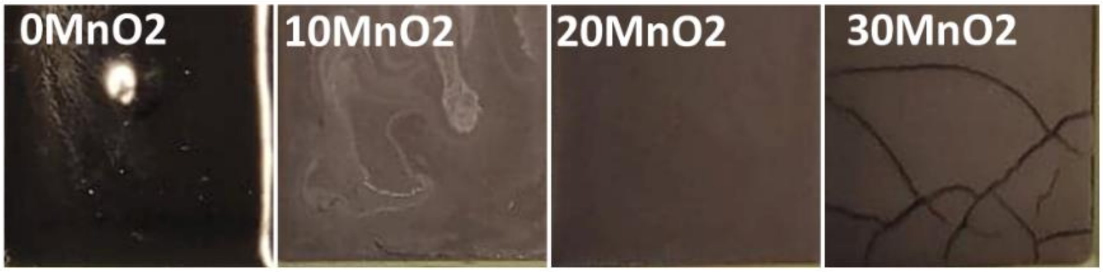

Figure 4-5. PFA resin with varying loadings of MnO_2 (0, 10, 20, and 30 wt% with respect to FA added).

The presence of MnO_2 within the resin was not observed in FTIR due to the overlapping peaks of from the PFA and due to the inherent limitations (at lower wavenumber ranges) of the FTIR equipment used. Cross-sectional SEM images with corresponding EDS mapping (**Figure 4.4c** and

d) show the good dispersion of MnO_2 along the thickness of the resin for both the 10 and 20% cases. This is attributed to the initial tip sonication followed by constant stirring during the initial polymerization step and the high viscosity of the PFA at the time of casting. The partially polymerized PFA is capable of successfully holding the MnO_2 particles in suspension while it cures yielding a homogeneous dispersion of MnO_2 in the cured resin as shown in the cross-section SEM images (see **Figure 4.6a-e**). Moreover, tip sonication successfully dissolves the citric acid into the FA – this is evidenced by the clear solution of FA after sonication when no MnO_2 is added (**Figure 4.2a** vs. **b**) – which improves the contact between monomer and initiator thereby ensuring the formation of branched species.

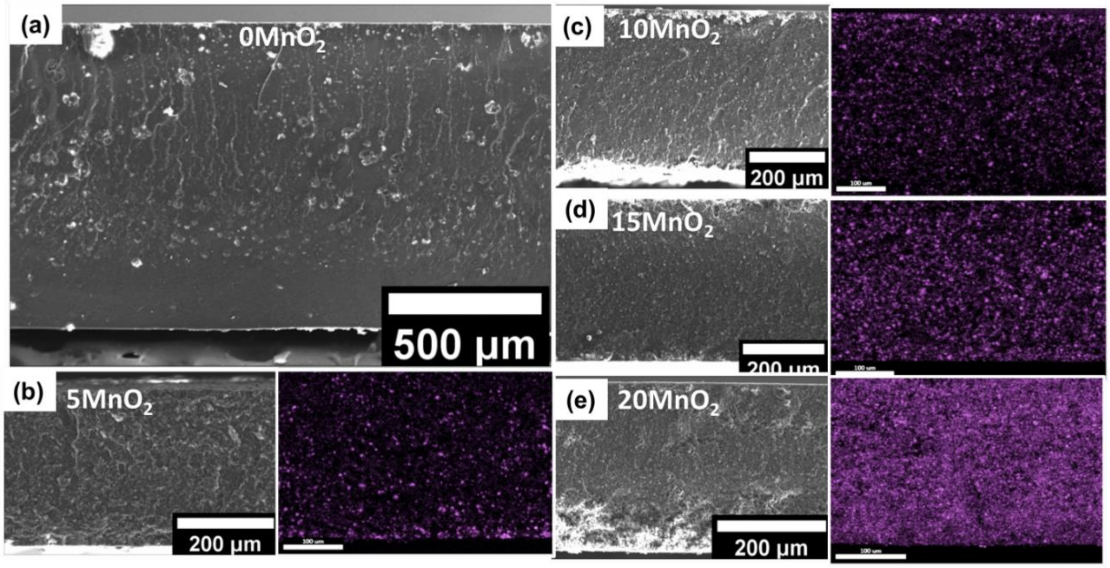

Figure 4-6. cross-section SE images with corresponding Mn kα map for (a) 0MnO2, (b) 5MnO2, (c) 10MnO2, (d) 15MnO2, and (e) 20MnO2 in PFA.

4.3.2 Laser-induced carbonization of PFA

As shown in Figure **4.7a**, the dark brown coloured and electrically insulating neat and MnO_2 loaded PFA films become black and electrically conductive upon irradiation with a CO_2 laser (λ = 10.6 µm) operated in a suitable power range (4.9 – 5.6 W) (**Figure 4.7b**). This is the result of laser-induced carbonization commonly attributed to the photothermal pyrolysis effect. In this process the light is absorbed by the precursor – in this case by the PFA – and leads to lattice vibrations. This results in localized temperatures up to 1000-2000°C which breaks down the covalent bonds, rearranges the aromatic structures, and releases gaseous by-products forming a more or less graphitized carbon.[278] This results in the formation of the highly conductive LIG. However, for fully cross-linked PFA, the quality of LIG formed depends on the laser irradiation parameters. The irradiated material is hereinafter referred to as "0Mn_xO_y" for LIG produced without MnO_2 loaded in the PFA and "10Mn_xO_y" and "20Mn_xO_y" for LIG produced from the 10MnO_2 and 20MnO_2 PFA samples, respectively. This is due to the MnO_2 phase transformation discussed later in the text.

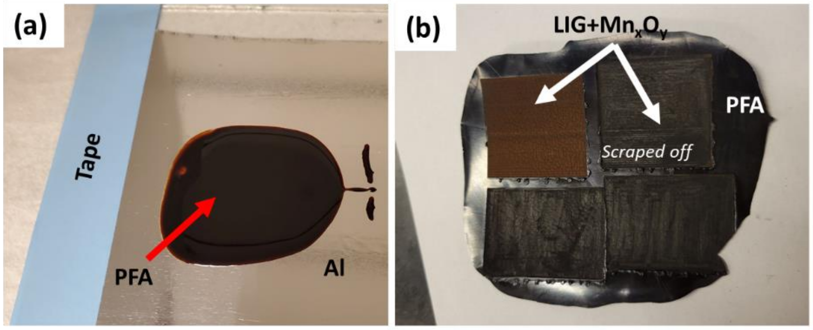

Figure 4-7. Images of PFA and LIG/Mn_xO_y (a) Wet casting of partially polymerized and viscous FA+MnO_2 and (b) subsequent thick resin recovered showing the irradiated LIG/MnO/Mn_3O_4 (before and after scraping the powder off)

Sheet resistance, using a 4-point probe, and Raman spectroscopy measurements were used to explore the effect of laser power (at a set scan rate of 10 mm/s) on the formation of the LIG. The sheet resistance measurements are graphed in **Figure 4.8a** for loaded and unloaded irradiated PFA. For a pristine LIG sample that was not loaded with MnO_2 during polymerization catalyst ("0Mn_xO_y"), the LIG sheet resistance gradually lowers with increasing laser power. This trend has been observed in polyimide films and attributed to the degree of graphitization being dictated by thermal power.[278] The continuous decrease in sheet resistance indicates that the full carbonization range of the unloaded PFA is above the power range shown here. The loaded LIG samples ("10Mn_xO_y" and "20Mn_xO_y") exhibit an initial decrease in sheet resistance with progressively higher powers. At 5.3W a pivotal point is reached for the loaded LIG samples where the sheet resistance measured is 3.3 Ω per square ± 12.4% and 7.1 Ω per square ± 5.3% for 10Mn_xO_y and 20Mn_xO_y, respectively. This translates to an electrical conductivity of 18.8 S/cm and 10.0 S/cm for 10Mn_xO_y and 20Mn_xO_y, respectively. Further increasing the power results in increasing sheet resistances which indicates an optimal power setting exists at around 5.3 W. For both loaded and unloaded PFA, the threshold power required for efficient formation of LIG is found to be a minimum of ~5 W. However, this power range results in poor carbonization and high sheet resistance. Conversely, a power higher than 5.6 W results in complete ablation of the loaded PFA indicating a limited carbonization range when compared to unloaded PFA.

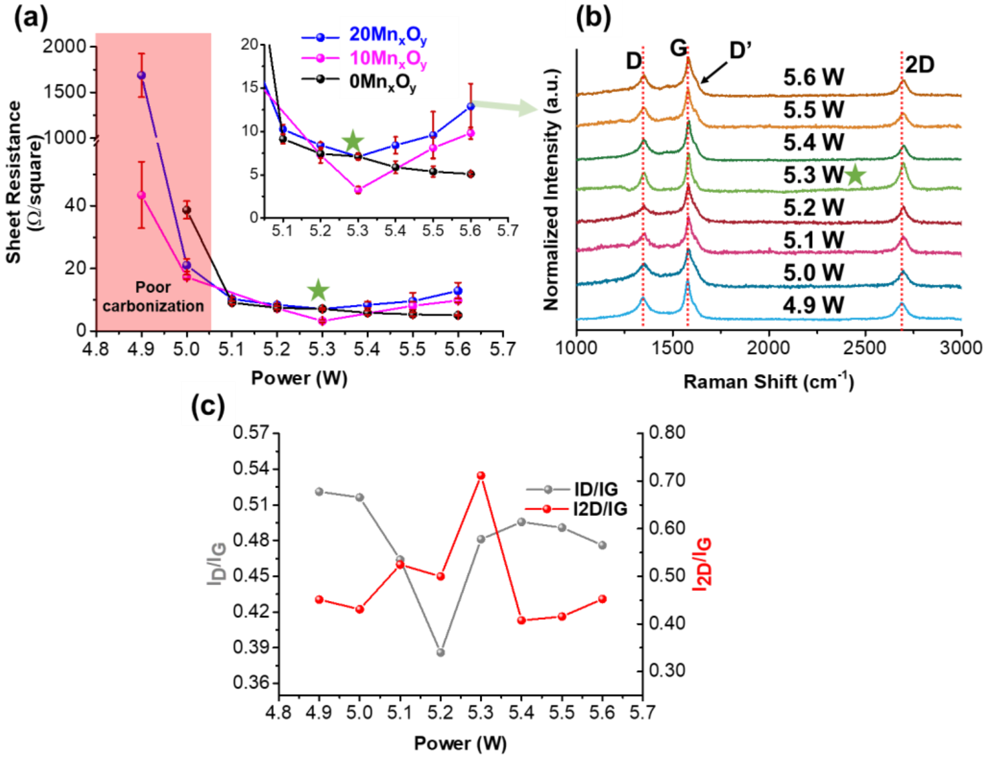

Figure 4-8. Effect of irradiation parameters on LIG quality. (a) Calculated resistivity values for loaded (“10Mn$_x$O$_y$” and “20Mn$_x$O$_y$”) and unloaded (“0Mn$_x$O$_y$”) LIG scribed at varying laser powers. (b) Raman analysis of loaded PFA irradiated at varying laser powers with (c) corresponding I$_D$/I$_G$ and I$_{2D}$/I$_G$ ratios.

Raman spectra for LIG loaded with MnO_2 catalyst and irradiated at a range of powers are given in **Figure 4.8b**. For carbonaceous materials, the three readily visible bands are identified as the D, G, and 2D bands. The D band, seen in ~1347 cm^{-1}, is attributed to *sp3* out-of-plane vibrations or bent *sp2* carbon bonds and referred to as the so-called “disorder band”. A shoulder D’ band at ~1650 cm^{-1} is observed due to surface charges. The G band located in ~1580 cm^{-1} is characteristic of *sp2* in-plane stretching of carbon atoms in the hexagonal ring. The 2D band, also referred to as the G’ band, is located at ~2700 cm^{-1} and dependent on the stacking order of basal planes.[428,429] The occurrence of the latter is characteristic of graphene materials. Lorentzian peak fitting of the spectra shows the 2D band can be modeled by a single peak with a FWHM value between 40-60 cm^{-1} which is within the range found in literature [278,308,429] for laser-induced graphene. Analyzing the ratio of the integrated intensities for I_D/I_G and I_{2D}/I_G in **Figure 4.8c** reveals an initially decreasing I_D/I_G ratio. Lin *et al* documents this trend and attributes the behaviour to increased surface temperatures resulting in the degradation of LIG quality.[278] A similar trend is observed for the sheet resistance measurements with loaded LIG but not for the pristine LIG. This could indicate the presence of MnO_2 during irradiation negatively alters the thermal diffusion properties of LIG allowing for a high localized temperature resulting in more defects within the LIG. An $I_{2D}/I_G<1$ is characteristic of multilayer graphene, as the number of layers increases the 2D peak undergoes complex changes including a reduction in intensity relative to the G peak. The I_{2D}/I_G ratio reaches a peak at 0.71 when a laser power of 5.3W is used which implies the presence of few-layered graphene. These improved graphene features, combined with the lower sheet resistance experienced, show the optimal laser power for MnO_2-loaded PFA is 5.3 W. Thus, all further irradiations will be performed with a laser power of 5.3 W and a scanning rate of 10 mm/s which translates to a fluence of 8.83 J/mm^2 (for an assumed laser spot size of 60 µm).

4.3.3 Laser-induced phase transformation

X-ray diffraction (XRD) was used to investigate the microstructure of MnO_2 with the diffractograms given in **Figure 4.9a**. The pristine MnO_2 material is composed of γ-MnO_2 and ε-MnO_2 with the former being a major component. The γ-MnO_2 exhibits low intensity, broad peaks at 22.7°, 37.5°, 43.0°, 56.6°, and 67.4°. This γ-MnO_2 polymorph has been shown to contain a ramsdellite structure and pyrolusite intergrowth which results in a somewhat amorphous structure leading to the loss of long-range order.[430] This is seen in the low intensity of the final high angle peak. Irradiation of the loaded PFA material leads to the appearance of manganosite, MnO, and hausmannite, Mn_3O_4. The oxidation state for Mn in manganosite is Mn^{2+} and in hausmannite it is a mixture of Mn^{2+} and Mn^{3+} compared to the initial oxidation state of Mn^{4+} of γ-MnO_2. This indicates the irradiation process causes phase transformation and reduction of the initial γ-MnO_2 into the lower oxidation state polymorphs with higher temperature stability due to the localized high temperatures.[431] The thermal stability of an Mn-O system (in air) from least to most stable is $MnO_2<Mn_2O_3<Mn_3O_4<MnO$.[432–434] The mixed phase indicates there is uneven heat transfer within the PFA which prevents complete transformation to the thermally highest stable phase, MnO. This mixed phase is present regardless of the amount of MnO_2 loaded as seen in the XRD data in **Figure 4.9a**. Moreover, XRD shows the presence of only MnO and Mn_3O_4 in all compositions which

indicates the large agglomerates formed are also MnO/Mn$_3$O$_4$ as opposed to metallic Mn (**Figure 4.9b**).

Within the composite powder, the MnO/Mn$_3$O$_4$ is identified via elemental and contrast differences in backscattered electrons (BSE) images and EDS mapping shown in **Figure 4.9c**. The EDS maps for Mn kα and C kα showed an excellent dispersion of the MnO/Mn$_3$O$_4$ and LIG material within the pellet. The pristine MnO$_2$ material has an initial particle size of 4.72 µm ± 36.9% (taken by measuring 100 particles from SEM images). After irradiation the particle size remains virtually unchanged at 5.52 µm ± 35.7%. However, large MnO/Mn$_x$O$_y$ agglomerates were sporadically observed (**Figure 4.9d**). The sizes of these large agglomerates vary greatly and there is no discernible pattern between the different compositions. These agglomerates are spherical which do not coincide with the initial particle shape of MnO$_2$ (**Figure 4.10a**) and most surrounding particles. This could be a result of localized melting of MnO$_2$ particles to form dense spherical aggregates. EDS analysis (**Figure 4.10b**) shows the large agglomerate yields Mn kα and O kα signals.

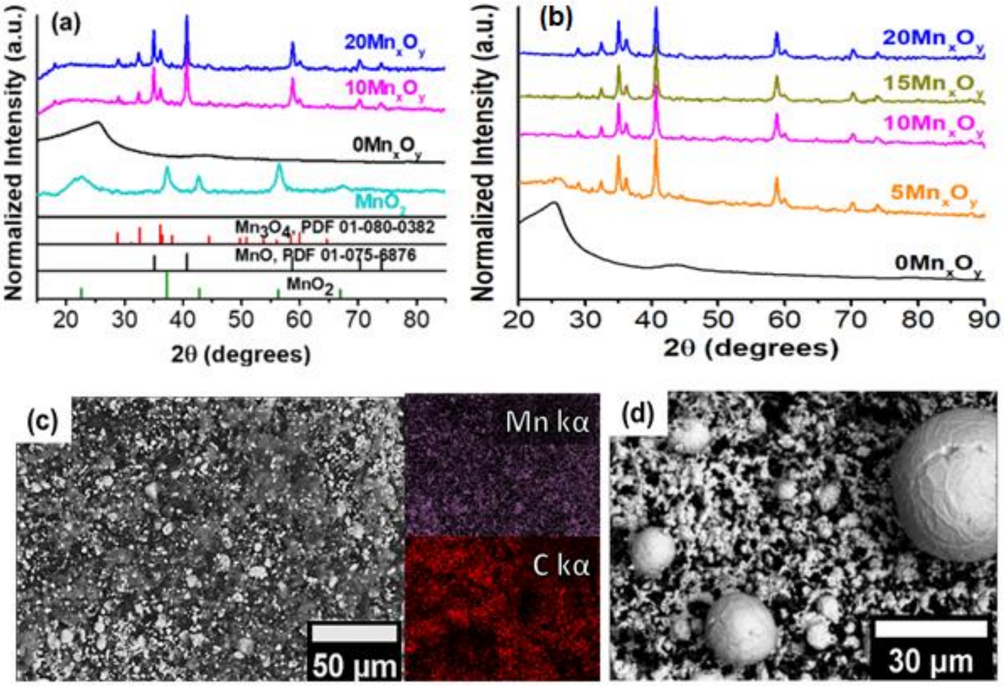

Figure 4-9.Laser-induced structural changes of MnO$_2$. (a) XRD spectra for the pristine MnO$_2$ ("MnO$_2$"), LIG produced with no MnO$_2$ ("0Mn$_x$O$_y$"), and LIG loaded with MnO$_2$ ("10Mn$_x$O$_y$" and "20Mn$_x$O$_y$"). The data is matched with manganosite (MnO, PDF 01-075-6876), hausmannite (Mn$_3$O$_4$, PDF 01-080-0382), and manganese dioxide, (b) XRD for

all samples compared to LIG from neat PFA, (c) BSE SEM image of $10Mn_xO_y$ with accompanying EDS Mn kα and C kα; (e) BSE SEM of large agglomerate observed.

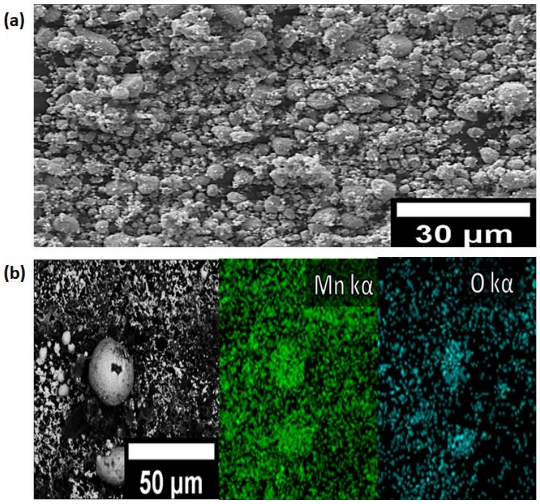

Figure 4-10. SEM images for Tosoh MnO_2 (a) SE image of Tosoh MnO_2, and (b) BSE and EDS Mn kα and O kα maps for the agglomerates observed.

Rietveld refinement (model shown in **Figure 4.11a**) was performed on the $10Mn_xO_y$ sample indicating the remaining material likely consisted of 85 wt% MnO with the remaining 15 wt% Mn_3O_4. Determining the actual composition of MnO/Mn_3O_4 within the composite material proved difficult using thermogravimetric analysis as both MnO/Mn_3O_4 and LIG have similar decomposition temperatures (**Figure 4.11b**).[435–438] Using ICP-MS proved difficult as the composite material is not completely digested by hazardous concentrated matrices such as aqua regia – likely due to LIG stability. Therefore, EDS analysis was performed on the composite material (which was prepared via pressing into a thick pellet to avoid detection of the sample holder) to determine Mn wt%. The results showed the mixed-phase materials were composed of 19.1 wt% ±1.5%, 26.7 wt% ±1.5%, 34.8 wt% ± 1.4%, and 40.9 wt% ± 1.4% for $5Mn_xO_y$, $10Mn_xO_y$, $15Mn_xO_y$, and $20Mn_xO_y$ respectively (**Figure 4.9c**). This indicates increasing the amount of MnO_2 added during polymerization results in an increase in catalyst content within the irradiated composite material. Thus, while the MnO_2 undergoes phase transformation due to the high temperature conditions, it is not significantly ablated.

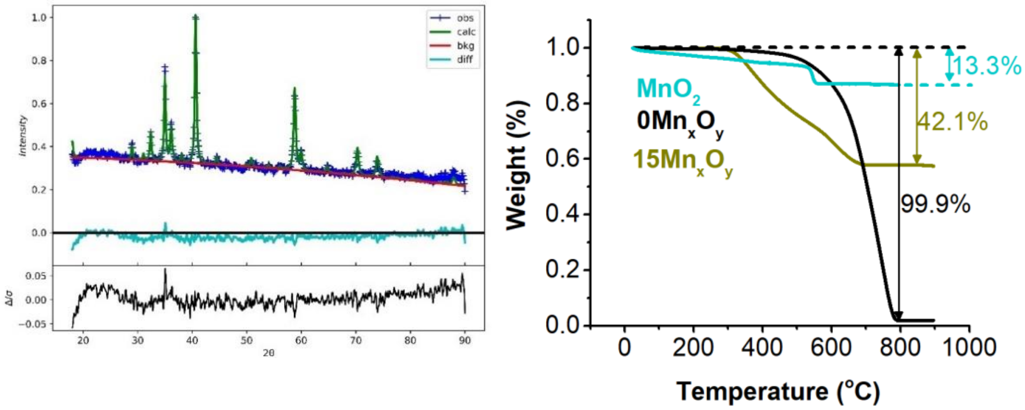

Figure 4-11. LIG-$10Mn_xO_y$ characterizations. (a) GSAS ii Rietveld Refinement fit of $10Mn_xO_y$ with R_W=4.757 and (b) TGA of Pristine MnO_2, $0Mn_xO_y$, and $15Mn_xO_y$ in air with a ramping rate of 5 °C/min.

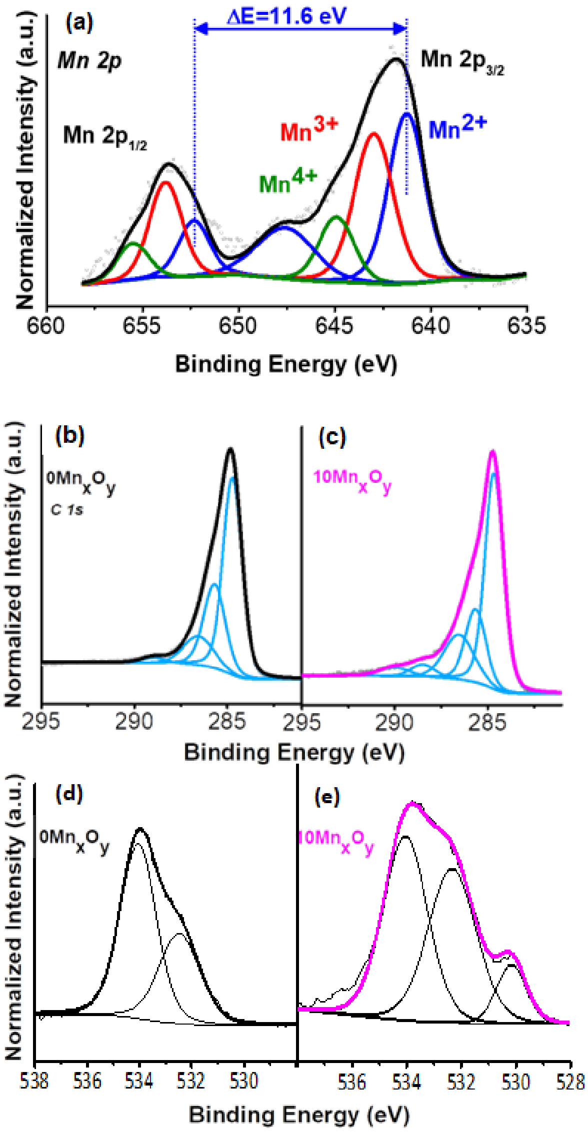

Figure 4-12. XPS analysis of different samples (a) XPS Mn 2p for $10Mn_xO_y$, (b,c) XPS C 1s for $0Mn_xO_y$ and $10Mn_xO_y$, and (d,e) XPS O 1s for $0Mn_xO_y$ and $10Mn_xO_y$

XPS spectra for Mn 2p of the loaded powders ($10Mn_xO_y$) are shown in Figure **4.12a**. They show Mn $2p_{3/2}$ and $2p_{1/2}$ peaks at 641.4 eV and 653.0 eV (ΔE=11.6 eV) which, along with a satellite peak at 647.7 eV, correspond to the Mn^{2+} from manganosite. The hausmannite is characterized by Mn $2p_{3/2}$ and $2p_{1/2}$ peaks at 643.1 eV and 654.6 eV (ΔE=10.8 eV) corresponding to Mn^{3+} and by Mn $2p_{3/2}$ and $2p_{1/2}$ peaks at 645.0 eV and 656.2 eV (ΔE=10.6 eV) corresponding to Mn^{4+}.[439,440] The O 1s for the loaded $10MnO_2$ shows a peak at 530.2 eV corresponding to Mn-O bonds which could likely be deconvoluted into two closely related peaks for Mn-O in MnO and in Mn_3O_4 (as shown in **Figure 4.12b,c**). As XPS is a surface analysis technique with a penetration depth of ~10 nm, the presence of Mn oxidation states corresponding to MnO and Mn_3O_4 indicate the irradiation completely transforms MnO_2 particles into MnO or Mn_3O_4 as opposed to a core-shell system.

The C 1s spectrum for the unloaded ($0Mn_xO_y$) sample (**Figure 4.12d,e**) shows a dominant C-C peak at 284.7 eV and additional C-O, C=O, and O-C=O peaks at 285.7, 286.5, and 288.96 eV. This supports the Raman data indicating that the LIG is predominantly *sp2* carbon. The loaded LIG ("$10Mn_xO_y$") peaks are deconvoluted by setting the peak positions and FWHM determined via the unloaded LIG (The FWHM values and area ratios can be seen in **Tables 4.1a,b**. A similar LIG structure is observed for the loaded ($10Mn_xO_y$) material which indicates the quality of the LIG is not damaged by the presence of MnO_2 during irradiation. A new peak appears at 290 eV, this is attributed to the π-π* (HOMO-LUMO) transition as it is located ~5.3 eV from the main C-C peak. This peak is a characteristic of sp2 hybridization indicating a more conductive carbon has been formed – this is supported by the sheet resistance measurements where $10Mn_xO_y$ has a lower resistance when 5.3 W is used as irradiation power.

Table 4-1. XPS C 1s peak assignments, binding energy, FWHM, and area ratio of (a) $0Mn_xO_y$ and $10Mn_xO_y$

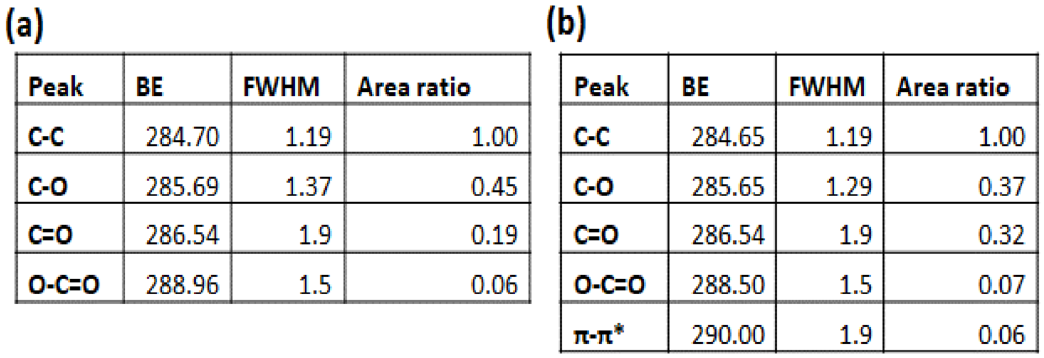

(a)

Peak	BE	FWHM	Area ratio
C-C	284.70	1.19	1.00
C-O	285.69	1.37	0.45
C=O	286.54	1.9	0.19
O-C=O	288.96	1.5	0.06

(b)

Peak	BE	FWHM	Area ratio
C-C	284.65	1.19	1.00
C-O	285.65	1.29	0.37
C=O	286.54	1.9	0.32
O-C=O	288.50	1.5	0.07
π-π*	290.00	1.9	0.06

4.3.4 Catalytic performance using RRDE

Rotating ring disk voltammetry was used to quantify the bifunctional capabilities towards oxygen reduction reaction (ORR) and the complimentary oxygen evolution reaction (OER) of the prepared composite materials. Linear sweep voltammograms (LSV) in the ORR direction (potential range of 0.9 V to -0.6 V vs. RHE) with a rotation of 1600 rpm and 5 mV/s scan rate are plotted in **Figure 4.13a** . The results show an increasing current density during the potential sweep for all materials which is significantly larger than current densities observed under N_2-purging (see **Figure 4.13a**) indicating the occurrence of O_2-fueled reactions. The potential is swept until -0.6V vs. RHE after which a rapid increase in current signaled the likely occurrence of the hydrogen evolution reaction (HER) in the 0.1 M KOH. A relatively low catalytic current of -1.5 mA/cm^2 at 0 V vs. RHE is observed for 0Mn_xO_y. Initially loading a catalyst content of 5Mn_xO_y improves the current to -2.1 mA/cm^2 showing an improvement in catalytic response with the presence of the mixed phase MnO/Mn_3O_4. This current response is further increased to -2.9 mA/cm^2 when the 10Mn_xO_y composition is used. However, the current response decreases to -2.5 and -2.6 mA/cm^2 when the composition is increased to 15Mn_xO_y and 20Mn_xO_y, respectively.

The onset potential, E_{onset}, is a useful metric which refers to the potential at which the reaction starts. The second order derivatives of the current with respect to voltage are plotted in **Figure 4.13b**.The onset potential is taken from the minimum (indicated with dotted lines) as it corresponds to the point of highest curvature of the LSV curve (which is what the tangent method estimates). For the composite materials the onset potential was determined to be 628, 641, 658, 628, and 642 mV for 0Mn_xO_y, 5Mn_xO_y, 10Mn_xO_y, 15Mn_xO_y, and 20Mn_xO_y, respectively. The higher catalytic current, combined with a lower E_{onset} (relative to OCV which sits at around 920 mV vs. RHE) suggests 10Mn_xO_y has an improved catalytic response towards ORR with respect to the other compositions.

The catalyst mediated ORR mechanism involves uptake of O_2 followed by the production of OH^- or HO_2^- using a 4- or 2-electron exchange pathway, respectively. The production of peroxide leads to reduced energy density within zinc-air batteries and is damaging to the catalyst and carbon support which compromises the energy conversion rate and battery long-term stability.[44,441,442] Thus, the determination of the *n* value and peroxide content is an important metric. The Koutecký-Levich (K-L) equation is used to calculate the number of transferred electrons, $n_{\text{K-L}}$. This equation (given as Eq. 7 and 8) is applicable in the mixed kinetic-diffusion control region.[443] The inverse of the limiting current is plotted with respect to the inverse square root of the rotation rate. The slope is then used to calculate the $n_{\text{K-L}}$ value. At a low overpotential of 0.466 vs. RHE, the calculated $n_{\text{K-L}}$ value for 0Mn_xO_y is 1.40. This value increases to 1.64 at a higher overpotential of 0 V vs. RHE (see **Figure 4.13c**). This indicates 0Mn_xO_y has a high affinity towards the 2-electron pathway. Increasing the mixed-phase MnO/Mn_3O_4 content results in an initially increasing $n_{\text{K-L}}$ value of 2.13 and 3.17 for 5Mn_xO_y and 10Mn_xO_y, respectively at a high overpotential of 0 V vs. RHE. Further increasing

MnO/Mn_3O_4 content yields $n_{K\text{-}L}$ values of 3.24 and 3.01 for 15Mn_xO_y and 20Mn_xO_y, respectively. All materials containing MnO/Mn_3O_4 do not display a significant change in $n_{K\text{-}L}$ value at high or low overpotentials. This indicates the 10Mn_xO_y and 15Mn_xO_y compositions have the highest affinity towards the 4-electron exchange reaction. The 10Mn_xO_y value is in line with previously reported *n* values which used the K-L method and analyzed manganese oxides mixed with carbon powders.[444–446]

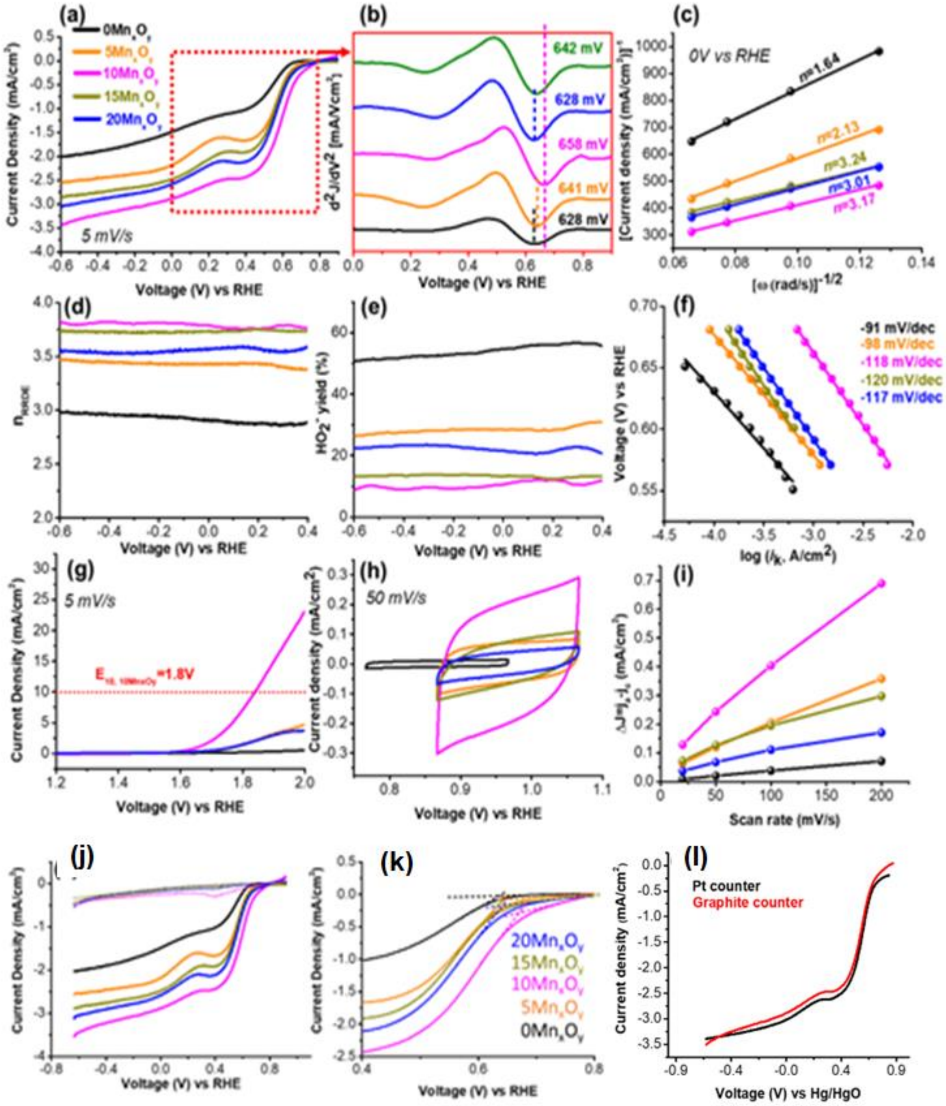

Figure 4-13. ORR performance of the different samples by RDE/RRDE tests. (a) Rotating ring disk electrode (RRDE) linear sweep voltammograms (LSV) in the ORR direction at 5 mV/s under O_2 flow at 1600 rpm and baseline corrected with respect to the electrochemical response under N_2 purged conditions; (b) second order differential of LSV curves

with labeled E_{onset} values; (c) Koutecky-Levich plots at -0.134 V vs RHE with calculated n values; (d-e) n_{RRDE} and hydrogen peroxide yield (HO_2^- yield) values calculated using RRDE data at 1600 rpm and Eq. 5 and 6; (f) Tafel plots for ORR; (g) OER LSV at 5 mV/s at 1600 rpm in under O_2 flow; (h) Cyclic voltammogram taken (CV) at 1600 rpm under O_2 in non-faradaic region carried out at 50 mV/s; and (i) Δj (j_a-j_c) vs scan rate taken from CVs at varying scan rates as per Eq. 3. (j) LSV ORR at 5 mV/s under O_2- (solid lines) and under N_2- (dotted lines) flow at 1600 rpm for different samples, (k) Closeup of the LSV showing the conventional tangent method used to find the onset potential, and (l) A comparison for the $10Mn_xO_y$ when a Pt counter or a graphite counter is used.

It is important to note that K-L is only valid for a one-step process and is not applicable for multi-step processes which often is the case in ORR. Therefore, the electron exchange value calculated using the collected ring current during RRDE, n_{RRDE}, is also presented in **Figure 4.13d**. In this test the Pt ring is held at a constant potential of 1.2 V vs. RHE to detect the peroxide formed while the disk undergoes a potential sweep in the ORR direction. The n_{RRDE} value can then be calculated from the current collected at the ring and disk using Eq. 5 . While the values differ, the trend remains the same. For $0Mn_xO_y$ the n_{RRDE} value changes from 2.88 to 2.97 at low and high overpotentials. For the loaded materials containing MnO/Mn_3O_4 the calculated n_{RRDE} values are 3.37-3.45, 3.80, 3.73, and 3.58 for $0Mn_xO_y$, $5Mn_xO_y$, $10Mn_xO_y$, $15Mn_xO_y$, and $20Mn_xO_y$, respectively, at low and high overpotentials. The unchanged n_{RRDE} values calculated for composite materials containing MnO/Mn_3O_4 ($10Mn_xO_y$, $15Mn_xO_y$, and $20Mn_xO_y$) at a wide potential range suggest a more stable ORR performance.

The amount of hydrogen peroxide yield (HO_2^- % yield) was also calculated using the RRDE data and Eq. 6. The results are plotted in **Figure 4.13e**. The highest hydrogen peroxide yield is given by the $0Mn_xO_y$ at 56.6% at low overpotentials (relative to OCV) with a decrease to 51.1% yield at high overpotentials indicating the pristine LIG has a high affinity towards hydrogen peroxide production. This is in line with the low electron exchange value calculated using the RRDE data (2.88-2.97 at low and high overpotentials) and the K-L analysis. Similarly, $5Mn_xO_y$ exhibits a peroxide yield of 30.9% which decreases to 26.5% for low and high overpotentials with a concomitant increase in n_{RRDE} value. This indicates the ORR catalysis mediated via pristine LIG ($0Mn_xO_y$) and $5Mn_xO_y$ likely proceeds via a two-step process[10] involving 1) production of peroxide intermediate $O_2 + H_2O + 2e \rightarrow OH^- + HO_2^-$ followed by 2) formation of hydroxyl $HO_2^- + H_2O + 2e \rightarrow 3OH^-$. This high affinity towards peroxide formation is consistent with undoped carbon materials previously reported in literature.[447,448] This hydrogen peroxide formation is greatly reduced by the presence of the mixed-phase MnO/Mn_3O_4. The lowest hydrogen peroxide yield at around 10.5% at low overpotentials is given by the 10Mn_xO_y meaning the increased current density shown in the LSV from the ORR does not also result in an increase the production of hydrogen peroxide. Similarly, this result is in line with the calculated n_{RRDE} values (3.80 at low and high overpotentials) favouring the 4-electron pathway. This hydrogen peroxide yield does not significantly increase at higher overpotentials (10.7%) suggesting the reaction pathway occurs through a synchronous pathway involving both the 4- and 2- electron pathway.

A Tafel plot (given in **Figure 4.13f**) can be made by plotting the voltage vs the log of the kinetic current. The latter is determined by correcting the LSV data (at 1600 rpm) with respect to the diffusion effects as shown in Eq. 9 . The data is then fitted to a linear regression where the Tafel slope indicates the amount of overpotential required to increase the reaction rate. The calculated slopes are 91, 98, 118, 120, and 117 mV/dec for 0Mn_xO_y, 5Mn_xO_y, 10Mn_xO_y, 15Mn_xO_y, and 20Mn_xO_y, respectively. The 91 mV/dec indicates fast reaction kinetics. However, the low calculated *n* value coupled with the high peroxide levels indicate a kinetically fast reaction favouring the 2-electron pathway. Increasing the MnO/Mn_3O_4 loading leads to a decrease in kinetics. However, the hydrogen peroxide and n_{RRDE} value calculation shows the presence of the mixed phase material favours the 4-electron reaction. The relatively slower kinetics exhibited by the MnO/Mn_3O_4-containing materials is characteristic of manganese oxides in 0.1 M KOH.[449–452]

The comparatively high limiting current combined with a low onset potential (relative to the OCV of the system), high electron exchange value (n_{RRDE}), and low peroxide yield indicates the optimal catalytic performance towards ORR is observed for the 10Mn_xO_y composition. Further increasing the loading yields a similar electron transfer performance and peroxide yield but fails to increase the catalytic current. There are several reasons that can explain this behaviour: 1) increasing the content of manganese oxide decreases the electrical conductivity of the samples (18.8 S/cm and 10.0 S/cm for 10Mn_xO_y and 20Mn_xO_y, respectively), 2) Mn_xO_y could agglomerate or cluster upon increasing content, leading to a decrease in surface area and hence the active sites for the ORR (**Figure 4.13h,i**), 3) if the amount of Mn_xO_y is too high, the graphene matrix might not able to effectively disperse the Mn_xO_y particles and 4) the increase in Mn_xO_y content can also lead to the formation of a large agglomerated particles of Mn_xO_y in the graphene matrix, which can impede the diffusion of reactants and products to and from the active sites which can result in a lower ORR activity and slower reaction kinetics.

Electrochemical evaluation of the oxygen evolution reaction (OER) is given in **Figure 4.13g** at 1600 rpm, 5 mV/s, 0.1M KOH, and 1600 rpm. A similar trend to the ORR is observed with $0Mn_xO_y$ and $5Mn_xO_y$ displaying a poor catalytic current towards OER. A minimal requirement of 10 mA/cm^2 (a reference value used in evaluation OER catalysts) is only achieved by $10Mn_xO_y$ at 1.8V vs RHE. This indicates that $10Mn_xO_y$ is the optimal bifunctional combination capable of catalyzing both the ORR and OER.

To understand if the performance increase and then drop of the mixed-phase composite materials are due to surface area attributes, cyclic voltammograms were performed in the non-faradaic range (just the double-layer capacitance) at varying scan rates of 5-200 mV/s. Plotting the difference in anodic and cathodic currents (ΔJ) vs the scan rate yields a slope which is directly proportional to the electrochemically active surface area (ECSA) as indicated in **Figure 4.13i**. Capacitive curves at 50 mV/s are presented in **Figure 4.13h** with corresponding ΔJ vs scan rate **Figure 4.13i.** The slope measured follows the same pattern as the ORR and OER performance where the highest value is observed from the $10Mn_xO_y$ indicating a larger ECSA when compared to the pristine $0Mn_xO_y$ and composite materials containing higher amounts of MnO/Mn_3O_4. This suggests further increasing the amount of MnO/Mn_3O_4 beyond $10Mn_xO_y$ does not introduce more accessible catalytic surface area. Instead, they likely transition from being isolated particles surrounded by conductive LIG to forming larger agglomerates of the insulating MnO/Mn_3O_4. The surface area of the materials was further probed using BET analysis. The pristine LIG and MnO_2 powders have a surface area of 7.2 and 42.4 m^2/g, respectively. However, BET analysis was not possible for the composite materials at any partial pressure range attempted. The electrochemical performance of LIG/10MnxOy catalyst is further compared with that of LIG/MnO,Mn_3O_4 catalysts previously reported in literature (**Table 4.2**), and essentially shows that LIG/$10Mn_xO_y$ catalysts possess competitive performance despite without post-synthesis treatment, nitrogen doping, furnace usage, or gas (Ar, N2, or He) flashing. Moreover, **Figure 4.13j** showed the linear sweep voltammetry of the different samples when the electrolyte saturated with O_2 and N_2. The onset potential was determined in another usual method which is the intersection of the tangents between the baseline and the signal current as shown in **Figure 4.13k**. Finally, using another counter electrode graphene instead of platinum was investigated and it performed the same results (**Figure 4.13l**).

Table 4-2. Comparison between the ORR performance of LIG -manganese oxides vs. RHE in 0.1 M KOH at 1600 rpm.

Catalysts	**Carbon precursor**	**MnOx loading**	**E_{onset} V vs RHE**	**I mA/cm^2 at -0.6 V**	**$E_{1/2}$ V vs RHE**	**ORR pathway**	**Ref.**
MnO/Mn_3O_4	PFA	10 wt.%	0.658	3.5	~0.5	4	In this work
Mn_3O_4	rGO	N/A	0.891	4.0	~0.692	4	[453]
Mn_xO_y/N-C-x	Zeolitic imidazole framework	N/A	0.987	5.0	0.871	4	[454]
MnO_x/C	Carbon black Chezacarb SH	13.82	1.081	2.6	1.031	4	[455]
(KB/ MnOx)	Ketjenblack carbon (KB)	10 wt.% MnO_x loaded	0.796	5.0	0.616	N/A	[456]
MnO@FLC	Malic acid	N/A	0.959	5.4	0.812	4	[457]
carbon black/manganese oxide	XC72 carbon black (Vulcan XC-72	50%MnO_x	0.910	2.7	0.720	4	[458]
Mn-N-C-160	rice	~20%	0.961	5.48	0.861	4	[459]
CCAC + MnO_2	HTC of corncobs	33.33%	−0.23	2.85	−0.32	4	[460].

4.3.5 ZAB performance of optimal LIG and MnO/Mn_3O_4 composite

The ORR and OER results indicate the 10Mn_xO_y composite had optimal performance, thus it was tested as a cathode in a ZAB and compared to conventional Pt/C (20 wt.%) catalyst as a benchmark. The 10Mn_xO_y was applied as a cathode catalyst onto a gas diffusion layer along with a zinc metal anode plate. The electrolyte was 6 M KOH and 0.2 M zinc acetate to ensure reversibility of the anode reaction for rechargeability. The homemade cell can be seen in **Figure 4.14a** with a more detailed schematic in **Figure 4.3**. The assembled ZAB gives an open-circuit voltage (OCV) of 1.49

and 1.33 V vs Zn for the Pt/C and 10Mn_xO_y cells, respectively, which remains stable over a 6 h period (**Figure 4.14b**). The increasing OCV of the Pt/C is attributed to the time taken for the electrolyte to infiltrate the porous carbon black matrix (Pt/C mixture had a surface area of 90 m^2/g).

Galvanostatic charge/discharge testing at 10 mA/cm^2 for 900 cycles (75 h) is presented in **Figure 4.14c** with more detailed charge/discharge profiles shown for several cycles in **Figure 4.14d**. After 60 cycles, there is negligible difference between the discharge and charge voltages of the Pt/C benchmark vs. the 10Mn_xO_y sample which were approximately 1.16 V vs. Zn on discharge and 2.07 V vs. Zn on charge. This relatively low charge/discharge voltage gap demonstrates that 10Mn_xO_y has, initially, good bifunctional performance comparable to the benchmark Pt/C. This yields a round-trip efficiency of ~56% (calculated from the ratio of $E_{discharge}/E_{charge}$) – this value of $\leq 60\%$ is typical of alkaline rechargeable ZAB due to high overpotentials at the air-cathode.[461,462] While Pt/C is the benchmark material for ORR, mechanistic studies of the ORR on Pt in concentrated alkaline conditions show ORR is inhibited due to strong OH^- adsorption onto the Pt surface.[461,463] Hence, in concentrated alkaline conditions, non-precious metal-based catalysts can compete with Pt/C. After 600 cycles the discharge voltages decrease to 0.92 and 1.04 for 10Mn_xO_y and Pt/C, respectively. Likewise, the charging voltages increase to 2.23 (round-trip efficiency of 41%) and 2.18 V (round-trip efficiency of 47%) for 10Mn_xO_y and Pt/C, respectively. The decrease in performance of the 10Mn_xO_y is likely due to the corrosion of the material due to peroxide formation that was observed during the RRDE tests. XPS C1s and Mn 2p spectra of the GDL before and after cycling are given in **Figure 4.15**. For the pristine GDL (air-sprayed with 10Mn_xO_y), the C 1s spectra can be deconvoluted to peaks attributed to C-C, C-O, C=O, and O-C=O at 284.5, 285.4, 286.8, and 288.4 eV, respectively (peak assignment, binding energy, and FHWM are given in **Table 3 and 4**). The GDL is Teflon-treated and these peaks are observed at 290.5, 292.2, and 293.7 eV for C-F, -CF_2, and CF_3, respectively.[464,465] After cycling, the C-C peak reduces and the C-O increases which could indicate loss of the carbon matrix into solution due to carbon oxidation – this is likely a result of peroxide formation. The Mn 2p spectra for the air sprayed GDL before cycling matches the spectrum for the 10Mn_xO_y given in **Figure 4.15b**. After cycling, the raw data becomes significantly noisier for the same scan time indicating less Mn 2p signal which could be a result of the MnO/Mn_3O_4 catalyst detaching during cycling along with the carbon. The deconvoluted peak area for Mn^{3+} and Mn^{4+} with respect to Mn^{2+} decreases which implies there is a disproportionate loss of Mn_3O_4 material with respect to MnO (details of peak assignment and FHWM are given in **Table 5 and 6.**

Galvanodynamic polarization curves are presented in **Figure 4.14e**. The initial drop during discharge and voltage jump during charge is due to the overpotential required to overcome the ORR and OER energy barriers, respectively. The potential gap between charge and discharge curves is thus a measure of resistance. The results show a slightly higher resistance experienced by the $10Mn_xO_y$ composite when compared to Pt/C. At 50 mA/cm^2 the voltage gap is 1.72 and 1.47 for the $10Mn_xO_y$ composite and Pt/C, respectively. The calculated power density shows peak powers at 48.3 and 69.0 mW/cm^2 for $10Mn_xO_y$ and Pt/C, respectively.

The results of galvanostatic rate performance testing is presented in **Figure 4.14f**, where the battery is discharged at varying current densities from 1-15 mA/cm^2. The $10Mn_xO_y$ has comparable rate capabilities to the commercial Pt/C with a fast dynamic response to increasing the discharge current density. At higher current densities the initial response is better for $10Mn_xO_y$ compared to Pt/C. After progressively faster current densities are applied it is lowered back to 1 mA/cm^2. The measured discharge potential recovers fast with no decline in the measured potential.

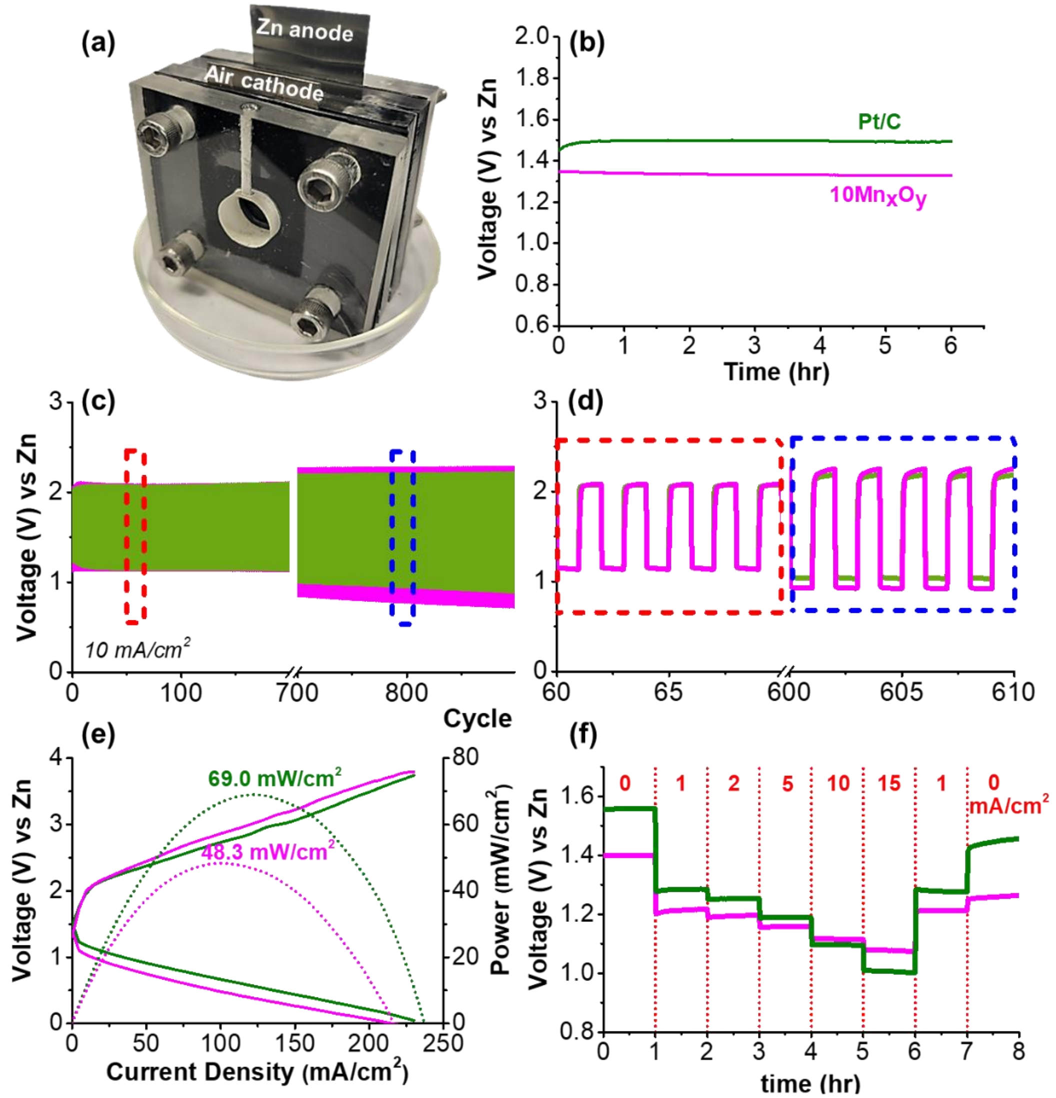

Figure 4-14. (a) Homemade ZAB setup; (b) OCV of Pt/C (20 wt%) and 10Mn$_x$O$_y$; (c) Galvanostatic charge/discharge at 10 mA/cm2 for 2.5 min charge/discharge and (d) closeup of red and blue squares; (e) galvanodynamic profiles and power density; and (f) rate discharge at varying current densities (1, 2, 5, 10, and 15 mA/cm^2).

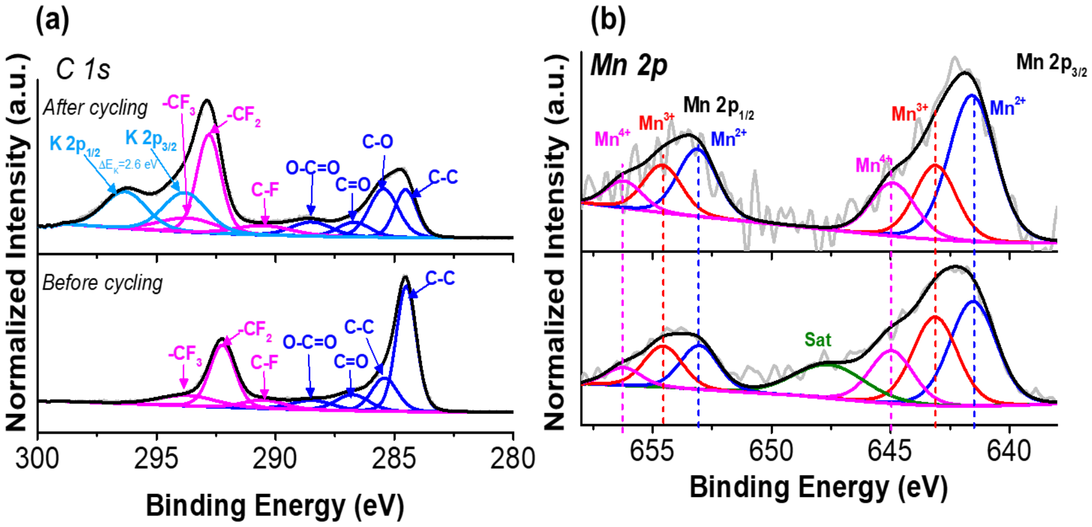

Figure 4-15. XPS analysis of GDL before (bottom) and after (top) galvanostatic cycling (j=10mA/cm^2 for 5 min cycles) of (a) C 1s and (b) Mn 2p.

Table 4-3. C1s peak assignments, binding energy, and FWHM for pristine GDL air-sprayed with 10Mn_xO_y.

Peak	**BE (eV)**	**FWHM**	**Area Ratio**
C-C	284.5	1	1.61
C-O	285.4	1.3	0.55
C=O	286.8	1.6	0.34
O-C=O	288.4	2	0.25
C-F	290.5	2.8	0.22
CF2-	292.2	1.2	1.00
CF3-	293.7	2.8	0.38

Table 4-4. C1s peak assignments, binding energy, and FWHM for cycled GDL air-sprayed with $10Mn_xO_y$

Peak	**BE (eV)**	**FWHM**	**Area Ratio**
C-C	284.5	1	0.52
C-O	285.4	1.4	0.73
C=O	286.7	1.6	0.25
O-C=O	288.5	2	0.30
C-F	290.0	2.8	0.23
CF2-	292.7	1.2	1.00
CF3-	293.6	2.8	0.41
K 2p 3/2	293.8	2.1	0.77
K 2p 1/2	296.4	2.1	0.75

Table 4-5. Mn 2p peak assignments, binding energy, and FWHM for pristine GDL air-sprayed with $10Mn_xO_y$

Peak		**BE (eV)**	**Peak distance**	**Area Ratio**	**FWHM**
2p 3/2	Mn^{2+}	641.5		1.00	2.3
	Mn^{3+}	643.1		0.83	2.2
	Mn^{4+}	644.9		0.48	2.1
Satellite		647.6		0.50	3.5
2p 1/2	Mn^{2+}	653.0	11.5	0.35	1.9
	Mn^{3+}	654.6	11.4	0.33	1.9
	Mn^{4+}	656.2	11.3	0.13	1.8

Table 4-6. Mn 2p peak assignments, binding energy, and FWHM for cycled GDL air-sprayed with $10Mn_xO_y$

		BE (eV)	Peak distance	Area Ratio	FWHM
2p 3/2	Mn^{2+}	641.6		1.00	2.3
	Mn^{3+}	643.1		0.46	2.1
	Mn^{4+}	644.9		0.35	2.2
2p 1/2	Mn^{2+}	653.1	11.5	0.39	1.9
	Mn^{3+}	654.6	11.5	0.27	1.9
	Mn^{4+}	656.2	11.3	0.15	1.8

4.4 Conclusion

In this work, a simple one-pot synthesis technique for the production of laser induced graphene supported manganese oxide with a composite of Mn_3O_4 and MnO (LIG-MnO/Mn_3O_4) as an air cathode was successfully carried out under ambient circumstances. The carbonization of the waste polymer poly furfuryl alcohol (PFA) generated from biomass and loaded with a composite of manganese oxides was accomplished using a low-cost CO_2 infrared laser system. In addition, a homogeneous dispersion of mixed manganese oxide catalyst was seen because the partly polymerized PFA can keep the mixed manganese oxide particles in suspension while it cures and carbonizes. The oxygen reduction reaction (ORR) of the LIG-MnO/Mn_3O_4 cathode could be tuned based on the amount of manganese oxide precursor used; low concentrations of manganese oxide tend to follow the 2e- ORR pathway, while high concentrations follow the 4e- ORR pathway. The LIG/MnO/Mn_3O_4 catalyst with 10 wt.% manganese oxide precursor (LIG-$10Mn_xO_y$) demonstrated the greatest catalytic activity towards ORR in comparison to the other concentrations, as increasing MnO_x content resulted in poor electrical conductivity and low surface area. When evaluated as an air cathode in a zinc-air battery (ZAB), the LIG-$10Mn_xO_y$ catalyst performed similarly to the industry standard benchmark Pt/C (20 wt.%).

Chapter 5

Direct Synthesis of Nitrogen-Doped Laser Induced Graphene with High Surface Area and Excellent Oxygen Reduction Performance

Biomass-derived carbon nanoparticles are regarded as significant sources of renewable energy. However, development of one-step processes combining porous architecture graphene with nitrogen doping has remained a challenging task. Herein, we design and present a facile, low-cost and general approach for synthesizing patternable, nitrogen-doped and porous graphene from chitosan/poly furfural alcohol (PFA) mixture using CO_2 laser in ambient air. Thermal irradiation-induced carbonization of a biomass film that consists of chitosan and PFA was achieved to produce nitrogen doped carbon with good oxygen reduction reaction (ORR) activity. Ball milling was found necessary to decrease the particle size of chitosan in order to improve its dispersion in furfuryl alcohol. This led to better ORR activity due to the positive impact of the milled chitosan on the electrochemical active sites. This study offers a workable synthesis method for the scalable manufacturing of high-performance carbon-based ORR catalysts produced from biomass sources.

Contributions

For this project, I designed the experiments in consultation with Dr. Pope and all experiments were entirely conducted by myself with the assistance from Hao Yu Zhang. I also wrote the manuscript and Dr. Pope and Dr. Manila helped with editing of the manuscript and the article is under preparation. The authors in order are; Tahani Aldhafeeri, Hao Yu Zhang, Manila Ozhukil Valappil and Michael Pope.

Funding Acknowledgements

This project was funded by Natural Sciences & Engineering Council of Canada’s Alliance Program, the Ontario Centre for Innovation, the University of Hafr Al Batin though the Saudi Arabian Cultural Bureau in Canada, and in collaboration with e-Zinc company (Mississauga, ON)

5.1 Introduction

The invention of inexpensive, ecologically friendly, biomass-based metal-free electrocatalysts for oxygen reduction reaction (ORR) promotion has gained attention, particularly in the context of the circular economy.[192] As mentioned in the previous chapters, there is extensive research on enhancing ORR and reducing Pt consumption and one of the most popular techniques involves alloying Pt with less expensive metals,[466] while the performance of Pt-alloys has demonstrated great progress, commercial production would still nonetheless need complicated synthesis procedure. [467,468] Metal oxide and nitride catalysts have also shown promise, but currently they still fall short of the activity and stability of Pt catalysts. [467,469] Many other strategies for enhanced ORR catalysts are under development, and the recent works on metal-free ORR catalysts are especially promising. The highlight of metal-free catalysts is the dramatic reduction in costs, due to the absence of metallic materials, and there are ongoing efforts to improve the activity of the ORR.

Metal-free ORR catalysts include carbon nanotubes, graphene and its derivatives or their hetero-atom doped variants (e.g. N, S, P or B-doped). Among these heteroatom dopants, nitrogen doping is especially effective in enhancing ORR activity and it is the most widely used dopant.[470] The exact mechanism in which nitrogen doping accelerates ORR kinetics is not well understood, however it is generally accepted that the slightly more electronegative nitrogen (3.04) induces a slight positive dipole on neighboring carbons (2.55).[467,471] This facilitates oxygen adsorption (potentially inducing side-on adsorption) onto the catalyst surface which is linked with enhanced ORR activity. Within the carbon backbone, there can also be several confirmations for bonding of heteroatom nitrogen. While the specific differences between the impact of pyridinic, pyrrolic and graphitic nitrogen are unresolved, it is generally agreed that the pyridinic nitrogen is most effective at catalysing the 4 electron ORR.[472,473]

To introduce nitrogen into the carbon-matrix, several methods have been explored and described in literature. In-situ methods such as chemical vapour deposition (CVD) has been used with nitrogen precursors such as NH_3,[474] urea,[475] MeCN,[476] acetonitrile,[477] to grow N-doped carbon nanotubes and graphene. Essentially, most of the precursors used in the CVD synthesis contain metals and careful washing is required to remove the residual metal atoms to avoid contamination [467,478.] Another common approach is post-processing doping, where the carbonization is done prior to nitrogen doping. Examples include direct modification and functionalization of the carbon structure with ammonia, (through a hydrothermal process)[479] and vapour annealing.[480] Pyrolysis, also known as thermal annealing, is another method to incorporate nitrogen into a carbon structure. Typically, this strategy involves combusting nitrogen containing precursors with the carbon framework under an inert atmosphere, resulting a fraction of the nitrogen atoms reorganizing and forming new bonds the carbon material.[481,482] Nitrogen precursors such as uric acid,[483] melamine,[478,484,485] hexamethylenetetramine,[486] urea,[487–490] dicyandiamide,[490] polypyyrole,[491] 1,3 – diaminobenzene/2,6 diaminopyridine,[492] and poly(o-phenylenediamine)[493] have been widely utilized for pyrolysis method to yield N-doped carbons.

Among several choices for nitrogen precursors to synthesize N-doped carbons, biomass-based precursors have become a recent popular choice as mentioned in **Chapter 2**.[494] Among them chitosan is a particularly interesting candidate as it is a low-cost, non-toxic biopolymer that can be easily derived from deacetylation of chitin, which is found in abundance in marine arthropods.[495] It is also the second most common biopolymer found in nature, after cellulose.[496] Its wide-spread availability, makes it a suitable candidate as a nitrogen precursor for application in metal-free ORR electrocatalysis. To exemplify a few, recently, Guo *et al.* fabricated hierarchical nitrogen-doped carbon nanoflowers using chitosan and urchin-like hierarchical silica spheres by emulsifying chitosan in 2% acetic acid (in water) with aminated urchin hierarchical silica particles followed by heating at 180 ^{o}C for 12 hours in a hydrothermal process. [497] After washing and drying, carbonization of the product was performed at various elevated temperature ranging from 600 ^{o}C to 1000 ^{o}C. The resulting nanoflower displayed an onset potential of 0.923 V (vs. RHE) in alkaline media with a specific surface area (SSA) of 873 m^2/g when carbonized at 800 ^{o}C. A similar work by Liu *et al.* also reported excellent ORR activity with an onset potential of 0.82 V (vs RHE) in alkaline media, which is only slightly lower than commercial Pt/C.[498] In their work, phytic acid-chitosan-graphene oxide hydrogels were prepared and pyrolyzed at 800 - 1000 ^{o}C to create a nitrogen/phosphorous doped carbon. The nitrogen and phosphorus content in the material were determined to be 0.93% and 0.65% , respectively.

Post-processing thermal carbonization of chitosan have also been explored. Chemical vapour deposition (CVD) of chitosan, specifically the nitrogen heterocyclics produced during thermal decomposition, and graphene oxide have also been utilized to prepare N-doped carbons. Kumar *et al.* used a one-pot thermal annealing process where graphene oxide reacted with volatile nitrogen heterocyclic compounds (derived from chitosan) at several hundred degrees celsius and under an argon atmosphere to create an electrocatalyst.[499] The ORR onset potential was found to be 0.78 V (vs RHE) and the number of electrons averaged at 2.15. A maximum of 4.3% nitrogen content was obtained. Another work utilized molten KCl held at 800 ºC to pyrolyze pure chitosan.[500] The pure carbonized chitosan displayed a SSA of 1654 m^2/g which the authors attributed to the dispersive effect and of liquid molten salt and the isolation function of the solid salt during the cooling process. This material exhibited an onset potential similar to Pt/C in alkaline media and the number of electrons transferred was calculated to be 3.9. XPS measurements also reported a nitrogen content of 3.96% with 37%/54%/9% in pyridinic, graphitic and oxidized-nitrogen forms.

Wet and dry ball milling is a facile technique for reducing particle size and mixing raw materials.[501–505.] Reducing the size of chitosan particles before mixing them with other materials can improve the dispersibility and homogeneity of the resulting mixture. Furthermore, small particle sizes can increase the surface area of the chitosan and improve its interactions with the other components of the mixture. This method has been extensively investigated recently and has the potential to produce several classes of nano-powder in a way that is environmentally friendly, repeatable, affordable, and scaled up.[501] Zhang *et al.* investigated the physicochemical and structural characteristics of milled chitosan.[506] They found that the crystalline structure of the milled chitosan exhibited amorphous morphology and decreased its thermal stability.

In literature, there are few works dedicated to using biomass-derived chitosan as a nitrogen dopant for metal-free ORR electrocatalysts. Out of these works, majority of them include challenging and harsh preparation procedures such as high temperature carbonization, annealing or CVD. Some of the main advantages of metal-free electrocatalysts is its cheap price and environmental sustainability. However, their tedious/hazardous synthesis may negate these advantages. To realize the full commercial ability of chitosan-based metal-free electrocatalysts, it is therefore equally essential to develop a facile preparation procedure to maximize its potential.

As mentioned in Chapter 2 and 3, Laser scribing is a method to induce pyrolyzation of carbonaceous materials through direct irradiation of the surface of the material[507]. Recently, there have been research demonstrating effective ORR performance from LIG containing other metal catalysts.[508] But nitrogen, sulfur, or/and boron doped LIG were always used in supercapacitor applications.[509–516] In the last chapters 4 and 5, we carbonized PFA that included catalysts and catalyst precursors by CO_2 laser, and it is worthwhile to design and investigate the carbonization on of PFA/nitrogen precursor to produce nitrogen doped LIG. Both chitosan and LIG have shown promising results as catalysts in for ORR, and research is ongoing to further understand and optimize their performance.

Towards this direction, this chapter discusses the attempts to prepare N-doped LIG by carbonization of PFA/chitosan and its subsequent usage as a metal-free electrocatalyst for ORR in ZAB. Nitrogen doped LIG derived from biomass nitrogen and graphene sources as an ORR catalyst hasn't been looked at yet and we are the first to produce this effective metal free catalyst. A facile 2-step synthesis strategy is developed involving a one-pot polymerization process followed by laser scribing to create N-LIG for ORR electrocatalysis. To have well-dispersed chitosan in the FA suspension, we used balls milling technique to reduce the size of the chitosan particles. Apparently, the fabrication method does not require expensive materials, toxic chemicals or harsh conditions and it is a relatively a fast process. These attributes are particularly attractive when considering the commercial potential of technologies requiring an air electrode.

5.2 Experimental Methods

5.2.1 Preparation of catalyst loaded PFA and Laser-induced carbonization

Various amounts of chitosan (mole wt= 50,000-190,000 Da), 250 µl acetic acid (glacial, ReagentPlus®, ≥99%) from Sigma-Aldrich were mixed with 4 ml of furfuryl alcohol (FA, Thermo Scientific™, Acros Organics, 98%) by tip ultrasonication at 40% power (BioLogics, Inc. Model 150 V/T ultrasonic homogenizer, 150 W) for 10 min. The mixture was heated at 90 °C with stirring 600 rpm for 15 min then a mixture of 4 ml FA and 68 mg of oxalic acid dihydrate (EMD, 99.5%) as the initiator that is partially polymerized (at 90 °C for 2 h) was added (as shown in **Figure 5.1**). After 1.5 to 3 h, the viscous mixture was casted on a foil substrate and cured in oven for 24 h at 80 °C. After polymerization is completed, the aluminum foil is peeled off to reveal the smooth PFA surface. This polymer layer is then placed in a CO_2 laser (BossLaser 1416L, 50W, and a laser spot diameter of 60 µm) to selectively irradiate the surface of the PFA. The resulting film was irradiated by CO_2 laser using 10 mm/s scan speed, 10.4% (5.2 W) power conditions.

Also, we tried to grind the chitosan by the ball milling machine (planetary ball mill pulverisette 5 machine), for 1h using 0.1mm- 30 mm 95% purity Zirconia beads grinding media at 3500 rpm. The samples labeled as mentioned in Table 5.1.

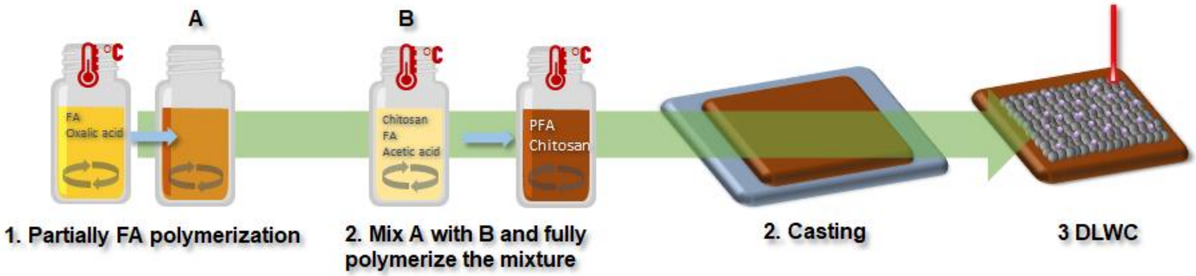

Figure 5-1. Nitrogen doped LIG synthesis method.

Table 5-1.Composition of samples prepared

Sample name	Chitosan (mg)	Milled by ball milling
N-LIG1	100	-
N-LIG2	500	-
Milled N-LIG1	100	Yes
Milled N-LIG2	500	Yes
LIG from neat PFA	0	-

5.2.2 Electrochemical characterization

The conditions for ORR performance and ZAB testing are same as mentioned in section 3.3.4 of Chapter 3

5.3 Results and Discussion

5.3.1 PFA composite and irradiation conditions

A schematic showing the synthesis of the composite PFA is shown in **Scheme 4.1**. This is a 4-step process consisting of 1) mixing of the FA monomer and oxalic acid initiator at 90 °C for 2 h to produce a viscous, partially polymerized suspension; 2) a mixture of chitosan , FA and acetic acid was added to the previous suspension 3) the viscous suspension is then cast onto aluminum foil using a film applicator and allowed to cure overnight in the oven at 70 °C, this produces a hardened resin; 4) Finally, the resin is carbonized via direct laser writing carbonization (DLWC) at 10 mm/s and a power of 5.2 W. We designed this synthesis method to avoid shrinkage caused by the chitosan while curing in the oven, if we dissolved the chitosan in 2% acetic acid solution as shown in **Figure 5.2a**, mixed all the reactant together (**Figure 5.2b**), **,** or increase the chitosan concentration more than 5.5% (**Figure 5.2c**). Our hypothesis about the reason of the sample's shrinkage after curing in oven could be due to the different moisture content in PFA and chitosan mixture. While polymerization of FA, water produced from the crosslinking FA reaction may be absorbed by chitosan causing more water content in chitosan than PFA. And when the chitosan's moisture is evaporated later in the oven, chitosan will shrink more than the dry polymer (PFA).[517,518] Due to the fact that the chitosan was not fully dissolved in the procedure and small particles remained, the N-LIG2 is observed to have a rougher surface than milled N-LIG-2, as illustrated in **Figure 5.2e**.

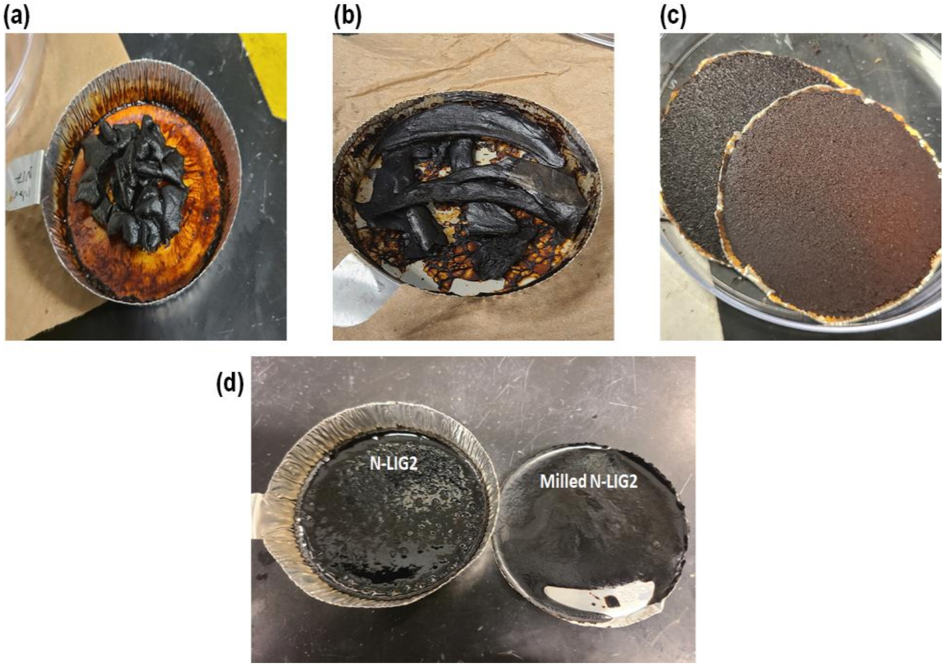

Figure 5-2. Images of samples with different synthesis methods. (a) chitosan dissolved in 2% acetic acid, added to FA, and after cured in oven , (b) when the reactants mixed together and cured in oven, (c) when increased the concentration of the chitosan more than 5.5%. and (d) samples milled N-LIG2(left) and N-LIG2(right).

5.3.2 Laser-induced carbonization of PFA

When the samples were exposed to a CO_2 laser operating in the appropriate power range (4.9–5.6 W), the electrically insulating neat chitosan loaded PFA films became black and electrically conductive (**Figure 5.3**). As mentioned in the previous chapters, this is the outcome of laser-induced carbonization, which is frequently ascribed to the photothermal pyrolysis phenomenon.

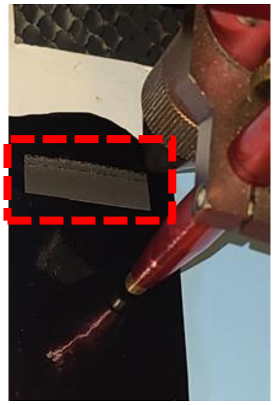

Figure 5-3. Milled N-LIG2 while exposed to CO_2 laser (the dotted line is LIG).

By using the multimeter, using 10.4% laser power condition while scribing the samples by CO_2 laser gave the lowest resistance. It should be noted that sheet resistance, which is a better accurate method that using the multimeter, should be done in the future to explore the effect of laser power (at a set scan rate of 10 mm/s) on the formation of the LIG.

As shown in the SEM analyses of N-LIG and milled N-LIG samples (**Figures 5.4a-d)**, the milled chitosan improved the pore size of LIG. This is likely due to the small particles of the chitosan distributed in PFA better than non-milled chitosan. **Figure 5.4e** shows the EDS analysis of the element contents in milled N-LIG2 sample, which showed 3.79 at.% nitrogen content. This percentage could be considered high nitrogen content in the final product even though we used 5 wt.% chitosan (chitosan has 6.6 to 7% nitrogen) 504 mixed with FA. This high percentage is due to the large reduction in PFA mass after canonization. Also, the high nitrogen content in milled N-LIG2 may result due to the good distribution of the small chitosan in PFA that protect the amino groups from decomposing during the laser treatment.

Further, XPS analysis of the milled N-LIG2 is presented in **Figure 5.4f**, confirming the successful doping of nitrogen into the LIG (1 at. %). The bonding states can be assigned to four dominant configurations: pyridinic-N (398.3 eV), pyrrolic-N (399.8 eV), quaternary-N (400.9 eV), and nitrogen oxides (403.3.3 and 405.6 eV), respectively. The relative content of quaternary N (44.4 %) is the highest compared to other nitrogen configurations (15.6 % for pyridinic-N, 8.5 % for pyrrolic-N) because both pyrrolic and pyridinic structures are unstable at high temperature and tend to transform into a more stable quaternary nitrogen configuration.[520,521]

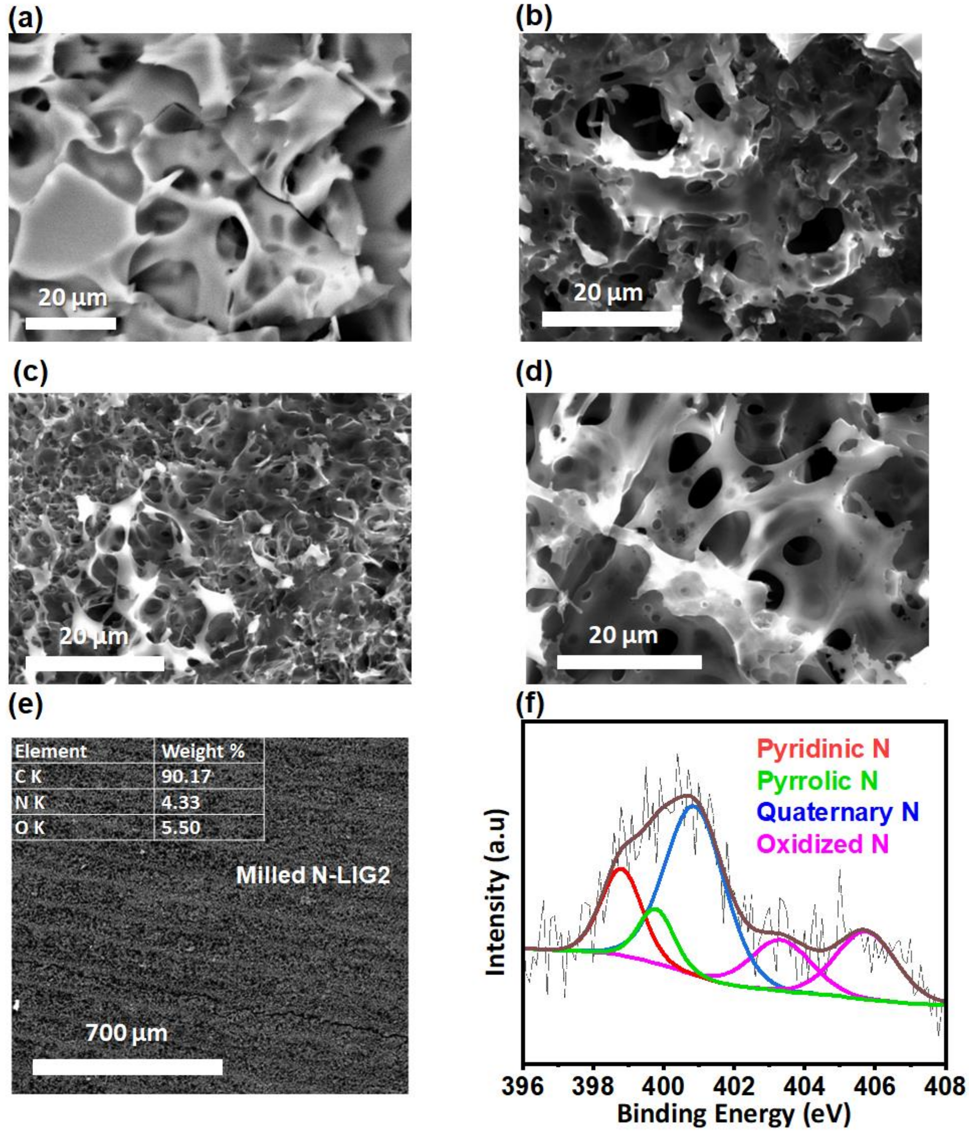

Element	Weight %
C K	90.17
N K	4.33
O K	5.50

Figure 5-4. SEM images for various N-LIG samples, the images were collected with the secondary electron (SE) detector, EDS/SEM and XPS N 1s spectrum analysis ; (a) N-LIG-1,(b) milled N-LIG1, (c) N-LIG2, (d) milled N-LIG2, (e) EDS analysis for sample milled N-LIG2 (inset includes elements content table), and (f) XPS N1s spectrum for sample milled N-LIG2.

5.3.3 Catalytic performance using RRDE

The functional abilities of the synthesized samples towards the oxygen reduction process (ORR) were measured via rotating disc voltammetry. **Figure 5.5a** shows the plot of linear sweep voltammograms (LSV) with a rotation of 1600 rpm in the potential range of 0.05 to -1 V vs. Hg/HgO. The results indicate that all samples undergo a rise in current density during the potential sweep that is much higher than current densities seen during N_2-purging, confirming the ORR.

A relatively low catalytic current of -0.39 mA/cm^2 at -1 V vs Hg/HgO is observed for LIG from neat PFA. Initially loading 100 mg chitosan content (in samples N-LIG1) improves the current to -2.25 mA/cm^2 showing an improvement in catalytic response with the presence of nitrogen dopant. This current response is further increased to -2.63 mA/cm^2 when the 500 mg chitosan is used (N-LIG2). However, the current response increased to -2.85 and -3.01 mA/cm^2 when chitosan grinded used in samples milled N-LIG1 and milled N-LIG2, respectively.

The onset potential is taken from the minimum as it corresponds to the point of highest curvature of the LSV curve. For the composite materials the onset potential was determined to be -168, -201, -211, -246, and -246 mV for milled N-LIG2, milled N-LIG1, N-LIG2, N-LIG1, and LIG from neat PFA, respectively. The higher catalytic current, combined with a lower E_{onset} suggests milled N-LIG2 has an improved catalytic response towards ORR with respect to the other compositions.

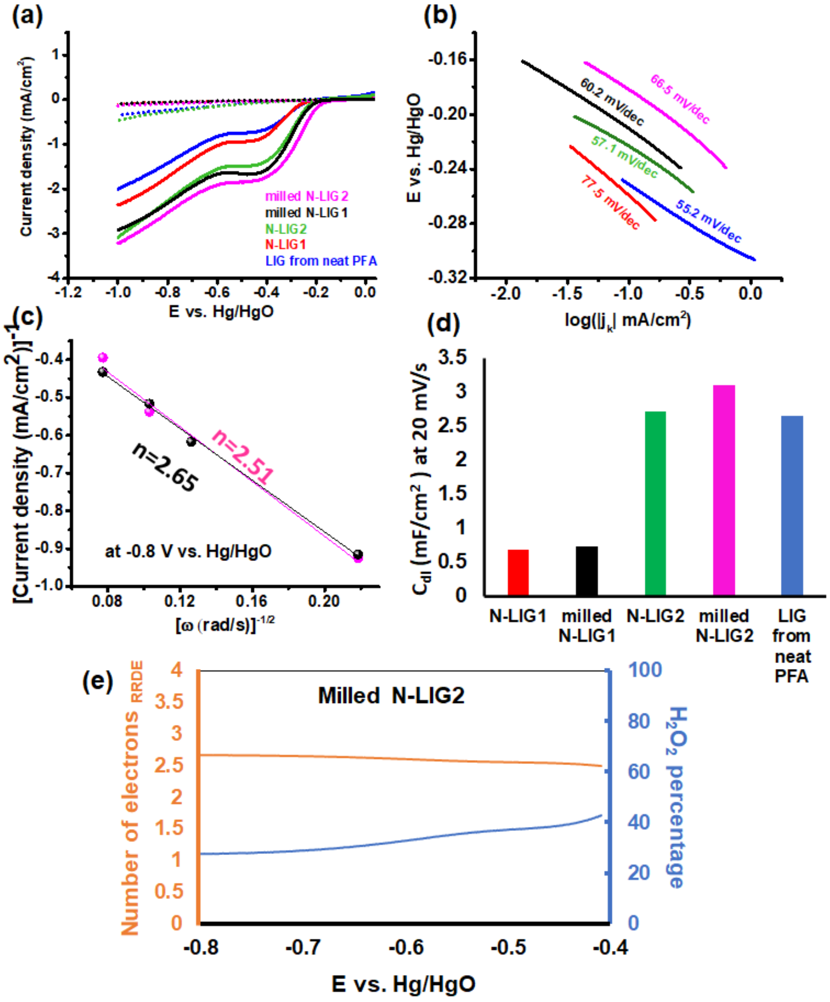

Figure 5-5. ORR performance for the different samples in 0.1 M KOH and using Pt wire as CE and Hg/Hg/O as RE;(a) linear sweep voltammetry while the electrolyte saturated with O2 and N2 (dotted line) at 1600 rpm, (b) Tafel plot, (c) Koutechy Levich graph for milled N-LIG1 and milled N-LIG2 at -0.8 V vs. Hg/HgO(d) double layer capacitance mF/cm^2 while using 20mV/s as scan rate, and (e) RRDE results; peroxide and number of electrons for sample milled N-LIG2.

A Tafel plot (given in **Figure 5.5b**) can be made by plotting the voltage vs the log of the kinetic current. The data is then fitted to a linear regression where the Tafel slope indicates the amount of overpotential required to increase the reaction rate. The calculated slopes are 66.5, 60.2, 57.1, 77.5, and 55.2 mV/dec for milled N-LIG2, milled N-LIG1, N-LIG2, N-LIG1, and LIG from neat PFA, respectively. The 55.2 mV/dec indicates fast reaction kinetics for the LIG from neat PFA. The reaction mechanism became faster and was improved by 11.3 mV/dec when milled chitosan was used in sample milled N-LIG1 compared to N-LIG1. However, when the concentration of the chitosan was increased in the samples to 500 mg instead of 100 mg, the reaction kinetics became slower by 9.7 mV/dec when milled chitosan used instead of non-milled chitosan. Increasing the chitosan loading results to a decrease in kinetics and using milled chitosan slower the mechanism of the ORR than the non-milled.

To understand the performance increase by the pretreatment of the chitosan, cyclic voltammograms were performed in the non-faradaic range (0 - 0.1 V vs. Hg/HgO) at scan rate 20 mV/s. Double layer capacitance at scan rate 20 mV/s are presented in **Figur**e **5.5d**. The milled N-LIG2 showed the largest C_{dl} when compared to other samples. Also, the C_{dl} of the milled N-LIG1 and milled N-LIG2 were higher than non-milled N-LIG samples. This suggests decreasing the size of the chitosan before mixing it with the reactants introduce more accessible catalytic surface area. Moreover, LIG from neat PFA has higher C_{dl} than N-LIG1 and milled N-LIG1, however the ORR performance of LIG from neat PFA was poor. Nevertheless, the low calculated *n* value (~2.7) of the milled N-LIG2 sample coupled with the high peroxide levels (43.1% to 26.2% at -0.4 to -0.9 V vs. Hg/HgO) indicate a kinetically slow ORR favouring the 2-electron pathway as shown in **Figure 5.5e.**

The results presented here demonstrate that the catalysis for the reduction of oxygen is not primarily driven by surface areas but rather by nitrogen concentration, nitrogen bonding configurations, and textural texture. Milled N-LIG2 performed excellent onset potential and good ORR performance compared to recent ORR catalysts with higher nitrogen contents as shown in **Table 5.2.**

Table 5-2. ORR performance comparison vs. RHE in 0.1 M KOH and at 1600 rpm**.**

Catalyst	Synthesis method	Nitrogen source	E_{onset} V (vs. RHE)	J (mA/cm^2) at 0.1 V vs. RHE	Nitrogen content	Ref.
NrGO	thermal pyrolysis process	Polyaniline and ammonium persulfate	0.99	-6.2	3.8 ± 0.4 at.%	505
N-rGO	electrochemical method	urea	0.78	-7.5	6.8 at. %	506
N-doped graphen	direct magnesium reduction of graphitic carbon nitride (g-C3N4) at high temperature	melamine	0.79	−4.8	5.4 at.%	507
NrGO	thermal annealing	urea	0.88	-4.1	19.8 wt%	508
porous N-doped graphene layers	high-temperature treatment	chitosan and graphitic carbon nitride	0.98	-5.5	4.12 at.%	509
Milled N-LIG	Irradiation carbonization by CO_2 laser	chitosan	0.76	-3.4	3.79 at.%	this work

Note that, to complete the electrochemical performance analysis of these nitrogen doped samples, there are several important tests should be done in the future:

1) RRDE tests for all samples to investigate the effect of the milled step on the peroxide percentage and number of the electrons.
2) To confirm the results of ECSA, different scan rates should be used to determine the C_{dl} as a slope of the scan rate vs. current density plot.
3) OER performance could be interesting to study.

4) ZAB tests should be done to investigate the charging and discharging behavior of the nitrogen doped LIG and to evaluate the power density and discharge capacity.

5.4 Conclusion

We developed and proposed a simple, affordable, and all-purpose method for creating porous, nitrogen-doped, patternable graphene from a chitosan/poly furfural alcohol (PFA) combination utilizing a CO_2 laser. A biomass film made of chitosan and PFA was thermally irradiated to carbonize it, producing nitrogen-doped carbon with excellent oxygen reduction reaction (ORR) activity. Investigations have been done into ORR activities and it showed that reducing the size of the chitosan by ball milling technique improved the ORR performance. And this result was due to the increase of the electrochemical active surface area leading to an increase of active sites. Moreover, SEM images showed that the pores size of the nitrogen doped LIG from milled chitosan was bigger than the pores size of the non-milled chitosan. The nitrogen doped LIG followed the two electrons ORR pathway and produced up to 40% peroxide in the potential range (-0.4 to -0.8 V vs. Hg/HgO). This study could be continued to enhance the ORR performance and reduce the peroxide performed. A practical synthesis technique for producing high-performance carbon-based ORR catalysts from biomass sources is presented in this paper.

Chapter 6

Conclusions and Future Works

This chapter includes a brief summary of the studies and the conclusions that were reached, projecting LIG-PtCoO$_x$, LIG-Mn$_x$O$_y$, and nitrogen doped LIG as potential materials for future energy storage applications. Furthermore, the chapter also covers these projects' limitations and potential workarounds. Although the use of LIG-PtCoO$_x$, LIG-Mn$_x$O$_y$, and nitrogen doped LIG for electrocatalytic applications has only been examined in this study, these materials have potential for usage in a wide range of applications, including energy storage, electrochemical sensors, and supercapacitors.

6.1 Conclusion:

The decarbonization of transportation and the electrical grid has a lot of potential with the aid of fuel cells and metal-air batteries. The air-breathing cathodes of these technologies must be improved in order to address issues like the expensive platinum (Pt) catalyst needed to speed up the kinetics of the oxygen reduction reaction (ORR) and the stability of Pt/C interfaces during prolonged cycling. These issues must be addressed in order to promote widespread adoption of these technologies. There are several methods to enhance the performance and stability of ORR catalysts while minimizing costs, including decreasing the amount of Pt used, employing non-precious metal catalysts, incorporating heteroatom doped carbon, and utilizing a combination of these approaches. Even so, there are still significant stability problems with these designs. When the catalysts nanoparticles are physiosorbed to a carbon surface, they may quickly aggregate. Furthermore, the number of active sites accessible for catalysis decreases as a result of metal catalyst dissolution and particle coalescence, which over time causes coarsening. Additionally, catalyst separation from the support or carbon corrosion and oxide production at high potentials might increase coarsening. Thus, current projects have concentrated on the creation of methods to more firmly anchor and embedded different catalysts nanoparticles to the graphene matrix.

Accordingly, **Chapter 2** begins with a brief literature overview of zinc-air batteries and the various electrocatalysts used for the air electrodes. Various synthesis approaches for the electrocatalysts, advantages, and limitations for using each type of the ORR catalysts were also discussed along withmethods for patterning air cathodes. The laser induced graphene technique was explained including the materials used as LIG precursors and the technique used for doping various catalyst in LIG. Few attempts have been made to synthesize catalysts in laser induced graphene, while casting the catalysts on the surface of the LIG was the common method used to prepare LIG/catalysts. Mixing the catalyst’s precursor with the LIG precursor to embed the catalysts in the LIG matrix remains highly unexplored.

Chapter 3 begins with a brief overview of various platinum/transition metal catalysts used for ORR and their limitations. Additionally, a brief discussion of the laser-induced graphene technology and the few studies that used it to prepare the air cathode catalysts are also included. In order to create effective, bifunctional air catalysts, spherical, mixed of platinum and cobalt oxides nanoalloys and core-shell nanoparticle catalysts were embedded inside a laser induced graphene matrix. A straightforward synthesis method at ambient conditions was shown to prepare nanoparticles that are significantly smaller than 2 nm and smaller than most other reports. These features together led to high catalyst activity and stability towards oxygen reduction reaction. This method used biomass carbon precursor (poly furfuryl alcohol) and low concentrations of catalyst precursors, as well as laser induced graphene technology. The resultant LIG-PtCoOx-1 exhibits good ORR activity that is equivalent to commercial Pt/C with a similar composition, while only having an extremely small amount of Pt (1.99 wt %) and CoOx (1.40 wt%) in it. The LIG-PtCoOx-1 cathode also provides a high open circuit voltage of 1.23 V, a high-power density of 67.1 mW/cm^2, a high specific capacity based on consumed Zn, and exceptional long-term stability of up to 118 h with a low overvoltage between charging and discharging in a homemade zinc-air battery. As a result, this hybrid catalyst shows a general design approach for second-generation high performance electrocatalysts in addition to having the potential to reduce the cost of commercial catalysts.

A lot of efforts in **Chapter 3** have been expended in the optimization of the catalyst’s concentration, however, increasing the concentration of the catalyst was a challenge. Therefore, looking for non-platinum catalysts was the goal for **Chapter 4**. Developing a method to prepare manganese oxide decorated LIG pattern with an excellent distribution and a good ORR performance was investigated. The fabrication of laser induced graphene supported manganese oxide using a composite of Mn_3O_4 and MnO (LIG-10Mn_xO_y) as an air cathode was effectively accomplished in this study using a straightforward one-pot synthesis process. By using a low-cost CO_2 infrared laser system (used in all projects), poly furfuryl alcohol (PFA) made from biomass and loaded with a mixture of manganese oxides was carbonized. Catalyst optimization was investigated and compared to the other concentrations, the LIG-10Mn_xO_y catalyst with a 10 wt.% manganese oxide precursor (LIG-10Mn_xO_y) showed the highest catalytic activity towards ORR. The performance of the LIG-10MnxOy catalyst as an air cathode in a zinc-air battery (ZAB) was comparable to that of the benchmark Pt/C (20 wt.%) used as the industry standard.

Chapter 5 explores the potential of laser scribing to obtain nitrogen doped LIG as a catalyst support material. Accordingly. The chapter discusses the approach to synthesize nitrogen doped LIG from biomass nitrogen source (chitosan). Decreasing the size of chitosan particles before mixing it with the furfuryl alcohol showed a significant improvement in the electrochemically accessible surface area, which enhances the ORR performance. Additional experiments were recommended to investigate the effect of the nitrogen doped on the graphite crystal quality, specific surface area analysis, pore size distribution, nitrogen content, and the nitrogen configurations.

The major accomplishments of this thesis could be therefore summarized as follows:

1. Simultaneous carbonization of a biomass polymer mixed and reduction of low concentration metal catalysts precursors using CO_2 laser to produce catalyst embedded LIG.
2. Synthesis of spherical $PtCoO_x$ nanoalloys and core-shell nanoparticles embedded in a three-dimensional LIG matrix as air cathode by a facile synthesis route.
3. Beneficial effect of the ultra-small LIG-$PtCoO_x$ nanoalloy and core-shell nanoparticles for ORR in air cathode of zinc-air batteries (ZABs).
4. Synthesis of LIG embedded with optimum content of manganese oxides for effective air cathode for ZABs.
5. Simultaneous nitrogen doping and carbonization of biomass nitrogen source (chitosan) by laser scribing to produce nitrogen doped LIG using , as a potential air cathode support for ZABs.

Even though these techniques offered for the preparation of $PtCoO_x$ nanoalloy embedded LIG , Mn_xO_y and nitrogen doped LIG propose various novel possibilities of commercial relevance for different energy storage applications, there are several limitations. The main drawback of using furfuryl alcohol as a reducing agent and a graphene precursor is that FA is considered as poor reducing agent, which decreases the presence of the platinum metal in the samples. A higher content of catalysts could result in more efficient ORR performance which can be eventually used to explore many new applications in various domains. Further, various lasering conditions could severely affect the the phases of the metal catalysts, as evidenced in Chapter 4 for manganese oxide, yielding undesired phase transformations. As for nitrogen doped LIG, any limitations in achieving optimum nitrogen content with chitosan as nitrogen source for optimal ZAB electrode performance also needs to be addressed.

6.2 Future work

This thesis described efforts to create and develop laser induced graphene composite electrocatalysts as stable air cathode for alkaline zinc air batteries and brings several prospects to be considered as future work to address the limitations as mentioned above.

LIG-PtCoO$_x$

Future research that builds on this concept is to increase the activity and longevity of platinum-transition metal-based bifunctional catalysts by nano-structuring. The following steps must be taken in order to successfully design and develop the bifunctionally active and durable electrocatalysts. A strong reducing agent could be used with furfuryl alcohol to increase the platinum metal presented in the samples. Moreover, due to the decrease in PFA weight after irradiation carbonization by CO_2 laser, graphite or graphene oxide may improve the surface area and affect the ORR performance. Changing the conditions in the CO_2 laser; such as the laser power, speed of the lasering, and the distance between the sample and the laser pen (focus), can influence on the concentration of the catalysts presented in the LIG and the morphology of the LIG. Alternate transition metal precursors could be used such nickel acetylacetonate and iron acetylacetone with platinum acetylacetonate or cobalt acetate using the same synthesis method. In addition, instead of pristine LIG, N-LIG could be used as a support for LIG-PtCoO$_x$ which could further improve the ORR performance. Investigating wetting properties of the air cathodes are also essential to control flooding issues during ZAB operation, and any strategies to manipulate the hydrophobicity using various carbon precursors and/or lasering conditions are potential future investigations.

LIG-MnxOy

The LIG-Mn$_x$O$_y$ has a good ORR activity as decribed in chapter 4. However, their nucleation and growth mechanisms and phase changes according to the laser conditions are still unknown. It may be beneficial to sort out the mechanism(s) and then control the process to achieve higher ORR activity and stability. The sample morphology would need to be investigated and a hydrophobic surface is required to prevent flooding. Nitrogen atoms could be doped using the same synthesis method in chapter 6 to improve the overall ORR performance by developing N-LIG-Mn_xO_y catalyst.

N-LIG

As mentioned in chapter 6, many characterizations analysis should be determined using different tests such as :

1. FTIR to explore the effect of the chitosan on the polymerization of PFA
2. Sheet resistance at different laser powers.
3. The molecular vibration and rotation of LIG and N-LIG should be characterized by the Raman spectra.
4. XRD patterns of LIG and N-LIG should be investigated to study the effect of the nitrogen doped on the graphite crystal quality.
5. The specific surface area analysis and pore size distribution of N-LIG and LIG by Brunauer, Emmett and Teller (BET) test.
6. XPS measurement should be used as an evaluation method to investigate the nitrogen content, nitrogen configurations, and C,N, and O spectrums.

Moreover, oxygen evolution reaction performance could be tested. ZAB tests should be investigated. Melamine and urea, which have higher nitrogen contents than chitosan could be incorporated with chitosan in PFA to produce higher nitrogen concentration in LIG.

ZAB design

To have higher cycle life and higher power density, the battery design needs to be optimized. Flooding, precipitation of K_2CO_3, and electrolyte evaporation are the three main issues for aqueous cell systems. These problems could be solved by using a solid-state electrolyte. Furthermore, the optimal configurations and other characteristics, including temperature, humidity, and air/oxygen flow rate, may be investigated using battery modelling. The distance between the electrodes should be optimized and the channels for flowing air or oxygen should be introduced to the ZAB cell.

Other potential applications of LIG-metal oxide electrocatalysts

The utilization of ORR (Oxygen Reduction Reaction) is mostly associated with the conversion and storage of energy. The ORR is an important reaction in fuel cells because it transforms oxygen into water while also releasing electrical energy. There are many applications that our air cathode could be used in such as:

- Fuel Cells: polymer electrolyte membrane (PEM), direct methanol (DMFCs), alkaline fuel cells (AFCs), and phosphoric acid fuel cells (PAFCs).
- Metal-Air Batteries: aluminum-air batteries and lithium-air batteries.
- Water Electrolysis
- Carbon Capture: the reduction of oxygen to generate water in a confined environment using ORR may also be employed in carbon capture systems to stop the release of carbon dioxide into the atmosphere.

References

---

(1) Suntivich, J.; Gasteiger, H. A.; Yabuuchi, N.; Nakanishi, H.; Goodenough, J. B.; Shao-Horn, Y. Design Principles for Oxygen-Reduction Activity on Perovskite Oxide Catalysts for Fuel Cells and Metal–Air Batteries. *Nature Chemistry 2011 3:7* **2011**, *3* (7), 546–550. https://doi.org/10.1038/nchem.1069.

(2) Xia, W.; Mahmood, A.; Liang, Z.; Zou, R.; Guo, S. Earth-Abundant Nanomaterials for Oxygen Reduction. *Angewandte Chemie International Edition* **2016**, *55* (8), 2650–2676. https://doi.org/10.1002/ANIE.201504830.

(3) *U. S. Global Energy Outlook for 2012 - United States Congress, United States Senate, Committee on Energy and Natural Resources - Google Books*; CreateSpace Independent Publishing Platform, 2012.

(4) *Global Energy Review: CO2 Emissions in 2020 – Analysis - IEA*. https://www.iea.org/articles/global-energy-review-co2-emissions-in-2020 (accessed 2023-04-16).

(5) McLarnon, F. R.; Cairns, E. J. The Secondary Alkaline Zinc Electrode. *J Electrochem Soc* **1991**, *138* (2), 645–656. https://doi.org/10.1149/1.2085653/XML.

(6) Mohamad, A. A. Zn/Gelled 6 M KOH/O2 Zinc–Air Battery. *J Power Sources* **2006**, *159* (1), 752–757. https://doi.org/10.1016/J.JPOWSOUR.2005.10.110.

(7) Yadav, G. G.; Wei, X.; Meeus, M. Primary Zinc-Air Batteries. *Electrochemical Power Sources: Fundamentals, Systems, and Applications Metal-Air Batteries: Present and Perspectives* **2021**, 23–45. https://doi.org/10.1016/B978-0-444-64333-9.00003-5.

(8) He, W.; Guo, W.; Wu, H.; Lin, L.; Liu, Q.; Han, X.; Xie, Q.; Liu, P.; Zheng, H.; Wang, L.; Yu, X.; Peng, D.-L.; He, W.; Guo, W.; Wu, H.; Lin, L.; Liu, Q.; Han, X.; Xie, Q.; Liu, P.; Zheng, H.; Wang, L.; Peng, D.; Yu, X. Challenges and Recent Advances in High Capacity Li-Rich Cathode Materials for High Energy Density Lithium-Ion

Batteries. *Advanced Materials* **2021**, *33* (50), 2005937. https://doi.org/10.1002/ADMA.202005937.

(9) Li, M.; Lu, J.; Chen, Z.; Amine, K. 30 Years of Lithium-Ion Batteries. *Advanced Materials* **2018**, *30* (33), 1800561. https://doi.org/10.1002/ADMA.201800561.

(10) Akinyele, D. O.; Rayudu, R. K. Review of Energy Storage Technologies for Sustainable Power Networks. *Sustainable Energy Technologies and Assessments* **2014**, *8*, 74–91. https://doi.org/10.1016/J.SETA.2014.07.004.

(11) Guarnieri, M.; Mattavelli, P.; Petrone, G.; Spagnuolo, G. Vanadium Redox Flow Batteries: Potentials and Challenges of an Emerging Storage Technology. *IEEE Industrial Electronics Magazine* **2016**, *10* (4), 20–31. https://doi.org/10.1109/MIE.2016.2611760.

(12) Hannan, M. A.; Hoque, M. M.; Mohamed, A.; Ayob, A. Review of Energy Storage Systems for Electric Vehicle Applications: Issues and Challenges. *Renewable and Sustainable Energy Reviews* **2017**, *69*, 771–789. https://doi.org/10.1016/J.RSER.2016.11.171.

(13) Yuan, H.; Hou, Y.; Abu-Reesh, I. M.; Chen, J.; He, Z. Oxygen Reduction Reaction Catalysts Used in Microbial Fuel Cells for Energy-Efficient Wastewater Treatment: A Review. *Mater Horiz* **2016**, *3* (5), 382–401. https://doi.org/10.1039/C6MH00093B.

(14) Li, Y.; Li, Q.; Wang, H.; Zhang, L.; Wilkinson, D. P.; Zhang, J. Recent Progresses in Oxygen Reduction Reaction Electrocatalysts for Electrochemical Energy Applications. *Electrochemical Energy Reviews 2019 2:4* **2019**, *2* (4), 518–538. https://doi.org/10.1007/S41918-019-00052-4.

(15) Wu, J.; Yang, H. Platinum-Based Oxygen Reduction Electrocatalysts. *Acc Chem Res* **2013**, *46* (8), 1848–1857. https://doi.org/10.1021/AR300359W/ASSET/IMAGES/LARGE/AR-2012-00359W_0013.JPEG.

---

(16) Shao, M.; Chang, Q.; Dodelet, J. P.; Chenitz, R. Recent Advances in Electrocatalysts for Oxygen Reduction Reaction. *Chem Rev* **2016**, *116* (6), 3594–3657. https://doi.org/10.1021/ACS.CHEMREV.5B00462/ASSET/IMAGES/LARGE/CR-2015-00462U_0038.JPEG.

(17) Luo, J.; Tian, X.; Zeng, J.; Li, Y.; Song, H.; Liao, S. Limitations and Improvement Strategies for Early-Transition-Metal Nitrides as Competitive Catalysts toward the Oxygen Reduction Reaction. *ACS Catal* **2016**, *6* (9), 6165–6174. https://doi.org/10.1021/ACSCATAL.6B01618/ASSET/IMAGES/LARGE/CS-2016-01618F_0005.JPEG.

(18) Rezaei, B.; Taghipour Jahromi, A. R.; Ensafi, A. A. Porous Magnetic Iron- Manganese Oxide Nanocubes Derived from Metal Organic Framework Deposited on Reduced Graphene Oxide Nanoflake as a Bi-Functional Electrocatalyst for Hydrogen Evolution and Oxygen Reduction Reaction. *Electrochim Acta* **2018**, *283*, 1359–1365. https://doi.org/10.1016/J.ELECTACTA.2018.07.105.

(19) Oezaslan, M.; Heggen, M.; Strasser, P. Size-Dependent Morphology of Dealloyed Bimetallic Catalysts: Linking the Nano to the Macro Scale. *J Am Chem Soc* **2012**, *134* (1), 514–524. https://doi.org/10.1021/JA2088162/SUPPL_FILE/JA2088162_SI_002.PDF.

(20) Wang, C.; Chi, M.; Wang, G.; Van Der Vliet, D.; Li, D.; More, K.; Wang, H. H.; Schlueter, J. A.; Markovic, N. M.; Stamenkovic, V. R. Correlation Between Surface Chemistry and Electrocatalytic Properties of Monodisperse PtxNi1-x Nanoparticles. *Adv Funct Mater* **2011**, *21* (1), 147–152. https://doi.org/10.1002/ADFM.201001138.

(21) Stamenkovic, V. R.; Mun, B. S.; Arenz, M.; Mayrhofer, K. J. J.; Lucas, C. A.; Wang, G.; Ross, P. N.; Markovic, N. M. Trends in Electrocatalysis on Extended and Nanoscale Pt-Bimetallic Alloy Surfaces. *Nature Materials 2007 6:3* **2007**, *6* (3), 241–247. https://doi.org/10.1038/nmat1840.

---

(22) Stamenković, V.; Schmidt, T. J.; Ross, P. N.; Marković, N. M. Surface Composition Effects in Electrocatalysis: Kinetics of Oxygen Reduction on Well-Defined Pt3Ni and Pt3Co Alloy Surfaces. *Journal of Physical Chemistry B* **2002**, *106* (46), 11970–11979. https://doi.org/10.1021/JP021182H/ASSET/IMAGES/LARGE/JP021182HF1.JPEG.

(23) Stamenkovic, V.; Mun, B. S.; Mayrhofer, K. J. J.; Ross, P. N.; Markovic, N. M.; Rossmeisl, J.; Greeley, J.; Nørskov, J. K. Changing the Activity of Electrocatalysts for Oxygen Reduction by Tuning the Surface Electronic Structure. *Angewandte Chemie International Edition* **2006**, *45* (18), 2897–2901. https://doi.org/10.1002/ANIE.200504386.

(24) Żółtowski, P.; Dražić, D. M.; Vorkapić, L. Carbon-Air Electrode with Regenerative Short Time Overload Capacity: Part 1. Effect of Manganese Dioxide. *J Appl Electrochem* **1973**, *3* (4), 271–283. https://doi.org/10.1007/BF00613033/METRICS.

(25) Morita, M.; Iwakura, C.; Tamura, H. The Anodic Characteristics of Manganese Dioxide Electrodes Prepared by Thermal Decomposition of Manganese Nitrate. *Electrochim Acta* **1977**, *22* (4), 325–328. https://doi.org/10.1016/0013-4686(77)85081-0.

(26) *MineralPrices.com*. https://mineralprices.com/ (accessed 2023-04-16).

(27) Choi, K.; Lee, S.; Shim, Y.; Oh, J.; Kim, S.; Park, S. Electrocatalytic Performances of N-Doped Graphene with Anchored Iridium Species in Oxygen Reduction Reaction. *2d Mater* **2015**, *2* (3), 034019. https://doi.org/10.1088/2053-1583/2/3/034019.

(28) Zhao, Y.; Yang, L.; Chen, S.; Wang, X.; Ma, Y.; Wu, Q.; Jiang, Y.; Qian, W.; Hu, Z. Can Boron and Nitrogen Co-Doping Improve Oxygen Reduction Reaction Activity of Carbon Nanotubes? *J Am Chem Soc* **2013**, *135* (4), 1201–1204. https://doi.org/10.1021/JA310566Z/SUPPL_FILE/JA310566Z_SI_001.PDF.

(29) Wu, G.; Santandreu, A.; Kellogg, W.; Gupta, S.; Ogoke, O.; Zhang, H.; Wang, H. L.; Dai, L. Carbon Nanocomposite Catalysts for Oxygen Reduction and Evolution

Reactions: From Nitrogen Doping to Transition-Metal Addition. *Nano Energy* **2016**, *29*, 83–110. https://doi.org/10.1016/J.NANOEN.2015.12.032.

(30) Wu, J.; Pan, Z.; Zhang, Y.; Wang, B.; Peng, H. The Recent Progress of Nitrogen-Doped Carbon Nanomaterials for Electrochemical Batteries. *J Mater Chem A Mater* **2018**, *6* (27), 12932–12944. https://doi.org/10.1039/C8TA03968B.

(31) Wan, Z.; Sun, Y.; Tsang, D. C. W.; Khan, E.; Yip, A. C. K.; Ng, Y. H.; Rinklebe, J.; Ok, Y. S. Customised Fabrication of Nitrogen-Doped Biochar for Environmental and Energy Applications. *Chemical Engineering Journal* **2020**, *401*, 126136. https://doi.org/10.1016/J.CEJ.2020.126136.

(32) Job, R. Electrochemical Energy Storage. *Electrochemical Energy Storage* **2020**. https://doi.org/10.1515/9783110484427/HTML.

(33) Parker, J. F.; Chervin, C. N.; Pala, I. R.; Machler, M.; Burz, M. F.; Long, J. W.; Rolison, D. R. Rechargeable Nickel-3D Zinc Batteries: An Energy-Dense, Safer Alternative to Lithium-Ion. *Science (1979)* **2017**, *356* (6336), 415–418. https://doi.org/10.1126/SCIENCE.AAK9991/SUPPL_FILE/AAK9991_PARKER_SM.PDF.

(34) Sun, J.; Wang, N.; Qiu, Z.; Xing, L.; Du, L. Recent Progress of Non-Noble Metal Catalysts for Oxygen Electrode in Zn-Air Batteries: A Mini Review. *Catalysts 2022, Vol. 12, Page 843* **2022**, *12* (8), 843. https://doi.org/10.3390/CATAL12080843.

(35) Cromptom, T. P. J.; Crompton, T. R. *Battery Reference Book* , third.; Newnes, 2000.

(36) Ge, X.; Sumboja, A.; Wuu, D.; An, T.; Li, B.; Goh, F. W. T.; Hor, T. S. A.; Zong, Y.; Liu, Z. Oxygen Reduction in Alkaline Media: From Mechanisms to Recent Advances of Catalysts. *ACS Catal* **2015**, *5* (8), 4643–4667. https://doi.org/10.1021/ACSCATAL.5B00524/ASSET/IMAGES/LARGE/CS-2015-005246_0016.JPEG.

(37) Khotseng, L.; Khotseng, L. Oxygen Reduction Reaction. *Electrocatalysts for Fuel Cells and Hydrogen Evolution - Theory to Design* **2018**. https://doi.org/10.5772/INTECHOPEN.79098.

(38) Du, C.; Sun, Y.; Shen, T.; Yin, G.; Zhang, J. Applications of RDE and RRDE Methods in Oxygen Reduction Reaction. *Rotating Electrode Methods and Oxygen Reduction Electrocatalysts* **2014**, 231–277. https://doi.org/10.1016/B978-0-444-63278-4.00007-0.

(39) Schröder, D. Analysis of Reaction and Transport Processes in Zinc Air Batteries. *Analysis of Reaction and Transport Processes in Zinc Air Batteries* **2016**, 1–231. https://doi.org/10.1007/978-3-658-12291-1/COVER.

(40) Pei, P.; Wang, K.; Ma, Z. Technologies for Extending Zinc–Air Battery's Cyclelife: A Review. *Appl Energy* **2014**, *128*, 315–324. https://doi.org/10.1016/J.APENERGY.2014.04.095.

(41) Mokhatab, S. A Review of: "Energy in the 21st Century." *http://dx.doi.org/10.1080/15567240601027977* **2006**, *1* (4), 429–429. https://doi.org/10.1080/15567240601027977.

(42) Cano, Z. P.; Banham, D.; Ye, S.; Hintennach, A.; Lu, J.; Fowler, M.; Chen, Z. Batteries and Fuel Cells for Emerging Electric Vehicle Markets. *Nature Energy 2018 3:4* **2018**, *3* (4), 279–289. https://doi.org/10.1038/s41560-018-0108-1.

(43) Liu, D.; Tong, Y.; Yan, X.; Liang, J.; Dou, S. X. Recent Advances in Carbon-Based Bifunctional Oxygen Catalysts for Zinc-Air Batteries. *Batter Supercaps* **2019**, *2* (9), 743–765. https://doi.org/10.1002/BATT.201900052.

(44) Fu, J.; Cano, Z. P.; Park, M. G.; Yu, A.; Fowler, M.; Chen, Z. Electrically Rechargeable Zinc–Air Batteries: Progress, Challenges, and Perspectives. *Advanced Materials* **2017**, *29* (7), 1604685. https://doi.org/10.1002/ADMA.201604685.

(45) Zhang, J.; Zhou, Q.; Tang, Y.; Zhang, L.; Li, Y. Zinc–Air Batteries: Are They Ready for Prime Time? *Chem Sci* **2019**, *10* (39), 8924–8929. https://doi.org/10.1039/C9SC04221K.

(46) Zhao, Z.; Fan, X.; Ding, J.; Hu, W.; Zhong, C.; Lu, J. Challenges in Zinc Electrodes for Alkaline Zinc-Air Batteries: Obstacles to Commercialization. *ACS Energy Lett* **2019**, *4* (9), 2259–2270. https://doi.org/10.1021/ACSENERGYLETT.9B01541/ASSET/IMAGES/MEDIUM/NZ9B01541_0005.GIF.

(47) Einerhand, R. E. F.; Visscher, W. H. M.; Barendrecht, E. Hydrogen Production during Zinc Deposition from Alkaline Zincate Solutions. *J Appl Electrochem* **1988**, *18* (6), 799–806. https://doi.org/10.1007/BF01016034/METRICS.

(48) Parker, J. F.; Chervin, C. N.; Nelson, E. S.; Rolison, D. R.; Long, J. W. Wiring Zinc in Three Dimensions Re-Writes Battery Performance—Dendrite-Free Cycling. *Energy Environ Sci* **2014**, *7* (3), 1117–1124. https://doi.org/10.1039/C3EE43754J.

(49) Masri, M. N.; Mohamad, A. A. Effect of Adding Carbon Black to a Porous Zinc Anode in a Zinc-Air Battery. *J Electrochem Soc* **2013**, *160* (4), A715–A721. https://doi.org/10.1149/2.007306JES/XML.

(50) Aremu, E. O.; Park, D. J.; Ryu, K. S. The Effects of Anode Additives towards Suppressing Dendrite Growth and Hydrogen Gas Evolution Reaction in Zn-Air Secondary Batteries. *Ionics (Kiel)* **2019**, *25* (9), 4197–4207. https://doi.org/10.1007/S11581-019-02973-Y/TABLES/6.

(51) Xiao, Y.; Shi, J.; Zhao, F.; Zhang, Z.; He, W. Effects of Electrolyte Additives on the Properties of Zinc-Bismuth Electrodes in Zinc-Air Batteries. *J Electrochem Soc* **2018**, *165* (2), A47–A54. https://doi.org/10.1149/2.0251802JES/XML.

(52) Lee, S. M.; Kim, Y. J.; Eom, S. W.; Choi, N. S.; Kim, K. W.; Cho, S. B. Improvement in Self-Discharge of Zn Anode by Applying Surface Modification for Zn–Air Batteries with High Energy Density. *J Power Sources* **2013**, *227*, 177–184. https://doi.org/10.1016/J.JPOWSOUR.2012.11.046.

(53) McLarnon, F. R.; Cairns, E. J. The Secondary Alkaline Zinc Electrode. *J Electrochem Soc* **1991**, *138* (2), 645–656. https://doi.org/10.1149/1.2085653/XML.

---

(54) R. Mainar, A.; Leonet, O.; Bengoechea, M.; Boyano, I.; De Meatza, I.; Kvasha, A.; Guerfi, A.; Alberto Blázquez, J. Alkaline Aqueous Electrolytes for Secondary Zinc–Air Batteries: An Overview. *Int J Energy Res* **2016**, *40* (8), 1032–1049. https://doi.org/10.1002/ER.3499.

(55) Hosseini, S.; Masoudi Soltani, S.; Li, Y. Y. Current Status and Technical Challenges of Electrolytes in Zinc–Air Batteries: An in-Depth Review. *Chemical Engineering Journal* **2021**, *408*, 127241. https://doi.org/10.1016/J.CEJ.2020.127241.

(56) Hawes, G. F.; Rehman, S.; Rangom, Y.; Pope, M. A. Advanced Manufacturing Approaches for Electrochemical Energy Storage Devices. *International Materials Reviews* **2022**. https://doi.org/10.1080/09506608.2022.2086388.

(57) Yu, J.; Li, B.-Q.; Zhao, C.-X.; Liu, J.-N.; Zhang, Q.; Yu, J.; Li, B.; Zhao, C.; Liu, J.; Zhang, Q. Asymmetric Air Cathode Design for Enhanced Interfacial Electrocatalytic Reactions in High-Performance Zinc–Air Batteries. *Advanced Materials* **2020**, *32* (12), 1908488. https://doi.org/10.1002/ADMA.201908488.

(58) Wang, X.; Sebastian, P. J.; Smit, M. A.; Yang, H.; Gamboa, S. A. Studies on the Oxygen Reduction Catalyst for Zinc–Air Battery Electrode. *J Power Sources* **2003**, *124* (1), 278–284. https://doi.org/10.1016/S0378-7753(03)00737-7.

(59) Pei, P.; Wang, K.; Ma, Z. Technologies for Extending Zinc–Air Battery's Cyclelife: A Review. *Appl Energy* **2014**, *128*, 315–324. https://doi.org/10.1016/J.APENERGY.2014.04.095.

(60) Zhang, J.; Zhao, Z.; Xia, Z.; Dai, L. A Metal-Free Bifunctional Electrocatalyst for Oxygen Reduction and Oxygen Evolution Reactions. *Nature Nanotechnology 2015 10:5* **2015**, *10* (5), 444–452. https://doi.org/10.1038/nnano.2015.48.

(61) Ling, T.; Yan, D. Y.; Jiao, Y.; Wang, H.; Zheng, Y.; Zheng, X.; Mao, J.; Du, X. W.; Hu, Z.; Jaroniec, M.; Qiao, S. Z. Engineering Surface Atomic Structure of Single-Crystal Cobalt (II) Oxide Nanorods for Superior Electrocatalysis. *Nature Communications 2016 7:1* **2016**, *7* (1), 1–8. https://doi.org/10.1038/ncomms12876.

---

(62) Reier, T.; Oezaslan, M.; Strasser, P. Electrocatalytic Oxygen Evolution Reaction (OER) on Ru, Ir, and Pt Catalysts: A Comparative Study of Nanoparticles and Bulk Materials. *ACS Catal* **2012**, *2* (8), 1765–1772. https://doi.org/10.1021/CS3003098/ASSET/IMAGES/LARGE/CS-2012-003098_0008.JPEG.

(63) Suen, N. T.; Hung, S. F.; Quan, Q.; Zhang, N.; Xu, Y. J.; Chen, H. M. Electrocatalysis for the Oxygen Evolution Reaction: Recent Development and Future Perspectives. *Chem Soc Rev* **2017**, *46* (2), 337–365. https://doi.org/10.1039/C6CS00328A.

(64) Ahn, S. H.; Yu, X.; Manthiram, A. “Wiring” Fe-Nx-Embedded Porous Carbon Framework onto 1D Nanotubes for Efficient Oxygen Reduction Reaction in Alkaline and Acidic Media. *Advanced Materials* **2017**, *29* (26), 1606534. https://doi.org/10.1002/ADMA.201606534.

(65) Lao-atiman, W.; Bumroongsil, K.; Arpornwichanop, A.; Bumroongsakulsawat, P.; Olaru, S.; Kheawhom, S. Model-Based Analysis of an Integrated Zinc-Air Flow Battery/Zinc Electrolyzer System. *Front Energy Res* **2019**, *7* (FEB), 15. https://doi.org/10.3389/FENRG.2019.00015/BIBTEX.

(66) Sevim, M.; Francia, C.; Amici, J.; Vankova, S.; Şener, T.; Metin, Ö. Bimetallic MPt (M: Co, Cu, Ni) Alloy Nanoparticles Assembled on Reduced Graphene Oxide as High Performance Cathode Catalysts for Rechargable Lithium-Oxygen Batteries. *J Alloys Compd* **2016**, *683*, 231–240. https://doi.org/10.1016/J.JALLCOM.2016.05.094.

(67) Sevim, M.; Şener, T.; Metin, Ö. Monodisperse MPd (M: Co, Ni, Cu) Alloy Nanoparticles Supported on Reduced Graphene Oxide as Cathode Catalysts for the Lithium-Air Battery. *Int J Hydrogen Energy* **2015**, *40* (34), 10876–10882. https://doi.org/10.1016/J.IJHYDENE.2015.07.036.

(68) Li, Y.; Dai, H. Recent Advances in Zinc–Air Batteries. *Chem Soc Rev* **2014**, *43* (15), 5257–5275. https://doi.org/10.1039/C4CS00015C.

---

(69) Wang, Y. J.; Zhao, N.; Fang, B.; Li, H.; Bi, X. T.; Wang, H. Carbon-Supported Pt-Based Alloy Electrocatalysts for the Oxygen Reduction Reaction in Polymer Electrolyte Membrane Fuel Cells: Particle Size, Shape, and Composition Manipulation and Their Impact to Activity. *Chem Rev* **2015**, *115* (9), 3433–3467. https://doi.org/10.1021/CR500519C/ASSET/IMAGES/LARGE/CR-2014-00519C_0007.JPEG.

(70) He, C.; Desai, S.; Brown, G.; Bollepalli, S. PEM Fuel Cell Catalysts: Cost, Performance, and Durability. *Electrochemical Society Interface* **2005**, *14* (3), 41–44. https://doi.org/10.1149/2.F07053IF/XML.

(71) Yu, X.; Ye, S. Recent Advances in Activity and Durability Enhancement of Pt/C Catalytic Cathode in PEMFC: Part II: Degradation Mechanism and Durability Enhancement of Carbon Supported Platinum Catalyst. *J Power Sources* **2007**, *172* (1), 145–154. https://doi.org/10.1016/J.JPOWSOUR.2007.07.048.

(72) Huang, L.; Zaman, S.; Tian, X.; Wang, Z.; Fang, W.; Xia, B. Y. Advanced Platinum-Based Oxygen Reduction Electrocatalysts for Fuel Cells. *Acc Chem Res* **2021**, *54* (2), 311–322. https://doi.org/10.1021/ACS.ACCOUNTS.0C00488/ASSET/IMAGES/LARGE/AR0C00488_0006.JPEG.

(73) Huang, L.; Zaman, S.; Tian, X.; Wang, Z.; Fang, W.; Xia, B. Y. Advanced Platinum-Based Oxygen Reduction Electrocatalysts for Fuel Cells. *Acc Chem Res* **2021**, *54* (2), 311–322. https://doi.org/10.1021/ACS.ACCOUNTS.0C00488/ASSET/IMAGES/LARGE/AR0C00488_0006.JPEG.

(74) Ma, S. Y.; Li, H. H.; Hu, B. C.; Cheng, X.; Fu, Q. Q.; Yu, S. H. Synthesis of Low Pt-Based Quaternary PtPdRuTe Nanotubes with Optimized Incorporation of Pd for Enhanced Electrocatalytic Activity. *J Am Chem Soc* **2017**, *139* (16), 5890–5895.

https://doi.org/10.1021/JACS.7B01482/ASSET/IMAGES/LARGE/JA-2017-01482Y_0005.JPEG.

(75) Strasser, P.; Fan, Q.; Devenney, M.; Weinberg, W. H.; Liu, P.; Nørskov, J. K. High Throughput Experimental and Theoretical Predictive Screening of Materials - A Comparative Study of Search Strategies for New Fuel Cell Anode Catalysts. *Journal of Physical Chemistry B* **2003**, *107* (40), 11013–11021. https://doi.org/10.1021/JP030508Z/ASSET/IMAGES/LARGE/JP030508ZF00009.JPEG.

(76) Nørskov, J. K.; Bligaard, T.; Rossmeisl, J.; Christensen, C. H. Towards the Computational Design of Solid Catalysts. *Nature Chemistry 2009 1:1* **2009**, *1* (1), 37–46. https://doi.org/10.1038/nchem.121.

(77) Huang, Q.; Yang, H.; Tang, Y.; Lu, T.; Akins, D. L. Carbon-Supported Pt–Co Alloy Nanoparticles for Oxygen Reduction Reaction. *Electrochem commun* **2006**, *8* (8), 1220–1224. https://doi.org/10.1016/J.ELECOM.2006.05.027.

(78) Paffett, M. T.; Beery, J. G.; Gottesfeld, S. Oxygen Reduction at Pt0.65Cr0.35, Pt0.2Cr0.8 and Roughened Platinum. *J Electrochem Soc* **1988**, *135* (6), 1431–1436. https://doi.org/10.1149/1.2096016/XML.

(79) Mukerjee, S.; Srinivasan, S.; Soriaga, M. P.; Mcbreen, J. Effect of Preparation Conditions of Pt Alloys on Their Electronic, Structural, and Electrocatalytic Activities for Oxygen Reduction-XRD, XAS, and Electrochemical Studies. *J. Phys. Chem* **1995**, *99*, 4577–4589.

(80) Toda, T.; Igarashi, H.; Uchida, H.; Watanabe, M. Enhancement of the Electroreduction of Oxygen on Pt Alloys with Fe, Ni, and Co. *J Electrochem Soc* **1999**, *146* (10), 3750–3756. https://doi.org/10.1149/1.1392544/XML.

(81) Zhang, L.; Roling, L. T.; Wang, X.; Vara, M.; Chi, M.; Liu, J.; Choi, S. Il; Park, J.; Herron, J. A.; Xie, Z.; Mavrikakis, M.; Xia, Y. Platinum-Based Nanocages with Subnanometer-Thick Walls and Well-Defined, Controllable Facets. *Science (1979)*

2015, *349* (6246), 412–416. https://doi.org/10.1126/SCIENCE.AAB0801/SUPPL_FILE/ZHANG-SM.PDF.

(82) Zhong, H.; Wang, T.; Mo, Y.; Li, D.; Zheng, C.; Chen, Y. Three-Dimensional Stacked Graphite Sheets with Exposed Edge-Defects as Pt-Based Catalyst Support. *Electrochim Acta* **2022**, *404*, 139602. https://doi.org/10.1016/J.ELECTACTA.2021.139602.

(83) Qiao, Z.; Hwang, S.; Li, X.; Wang, C.; Samarakoon, W.; Karakalos, S.; Li, D.; Chen, M.; He, Y.; Wang, M.; Liu, Z.; Wang, G.; Zhou, H.; Feng, Z.; Su, D.; Spendelow, J. S.; Wu, G. 3D Porous Graphitic Nanocarbon for Enhancing the Performance and Durability of Pt Catalysts: A Balance between Graphitization and Hierarchical Porosity. *Energy Environ Sci* **2019**, *12* (9), 2830–2841. https://doi.org/10.1039/C9EE01899A.

(84) Sibul, R.; Kibena-Põldsepp, E.; Ratso, S.; Kook, M.; Sougrati, M. T.; Käärik, M.; Merisalu, M.; Aruväli, J.; Paiste, P.; Treshchalov, A.; Leis, J.; Kisand, V.; Sammelselg, V.; Holdcroft, S.; Jaouen, F.; Tammeveski, K. Iron- and Nitrogen-Doped Graphene-Based Catalysts for Fuel Cell Applications. *ChemElectroChem* **2020**, *7* (7), 1739–1747. https://doi.org/10.1002/CELC.202000011.

(85) Zeng, J.; Francia, C.; Dumitrescu, M. A.; Monteverde Videla, A. H. A.; Ijeri, V. S.; Specchia, S.; Spinelli, P. Electrochemical Performance of Pt-Based Catalysts Supported on Different Ordered Mesoporous Carbons (Pt/OMCs) for Oxygen Reduction Reaction. *Ind Eng Chem Res* **2012**, *51* (22), 7500–7509. https://doi.org/10.1021/IE2016619/ASSET/IMAGES/LARGE/IE-2011-016619_0010.JPEG.

(86) Landsman, D. A.; Hartford, W.; Luczak, F. J. Noble Metal-Chromium Alloy Catalysts and Electrochemical Cell. **1980**.

(87) Jalan, V. M.; Landsman, D. A.; Lee, J. M. Electrochemical Cell Electrodes Incorporating Noble Metal-Base Metal Alloy Catalysts. **1978**.

(88) Wang, C.; Chi, M.; Li, D.; Strmcnik, D.; Van Der Vliet, D.; Wang, G.; Komanicky, V.; Chang, K. C.; Paulikas, A. P.; Tripkovic, D.; Pearson, J.; More, K. L.; Markovic, N. M.; Stamenkovic, V. R. Design and Synthesis of Bimetallic Electrocatalyst with Multilayered Pt-Skin Surfaces. *J Am Chem Soc* **2011**, *133* (36), 14396–14403. https://doi.org/10.1021/JA2047655/SUPPL_FILE/JA2047655_SI_001.PDF.

(89) Jalan, V. M.; Landsman, D. A.; Hartford, W. Noble Metal-Refractory Metal Alloys as Catalysts and Method for Making. **1978**.

(90) Chen, S.; Gasteiger, H. A.; Hayakawa, K.; Tada, T.; Shao-Horn, Y. Platinum-Alloy Cathode Catalyst Degradation in Proton Exchange Membrane Fuel Cells: Nanometer-Scale Compositional and Morphological Changes. *J Electrochem Soc* **2010**, *157* (1), A82. https://doi.org/10.1149/1.3258275/XML.

(91) Gasteiger, H. A.; Kocha, S. S.; Sompalli, B.; Wagner, F. T. Activity Benchmarks and Requirements for Pt, Pt-Alloy, and Non-Pt Oxygen Reduction Catalysts for PEMFCs. *Appl Catal B* **2005**, *56* (1–2), 9–35. https://doi.org/10.1016/J.APCATB.2004.06.021.

(92) Shao, M.; Chang, Q.; Dodelet, J. P.; Chenitz, R. Recent Advances in Electrocatalysts for Oxygen Reduction Reaction. *Chem Rev* **2016**, *116* (6), 3594–3657. https://doi.org/10.1021/ACS.CHEMREV.5B00462/ASSET/IMAGES/LARGE/CR-2015-00462U_0038.JPEG.

(93) Stephens, I. E. L.; Bondarenko, A. S.; Grønbjerg, U.; Rossmeisl, J.; Chorkendorff, I. Understanding the Electrocatalysis of Oxygen Reduction on Platinum and Its Alloys. *Energy Environ Sci* **2012**, *5* (5), 6744–6762. https://doi.org/10.1039/C2EE03590A.

(94) Jia, Q.; Liang, W.; Bates, M. K.; Mani, P.; Lee, W.; Mukerjee, S. Activity Descriptor Identification for Oxygen Reduction on Platinum-Based Bimetallic Nanoparticles: In Situ Observation of the Linear Composition-Strain-Activity Relationship. *ACS Nano* **2015**, *9* (1), 387–400. https://doi.org/10.1021/NN506721F/SUPPL_FILE/NN506721F_SI_001.PDF.

(95) Stamenkovic, V. R.; Mun, B. S.; Arenz, M.; Mayrhofer, K. J. J.; Lucas, C. A.; Wang, G.; Ross, P. N.; Markovic, N. M. Trends in Electrocatalysis on Extended and Nanoscale Pt-Bimetallic Alloy Surfaces. *Nature Materials 2007 6:3* **2007**, *6* (3), 241–247. https://doi.org/10.1038/nmat1840.

(96) Hwang, S. J.; Kim, S. K.; Lee, J. G.; Lee, S. C.; Jang, J. H.; Kim, P.; Lim, T. H.; Sung, Y. E.; Yoo, S. J. Role of Electronic Perturbation in Stability and Activity of Pt-Based Alloy Nanocatalysts for Oxygen Reduction. *J Am Chem Soc* **2012**, *134* (48), 19508–19511. https://doi.org/10.1021/JA307951Y/SUPPL_FILE/JA307951Y_SI_001.PDF.

(97) Jeon, T. Y.; Yoo, S. J.; Cho, Y. H.; Lee, K. S.; Kang, S. H.; Sung, Y. E. Influence of Oxide on the Oxygen Reduction Reaction of Carbon-Supported Pt-Ni Alloy Nanoparticles. *Journal of Physical Chemistry C* **2009**, *113* (45), 19732–19739. https://doi.org/10.1021/JP9076273/SUPPL_FILE/JP9076273_SI_001.PDF.

(98) Coleman, E. J.; Chowdhury, M. H.; Co, A. C. Insights into the Oxygen Reduction Reaction Activity of Pt/C and PtCu/C Catalysts. *ACS Catal* **2015**, *5* (2), 1245–1253. https://doi.org/10.1021/CS501762G/ASSET/IMAGES/LARGE/CS-2014-01762G_0011.JPEG.

(99) Greeley, J.; Stephens, I. E. L.; Bondarenko, A. S.; Johansson, T. P.; Hansen, H. A.; Jaramillo, T. F.; Rossmeisl, J.; Chorkendorff, I.; Nørskov, J. K. Alloys of Platinum and Early Transition Metals as Oxygen Reduction Electrocatalysts. *Nature Chemistry 2009 1:7* **2009**, *1* (7), 552–556. https://doi.org/10.1038/nchem.367.

(100) Nørskov, J. K.; Rossmeisl, J.; Logadottir, A.; Lindqvist, L.; Kitchin, J. R.; Bligaard, T.; Jónsson, H. Origin of the Overpotential for Oxygen Reduction at a Fuel-Cell Cathode. *Journal of Physical Chemistry B* **2004**, *108* (46), 17886–17892. https://doi.org/10.1021/JP047349J/ASSET/IMAGES/LARGE/JP047349JF00008.JPEG.

(101) Nørskov, J. K.; Rossmeisl, J.; Logadottir, A.; Lindqvist, L.; Kitchin, J. R.; Bligaard, T.; Jónsson, H. Origin of the Overpotential for Oxygen Reduction at a Fuel-Cell Cathode.

Journal of Physical Chemistry B **2004**, *108* (46), 17886–17892. https://doi.org/10.1021/JP047349J/ASSET/IMAGES/LARGE/JP047349JF00008.JPEG.

(102) Rossmeisl, J.; Logadottir, A.; Nørskov, J. K. Electrolysis of Water on (Oxidized) Metal Surfaces. *Chem Phys* **2005**, *319* (1–3), 178–184. https://doi.org/10.1016/J.CHEMPHYS.2005.05.038.

(103) Koper, M. T. M. Thermodynamic Theory of Multi-Electron Transfer Reactions: Implications for Electrocatalysis. *Journal of Electroanalytical Chemistry* **2011**, *660* (2), 254–260. https://doi.org/10.1016/J.JELECHEM.2010.10.004.

(104) Kulkarni, A.; Siahrostami, S.; Patel, A.; Nørskov, J. K. Understanding Catalytic Activity Trends in the Oxygen Reduction Reaction. *Chem Rev* **2018**, *118* (5), 2302–2312. https://doi.org/10.1021/ACS.CHEMREV.7B00488/ASSET/IMAGES/LARGE/CR-2017-00488T_0008.JPEG.

(105) Wang, Y.; Wang, D.; Li, Y. A Fundamental Comprehension and Recent Progress in Advanced Pt-Based ORR Nanocatalysts. *SmartMat* **2021**, *2* (1), 56–75. https://doi.org/10.1002/SMM2.1023.

(106) Stephens, I. E. L.; Bondarenko, A. S.; Bech, L.; Chorkendorff, I. Oxygen Electroreduction Activity and X-Ray Photoelectron Spectroscopy of Platinum and Early Transition Metal Alloys. *ChemCatChem* **2012**, *4* (3), 341–349. https://doi.org/10.1002/CCTC.201100343.

(107) Stamenkovic, V. R.; Mun, B. S.; Arenz, M.; Mayrhofer, K. J. J.; Lucas, C. A.; Wang, G.; Ross, P. N.; Markovic, N. M. Trends in Electrocatalysis on Extended and Nanoscale Pt-Bimetallic Alloy Surfaces. *Nature Materials 2007 6:3* **2007**, *6* (3), 241–247. https://doi.org/10.1038/nmat1840.

(108) Li, M.; Lei, Y.; Sheng, N.; Ohtsuka, T. Preparation of Low-Platinum-Content Platinum–Nickel, Platinum–Cobalt Binary Alloy and Platinum–Nickel–Cobalt Ternary

Alloy Catalysts for Oxygen Reduction Reaction in Polymer Electrolyte Fuel Cells. *J Power Sources* **2015**, *294*, 420–429. https://doi.org/10.1016/J.JPOWSOUR.2015.06.084.

(109) Khorsand, S.; Raeissi, K.; Ashrafizadeh, F.; Arenas, M. A. Super-Hydrophobic Nickel–Cobalt Alloy Coating with Micro-Nano Flower-like Structure. *Chemical Engineering Journal* **2015**, *273*, 638–646. https://doi.org/10.1016/J.CEJ.2015.03.076.

(110) Zhang, W.; Li, F.; Shi, F.; Hu, H.; Liang, J.; Yang, H.; Ye, Y.; Mao, Z.; Shang, W.; Deng, T.; Ke, X.; Wu, J. Tensile-Strained Platinum-Cobalt Alloy Surface on Palladium Octahedra as a Highly Durable Oxygen Reduction Catalyst. *ACS Appl Mater Interfaces* **2023**, *15* (3), 3993–4000. https://doi.org/10.1021/ACSAMI.2C18600/ASSET/IMAGES/LARGE/AM2C18600_0005.JPEG.

(111) Mattei, J. G.; Grammatikopoulos, P.; Zhao, J.; Singh, V.; Vernieres, J.; Steinhauer, S.; Porkovich, A.; Danielson, E.; Nordlund, K.; Djurabekova, F.; Sowwan, M. Gas-Phase Synthesis of Trimetallic Nanoparticles. *Chemistry of Materials* **2019**, *31* (6), 2151–2163. https://doi.org/10.1021/ACS.CHEMMATER.9B00129/ASSET/IMAGES/LARGE/CM-2019-001292_0008.JPEG.

(112) Kashyap, A.; Singh, N. K.; Soni, M.; Soni, A. Deposition of Thin Films by Chemical Solution-Assisted Techniques. *Chemical Solution Synthesis for Materials Design and Thin Film Device Applications* **2021**, 79–117. https://doi.org/10.1016/B978-0-12-819718-9.00014-5.

(113) Carpenter, M. K.; Moylan, T. E.; Kukreja, R. S.; Atwan, M. H.; Tessema, M. M. Solvothermal Synthesis of Platinum Alloy Nanoparticles for Oxygen Reduction Electrocatalysis. *J Am Chem Soc* **2012**, *134* (20), 8535–8542. https://doi.org/10.1021/JA300756Y/SUPPL_FILE/JA300756Y_SI_001.PDF.

(114) Chen, Z.; Hao, C.; Yan, B.; Chen, Q.; Feng, H.; Mao, X.; Cen, J.; Tian, Z. Q.; Tsiakaras, P.; Shen, P. K. ZIF-Mg(OH)2 Dual Template Assisted Self-Confinement of Small PtCo NPs as Promising Oxygen Reduction Reaction in PEM Fuel Cell. *Adv Energy Mater* **2022**, *12* (32), 2201600. https://doi.org/10.1002/AENM.202201600.

(115) Bokov, D.; Turki Jalil, A.; Chupradit, S.; Suksatan, W.; Javed Ansari, M.; Shewael, I. H.; Valiev, G. H.; Kianfar, E. Nanomaterial by Sol-Gel Method: Synthesis and Application. *Advances in Materials Science and Engineering* **2021**, *2021*. https://doi.org/10.1155/2021/5102014.

(116) Homma, Y.; Liu, H.; Takagi, D.; Kobayashi, Y. Single-Walled Carbon Nanotube Growth with Non-Iron-Group “Catalysts” by Chemical Vapor Deposition. *Nano Res* **2009**, *2* (10), 793–799. https://doi.org/10.1007/S12274-009-9082-Z/METRICS.

(117) Xu, C.; Yang, J.; Liu, E.; Jia, Q.; Veith, G. M.; Nair, G.; DiPietro, S.; Sun, K.; Chen, J.; Pietrasz, P.; Lu, Z.; Jagner, M.; Gath, K. K.; Mukerjee, S.; Waldecker, J. R. Physical Vapor Deposition Process for Engineering Pt Based Oxygen Reduction Reaction Catalysts on NbOx Templated Carbon Support. *J Power Sources* **2020**, *451*, 227709. https://doi.org/10.1016/J.JPOWSOUR.2020.227709.

(118) Xia, Y.; Gilroy, K. D.; Peng, H. C.; Xia, X. Seed-Mediated Growth of Colloidal Metal Nanocrystals. *Angewandte Chemie International Edition* **2017**, *56* (1), 60–95. https://doi.org/10.1002/ANIE.201604731.

(119) Wang, D.; Xin, H. L.; Hovden, R.; Wang, H.; Yu, Y.; Muller, D. A.; Disalvo, F. J.; Abruña, H. D. Structurally Ordered Intermetallic Platinum–Cobalt Core–Shell Nanoparticles with Enhanced Activity and Stability as Oxygen Reduction Electrocatalysts. *Nature Materials 2012 12:1* **2012**, *12* (1), 81–87. https://doi.org/10.1038/nmat3458.

(120) Cai, Y.; Adzic, R. R. Platinum Monolayer Electrocatalysts for the Oxygen Reduction Reaction: Improvements Induced by Surface and Subsurface Modifications of Cores. *Advances in Physical Chemistry* **2011**, *2011*, 16. https://doi.org/10.1155/2011/530397.

(121) Peng, Z.; Yang, H. Designer Platinum Nanoparticles: Control of Shape, Composition in Alloy, Nanostructure and Electrocatalytic Property. *Nano Today* **2009**, *4* (2), 143–164. https://doi.org/10.1016/J.NANTOD.2008.10.010.

(122) Wang, X. X.; Hwang, S.; Pan, Y. T.; Chen, K.; He, Y.; Karakalos, S.; Zhang, H.; Spendelow, J. S.; Su, D.; Wu, G. Ordered Pt3Co Intermetallic Nanoparticles Derived from Metal-Organic Frameworks for Oxygen Reduction. *Nano Lett* **2018**, *18* (7), 4163–4171. https://doi.org/10.1021/ACS.NANOLETT.8B00978/ASSET/IMAGES/LARGE/NL-2018-00978G_0006.JPEG.

(123) Weber, P.; Weber, D. J.; Dosche, C.; Oezaslan, M. Highly Durable Pt-Based Core-Shell Catalysts with Metallic and Oxidized Co Species for Boosting the Oxygen Reduction Reaction. *ACS Catal* **2022**, *12* (11), 6394–6408. https://doi.org/10.1021/ACSCATAL.2C00514/ASSET/IMAGES/LARGE/CS2C00514_0009.JPEG.

(124) Hu, S.; Tian, M.; Ribeiro, E. L.; Duscher, G.; Mukherjee, D. Tandem Laser Ablation Synthesis in Solution-Galvanic Replacement Reaction (LASiS-GRR) for the Production of PtCo Nanoalloys as Oxygen Reduction Electrocatalysts. *J Power Sources* **2016**, *306*, 413–423. https://doi.org/10.1016/J.JPOWSOUR.2015.11.078.

(125) Kim, M.; Osone, S.; Kim, T.; Higashi, H.; Seto, T. Synthesis of Nanoparticles by Laser Ablation: A Review. *KONA Powder and Particle Journal* **2017**, *34* (34), 80–90. https://doi.org/10.14356/KONA.2017009.

(126) Matin, M. A.; Jang, J. H.; Kwon, Y. U. One-Pot Sonication-Assisted Polyol Synthesis of Trimetallic Core–Shell (Pd,Co)@Pt Nanoparticles for Enhanced Electrocatalysis. *Int J Hydrogen Energy* **2014**, *39* (8), 3710–3718. https://doi.org/10.1016/J.IJHYDENE.2013.12.137.

(127) He, M.; Jin, X.; Chen, F.; Chen, J.; Min, J.; Duan, H.; Kuang, X.; Li, J.; Wu, Z.; Li, J. Synergistic Effect of Mn3+ and Oxygen Vacancy on the Bifunctional Oxygen

Electrocatalytic Performance of MnOX/CNTs Composites. *J Alloys Compd* **2023**, *933*, 167728. https://doi.org/10.1016/J.JALLCOM.2022.167728.

(128) Gnana kumar, G.; Awan, Z.; Suk Nahm, K.; Stanley Xavier, J. Nanotubular MnO2/Graphene Oxide Composites for the Application of Open Air-Breathing Cathode Microbial Fuel Cells. *Biosens Bioelectron* **2014**, *53*, 528–534. https://doi.org/10.1016/J.BIOS.2013.10.012.

(129) Tompsett, D. A.; Parker, S. C.; Islam, M. S. Rutile (β-)MnO2 Surfaces and Vacancy Formation for High Electrochemical and Catalytic Performance. *J Am Chem Soc* **2014**, *136* (4), 1418–1426. https://doi.org/10.1021/JA4092962/SUPPL_FILE/JA4092962_SI_001.PDF.

(130) Roche, I.; Chaînet, E.; Chatenet, M.; Vondrák, J. Carbon-Supported Manganese Oxide Nanoparticles as Electrocatalysts for the Oxygen Reduction Reaction (ORR) in Alkaline Medium: Physical Characterizations and ORR Mechanism. *Journal of Physical Chemistry C* **2007**, *111* (3), 1434–1443. https://doi.org/10.1021/JP0647986/ASSET/IMAGES/MEDIUM/JP0647986E00031.GIF.

(131) Gorlin, Y.; Jaramillo, T. F. A Bifunctional Nonprecious Metal Catalyst for Oxygen Reduction and Water Oxidation. *J Am Chem Soc* **2010**, *132* (39), 13612–13614. https://doi.org/10.1021/JA104587V/SUPPL_FILE/JA104587V_SI_001.PDF.

(132) Liu, Y.; Zhitomirsky, I. Aqueous Electrostatic Dispersion and Heterocoagulation of Multiwalled Carbon Nanotubes and Manganese Dioxide for the Fabrication of Supercapacitor Electrodes and Devices. *RSC Adv* **2014**, *4* (85), 45481–45489. https://doi.org/10.1039/C4RA05879H.

(133) Electrochemical Performance of Carbon/MnO 2 Nanocomposites Prepared via Molecular Bridging as Supercapacitor Electrode Materials. https://doi.org/10.1149/2.0221505jes.

---

(134) Ramirez-Castro, C.; Crosnier, O.; Athouël, L.; Retoux, R.; Bélanger, D.; Brousse, T. Electrochemical Performance of Carbon/MnO 2 Nanocomposites Prepared via Molecular Bridging as Supercapacitor Electrode Materials . *J Electrochem Soc* **2015**, *162* (5), A5179–A5184. https://doi.org/10.1149/2.0221505JES/XML.

(135) Kong, F.; Longo, R. C.; Zhang, H.; Liang, C.; Zheng, Y.; Cho, K. Charge-Transfer Modified Embedded-Atom Method for Manganese Oxides: Nanostructuring Effects on MnO2 Nanorods. *Comput Mater Sci* **2016**, *121*, 191–203. https://doi.org/10.1016/J.COMMATSCI.2016.04.029.

(136) Wen, Q.; Wang, S.; Yan, J.; Cong, L.; Pan, Z.; Ren, Y.; Fan, Z. MnO2–Graphene Hybrid as an Alternative Cathodic Catalyst to Platinum in Microbial Fuel Cells. *J Power Sources* **2012**, *216*, 187–191. https://doi.org/10.1016/J.JPOWSOUR.2012.05.023.

(137) Ahmad, T.; Ramanujachary, K. V.; Lofland, S. E.; Ganguli, A. K. Nanorods of Manganese Oxalate : A Single Source Precursor to Different Manganese Oxide Nanoparticles (MnO, Mn 2 O 3 , Mn 3 O 4). *J Mater Chem* **2004**, *14* (23), 3406–3410. https://doi.org/10.1039/B409010A.

(138) Qiu, W.; Xiao, H.; Gao, H. Defect Engineering Tuning of MnO2 Nanorods Bifunctional Cathode for Flexible Asymmetric Supercapacitors and Microbial Fuel Cells. *J Power Sources* **2021**, *491*, 229583. https://doi.org/10.1016/J.JPOWSOUR.2021.229583.

(139) Yu, J.; Zeng, T.; Wang, H.; Zhang, H.; Sun, Y.; Chen, L.; Song, S.; Li, L.; Shi, H. Oxygen-Defective MnO2−x Rattle-Type Microspheres Mediated Singlet Oxygen Oxidation of Organics by Peroxymonosulfate Activation. *Chemical Engineering Journal* **2020**, *394*, 124458. https://doi.org/10.1016/J.CEJ.2020.124458.

(140) Zhao, C.; Yu, C.; Huang, H.; Han, X.; Liu, Z.; Qiu, J. Co Ion-Intercalation Amorphous and Ultrathin Microstructure for High-Rate Oxygen Evolution. *Energy Storage Mater* **2018**, *10*, 291–296. https://doi.org/10.1016/J.ENSM.2017.07.002.

(141) Mathur, A.; Halder, A. One-Step Synthesis of Bifunctional Iron-Doped Manganese Oxide Nanorods for Rechargeable Zinc–Air Batteries. *Catal Sci Technol* **2019**, *9* (5), 1245–1254. https://doi.org/10.1039/C8CY02498G.

(142) Li, G.; Jiang, M.; Liao, Q.; Ding, R.; Gao, Y.; Jiang, L.; Zhang, D.; Chen, S.; He, H. Directly Anchoring Ag Single Atoms on α-MnO2 Nanorods as Efficient Oxygen Reduction Catalysts for Mg-Air Fuel Cell. *J Alloys Compd* **2021**, *858*, 157672. https://doi.org/10.1016/J.JALLCOM.2020.157672.

(143) Zhao, Y.; Zhu, Z.; Wang, A.; Xiao, L.; Hou, L. Facile Synthesis of N, S Co-Doped Hierarchical Porous Carbon/MnO2 Composites for Supercapacitor Electrodes via Sodium Alginate Crosslinking. *J Alloys Compd* **2022**, *923*, 166333. https://doi.org/10.1016/J.JALLCOM.2022.166333.

(144) Julien, C.; Massot, M.; Rangan, S.; Lemal, M.; Guyomard, D. Study of Structural Defects in γ-MnO2 by Raman Spectroscopy. *Journal of Raman Spectroscopy* **2002**, *33* (4), 223–228. https://doi.org/10.1002/JRS.838.

(145) Roche, I.; Chaînet, E.; Chatenet, M.; Vondrák, J. Carbon-Supported Manganese Oxide Nanoparticles as Electrocatalysts for the Oxygen Reduction Reaction (ORR) in Alkaline Medium: Physical Characterizations and ORR Mechanism. *Journal of Physical Chemistry C* **2007**, *111* (3), 1434–1443. https://doi.org/10.1021/JP0647986/ASSET/IMAGES/MEDIUM/JP0647986E00031.GIF.

(146) Zurowski, A.; Łukaszewski, M.; Czerwiński, A. Electrosorption of Hydrogen into Palladium–Rhodium Alloys: Part 2. Pd-Rich Electrodes of Various Thickness. *Electrochim Acta* **2008**, *53* (27), 7812–7816. https://doi.org/10.1016/J.ELECTACTA.2008.05.052.

(147) Sun, W.; Hsu, A.; Chen, R. Carbon-Supported Tetragonal MnOOH Catalysts for Oxygen Reduction Reaction in Alkaline Media. *J Power Sources* **2011**, *196* (2), 627–635. https://doi.org/10.1016/J.JPOWSOUR.2010.07.082.

(148) Chen, Z.; Chen, Z.; Yu, A.; Ahmed, R.; Wang, H.; Li, H. Manganese Dioxide Nanotube and Nitrogen-Doped Carbon Nanotube Based Composite Bifunctional Catalyst for Rechargeable Zinc-Air Battery. *Electrochim Acta* **2012**, *69*, 295–300. https://doi.org/10.1016/J.ELECTACTA.2012.03.001.

(149) Cao, Y. L.; Yang, H. X.; Ai, X. P.; Xiao, L. F. The Mechanism of Oxygen Reduction on MnO2-Catalyzed Air Cathode in Alkaline Solution. *Journal of Electroanalytical Chemistry* **2003**, *557*, 127–134. https://doi.org/10.1016/S0022-0728(03)00355-3.

(150) Augustin, M.; Yezerska, O.; Fenske, D.; Bardenhagen, I.; Westphal, A.; Knipper, M.; Plaggenborg, T.; Kolny-Olesiak, J.; Parisi, J. Mechanistic Study on the Activity of Manganese Oxide Catalysts for Oxygen Reduction Reaction in an Aprotic Electrolyte. *Electrochim Acta* **2015**, *158*, 383–389. https://doi.org/10.1016/J.ELECTACTA.2015.01.163.

(151) Revathi, C.; Kumar, R. T. R. Electro Catalytic Properties of α, β, γ, ϵ - MnO2 and γ - MnOOH Nanoparticles: Role of Polymorphs on Enzyme Free H2O2 Sensing. *Electroanalysis* **2017**, *29* (5), 1481–1489. https://doi.org/10.1002/ELAN.201600608.

(152) Huang, Y.; Lin, Y.; Li, W. Controllable Syntheses of α- and δ-MnO2 as Cathode Catalysts for Zinc-Air Battery. *Electrochim Acta* **2013**, *99*, 161–165. https://doi.org/10.1016/J.ELECTACTA.2013.03.088.

(153) Worku, A. K.; Ayele, D. W.; Habtu, N. G.; Teshager, M. A.; Workineh, Z. G. Recent Progress in MnO2-Based Oxygen Electrocatalysts for Rechargeable Zinc-Air Batteries. *Materials Today Sustainability* **2021**, *13*, 100072. https://doi.org/10.1016/J.MTSUST.2021.100072.

(154) Shao, C.; Yin, K.; Liao, F.; Zhu, W.; Shi, H.; Shao, M. Rod-Shaped α-MnO2 Electrocatalysts with High Mn3+ Content for Oxygen Reduction Reaction and Zn-Air Battery. *J Alloys Compd* **2021**, *860*, 158427. https://doi.org/10.1016/J.JALLCOM.2020.158427.

---

(155) Li, W.; Wang, D.; Zhang, Y.; Tao, L.; Wang, T.; Zou, Y.; Wang, Y.; Chen, R.; Wang, S. Defect Engineering for Fuel-Cell Electrocatalysts. *Advanced Materials* **2020**, *32* (19), 1907879. https://doi.org/10.1002/ADMA.201907879.

(156) Wang, Y.; Zhang, Y. Z.; Gao, Y. Q.; Sheng, G.; ten Elshof, J. E. Defect Engineering of MnO2 Nanosheets by Substitutional Doping for Printable Solid-State Micro-Supercapacitors. *Nano Energy* **2020**, *68*, 104306. https://doi.org/10.1016/J.NANOEN.2019.104306.

(157) Zhai, T.; Xie, S.; Yu, M.; Fang, P.; Liang, C.; Lu, X.; Tong, Y. Oxygen Vacancies Enhancing Capacitive Properties of MnO2 Nanorods for Wearable Asymmetric Supercapacitors. *Nano Energy* **2014**, *8*, 255–263. https://doi.org/10.1016/J.NANOEN.2014.06.013.

(158) Liu, X.; He, Z.; Li, T.; Wang, X.; Zhao, C.; Liu, S.; Liu, Y.; Fan, Z.; He, H. Enhancing Oxygen Reduction Activity of α-MnO2 by Defect-Engineering and N Doping through Plasma Treatments. *J Mater Sci* **2023**, *58* (7), 3066–3077. https://doi.org/10.1007/S10853-023-08178-Z/FIGURES/6.

(159) Selvakumar, K.; Duraisamy, V.; Venkateshwaran, S.; Arumugam, N.; Almansour, A. I.; Wang, Y.; Xiaoteng Liu, T.; Murugesan Senthil Kumar, S. Development of α-MnO2 Nanowire with Ni- and (Ni, Co)-Cation Doping as an Efficient Bifunctional Oxygen Evolution and Oxygen Reduction Reaction Catalyst. *ChemElectroChem* **2022**, *9* (2), e202101303. https://doi.org/10.1002/CELC.202101303.

(160) Periyasamy, G.; Patil, I. M.; Kakade, B.; Veluswamy, P.; Archana, J.; Ikeda, H.; Annamalai, K. Reduced Graphene Oxide-Wrapped α-Mn2O3/α-MnO2 Nanowires for Electrocatalytic Oxygen Reduction in Alkaline Medium. *Journal of Materials Science: Materials in Electronics* **2022**, *33* (11), 8644–8654. https://doi.org/10.1007/S10854-021-06721-9/FIGURES/9.

(161) Cheng, F.; Su, Y.; Liang, J.; Tao, Z.; Chen, J. MnO2-Based Nanostructures as Catalysts for Electrochemical Oxygen Reduction in Alkaline Media. *Chemistry of*

Materials **2010**, *22* (3), 898–905. https://doi.org/10.1021/CM901698S/ASSET/IMAGES/LARGE/CM-2009-01698S_0010.JPEG.

(162) Cheng, F.; Shen, J.; Peng, B.; Pan, Y.; Tao, Z.; Chen, J. Rapid Room-Temperature Synthesis of Nanocrystalline Spinels as Oxygen Reduction and Evolution Electrocatalysts. *Nature Chemistry 2010 3:1* **2010**, *3* (1), 79–84. https://doi.org/10.1038/nchem.931.

(163) Zhao, Y.; Yang, L.; Chen, S.; Wang, X.; Ma, Y.; Wu, Q.; Jiang, Y.; Qian, W.; Hu, Z. Can Boron and Nitrogen Co-Doping Improve Oxygen Reduction Reaction Activity of Carbon Nanotubes? *J Am Chem Soc* **2013**, *135* (4), 1201–1204. https://doi.org/10.1021/JA310566Z/SUPPL_FILE/JA310566Z_SI_001.PDF.

(164) Guo, H. L.; Su, P.; Kang, X.; Ning, S. K. Synthesis and Characterization of Nitrogen-Doped Graphene Hydrogels by Hydrothermal Route with Urea as Reducing-Doping Agents. *J Mater Chem A Mater* **2013**, *1* (6), 2248–2255. https://doi.org/10.1039/C2TA00887D.

(165) Fan, X.; Zheng, W. T.; Kuo, J. L. Oxygen Reduction Reaction on Active Sites of Heteroatom-Doped Graphene. *RSC Adv* **2013**, *3* (16), 5498–5505. https://doi.org/10.1039/C3RA23016C.

(166) Xue, Y.; Liu, J.; Chen, H.; Wang, R.; Li, D.; Qu, J.; Dai, L. Nitrogen-Doped Graphene Foams as Metal-Free Counter Electrodes in High-Performance Dye-Sensitized Solar Cells. *Angewandte Chemie International Edition* **2012**, *51* (48), 12124–12127. https://doi.org/10.1002/ANIE.201207277.

(167) Zhao, Y.; Yang, L.; Chen, S.; Wang, X.; Ma, Y.; Wu, Q.; Jiang, Y.; Qian, W.; Hu, Z. Can Boron and Nitrogen Co-Doping Improve Oxygen Reduction Reaction Activity of Carbon Nanotubes? *J Am Chem Soc* **2013**, *135* (4), 1201–1204. https://doi.org/10.1021/JA310566Z/SUPPL_FILE/JA310566Z_SI_001.PDF.

(168) Wen, Z.; Wang, X.; Mao, S.; Bo, Z.; Kim, H.; Cui, S.; Lu, G.; Feng, X.; Chen, J. Crumpled Nitrogen-Doped Graphene Nanosheets with Ultrahigh Pore Volume for High-Performance Supercapacitor. *Advanced Materials* **2012**, *24* (41), 5610–5616. https://doi.org/10.1002/ADMA.201201920.

(169) Xue, Y.; Liu, J.; Chen, H.; Wang, R.; Li, D.; Qu, J.; Dai, L. Back Cover: Nitrogen-Doped Graphene Foams as Metal-Free Counter Electrodes in High-Performance Dye-Sensitized Solar Cells (Angew. Chem. Int. Ed. 48/2012). *Angewandte Chemie International Edition* **2012**, *51* (48), 12134–12134. https://doi.org/10.1002/ANIE.201208588.

(170) Fan, X.; Zheng, W. T.; Kuo, J. L. Oxygen Reduction Reaction on Active Sites of Heteroatom-Doped Graphene. *RSC Adv* **2013**, *3* (16), 5498–5505. https://doi.org/10.1039/C3RA23016C.

(171) Yu, D.; Zhang, Q.; Dai, L. Highly Efficient Metal-Free Growth of Nitrogen-Doped Single-Walled Carbon Nanotubes on Plasma-Etched Substrates for Oxygen Reduction. *J Am Chem Soc* **2010**, *132* (43), 15127–15129. https://doi.org/10.1021/JA105617Z/SUPPL_FILE/JA105617Z_SI_001.PDF.

(172) Yoo, E.; Nakamura, J.; Zhou, H. N-Doped Graphene Nanosheets for Li–Air Fuel Cells under Acidic Conditions. *Energy Environ Sci* **2012**, *5* (5), 6928–6932. https://doi.org/10.1039/C2EE02830A.

(173) Zhao, Y.; Yang, L.; Chen, S.; Wang, X.; Ma, Y.; Wu, Q.; Jiang, Y.; Qian, W.; Hu, Z. Can Boron and Nitrogen Co-Doping Improve Oxygen Reduction Reaction Activity of Carbon Nanotubes? *J Am Chem Soc* **2013**, *135* (4), 1201–1204. https://doi.org/10.1021/JA310566Z/SUPPL_FILE/JA310566Z_SI_001.PDF.

(174) Qu, L.; Liu, Y.; Baek, J. B.; Dai, L. Nitrogen-Doped Graphene as Efficient Metal-Free Electrocatalyst for Oxygen Reduction in Fuel Cells. *ACS Nano* **2010**, *4* (3), 1321–1326. https://doi.org/10.1021/NN901850U/SUPPL_FILE/NN901850U_SI_001.PDF.

(175) Tang, Y.; Allen, B. L.; Kauffman, D. R.; Star, A. Electrocatalytic Activity of Nitrogen-Doped Carbon Nanotube Cups. *J Am Chem Soc* **2009**, *131* (37), 13200–13201. https://doi.org/10.1021/JA904595T/SUPPL_FILE/JA904595T_SI_001.PDF.

(176) Gong, K.; Du, F.; Xia, Z.; Durstock, M.; Dai, L. Nitrogen-Doped Carbon Nanotube Arrays with High Electrocatalytic Activity for Oxygen Reduction. *Science (1979)* **2009**, *323* (5915), 760–764. https://doi.org/10.1126/SCIENCE.1168049/SUPPL_FILE/GONG.SOM.PDF.

(177) Zhang, L.; Xia, Z. Mechanisms of Oxygen Reduction Reaction on Nitrogen-Doped Graphene for Fuel Cells. *Journal of Physical Chemistry C* **2011**, *115* (22), 11170–11176. https://doi.org/10.1021/JP201991J/ASSET/IMAGES/LARGE/JP-2011-01991J_0005.JPEG.

(178) Latil, S.; Roche, S.; Mayou, D.; Charlier, J. C. Mesoscopic Transport in Chemically Doped Carbon Nanotubes. *Phys Rev Lett* **2004**, *92* (25 I), 256805. https://doi.org/10.1103/PHYSREVLETT.92.256805/FIGURES/4/MEDIUM.

(179) Jeon, I. Y.; Noh, H. J.; Baek, J. B. Nitrogen-Doped Carbon Nanomaterials: Synthesis, Characteristics and Applications. *Chem Asian J* **2020**, *15* (15), 2282–2293. https://doi.org/10.1002/ASIA.201901318.

(180) Ranjbar Sahraie, N.; Paraknowitsch, J. P.; Göbel, C.; Thomas, A.; Strasser, P. Noble-Metal-Free Electrocatalysts with Enhanced ORR Performance by Task-Specific Functionalization of Carbon Using Ionic Liquid Precursor Systems. *J Am Chem Soc* **2014**, *136* (41), 14486–14497. https://doi.org/10.1021/JA506553R/SUPPL_FILE/JA506553R_SI_001.PDF.

(181) Xia, Y.; Mokaya, R. Synthesis of Ordered Mesoporous Carbon and Nitrogen-Doped Carbon Materials with Graphitic Pore Walls via a Simple Chemical Vapor Deposition Method. *Advanced Materials* **2004**, *16* (17), 1553–1558. https://doi.org/10.1002/ADMA.200400391.

(182) Yang, Z.; Xia, Y.; Sun, X.; Mokaya, R. Preparation and Hydrogen Storage Properties of Zeolite-Templated Carbon Materials Nanocast via Chemical Vapor Deposition: Effect of the Zeolite Template and Nitrogen Doping. *Journal of Physical Chemistry B* **2006**, *110* (37), 18424–18431. https://doi.org/10.1021/JP0639849/SUPPL_FILE/JP0639849SI20060807_100613.PDF.

(183) Liu, H.; Liu, Y.; Zhu, D. Chemical Doping of Graphene. *J Mater Chem* **2011**, *21* (10), 3335–3345. https://doi.org/10.1039/C0JM02922J.

(184) Jiang, F.; Zhang, J.; Li, N.; Liu, C.; Zhou, Y.; Yu, X.; Sun, L.; Song, Y.; Zhang, S.; Wang, Z. Nitrogen-Doped Graphene Prepared by Thermal Annealing of Fluorinated Graphene Oxide as Supercapacitor Electrode. *Journal of Chemical Technology & Biotechnology* **2019**, *94* (11), 3530–3537. https://doi.org/10.1002/JCTB.6147.

(185) Sheng, Z. H.; Shao, L.; Chen, J. J.; Bao, W. J.; Wang, F. Bin; Xia, X. H. Catalyst-Free Synthesis of Nitrogen-Doped Graphene via Thermal Annealing Graphite Oxide with Melamine and Its Excellent Electrocatalysis. *ACS Nano* **2011**, *5* (6), 4350–4358. https://doi.org/10.1021/NN103584T/SUPPL_FILE/NN103584T_SI_001.PDF.

(186) Usachov, D.; Vilkov, O.; Grüneis, A.; Haberer, D.; Fedorov, A.; Adamchuk, V. K.; Preobrajenski, A. B.; Dudin, P.; Barinov, A.; Oehzelt, M.; Laubschat, C.; Vyalikh, D. V. Nitrogen-Doped Graphene: Efficient Growth, Structure, and Electronic Properties. *Nano Lett* **2011**, *11* (12), 5401–5407. https://doi.org/10.1021/NL2031037/ASSET/IMAGES/LARGE/NL-2011-031037_0005.JPEG.

(187) Cress, C. D.; Schmucker, S. W.; Friedman, A. L.; Dev, P.; Culbertson, J. C.; Lyding, J. W.; Robinson, J. T. Nitrogen-Doped Graphene and Twisted Bilayer Graphene via Hyperthermal Ion Implantation with Depth Control. *ACS Nano* **2016**, *10* (3), 3714–3722. https://doi.org/10.1021/ACSNANO.6B00252/ASSET/IMAGES/LARGE/NN-2016-00252E_0005.JPEG.

(188) Qiao, Y.; Kong, F.; Zhang, C.; Li, R.; Kong, A.; Shan, Y. Highly Efficient Oxygen Electrode Catalyst Derived from Chitosan Biomass by Molten Salt Pyrolysis for Zinc-Air Battery. *Electrochim Acta* **2020**, *339*, 135923. https://doi.org/10.1016/J.ELECTACTA.2020.135923.

(189) Geng, D.; Chen, Y.; Chen, Y.; Li, Y.; Li, R.; Sun, X.; Ye, S.; Knights, S. High Oxygen - Reduction Activity and Durability of Nitrogen -Doped Graphene. *Energy Environ Sci* **2011**, *4* (3), 760–764. https://doi.org/10.1039/C0EE00326C.

(190) Longhi, M.; Marzorati, S.; Checchia, S.; Sacchi, B.; Santo, N.; Zaffino, C.; Scavini, M. Sugar-Based Catalysts for Oxygen Reduction Reaction. Effects of the Functionalization of the Nitrogen Precursors on the Electrocatalytic Activity. *Electrochim Acta* **2016**, *222*, 781–792. https://doi.org/10.1016/J.ELECTACTA.2016.11.036.

(191) Gao, S.; Fan, H.; Zhang, S. Nitrogen-Enriched Carbon from Bamboo Fungus with Superior Oxygen Reduction Reaction Activity. *J Mater Chem A Mater* **2014**, *2* (43), 18263–18270. https://doi.org/10.1039/C4TA03558E.

(192) Borghei, M.; Lehtonen, J.; Liu, L.; Rojas, O. J.; Borghei, E. M.; Lehtonen, J.; Rojas, O. J.; Liu, L. Advanced Biomass-Derived Electrocatalysts for the Oxygen Reduction Reaction. *Advanced Materials* **2018**, *30* (24), 1703691. https://doi.org/10.1002/ADMA.201703691.

(193) Wu, Z.; Song, M.; Wang, J.; Liu, X. Recent Progress in Nitrogen-Doped Metal-Free Electrocatalysts for Oxygen Reduction Reaction. *Catalysts 2018, Vol. 8, Page 196* **2018**, *8* (5), 196. https://doi.org/10.3390/CATAL8050196.

(194) Wang, C.; Xie, N. H.; Zhang, Y.; Huang, Z.; Xia, K.; Wang, H.; Guo, S.; Xu, B. Q.; Zhang, Y. Silk-Derived Highly Active Oxygen Electrocatalysts for Flexible and Rechargeable Zn-Air Batteries. *Chemistry of Materials* **2019**, *31* (3), 1023–1029. https://doi.org/10.1021/ACS.CHEMMATER.8B04572/ASSET/IMAGES/LARGE/CM-2018-04572A_0004.JPEG.

(195) Pan, F.; Cao, Z.; Zhao, Q.; Liang, H.; Zhang, J. Nitrogen-Doped Porous Carbon Nanosheets Made from Biomass as Highly Active Electrocatalyst for Oxygen Reduction Reaction. *J Power Sources* **2014**, *272*, 8–15. https://doi.org/10.1016/J.JPOWSOUR.2014.07.180.

(196) Inagaki, M.; Toyoda, M.; Soneda, Y.; Morishita, T. Nitrogen-Doped Carbon Materials. *Carbon N Y* **2018**, *132*, 104–140. https://doi.org/10.1016/J.CARBON.2018.02.024.

(197) Khan, A.; Goepel, M.; Colmenares, J. C.; Gläser, R. Chitosan-Based N-Doped Carbon Materials for Electrocatalytic and Photocatalytic Applications. *ACS Sustain Chem Eng* **2020**, *8* (12), 4708–4727. https://doi.org/10.1021/ACSSUSCHEMENG.9B07522.

(198) Lai, L.; Potts, J. R.; Zhan, D.; Wang, L.; Poh, C. K.; Tang, C.; Gong, H.; Shen, Z.; Lin, J.; Ruoff, R. S. Exploration of the Active Center Structure of Nitrogen-Doped Graphene-Based Catalysts for Oxygen Reduction Reaction. *Energy Environ Sci* **2012**, *5* (7), 7936–7942. https://doi.org/10.1039/C2EE21802J.

(199) Yang, H. Bin; Miao, J.; Hung, S. F.; Chen, J.; Tao, H. B.; Wang, X.; Zhang, L.; Chen, R.; Gao, J.; Chen, H. M.; Dai, L.; Liu, B. Identification of Catalytic Sites for Oxygen Reduction and Oxygen Evolution in N-Doped Graphene Materials: Development of Highly Efficient Metal-Free Bifunctional Electrocatalyst. *Sci Adv* **2016**, *2* (4). https://doi.org/10.1126/sciadv.1501122.

(200) Lai, L.; Potts, J. R.; Zhan, D.; Wang, L.; Poh, C. K.; Tang, C.; Gong, H.; Shen, Z.; Lin, J.; Ruoff, R. S. Exploration of the Active Center Structure of Nitrogen-Doped Graphene-Based Catalysts for Oxygen Reduction Reaction. *Energy Environ Sci* **2012**, *5* (7), 7936–7942. https://doi.org/10.1039/C2EE21802J.

(201) Biddinger, E. J.; Ozkan, U. S. Role of Graphitic Edge Plane Exposure in Carbon Nanostructures for Oxygen Reduction Reaction. *Journal of Physical Chemistry C* **2010**, *114* (36), 15306–15314. https://doi.org/10.1021/JP104074T/ASSET/IMAGES/LARGE/JP-2010-04074T_0003.JPEG.

(202) Li, M.; Zhang, L.; Xu, Q.; Niu, J.; Xia, Z. N-Doped Graphene as Catalysts for Oxygen Reduction and Oxygen Evolution Reactions: Theoretical Considerations. *J Catal* **2014**, *314*, 66–72. https://doi.org/10.1016/J.JCAT.2014.03.011.

(203) Wei, D.; Liu, Y.; Wang, Y.; Zhang, H.; Huang, L.; Yu, G. Synthesis of N-Doped Graphene by Chemical Vapor Deposition and Its Electrical Properties. *Nano Lett* **2009**, *9* (5), 1752–1758. https://doi.org/10.1021/NL803279T/SUPPL_FILE/NL803279T_SI_001.PDF.

(204) Maddi, C.; Bourquard, F.; Barnier, V.; Avila, J.; Asensio, M. C.; Tite, T.; Donnet, C.; Garrelie, F. Nano-Architecture of Nitrogen-Doped Graphene Films Synthesized from a Solid CN Source. *Scientific Reports 2018 8:1* **2018**, *8* (1), 1–13. https://doi.org/10.1038/s41598-018-21639-9.

(205) Duan, X.; Ao, Z.; Sun, H.; Zhou, L.; Wang, G.; Wang, S. Insights into N-Doping in Single-Walled Carbon Nanotubes for Enhanced Activation of Superoxides: A Mechanistic Study. *Chemical Communications* **2015**, *51* (83), 15249–15252. https://doi.org/10.1039/C5CC05101K.

(206) Ren, W.; Nie, G.; Zhou, P.; Zhang, H.; Duan, X.; Wang, S. The Intrinsic Nature of Persulfate Activation and N-Doping in Carbocatalysis. *Environ Sci Technol* **2020**, *54* (10), 6438–6447. https://doi.org/10.1021/ACS.EST.0C01161/ASSET/IMAGES/LARGE/ES0C01161_0005.JPEG.

(207) Yutomo, E. B.; Noor, F. A.; Winata, T. Effect of the Number of Nitrogen Dopants on the Electronic and Magnetic Properties of Graphitic and Pyridinic N-Doped Graphene – a Density-Functional Study. *RSC Adv* **2021**, *11* (30), 18371. https://doi.org/10.1039/D1RA01095F.

(208) Jiang, L.; van Dijk, B.; Wu, L.; Maheu, C.; Hofmann, J. P.; Tudor, V.; Koper, M. T. M.; Hetterscheid, D. G. H.; Schneider, G. F. Predoped Oxygenated Defects Activate Nitrogen-Doped Graphene for the Oxygen Reduction Reaction. *ACS Catal* **2022**, *12*

(1), 173–182. https://doi.org/10.1021/ACSCATAL.1C03662/ASSET/IMAGES/LARGE/CS1C03662_0004.JPEG.

(209) Xiong, D.; Li, X.; Fan, L.; Bai, Z. Three-Dimensional Heteroatom-Doped Nanocarbon for Metal-Free Oxygen Reduction Electrocatalysis: A Review. *Catalysts 2018, Vol. 8, Page 301* **2018**, *8* (8), 301. https://doi.org/10.3390/CATAL8080301.

(210) Kim, H.; Lee, K.; Woo, S. I.; Jung, Y. On the Mechanism of Enhanced Oxygen Reduction Reaction in Nitrogen -Doped Graphene Nanoribbons. *Physical Chemistry Chemical Physics* **2011**, *13* (39), 17505–17510. https://doi.org/10.1039/C1CP21665A.

(211) Wu, J.; Ma, L.; Yadav, R. M.; Yang, Y.; Zhang, X.; Vajtai, R.; Lou, J.; Ajayan, P. M. Nitrogen-Doped Graphene with Pyridinic Dominance as a Highly Active and Stable Electrocatalyst for Oxygen Reduction. *ACS Appl Mater Interfaces* **2015**, *7* (27), 14763–14769. https://doi.org/10.1021/ACSAMI.5B02902/SUPPL_FILE/AM5B02902_SI_001.PDF.

(212) Zheng, Y.; Chen, S.; Yu, X.; Li, K.; Ni, X.; Ye, L. Nitrogen-Doped Carbon Spheres with Precisely-Constructed Pyridinic-N Active Sites for Efficient Oxygen Reduction. *Appl Surf Sci* **2022**, *598*, 153786. https://doi.org/10.1016/J.APSUSC.2022.153786.

(213) Luo, J.; Wang, K.; Hua, X.; Wang, W.; Li, J.; Zhang, S.; Chen, S.; Luo, J.; Wang, K.; Hua, X.; Wang, W.; Li, J.; Zhang, S.; Chen, S. Pyridinic-N Protected Synthesis of 3D Nitrogen-Doped Porous Carbon with Increased Mesoporous Defects for Oxygen Reduction. *Small* **2019**, *15* (11), 1805325. https://doi.org/10.1002/SMLL.201805325.

(214) Unni, S. M.; Devulapally, S.; Karjule, N.; Kurungot, S. Graphene Enriched with Pyrrolic Coordination of the Doped Nitrogen as an Efficient Metal-Free Electrocatalyst for Oxygen Reduction. *J Mater Chem* **2012**, *22* (44), 23506–23513. https://doi.org/10.1039/C2JM35547G.

(215) Lin, Z.; Waller, G. H.; Liu, Y.; Liu, M.; Wong, C. ping. 3D Nitrogen-Doped Graphene Prepared by Pyrolysis of Graphene Oxide with Polypyrrole for Electrocatalysis of

Oxygen Reduction Reaction. *Nano Energy* **2013**, *2* (2), 241–248. https://doi.org/10.1016/J.NANOEN.2012.09.002.

(216) Luo, Z.; Lim, S.; Tian, Z.; Shang, J.; Lai, L.; MacDonald, B.; Fu, C.; Shen, Z.; Yu, T.; Lin, J. Pyridinic N Doped Graphene : Synthesis, Electronic Structure, and Electrocatalytic Property. *J Mater Chem* **2011**, *21* (22), 8038–8044. https://doi.org/10.1039/C1JM10845J.

(217) Unni, S. M.; Devulapally, S.; Karjule, N.; Kurungot, S. Graphene Enriched with Pyrrolic Coordination of the Doped Nitrogen as an Efficient Metal-Free Electrocatalyst for Oxygen Reduction. *J Mater Chem* **2012**, *22* (44), 23506–23513. https://doi.org/10.1039/C2JM35547G.

(218) Carrillo-Rodríguez, J. C.; Garay-Tapia, A. M.; Escobar-Morales, B.; Escorcia-García, J.; Ochoa-Lara, M. T.; Rodríguez-Varela, F. J.; Alonso-Lemus, I. L. Insight into the Performance and Stability of N-Doped Ordered Mesoporous Carbon Hollow Spheres for the ORR: Influence of the Nitrogen Species on Their Catalytic Activity after ADT. *Int J Hydrogen Energy* **2021**, *46* (51), 26087–26100. https://doi.org/10.1016/J.IJHYDENE.2021.01.047.

(219) Liao, Y.; Gao, Y.; Zhu, S.; Zheng, J.; Chen, Z.; Yin, C.; Lou, X.; Zhang, D. Facile Fabrication of N-Doped Graphene as Efficient Electrocatalyst for Oxygen Reduction Reaction. *ACS Appl Mater Interfaces* **2015**, *7* (35), 19619–19625. https://doi.org/10.1021/ACSAMI.5B05649/SUPPL_FILE/AM5B05649_SI_001.PDF.

(220) Ratso, S.; Kruusenberg, I.; Joost, U.; Saar, R.; Tammeveski, K. Enhanced Oxygen Reduction Reaction Activity of Nitrogen-Doped Graphene/Multi-Walled Carbon Nanotube Catalysts in Alkaline Media. *Int J Hydrogen Energy* **2016**, *41* (47), 22510–22519. https://doi.org/10.1016/J.IJHYDENE.2016.02.021.

(221) Deng, H.; Li, Q.; Liu, J.; Wang, F. Active Sites for Oxygen Reduction Reaction on Nitrogen-Doped Carbon Nanotubes Derived from Polyaniline. *Carbon N Y* **2017**, *112*, 219–229. https://doi.org/10.1016/J.CARBON.2016.11.014.

---

(222) Quílez-Bermejo, J.; Melle-Franco, M.; San-Fabián, E.; Morallón, E.; Cazorla-Amorós, D. Towards Understanding the Active Sites for the ORR in N-Doped Carbon Materials through Fine-Tuning of Nitrogen Functionalities: An Experimental and Computational Approach. *J Mater Chem A Mater* **2019**, *7* (42), 24239–24250. https://doi.org/10.1039/C9TA07932G.

(223) Ikeda, T.; Boero, M.; Huang, S. F.; Terakura, K.; Oshima, M.; Ozaki, J. I. Carbon Alloy Catalysts: Active Sites for Oxygen Reduction Reaction. *Journal of Physical Chemistry C* **2008**, *112* (38), 14706–14709. https://doi.org/10.1021/JP806084D/ASSET/IMAGES/MEDIUM/JP-2008-06084D_0005.GIF.

(224) Lai, L.; Potts, J. R.; Zhan, D.; Wang, L.; Poh, C. K.; Tang, C.; Gong, H.; Shen, Z.; Lin, J.; Ruoff, R. S. Exploration of the Active Center Structure of Nitrogen-Doped Graphene-Based Catalysts for Oxygen Reduction Reaction. *Energy Environ Sci* **2012**, *5* (7), 7936–7942. https://doi.org/10.1039/C2EE21802J.

(225) Luo, Z.; Lim, S.; Tian, Z.; Shang, J.; Lai, L.; MacDonald, B.; Fu, C.; Shen, Z.; Yu, T.; Lin, J. Pyridinic N Doped Graphene : Synthesis, Electronic Structure, and Electrocatalytic Property. *J Mater Chem* **2011**, *21* (22), 8038–8044. https://doi.org/10.1039/C1JM10845J.

(226) Majeed, S.; Zhao, J.; Zhang, L.; Anjum, S.; Liu, Z.; Xu, G. Synthesis and Electrochemical Applications of Nitrogen-Doped Carbon Nanomaterials. *Nanotechnol Rev* **2013**, *2* (6), 615–635. https://doi.org/10.1515/NTREV-2013-0007/ASSET/GRAPHIC/NTREV-2013-0007_CV6.JPG.

(227) Yang, H. Bin; Miao, J.; Hung, S. F.; Chen, J.; Tao, H. B.; Wang, X.; Zhang, L.; Chen, R.; Gao, J.; Chen, H. M.; Dai, L.; Liu, B. Identification of Catalytic Sites for Oxygen Reduction and Oxygen Evolution in N-Doped Graphene Materials: Development of Highly Efficient Metal-Free Bifunctional Electrocatalyst. *Sci Adv* **2016**, *2* (4).

https://doi.org/10.1126/SCIADV.1501122/SUPPL_FILE/1501122_VIDEORES_S1_TO_S3.ZIP.

(228) Quílez-Bermejo, J.; Pérez-Rodríguez, S.; Canevesi, R.; Torres, D.; Morallón, E.; Cazorla-Amorós, D.; Celzard, A.; Fierro, V. Easy Enrichment of Graphitic Nitrogen to Prepare Highly Catalytic Carbons for Oxygen Reduction Reaction. *Carbon N Y* **2022**, *196*, 708–717. https://doi.org/10.1016/J.CARBON.2022.05.032.

(229) Lai, Q.; Zheng, H.; Tang, Z.; Bi, D.; Chen, N.; Liu, X.; Zheng, J.; Liang, Y. Balance of N-Doping Engineering and Carbon Chemistry to Expose Edge Graphitic N Sites for Enhanced Oxygen Reduction Electrocatalysis. *ACS Appl Mater Interfaces* **2021**, *13* (51), 61129–61138. https://doi.org/10.1021/ACSAMI.1C18451/ASSET/IMAGES/MEDIUM/AM1C18451_M006.GIF.

(230) Lai, L.; Potts, J. R.; Zhan, D.; Wang, L.; Poh, C. K.; Tang, C.; Gong, H.; Shen, Z.; Lin, J.; Ruoff, R. S. Exploration of the Active Center Structure of Nitrogen-Doped Graphene-Based Catalysts for Oxygen Reduction Reaction. *Energy Environ Sci* **2012**, *5* (7), 7936–7942. https://doi.org/10.1039/C2EE21802J.

(231) Quí Lez-Bermejo, J.; Moralló, E.; Cazorla-Amoró, D.; Li, R.; Chemcomm, /; Communication, C. Oxygen-Reduction Catalysis of N-Doped Carbons Prepared via Heat Treatment of Polyaniline at over 1100 °C. *Chemical Communications* **2018**, *54* (35), 4441–4444. https://doi.org/10.1039/C8CC02105H.

(232) Wang, X.; Liu, Y.; Zhu, D.; Zhang, L.; Ma, H.; Yao, N.; Zhang, B. Controllable Growth, Structure, and Low Field Emission of Well-Aligned CNx Nanotubes. *Journal of Physical Chemistry B* **2002**, *106* (9), 2186–2190. https://doi.org/10.1021/JP013007R/ASSET/IMAGES/LARGE/JP013007RF00006.JPEG.

---

(233) Casanovas, J.; Ricart, J. M.; Rubio, J.; Illas, F.; Miguel Jiménez-Mateos, J. Origin of the Large N 1s Binding Energy in X-Ray Photoelectron Spectra of Calcined Carbonaceous Materials. **1996**.

(234) Lai, L.; Potts, J. R.; Zhan, D.; Wang, L.; Poh, C. K.; Tang, C.; Gong, H.; Shen, Z.; Lin, J.; Ruoff, R. S. Exploration of the Active Center Structure of Nitrogen-Doped Graphene-Based Catalysts for Oxygen Reduction Reaction. *Energy Environ Sci* **2012**, *5* (7), 7936–7942. https://doi.org/10.1039/C2EE21802J.

(235) Liao, Y.; Gao, Y.; Zhu, S.; Zheng, J.; Chen, Z.; Yin, C.; Lou, X.; Zhang, D. Facile Fabrication of N-Doped Graphene as Efficient Electrocatalyst for Oxygen Reduction Reaction. *ACS Appl Mater Interfaces* **2015**, *7* (35), 19619–19625. https://doi.org/10.1021/ACSAMI.5B05649/ASSET/IMAGES/LARGE/AM-2015-05649C_0008.JPEG.

(236) Liu, X.; Li, L.; Zhou, W.; Zhou, Y.; Niu, W.; Chen, S. High-Performance Electrocatalysts for Oxygen Reduction Based on Nitrogen-Doped Porous Carbon from Hydrothermal Treatment of Glucose and Dicyandiamide. *ChemElectroChem* **2015**, *2* (6), 803–810. https://doi.org/10.1002/CELC.201500002.

(237) Ning, R.; Ge, C.; Liu, Q.; Tian, J.; Asiri, A. M.; Alamry, K. A.; Li, C. M.; Sun, X. Hierarchically Porous N-Doped Carbon Nanoflakes: Large-Scale Facile Synthesis and Application as an Oxygen Reduction Reaction Electrocatalyst with High Activity. *Carbon N Y* **2014**, *78*, 60–69. https://doi.org/10.1016/J.CARBON.2014.06.048.

(238) Massaglia, G.; Sacco, A.; Castellino, M.; Chiodoni, A.; Frascella, F.; Bianco, S.; Pirri, C. F.; Quaglio, M. N-Doping Modification by Plasma Treatment in Polyacrylonitrile Derived Carbon-Based Nanofibers for Oxygen Reduction Reaction. *Int J Hydrogen Energy* **2021**, *46* (26), 13845–13854. https://doi.org/10.1016/J.IJHYDENE.2020.09.149.

(239) Lin, Z.; Waller, G.; Liu, Y.; Liu, M.; Wong, C. P. Facile Synthesis of Nitrogen-Doped Graphene via Pyrolysis of Graphene Oxide and Urea, and Its Electrocatalytic Activity

toward the Oxygen-Reduction Reaction. *Adv Energy Mater* **2012**, *2* (7), 884–888. https://doi.org/10.1002/AENM.201200038.

(240) Peng, H.; Liu, F.; Liu, X.; Liao, S.; You, C.; Tian, X.; Nan, H.; Luo, F.; Song, H.; Fu, Z.; Huang, P. Effect of Transition Metals on the Structure and Performance of the Doped Carbon Catalysts Derived from Polyaniline and Melamine for ORR Application. *ACS Catal* **2014**, *4* (10), 3797–3805. https://doi.org/10.1021/CS500744X/SUPPL_FILE/CS500744X_SI_001.PDF.

(241) Weththasinha, H. A. B. M. D.; Yan, Z.; Gao, L.; Li, Y.; Pan, D.; Zhang, M.; Lv, X.; Wei, W.; Xie, J. Nitrogen Doped Lotus Stem Carbon as Electrocatalyst Comparable to Pt/C for Oxygen Reduction Reaction in Alkaline Media. *Int J Hydrogen Energy* **2017**, *42* (32), 20560–20567. https://doi.org/10.1016/J.IJHYDENE.2017.06.011.

(242) Li, Y.; Zhang, H.; Wang, Y.; Liu, P.; Yang, H.; Yao, X.; Wang, D.; Tang, Z.; Zhao, H. A Self-Sponsored Doping Approach for Controllable Synthesis of S and N Co-Doped Trimodal-Porous Structured Graphitic Carbon Electrocatalysts. *Energy Environ Sci* **2014**, *7* (11), 3720–3726. https://doi.org/10.1039/C4EE01779J.

(243) She, Y.; Lu, Z.; Ni, M.; Li, L.; Leung, M. K. H. Facile Synthesis of Nitrogen and Sulfur Codoped Carbon from Ionic Liquid as Metal-Free Catalyst for Oxygen Reduction Reaction. *ACS Appl Mater Interfaces* **2015**, *7* (13), 7214–7221. https://doi.org/10.1021/ACSAMI.5B00222/SUPPL_FILE/AM5B00222_SI_001.PDF.

(244) Chen, P.; Wang, L. K.; Wang, G.; Gao, M. R.; Ge, J.; Yuan, W. J.; Shen, Y. H.; Xie, A. J.; Yu, S. H. Nitrogen-Doped Nanoporous Carbon Nanosheets Derived from Plant Biomass: An Efficient Catalyst for Oxygen Reduction Reaction. *Energy Environ Sci* **2014**, *7* (12), 4095–4103. https://doi.org/10.1039/C4EE02531H.

(245) Zhou, H.; Zhang, J.; Zhu, J.; Liu, Z.; Zhang, C.; Mu, S. A Self-Template and KOH Activation Co-Coupling Strategy to Synthesize Ultrahigh Surface Area Nitrogen-Doped Porous Graphene for Oxygen Reduction. *RSC Adv* **2016**, *6* (77), 73292–73300. https://doi.org/10.1039/C6RA16703A.

(246) Pan, F.; Cao, Z.; Zhao, Q.; Liang, H.; Zhang, J. Nitrogen-Doped Porous Carbon Nanosheets Made from Biomass as Highly Active Electrocatalyst for Oxygen Reduction Reaction. *J Power Sources* **2014**, *272*, 8–15. https://doi.org/10.1016/J.JPOWSOUR.2014.07.180.

(247) Psarras, G. C. Nanographite-Polymer Composites. *Carbon Nanomaterials Sourcebook: Nanoparticles, Nanocapsules, Nanofibers, Nanoporous Structures, and Nanocomposites* **2016**, *2*, 647–673. https://doi.org/10.1201/b19568-35.

(248) Wang, Z.; Li, P.; Chen, Y.; Liu, J.; Tian, H.; Zhou, J.; Zhang, W.; Li, Y. Synthesis of Nitrogen-Doped Graphene by Chemical Vapour Deposition Using Melamine as the Sole Solid Source of Carbon and Nitrogen. *J Mater Chem C Mater* **2014**, *2* (35), 7396–7401. https://doi.org/10.1039/C4TC00924J.

(249) Skinner, C. G.; Thomas, J. D.; Osterloh, J. D. Melamine Toxicity. *Journal of Medical Toxicology* **2010**, *6* (1), 50–55. https://doi.org/10.1007/S13181-010-0038-1/TABLES/1.

(250) Li, M.; Xue, J. Integrated Synthesis of Nitrogen-Doped Mesoporous Carbon from Melamine Resins with Superior Performance in Supercapacitors. *Journal of Physical Chemistry C* **2014**, *118* (5), 2507–2517. https://doi.org/10.1021/JP410198R/SUPPL_FILE/JP410198R_SI_001.PDF.

(251) Yan, X. L.; Li, H. F.; Wang, C.; Jiang, B. B.; Hu, H. Y.; Xie, N.; Wu, M. H.; Vinodgopal, K.; Dai, G. P. Melamine as a Single Source for Fabrication of Mesoscopic 3D Composites of N-Doped Carbon Nanotubes on Graphene. *RSC Adv* **2018**, *8* (22), 12157. https://doi.org/10.1039/C8RA01577E.

(252) Shi, Y.; Liu, G.; Jin, R.; Xu, H.; Wang, Q.; Gao, S. Carbon Materials from Melamine Sponges for Supercapacitors and Lithium Battery Electrode Materials: A Review. *Carbon Energy* **2019**, *1* (2), 253–275. https://doi.org/10.1002/CEY2.19.

(253) Sheng, Z. H.; Shao, L.; Chen, J. J.; Bao, W. J.; Wang, F. Bin; Xia, X. H. Catalyst-Free Synthesis of Nitrogen-Doped Graphene via Thermal Annealing Graphite Oxide with

Melamine and Its Excellent Electrocatalysis. *ACS Nano* **2011**, *5* (6), 4350–4358. https://doi.org/10.1021/NN103584T/SUPPL_FILE/NN103584T_SI_001.PDF.

(254) Ma, Z.; Zhang, H.; Yang, Z.; Ji, G.; Yu, B.; Liu, X.; Liu, Z. Mesoporous Nitrogen-Doped Carbons with High Nitrogen Contents and Ultrahigh Surface Areas: Synthesis and Applications in Catalysis. *Green Chemistry* **2016**, *18* (7), 1976–1982. https://doi.org/10.1039/C5GC01920F.

(255) Zhang, J.; Chen, G.; Zhang, Q.; Kang, F.; You, B. Self-Assembly Synthesis of N-Doped Carbon Aerogels for Supercapacitor and Electrocatalytic Oxygen Reduction. *ACS Appl Mater Interfaces* **2015**, *7* (23), 12760–12766. https://doi.org/10.1021/ACSAMI.5B01660/SUPPL_FILE/AM5B01660_SI_001.PDF.

(256) Ilnicka, A.; Lukaszewicz, J. P.; Shimanoe, K.; Yuasa, M. Urea Treatment of Nitrogen-Doped Carbon Leads to Enhanced Performance for the Oxygen Reduction Reaction. *J Mater Res* **2018**, *33* (11), 1612–1624. https://doi.org/10.1557/JMR.2018.116/FIGURES/7.

(257) Wang, B.; Li, S.; Wu, X.; Liu, J.; Chen, J. Biomass Chitin-Derived Honeycomb-like Nitrogen-Doped Carbon/Graphene Nanosheet Networks for Applications in Efficient Oxygen Reduction and Robust Lithium Storage. *J Mater Chem A Mater* **2016**, *4* (30), 11789–11799. https://doi.org/10.1039/C6TA02858F.

(258) Kong, F.; Qiao, Y.; Zhang, C.; Fan, X.; Zhao, Q.; Kong, A.; Shan, Y. Oriented Synthesis of Pyridinic-N Dopant within the Highly Efficient Multifunction Carbon-Based Materials for Oxygen Transformation and Energy Storage. *ACS Sustain Chem Eng* **2020**, *8* (28), 10431–10443. https://doi.org/10.1021/ACSSUSCHEMENG.0C02301/ASSET/IMAGES/LARGE/SC0C02301_0007.JPEG.

(259) Rocha, I. M.; Soares, O. S. G. P.; Fernandes, D. M.; Freire, C.; Figueiredo, J. L.; Pereira, M. F. R. N-Doped Carbon Nanotubes for the Oxygen Reduction Reaction in Alkaline Medium: Synergistic Relationship between Pyridinic and Quaternary

Nitrogen. *ChemistrySelect* **2016**, *1* (10), 2522–2530. https://doi.org/10.1002/SLCT.201600615.

(260) Wu, T. X.; Wang, G. Z.; Zhang, X.; Chen, C.; Zhang, Y. X.; Zhao, H. J. Transforming Chitosan into N-Doped Graphitic Carbon Electrocatalysts. *Chemical Communications* **2014**, *51* (7), 1334–1337. https://doi.org/10.1039/C4CC09355K.

(261) Primo, A.; Atienzar, P.; Sanchez, E.; Delgado, J. M.; García, H. From Biomass Wastes to Large-Area, High-Quality, N-Doped Graphene : Catalyst -Free Carbonization of Chitosan Coatings on Arbitrary Substrates. *Chemical Communications* **2012**, *48* (74), 9254–9256. https://doi.org/10.1039/C2CC34978G.

(262) Hao, P.; Zhao, Z.; Leng, Y.; Tian, J.; Sang, Y.; Boughton, R. I.; Wong, C. P.; Liu, H.; Yang, B. Graphene-Based Nitrogen Self-Doped Hierarchical Porous Carbon Aerogels Derived from Chitosan for High Performance Supercapacitors. *Nano Energy* **2015**, *15*, 9–23. https://doi.org/10.1016/J.NANOEN.2015.02.035.

(263) Zhang, B.; Wang, C.; Liu, D.; Liu, Y.; Yu, X.; Wang, L. Boosting ORR Electrocatalytic Performance of Metal-Free Mesoporous Biomass Carbon by Synergism of Huge Specific Surface Area and Ultrahigh Pyridinic Nitrogen Doping. *ACS Sustain Chem Eng* **2018**, *6* (11), 13807–13812. https://doi.org/10.1021/ACSSUSCHEMENG.8B01876/ASSET/IMAGES/LARGE/SC-2018-01876J_0005.JPEG.

(264) Liu, Q.; Duan, Y.; Zhao, Q.; Pan, F.; Zhang, B.; Zhang, J. Direct Synthesis of Nitrogen-Doped Carbon Nanosheets with High Surface Area and Excellent Oxygen Reduction Performance. *Langmuir* **2014**, *30* (27), 8238–8245. https://doi.org/10.1021/LA404995Y/SUPPL_FILE/LA404995Y_SI_001.PDF.

(265) Guo, D.; Wei, H.; Chen, X.; Liu, M.; Ding, F.; Yang, Z.; Yang, Y.; Wang, S.; Yang, K.; Huang, S. 3D Hierarchical Nitrogen-Doped Carbon Nanoflower Derived from Chitosan for Efficient Electrocatalytic Oxygen Reduction and High Performance

Lithium–Sulfur Batteries. *J Mater Chem A Mater* **2017**, *5* (34), 18193–18206. https://doi.org/10.1039/C7TA04728B.

(266) Wittmar, A. S. M.; Ropertz, M.; Braun, M.; Hagemann, U.; Andronescu, C.; Ulbricht, M. Preparation of N-Doped Carbon Materials from Cellulose:Chitosan Blends and Their Potential Application in Electrocatalytic Oxygen Reduction. *Polymer Bulletin* **2022**, 1–19. https://doi.org/10.1007/S00289-022-04429-2/TABLES/3.

(267) Rybarczyk, M. K.; Lieder, M.; Jablonska, M. N-Doped Mesoporous Carbon Nanosheets Obtained by Pyrolysis of a Chitosan–Melamine Mixture for the Oxygen Reduction Reaction in Alkaline Media. *RSC Adv* **2015**, *5* (56), 44969–44977. https://doi.org/10.1039/C5RA05725F.

(268) Aghabarari, B.; Martínez-Huerta, M. V.; Ghiaci, M.; Fierro, J. L. G.; Peña, M. A. Hybrid Chitosan Derivative–Carbon Support for Oxygen Reduction Reactions. *RSC Adv* **2013**, *3* (16), 5378–5381. https://doi.org/10.1039/C3RA22416C.

(269) Pang, Y.; Cao, Y.; Chu, Y.; Liu, M.; Snyder, K.; MacKenzie, D.; Cao, C.; Pang, Y.; Cao, Y.; Chu, Y.; Cao, C.; Liu, M.; Snyder, K.; MacKenzie, D. Additive Manufacturing of Batteries. *Adv Funct Mater* **2020**, *30* (1), 1906244. https://doi.org/10.1002/ADFM.201906244.

(270) Ambaye, A. D.; Kefeni, K. K.; Mishra, S. B.; Nxumalo, E. N.; Ntsendwana, B. Recent Developments in Nanotechnology-Based Printing Electrode Systems for Electrochemical Sensors. *Talanta* **2021**, *225*, 121951. https://doi.org/10.1016/J.TALANTA.2020.121951.

(271) Deiner, L. J.; Reitz, T. L. Inkjet and Aerosol Jet Printing of Electrochemical Devices for Energy Conversion and Storage. *Adv Eng Mater* **2017**, *19* (7), 1600878. https://doi.org/10.1002/ADEM.201600878.

(272) Singh, M.; Haverinen, H. M.; Dhagat, P.; Jabbour, G. E. Inkjet Printing—Process and Its Applications. *Advanced Materials* **2010**, *22* (6), 673–685. https://doi.org/10.1002/ADMA.200901141.

---

(273) Costa Bassetto, V.; Xiao, J.; Oveisi, E.; Amstutz, V.; Liu, B.; Girault, H. H.; Lesch, A. Rapid Inkjet Printing of High Catalytic Activity Co3O4/N-RGO Layers for Oxygen Reduction Reaction. *Appl Catal A Gen* **2018**, *563*, 9–17. https://doi.org/10.1016/J.APCATA.2018.06.026.

(274) Deiner, L. J.; Reitz, T. L. Inkjet and Aerosol Jet Printing of Electrochemical Devices for Energy Conversion and Storage. *Adv Eng Mater* **2017**, *19* (7), 1600878. https://doi.org/10.1002/ADEM.201600878.

(275) Liu, G.; Ma, Z.; Li, G.; Yu, W.; Wang, P.; Meng, C.; Guo, S. All-Printed 3D Solid-State Rechargeable Zinc-Air Microbatteries. *ACS Appl Mater Interfaces* **2022**, *15*, 13073–13085. https://doi.org/10.1021/ACSAMI.2C22233/SUPPL_FILE/AM2C22233_SI_006.MP4.

(276) Ma, T.; Devin Mackenzie, J. Fully Printed, High Energy Density Flexible Zinc-Air Batteries Based on Solid Polymer Electrolytes and a Hierarchical Catalyst Current Collector. *Flexible and Printed Electronics* **2019**, *4* (1), 015010. https://doi.org/10.1088/2058-8585/AB0B91.

(277) Zhang, F.; Wei, M.; Viswanathan, V. V.; Swart, B.; Shao, Y.; Wu, G.; Zhou, C. 3D Printing Technologies for Electrochemical Energy Storage. *Nano Energy* **2017**, *40*, 418–431. https://doi.org/10.1016/J.NANOEN.2017.08.037.

(278) Lin, J.; Peng, Z.; Liu, Y.; Ruiz-Zepeda, F.; Ye, R.; Samuel, E. L. G.; Yacaman, M. J.; Yakobson, B. I.; Tour, J. M. Laser-Induced Porous Graphene Films from Commercial Polymers. *Nature Communications 2014 5:1* **2014**, *5* (1), 1–8. https://doi.org/10.1038/ncomms6714.

(279) Li, L.; Zhang, J.; Peng, Z.; Li, Y.; Gao, C.; Ji, Y.; Ye, R.; Kim, N. D.; Zhong, Q.; Yang, Y.; Fei, H.; Ruan, G.; Tour, J. M. High-Performance Pseudocapacitive Microsupercapacitors from Laser-Induced Graphene. *Adv Mater* **2015**, *28* (5), 838–845. https://doi.org/10.1002/ADMA.201503333.

---

(280) Li, Y.; Luong, D. X.; Zhang, J.; Tarkunde, Y. R.; Kittrell, C.; Sargunaraj, F.; Ji, Y.; Arnusch, C. J.; Tour, J. M. Laser-Induced Graphene in Controlled Atmospheres: From Superhydrophilic to Superhydrophobic Surfaces. *Advanced Materials* **2017**, *29* (27), 1700496. https://doi.org/10.1002/ADMA.201700496.

(281) Peng, Z.; Lin, J.; Ye, R.; Samuel, E. L. G.; Tour, J. M. Flexible and Stackable Laser-Induced Graphene Supercapacitors. *ACS Appl Mater Interfaces* **2015**, *7* (5), 3414–3419. https://doi.org/10.1021/AM509065D/SUPPL_FILE/AM509065D_SI_001.PDF.

(282) Alhajji, E.; Zhang, F.; Alshareef, H. N. Status and Prospects of Laser-Induced Graphene for Battery Applications. *Energy Technology* **2021**, *9* (10), 2100454. https://doi.org/10.1002/ENTE.202100454.

(283) Vivaldi, F. M.; Dallinger, A.; Bonini, A.; Poma, N.; Sembranti, L.; Biagini, D.; Salvo, P.; Greco, F.; Di Francesco, F. Three-Dimensional (3D) Laser-Induced Graphene: Structure, Properties, and Application to Chemical Sensing. *ACS Appl Mater Interfaces* **2021**, *13* (26), 30245–30260. https://doi.org/10.1021/ACSAMI.1C05614/ASSET/IMAGES/LARGE/AM1C05614_0010.JPEG.

(284) Yu, Y.; Joshi, P. C.; Wu, J.; Hu, A. Laser-Induced Carbon-Based Smart Flexible Sensor Array for Multiflavors Detection. *ACS Appl Mater Interfaces* **2018**, *10* (40), 34005–34012. https://doi.org/10.1021/ACSAMI.8B12626/ASSET/IMAGES/LARGE/AM-2018-12626H_0007.JPEG.

(285) Tao, L. Q.; Tian, H.; Liu, Y.; Ju, Z. Y.; Pang, Y.; Chen, Y. Q.; Wang, D. Y.; Tian, X. G.; Yan, J. C.; Deng, N. Q.; Yang, Y.; Ren, T. L. An Intelligent Artificial Throat with Sound-Sensing Ability Based on Laser Induced Graphene. *Nature Communications 2017 8:1* **2017**, *8* (1), 1–8. https://doi.org/10.1038/ncomms14579.

(286) Yan, W.; Yan, W.; Chen, T.; Xu, J.; Tian, Q.; Ho, D. Size-Tunable Flowerlike MoS2Nanospheres Combined with Laser-Induced Graphene Electrodes for

NO2Sensing. *ACS Appl Nano Mater* **2020**, *3* (3), 2545–2553. https://doi.org/10.1021/ACSANM.9B02614/ASSET/IMAGES/LARGE/AN9B02614_0009.JPEG.

(287) Ge, L.; Hong, Q.; Li, H.; Liu, C.; Li, F. Direct-Laser-Writing of Metal Sulfide-Graphene Nanocomposite Photoelectrode toward Sensitive Photoelectrochemical Sensing. *Adv Funct Mater* **2019**, *29* (38), 1904000. https://doi.org/10.1002/ADFM.201904000.

(288) Singh, S. P.; Ramanan, S.; Kaufman, Y.; Arnusch, C. J. Laser-Induced Graphene Biofilm Inhibition: Texture Does Matter. *ACS Appl Nano Mater* **2018**, *1* (4), 1713–1720. https://doi.org/10.1021/ACSANM.8B00175/ASSET/IMAGES/LARGE/AN-2018-001753_0006.JPEG.

(289) Singh, S. P.; Li, Y.; Be’Er, A.; Oren, Y.; Tour, J. M.; Arnusch, C. J. Laser-Induced Graphene Layers and Electrodes Prevents Microbial Fouling and Exerts Antimicrobial Action. *ACS Appl Mater Interfaces* **2017**, *9* (21), 18238–18247. https://doi.org/10.1021/ACSAMI.7B04863/SUPPL_FILE/AM7B04863_SI_002.MPG.

(290) Lamberti, A.; Serrapede, M.; Ferraro, G.; Fontana, M.; Perrucci, F.; Bianco, S.; Chiolerio, A.; Bocchini, S. All-SPEEK Flexible Supercapacitor Exploiting Laser-Induced Graphenization. *2d Mater* **2017**, *4* (3), 035012. https://doi.org/10.1088/2053-1583/AA790E.

(291) Singh, S. P.; Li, Y.; Zhang, J.; Tour, J. M.; Arnusch, C. J. Sulfur-Doped Laser-Induced Porous Graphene Derived from Polysulfone-Class Polymers and Membranes. *ACS Nano* **2018**, *12* (1), 289–297. https://doi.org/10.1021/ACSNANO.7B06263/ASSET/IMAGES/LARGE/NN-2017-06263H_0007.JPEG.

(292) Claro, P. I. C.; Marques, A. C.; Cunha, I.; Martins, R. F. P.; Pereira, L. M. N.; Marconcini, J. M.; Mattoso, L. H. C.; Fortunato, E. Tuning the Electrical Properties of Cellulose Nanocrystals through Laser-Induced Graphitization for UV Photodetectors.

ACS Appl Nano Mater **2021**, *4* (8), 8262–8272. https://doi.org/10.1021/ACSANM.1C01453/ASSET/IMAGES/MEDIUM/AN1C01453_M001.GIF.

(293) Tham, N. C. Y.; Sahoo, P. K.; Kim, Y.; Hegde, C.; Lee, S. W.; Kim, Y. J.; Murukeshan, V. M. Thermally Controlled Localized Porous Graphene for Integrated Graphene-Paper Electronics. *Adv Mater Technol* **2021**, *6* (5), 2001156. https://doi.org/10.1002/ADMT.202001156.

(294) Ataide, V. N.; Ameku, W. A.; Bacil, R. P.; Angnes, L.; De Araujo, W. R.; Paixão, T. R. L. C. Enhanced Performance of Pencil-Drawn Paper-Based Electrodes by Laser-Scribing Treatment. *RSC Adv* **2021**, *11* (3), 1644–1653. https://doi.org/10.1039/D0RA08874A.

(295) Vivaldi, F. M.; Dallinger, A.; Bonini, A.; Poma, N.; Sembranti, L.; Biagini, D.; Salvo, P.; Greco, F.; Di Francesco, F. Three-Dimensional (3D) Laser-Induced Graphene: Structure, Properties, and Application to Chemical Sensing. *ACS Appl Mater Interfaces* **2021**, *13* (26), 30245–30260. https://doi.org/10.1021/ACSAMI.1C05614/ASSET/IMAGES/LARGE/AM1C05614_0010.JPEG.

(296) Pranger, L.; Tannenbaum, R. Biobased Nanocomposites Prepared by in Situ Polymerization of Furfuryl Alcohol with Cellulose Whiskers or Montmorillonite Clay. *Macromolecules* **2008**, *41* (22), 8682–8687. https://doi.org/10.1021/MA8020213/SUPPL_FILE/MA8020213_SI_001.PDF.

(297) Ling, H. Y.; Su, Z.; Chen, H.; Hencz, L.; Zhang, M.; Tang, Y.; Zhang, S. Biomass-Derived Poly(Furfuryl Alcohol)–Protected Aluminum Anode for Lithium-Ion Batteries. *Energy Technology* **2019**, *7* (8), 1800995. https://doi.org/10.1002/ENTE.201800995.

---

(298) Kemp, K.; Griffiths, J.; Campbell, S.; Lovell, K. An Exploration of the Follow-up up Needs of Patients with Inflammatory Bowel Disease. *J Crohns Colitis* **2013**, *7* (9), e386–e395. https://doi.org/10.1016/J.CROHNS.2013.03.001/2/7-9-038.JPEG.

(299) Wang, F.; Mei, X.; Wang, K.; Dong, X.; Gao, M.; Zhai, Z.; Lv, J.; Zhu, C.; Duan, W.; Wang, W. Rapid and Low-Cost Laser Synthesis of Hierarchically Porous Graphene Materials as High-Performance Electrodes for Supercapacitors. *J Mater Sci* **2019**, *54* (7), 5658–5670. https://doi.org/10.1007/S10853-018-03247-0/FIGURES/6.

(300) Choura, M.; Belgacem, N. M.; Gandini, A. Acid-Catalyzed Polycondensation of Furfuryl Alcohol: Mechanisms of Chromophore Formation and Cross-Linking. *Macromolecules* **1996**, *29* (11), 3839–3850. https://doi.org/10.1021/MA951522F/ASSET/IMAGES/LARGE/MA951522FH00009.JPEG.

(301) Batista, P. S.; De Souza, M. F. Furfuryl Alcohol Conjugated Oligomer Pellicle Formation. *Polymer (Guildf)* **2000**, *41* (23), 8263–8269. https://doi.org/10.1016/S0032-3861(00)00178-6.

(302) Holbrook, B. P. M.; Rajagopalan, R.; Dronvajjala, K.; Choudhary, Y. K.; Foley, H. C. Molecular Sieving Carbon Catalysts for Liquid Phase Reactions: Study of Alkene Hydrogenation Using Platinum Embedded Nanoporous Carbon. *J Mol Catal A Chem* **2013**, *367*, 61–68. https://doi.org/10.1016/J.MOLCATA.2012.10.026.

(303) Rajagopalan, R.; Ponnaiyan, A.; Mankidy, P. J.; Brooks, A. W.; Yi, B.; Foley, H. C. Molecular Sieving Platinum Nanoparticle Catalysts Kinetically Frozen in Nanoporous Carbon. *Chemical Communications* **2004**, *0* (21), 2498–2499. https://doi.org/10.1039/B407854C.

(304) Lande, S.; Westin, M.; Schneider, M. Properties of Furfurylated Wood. *http://dx.doi.org/10.1080/0282758041001915* **2011**, *19*, 22–30. https://doi.org/10.1080/0282758041001915.

(305) Kyotani, T. Control of Pore Structure in Carbon. *Carbon N Y* **2000**, *38* (2), 269–286. https://doi.org/10.1016/S0008-6223(99)00142-6.

(306) Sakintuna, B.; Yürüm, Y. Templated Porous Carbons: A Review Article. *Ind Eng Chem Res* **2005**, *44* (9), 2893–2902. https://doi.org/10.1021/IE049080W/ASSET/IMAGES/LARGE/IE049080WF00006.JPEG.

(307) Lee, J.; Han, S.; Hyeon, T. Synthesis of New Nanoporous Carbon Materials Using Nanostructured Silica Materials as Templates. *J Mater Chem* **2004**, *14* (4), 478–486. https://doi.org/10.1039/B311541K.

(308) Hawes, G. F.; Yilman, D.; Noremberg, B. S.; Pope, M. A. Supercapacitors Fabricated via Laser-Induced Carbonization of Biomass-Derived Poly(Furfuryl Alcohol)/Graphene Oxide Composites. *ACS Appl Nano Mater* **2019**, *2* (10), 6312–6324. https://doi.org/10.1021/ACSANM.9B01284/ASSET/IMAGES/MEDIUM/AN9B01284_M003.GIF.

(309) Ren, M.; Zhang, J.; Tour, J. M. Laser-Induced Graphene Synthesis of Co3O4 in Graphene for Oxygen Electrocatalysis and Metal-Air Batteries. *Carbon N Y* **2018**, *139*, 880–887. https://doi.org/10.1016/J.CARBON.2018.07.051.

(310) Ren, M.; Zhang, J.; Tour, J. M. Laser-Induced Graphene Hybrid Catalysts for Rechargeable Zn-Air Batteries. *ACS Appl Energy Mater* **2019**, *2* (2), 1460–1468. https://doi.org/10.1021/ACSAEM.8B02011/SUPPL_FILE/AE8B02011_SI_003.AVI.

(311) Ren, M.; Zhang, J.; Tour, J. M. Laser-Induced Graphene Hybrid Catalysts for Rechargeable Zn-Air Batteries. *ACS Appl Energy Mater* **2019**, *2* (2), 1460–1468. https://doi.org/10.1021/ACSAEM.8B02011/SUPPL_FILE/AE8B02011_SI_003.AVI.

(312) Hui, X.; Xuan, X.; Kim, J.; Park, J. Y. A Highly Flexible and Selective Dopamine Sensor Based on Pt-Au Nanoparticle-Modified Laser-Induced Graphene. *Electrochim Acta* **2019**, *328*, 135066. https://doi.org/10.1016/J.ELECTACTA.2019.135066.

(313) Zhang, Y.; Zhu, H.; Sun, P.; Sun, C. K.; Huang, H.; Guan, S.; Liu, H.; Zhang, H.; Zhang, C.; Qin, K. R. Laser-Induced Graphene-Based Non-Enzymatic Sensor for Detection of Hydrogen Peroxide. *Electroanalysis* **2019**, *31* (7), 1334–1341. https://doi.org/10.1002/ELAN.201900043.

(314) Zhu, J.; Cho, M.; Li, Y.; Cho, I.; Suh, J. H.; Orbe, D. Del; Jeong, Y.; Ren, T. L.; Park, I. Biomimetic Turbinate-like Artificial Nose for Hydrogen Detection Based on 3D Porous Laser-Induced Graphene. *ACS Appl Mater Interfaces* **2019**, *11* (27), 24386–24394. https://doi.org/10.1021/ACSAMI.9B04495/ASSET/IMAGES/LARGE/AM-2019-04495A_0003.JPEG.

(315) Hui, X.; Xuan, X.; Kim, J.; Park, J. Y. A Highly Flexible and Selective Dopamine Sensor Based on Pt-Au Nanoparticle-Modified Laser-Induced Graphene. *Electrochim Acta* **2019**, *328*, 135066. https://doi.org/10.1016/J.ELECTACTA.2019.135066.

(316) Xu, R.; Wang, Z.; Gao, L.; Wang, S.; Zhao, J. Effective Design of MnO2 Nanoparticles Embedded in Laser-Induced Graphene as Shape-Controllable Electrodes for Flexible Planar Microsupercapacitors. *Appl Surf Sci* **2022**, *571*, 151385. https://doi.org/10.1016/J.APSUSC.2021.151385.

(317) Yuan, M.; Luo, F.; Rao, Y.; Yu, J.; Wang, Z.; Li, H.; Chen, X. SWCNT-Bridged Laser-Induced Graphene Fibers Decorated with MnO2 Nanoparticles for High-Performance Flexible Micro-Supercapacitors. *Carbon N Y* **2021**, *183*, 128–137. https://doi.org/10.1016/J.CARBON.2021.07.014.

(318) Sun, X.; Liu, X.; Xing, X.; Li, F. Electrodeposited with FeOOH and MnO2 on Laser-Induced Graphene for Multi-Assembly Supercapacitors. *J Alloys Compd* **2022**, *893*, 162230. https://doi.org/10.1016/J.JALLCOM.2021.162230.

(319) Liu, X.; Cheng, H.; Zhao, Y.; Wang, Y.; Li, F. Portable Electrochemical Biosensor Based on Laser-Induced Graphene and MnO2 Switch-Bridged DNA Signal Amplification for Sensitive Detection of Pesticide. *Biosens Bioelectron* **2022**, *199*, 113906. https://doi.org/10.1016/J.BIOS.2021.113906.

---

(320) Han, X.; Ye, R.; Chyan, Y.; Wang, T.; Zhang, C.; Shi, L.; Zhang, T.; Zhao, Y.; Tour, J. M. Laser-Induced Graphene from Wood Impregnated with Metal Salts and Use in Electrocatalysis. *ACS Appl Nano Mater* **2018**, *1* (9), 5053–5061. https://doi.org/10.1021/ACSANM.8B01163/ASSET/IMAGES/LARGE/AN-2018-01163P_0006.JPEG.

(321) Zhang, J.; Zhang, C.; Sha, J.; Fei, H.; Li, Y.; Tour, J. M. Efficient Water-Splitting Electrodes Based on Laser-Induced Graphene. *ACS Appl Mater Interfaces* **2017**, *9* (32), 26840–26847. https://doi.org/10.1021/ACSAMI.7B06727/SUPPL_FILE/AM7B06727_SI_003.MPG.

(322) Zou, J.; Dong, H.; Wu, H.; Huang, J.; Zeng, X.; Dou, Y.; Yao, Y.; Li, Z. Laser-Induced Rapid Construction of Co/N-Doped Honeycomb-like Carbon Networks as Oxygen Electrocatalyst Used in Zinc-Air Batteries. *Carbon N Y* **2022**, *200*, 462–471. https://doi.org/10.1016/J.CARBON.2022.08.078.

(323) Aldhafeeri, T. R.; Uceda, M.; Singh, A.; Valappil, M. O.; Fowler, M. W.; Pope, M. A. Embedded Platinum–Cobalt Nanoalloys in Biomass-Derived Laser-Induced Graphene as Stable, Air-Breathing Cathodes for Zinc–Air Batteries. *ACS Appl Nano Mater* **2023**. https://doi.org/10.1021/ACSANM.3C00564.

(324) Zhao, S.; Yang, Y.; Tang, Z. Insight into Structural Evolution, Active Sites, and Stability of Heterogeneous Electrocatalysts. *Angewandte Chemie International Edition* **2022**, *61* (11), e202110186. https://doi.org/10.1002/ANIE.202110186.

(325) Rismani-Yazdi, H.; Carver, S. M.; Christy, A. D.; Tuovinen, O. H. Cathodic Limitations in Microbial Fuel Cells: An Overview. *J Power Sources* **2008**, *180* (2), 683–694. https://doi.org/10.1016/J.JPOWSOUR.2008.02.074.

(326) Liu, M.; Zhao, Z.; Duan, X.; Huang, Y.; Liu, M.; Duan, X.; Zhao, Z.; Huang, Y. Nanoscale Structure Design for High-Performance Pt-Based ORR Catalysts. *Advanced Materials* **2019**, *31* (6), 1802234. https://doi.org/10.1002/ADMA.201802234.

---

(327) Zhu, X.; Huang, L.; Wei, M.; Tsiakaras, P.; Shen, P. K. Highly Stable Pt-Co Nanodendrite in Nanoframe with Pt Skin Structured Catalyst for Oxygen Reduction Electrocatalysis. *Appl Catal B* **2021**, *281*, 119460. https://doi.org/10.1016/J.APCATB.2020.119460.

(328) Toda, T.; Igarashi, H.; Watanabe, M. Role of Electronic Property of Pt and Pt Alloys on Electrocatalytic Reduction of Oxygen. *J Electrochem Soc* **1998**, *145* (12), 4185–4188. https://doi.org/10.1149/1.1838934/XML.

(329) Greeley, J.; Stephens, I. E. L.; Bondarenko, A. S.; Johansson, T. P.; Hansen, H. A.; Jaramillo, T. F.; Rossmeisl, J.; Chorkendorff, I.; Nørskov, J. K. Alloys of Platinum and Early Transition Metals as Oxygen Reduction Electrocatalysts. *Nature Chemistry 2009 1:7* **2009**, *1* (7), 552–556. https://doi.org/10.1038/nchem.367.

(330) Wang, D.; Xin, H. L.; Hovden, R.; Wang, H.; Yu, Y.; Muller, D. A.; Disalvo, F. J.; Abruña, H. D. Structurally Ordered Intermetallic Platinum–Cobalt Core–Shell Nanoparticles with Enhanced Activity and Stability as Oxygen Reduction Electrocatalysts. *Nature Materials 2012 12:1* **2012**, *12* (1), 81–87. https://doi.org/10.1038/nmat3458.

(331) Tian, X.; Zhao, X.; Su, Y. Q.; Wang, L.; Wang, H.; Dang, D.; Chi, B.; Liu, H.; Hensen, E. J. M.; Lou, X. W.; Xia, B. Y. Engineering Bunched Pt-Ni Alloy Nanocages for Efficient Oxygen Reduction in Practical Fuel Cells. *Science (1979)* **2019**, *366* (6467), 850–856. https://doi.org/10.1126/SCIENCE.AAW7493/SUPPL_FILE/AAW7493_TIAN_SM.PDF.

(332) Quílez-Bermejo, J.; Morallón, E.; Cazorla-Amorós, D. Metal-Free Heteroatom-Doped Carbon-Based Catalysts for ORR: A Critical Assessment about the Role of Heteroatoms. *Carbon N Y* **2020**, *165*, 434–454. https://doi.org/10.1016/J.CARBON.2020.04.068.

(333) Shao, M.; Chang, Q.; Dodelet, J. P.; Chenitz, R. Recent Advances in Electrocatalysts for Oxygen Reduction Reaction. *Chem Rev* **2016**, *116* (6), 3594–3657. https://doi.org/10.1021/ACS.CHEMREV.5B00462/ASSET/IMAGES/LARGE/CR-2015-00462U_0038.JPEG.

(334) Huang, K.; Zhang, L.; Xu, T.; Wei, H.; Zhang, R.; Zhang, X.; Ge, B.; Lei, M.; Ma, J. Y.; Liu, L. M.; Wu, H. −60 °C Solution Synthesis of Atomically Dispersed Cobalt Electrocatalyst with Superior Performance. *Nature Communications 2019 10:1* **2019**, *10* (1), 1–10. https://doi.org/10.1038/s41467-019-08484-8.

(335) Huang, K.; Wang, R.; Zhao, S.; Du, P.; Wang, H.; Wei, H.; Long, Y.; Deng, B.; Lei, M.; Ge, B.; Gou, H.; Zhang, R.; Wu, H. Atomic Species Derived CoOx Clusters on Nitrogen Doped Mesoporous Carbon as Advanced Bifunctional Electro-Catalysts for Zn-Air Battery. *Energy Storage Mater* **2020**, *29*, 156–162. https://doi.org/10.1016/J.ENSM.2020.03.026.

(336) Jung, W. S.; Lee, W. H.; Oh, H. S.; Popov, B. N. Highly Stable and Ordered Intermetallic PtCo Alloy Catalyst Supported on Graphitized Carbon Containing Co@CN for Oxygen Reduction Reaction. *J Mater Chem A Mater* **2020**, *8* (38), 19833–19842. https://doi.org/10.1039/D0TA05182A.

(337) Axnanda, S.; Cummins, K. D.; He, T.; Goodman, D. W.; Soriaga, M. P. Structural, Compositional and Electrochemical Characterization of Pt–Co Oxygen-Reduction Catalysts. *ChemPhysChem* **2010**, *11* (7), 1468–1475. https://doi.org/10.1002/CPHC.200900924.

(338) Vinayan, B. P.; Nagar, R.; Rajalakshmi, N.; Ramaprabhu, S. Novel Platinum–Cobalt Alloy Nanoparticles Dispersed on Nitrogen-Doped Graphene as a Cathode Electrocatalyst for PEMFC Applications. *Adv Funct Mater* **2012**, *22* (16), 3519–3526. https://doi.org/10.1002/ADFM.201102544.

(339) Paulus, U. A.; Wokaun, A.; Scherer, G. G.; Schmidt, T. J.; Stamenkovic, V.; Radmilovic, V.; Markovic, N. M.; Ross, P. N. Oxygen Reduction on Carbon-Supported

Pt-Ni and Pt-Co Alloy Catalysts. *Journal of Physical Chemistry B* **2002**, *106* (16), 4181–4191. https://doi.org/10.1021/JP013442L/ASSET/IMAGES/MEDIUM/JP013442LE00008.GIF.

(340) Huang, L.; Zaman, S.; Tian, X.; Wang, Z.; Fang, W.; Xia, B. Y. Advanced Platinum-Based Oxygen Reduction Electrocatalysts for Fuel Cells. *Cite This: Acc. Chem. Res* **2021**, *54*, 311–322. https://doi.org/10.1021/acs.accounts.0c00488.

(341) Salgado, J. R. C.; Antolini, E.; Gonzalez, E. R. Structure and Activity of Carbon-Supported Pt - Co Electrocatalysts for Oxygen Reduction. *Journal of Physical Chemistry B* **2004**, *108* (46), 17767–17774. https://doi.org/10.1021/JP0486649/ASSET/IMAGES/LARGE/JP0486649F00012.JPEG.

(342) Wu, K.; Zhang, L.; Yuan, Y.; Zhong, L.; Chen, Z.; Chi, X.; Lu, H.; Chen, Z.; Zou, R.; Li, T.; Jiang, C.; Chen, Y.; Peng, X.; Lu, J.; Wu, K.; Zhang, L.; Zhong, L.; Chi, X.; Lu, H.; Chen, Z.; Zou, R.; Li, T.; Jiang, C.; Chen, Y.; Peng, X. W.; Yuan, Y.; Lu, J. An Iron-Decorated Carbon Aerogel for Rechargeable Flow and Flexible Zn–Air Batteries. *Advanced Materials* **2020**, *32* (32), 2002292. https://doi.org/10.1002/ADMA.202002292.

(343) Uchida, M.; Aoyama, Y.; Eda, N.; Ohta, A. New Preparation Method for Polymer-Electrolyte Fuel Cells. *J Electrochem Soc* **1995**, *142* (2), 463–468. https://doi.org/10.1149/1.2044068/XML.

(344) Ahluwalia, R. K.; Papadias, D. D.; Kariuki, N. N.; Peng, J.-K.; Wang, X.; Tsai, Y.; Graczyk, D. G.; Myers, D. J. Potential Dependence of Pt and Co Dissolution from Platinum-Cobalt Alloy PEFC Catalysts Using Time-Resolved Measurements. *J Electrochem Soc* **2018**, *165* (6), F3024–F3035. https://doi.org/10.1149/2.0031806JES/XML.

(345) Zhan, G.; Fu, Z.; Sun, D.; Pan, Z.; Xiao, C.; Wu, S.; Chen, C.; Hu, G.; Wei, Z. Platinum Nanoparticles Decorated Robust Binary Transition Metal Nitride–Carbon Nanotubes Hybrid as an Efficient Electrocatalyst for the Methanol Oxidation Reaction. *J Power Sources* **2016**, *326*, 84–92. https://doi.org/10.1016/J.JPOWSOUR.2016.06.112.

(346) Shao-Horn, Y.; Sheng, W. C.; Chen, S.; Ferreira, P. J.; Holby, E. F.; Morgan, D. Instability of Supported Platinum Nanoparticles in Low-Temperature Fuel Cells. *Top Catal* **2007**, *46* (3–4), 285–305. https://doi.org/10.1007/S11244-007-9000-0/FIGURES/18.

(347) Wu, J.; Yuan, X. Z.; Martin, J. J.; Wang, H.; Zhang, J.; Shen, J.; Wu, S.; Merida, W. A Review of PEM Fuel Cell Durability: Degradation Mechanisms and Mitigation Strategies. *J Power Sources* **2008**, *184* (1), 104–119. https://doi.org/10.1016/J.JPOWSOUR.2008.06.006.

(348) Meng, H. Bin; Zhang, X. F.; Pu, Y. L.; Chen, X. L.; Feng, J. J.; Han, D. M.; Wang, A. J. One-Pot Solvothermal Synthesis of Reduced Graphene Oxide-Supported Uniform PtCo Nanocrystals for Efficient and Robust Electrocatalysis. *J Colloid Interface Sci* **2019**, *543*, 17–24. https://doi.org/10.1016/J.JCIS.2019.01.110.

(349) Terakawa, M. Laser-Induced Carbonization and Graphitization. *Handbook of Laser Micro- and Nano-Engineering* **2021**, 1–22. https://doi.org/10.1007/978-3-319-69537-2_65-1.

(350) Ye, R.; James, D. K.; Tour, J. M. Laser-Induced Graphene. *Acc Chem Res* **2018**, *51* (7), 1609–1620. https://doi.org/10.1021/ACS.ACCOUNTS.8B00084/ASSET/IMAGES/LARGE/AR-2018-00084A_0014.JPEG.

(351) Ye, R.; Peng, Z.; Wang, T.; Xu, Y.; Zhang, J.; Li, Y.; Nilewski, L. G.; Lin, J.; Tour, J. M. In Situ Formation of Metal Oxide Nanocrystals Embedded in Laser-Induced Graphene. *ACS Nano* **2015**, *9* (9), 9244–9251.

https://doi.org/10.1021/ACSNANO.5B04138/ASSET/IMAGES/LARGE/NN-2015-041389_0005.JPEG.

(352) Ren, M.; Zhang, J.; Tour, J. M. Laser-Induced Graphene Synthesis of Co3O4 in Graphene for Oxygen Electrocatalysis and Metal-Air Batteries. *Carbon N Y* **2018**, *139*, 880–887. https://doi.org/10.1016/J.CARBON.2018.07.051.

(353) Ye, R.; Peng, Z.; Wang, T.; Xu, Y.; Zhang, J.; Li, Y.; Nilewski, L. G.; Lin, J.; Tour, J. M. In Situ Formation of Metal Oxide Nanocrystals Embedded in Laser-Induced Graphene. *ACS Nano* **2015**, *9* (9), 9244–9251. https://doi.org/10.1021/acsnano.5b04138.

(354) Ren, M.; Zhang, J.; M. Tour, J. Laser-Induced Graphene Hybrid Catalysts for Rechargeable Zn-Air Batteries. *ACS Appl Energy Mater* **2019**, *2* (2), 1460–1468. https://doi.org/10.1021/acsaem.8b02011.

(355) Ren, M.; Zheng, H.; Lei, J.; Zhang, J.; Wang, X.; Yakobson, B. I.; Yao, Y.; Tour, J. M. CO2to Formic Acid Using Cu-Sn on Laser-Induced Graphene. *ACS Appl Mater Interfaces* **2020**, *12* (37), 41223–41229. https://doi.org/10.1021/ACSAMI.0C08964/ASSET/IMAGES/LARGE/AM0C08964_0007.JPEG.

(356) Zhang, J.; Zhang, C.; Sha, J.; Fei, H.; Li, Y.; Tour, J. M. Efficient Water-Splitting Electrodes Based on Laser-Induced Graphene. *ACS Appl Mater Interfaces* **2017**, *9* (32), 26840–26847. https://doi.org/10.1021/ACSAMI.7B06727/SUPPL_FILE/AM7B06727_SI_003.MPG.

(357) Du, P.; Huang, K.; Fan, X.; Ma, J.; Hussain, N.; Wang, R.; Deng, B.; Ge, B.; Tang, H.; Zhang, R.; Lei, M.; Wu, H. Wet-Milling Synthesis of Immobilized Pt/Ir Nanoclusters as Promising Heterogeneous Catalysts. *Nano Res* **2022**, *15* (4), 3065–3072. https://doi.org/10.1007/S12274-021-3963-1/METRICS.

(358) Zou, J.; Dong, H.; Wu, H.; Huang, J.; Zeng, X.; Dou, Y.; Yao, Y.; Li, Z. Laser-Induced Rapid Construction of Co/N-Doped Honeycomb-like Carbon Networks as Oxygen

Electrocatalyst Used in Zinc-Air Batteries. *Carbon N Y* **2022**, *200*, 462–471. https://doi.org/10.1016/J.CARBON.2022.08.078.

(359) Schmitt, C. R. Polyfurfuryl Alcohol Resins. *Polym Plast Technol Eng* **1974**, *3* (2), 121–158. https://doi.org/10.1080/03602557408545025.

(360) Peer, M.; Qajar, A.; Holbrook, B. P. M.; Rajagopalan, R.; Foley, H. C. Platinum Embedded within Carbon Nanospheres for Shape Selective Liquid Phase Hydrogenation. *Carbon N Y* **2013**, *57*, 485–497. https://doi.org/10.1016/J.CARBON.2013.02.024.

(361) Chen, H.; Liu, J.; Wu, X.; Ye, C.; Zhang, J.; Luo, J. L.; Fu, X. Z. Pt–Co Electrocatalysts: Syntheses, Morphologies, and Applications. *Small* **2022**, *18* (40), 2204100. https://doi.org/10.1002/SMLL.202204100.

(362) Yuan, R.; Bi, W.; Zhou, T.; Zhang, N.; Zhong, C.; Chu, W.; Yan, W.; Xu, Q.; Wu, C.; Xie, Y. Two-Dimensional Hierarchical Fe–N–C Electrocatalyst for Zn-Air Batteries with Ultrahigh Specific Capacity. *ACS Mater Lett* **2019**, *2* (1), 35–41. https://doi.org/10.1021/acsmaterialslett.9b00386.

(363) Choura, M.; Belgacem, N. M.; Gandini, A. Acid-Catalyzed Polycondensation of Furfuryl Alcohol: Mechanisms of Chromophore Formation and Cross-Linking. *Macromolecules* **1996**, *29* (11), 3839–3850. https://doi.org/10.1021/MA951522F/ASSET/IMAGES/LARGE/MA951522FH00009.JPEG.

(364) MacIntosh, K. L.; Beaumont, S. K. Nickel-Catalysed Vapour-Phase Hydrogenation of Furfural, Insights into Reactivity and Deactivation. *Top Catal* **2020**, *63* (15–18), 1446–1462. https://doi.org/10.1007/S11244-020-01341-9/FIGURES/17.

(365) Ong, H. K.; Sashikala, M.; Keng, O. H.; Pillai, S. M. Identification of Furfural Synthesized from Pentosan in Rice Husk (Pengenalpastian Furfural Yang Disintesis Daripada Pentosan Di Dalam Sekam Padi). *J. Trop. Agric. and Fd. Sc* **2007**, *35* (2), 305–312.

(366) Aswathy, B.; Suji, S.; Avadhani, G. S.; Aswathy, R.; Suganthi, S.; Sony, G. Microwave Assisted One Pot Synthesis of Biocompatible Gold Nanoparticles in Triton X-100 Aqueous Micellar Medium Using Tryptophan as Reducing Agent. *J Mol Liq* **2011**, *162* (3), 155–158. https://doi.org/10.1016/J.MOLLIQ.2011.06.019.

(367) Dehouche, F.; Archirel, P.; Remita, H.; Brodie-Linder, N.; Traverse, A. Alcohol to Water Catalyzed by Pt Nanoparticles: An Experimental and Computational Approach. *RSC Adv* **2012**, *2* (16), 6686–6694. https://doi.org/10.1039/C2RA20533E.

(368) Depoorter, A.; Kalalian, C.; Emmelin, C.; Lorentz, C.; George, C. Indoor Heterogeneous Photochemistry of Furfural Drives Emissions of Nitrous Acid. *Indoor Air* **2021**, *31* (3), 682–692. https://doi.org/10.1111/INA.12758.

(369) Backes, C.; Paton, K. R.; Hanlon, D.; Yuan, S.; Katsnelson, M. I.; Houston, J.; Smith, R. J.; McCloskey, D.; Donegan, J. F.; Coleman, J. N. Spectroscopic Metrics Allow in Situ Measurement of Mean Size and Thickness of Liquid-Exfoliated Few-Layer Graphene Nanosheets. *Nanoscale* **2016**, *8* (7), 4311–4323. https://doi.org/10.1039/C5NR08047A.

(370) Tian, N.; Zhou, Z. Y.; Sun, S. G.; Ding, Y.; Zhong, L. W. Synthesis of Tetrahexahedral Platinum Nanocrystals with High-Index Facets and High Electro-Oxidation Activity. *Science (1979)* **2007**, *316* (5825), 732–735. https://doi.org/10.1126/SCIENCE.1140484/SUPPL_FILE/TIAN_SOM.PDF.

(371) Creighton, J. A.; Eadon, D. G. Ultraviolet–Visible Absorption Spectra of the Colloidal Metallic Elements. *Journal of the Chemical Society, Faraday Transactions* **1991**, *87* (24), 3881–3891. https://doi.org/10.1039/FT9918703881.

(372) Yin, H.; Tang, H.; Wang, D.; Gao, Y.; Tang, Z. Facile Synthesis of Surfactant-Free Au Cluster/Graphene Hybrids for High-Performance Oxygen Reduction Reaction. *ACS Nano* **2012**, *6* (9), 8288–8297. https://doi.org/10.1021/NN302984X/SUPPL_FILE/NN302984X_SI_001.PDF.

(373) Liu, H.; Li, C.; Chen, D.; Cui, P.; Ye, F.; Yang, J. Uniformly Dispersed Platinum-Cobalt Alloy Nanoparticles with Stable Compositions on Carbon Substrates for Methanol Oxidation Reaction. *Scientific Reports 2017 7:1* **2017**, *7* (1), 1–8. https://doi.org/10.1038/s41598-017-10223-2.

(374) *Substituent effects on the volatility of metal β-diketonates - Fahlman - 2000 - Advanced Materials for Optics and Electronics - Wiley Online Library*. https://onlinelibrary.wiley.com/doi/abs/10.1002/1099-0712(200005/10)10:3/5%3C223::AID-AMO411%3E3.0.CO;2-M (accessed 2023-03-16).

(375) Park, A. H.; Shi, W.; Jung, J. U.; Kwon, Y. U. Mechanism Study of Single-Step Synthesis of Fe(Core)@Pt(Shell) Nanoparticles by Sonochemistry. *Ultrason Sonochem* **2021**, *77*, 105679. https://doi.org/10.1016/J.ULTSONCH.2021.105679.

(376) Deogratias, N.; Ji, M.; Zhang, Y.; Liu, J.; Zhang, J.; Zhu, H. Core@shell Sub-Ten-Nanometer Noble Metal Nanoparticles with a Controllable Thin Pt Shell and Their Catalytic Activity towards Oxygen Reduction. *Nano Res* **2015**, *8* (1), 271–280. https://doi.org/10.1007/S12274-014-0664-Z/METRICS.

(377) Lima, F. H. B.; Giz, M. J.; Ticianelli, E. A. Electrochemical Performance of Dispersed Pt-M (M =V, Cr and Co) Nanoparticles for the Oxygen Reduction Electrocatalysis. *J Mex Chem Soc* **2005**, *49* (2), 90–98.

(378) Jiang, S.; Ma, Y.; Jian, G.; Tao, H.; Wang, X.; Fan, Y.; Lu, Y.; Hu, Z.; Chen, Y. Facile Construction of Pt–Co/CNx Nanotube Electrocatalysts and Their Application to the Oxygen Reduction Reaction. *Advanced Materials* **2009**, *21* (48), 4953–4956. https://doi.org/10.1002/ADMA.200900677.

(379) Hirai, H.; Nakao, Y.; Toshima, N. Preparation of Colloidal Transition Metals in Polymers by Reduction with Alcohols or Ethers. **1979**. https://doi.org/10.1080/00222337908056685.

---

(380) Duff, D. G.; Edwards, P. P.; Johnson10, B. F. G. Formation of a Polymer-Protected Platinum Sol: A New Understanding of the Parameters Controlling Morphology. *J. Phys. Chem* **1995**, *99*, 15934–15944.

(381) Huang, K.; Xu, P.; He, X.; Wang, R.; Wang, Y.; Yang, H.; Zhang, R.; Lei, M.; Tang, H. Annealing-Free Platinum−Cobalt Alloy Nanoparticles on Nitrogen-Doped Mesoporous Carbon with Boosted Oxygen Electroreduction Performance. *ChemElectroChem* **2020**, *7* (15), 3341–3346. https://doi.org/10.1002/CELC.202000830.

(382) Sun, Y.; Zhang, X.; Luo, M.; Chen, X.; Wang, L.; Li, Y.; Li, M.; Qin, Y.; Li, C.; Xu, N.; Lu, G.; Gao, P.; Guo, S.; Catalysis Sun, O. Y.; Luo, M.; Li, Y.; Qin, Y.; Li, C.; Xu, N.; Guo, S.; Sun, Y.; Wang, L.; Zhang, X.; Lu, G.; Chen, X.; Li, M. Q.; Gao, P. Ultrathin PtPd-Based Nanorings with Abundant Step Atoms Enhance Oxygen Catalysis. *Advanced Materials* **2018**, *30* (38), 1802136. https://doi.org/10.1002/ADMA.201802136.

(383) Ma, X.; Meng, H.; Cai, M.; Shen, P. K. Bimetallic Carbide Nanocomposite Enhanced Pt Catalyst with High Activity and Stability for the Oxygen Reduction Reaction. *J Am Chem Soc* **2012**, *134* (4), 1954–1957. https://doi.org/10.1021/JA2093053/SUPPL_FILE/JA2093053_SI_001.PDF.

(384) Cheon, J. Y.; Kim, T.; Choi, Y.; Jeong, H. Y.; Kim, M. G.; Sa, Y. J.; Kim, J.; Lee, Z.; Yang, T. H.; Kwon, K.; Terasaki, O.; Park, G. G.; Adzic, R. R.; Joo, S. H. Ordered Mesoporous Porphyrinic Carbons with Very High Electrocatalytic Activity for the Oxygen Reduction Reaction. *Scientific Reports 2013 3:1* **2013**, *3* (1), 1–8. https://doi.org/10.1038/srep02715.

(385) Dai, S.; Chou, J. P.; Wang, K. W.; Hsu, Y. Y.; Hu, A.; Pan, X.; Chen, T. Y. Platinum-Trimer Decorated Cobalt-Palladium Core-Shell Nanocatalyst with Promising Performance for Oxygen Reduction Reaction. *Nature Communications 2019 10:1* **2019**, *10* (1), 1–10. https://doi.org/10.1038/s41467-019-08323-w.

---

(386) Vashisth, A.; Kowalik, M.; Gerringer, J. C.; Ashraf, C.; Van Duin, A. C. T.; Green, M. J. ReaxFF Simulations of Laser-Induced Graphene (LIG) Formation for Multifunctional Polymer Nanocomposites. *ACS Appl Nano Mater* **2020**, *3* (2), 1881–1890. https://doi.org/10.1021/ACSANM.9B02524/SUPPL_FILE/AN9B02524_SI_002.MPG.

(387) Wang, H.; Abruña, H. D. Comparative Study of Ru-Transition Metal Alloys and Oxides as Oxygen Evolution Reaction Electrocatalysts in Alkaline Media. *ACS Appl Energy Mater* **2022**, *5* (9), 11241–11253. https://doi.org/10.1021/ACSAEM.2C01545/ASSET/IMAGES/LARGE/AE2C01545_0011.JPEG.

(388) Selvakumar, K.; Kumar, S. M. S.; Thangamuthu, R.; Rajput, P.; Bhattacharyya, D.; Jha, S. N. 2D and 3D Silica-Template-Derived MnO2 Electrocatalysts towards Enhanced Oxygen Evolution and Oxygen Reduction Activity. *ChemElectroChem* **2018**, *5* (24), 3980–3990. https://doi.org/10.1002/CELC.201801143.

(389) Li, X.; Liu, Y.; Wen, J.; Qing, B.; Yang, M.; Liu, B.; Chen, H.; Li, H. N,S-Codoped Carbon Nanostructures Encapsulated with FeNi Nanoparticles as a Bifunctional Electrocatalyst for Rechargeable Zn-Air Batteries. *ACS Appl Nano Mater* **2022**. https://doi.org/10.1021/ACSANM.2C05107/ASSET/IMAGES/LARGE/AN2C05107_0007.JPEG.

(390) Li, Z.; Niu, W.; Yang, Z.; Zaman, N.; Samarakoon, W.; Wang, M.; Kara, A.; Lucero, M.; Vyas, M. V.; Cao, H.; Zhou, H.; Sterbinsky, G. E.; Feng, Z.; Du, Y.; Yang, Y. Stabilizing Atomic Pt with Trapped Interstitial F in Alloyed PtCo Nanosheets for High-Performance Zinc-Air Batteries. *Energy Environ Sci* **2020**, *13* (3), 884–895. https://doi.org/10.1039/C9EE02657F.

(391) Zhong, X.; Ye, S.; Tang, J.; Zhu, Y.; Wu, D.; Gu, M.; Pan, H.; Xu, B. Engineering Pt and Fe Dual-Metal Single Atoms Anchored on Nitrogen-Doped Carbon with High

Activity and Durability towards Oxygen Reduction Reaction for Zinc-Air Battery. *Appl Catal B* **2021**, *286*, 119891. https://doi.org/10.1016/J.APCATB.2021.119891.

(392) Paulus, U. A.; Schmidt, T. J.; Gasteiger, H. A.; Behm, R. J. Oxygen Reduction on a High-Surface Area Pt/Vulcan Carbon Catalyst: A Thin-Film Rotating Ring-Disk Electrode Study. *Journal of Electroanalytical Chemistry* **2001**, *495* (2), 134–145. https://doi.org/10.1016/S0022-0728(00)00407-1.

(393) Jiao, D.; Ma, Z.; Li, J.; Han, Y.; Mao, J.; Ling, T.; Qiao, S. Test Factors Affecting the Performance of Zinc–Air Battery. *Journal of Energy Chemistry* **2020**, *44*, 1–7. https://doi.org/10.1016/J.JECHEM.2019.09.008.

(394) Hosseini, S.; Masoudi Soltani, S.; Li, Y. Y. Current Status and Technical Challenges of Electrolytes in Zinc–Air Batteries: An in-Depth Review. *Chemical Engineering Journal* **2021**, *408*, 127241. https://doi.org/10.1016/J.CEJ.2020.127241.

(395) Sha, Y.; Peng, Y.; Huang, K.; Li, L.; Liu, Z.; Sha, Y.; Peng, Y.; Liu, Z.; Huang, K.; Li, L. 3D Binder-free Integrated Electrodes Prepared by Phase Separation and Laser Induction (PSLI) Method for Oxygen Electrocatalysis and Zinc–Air Battery. *Wiley Online Library* **2022**, *12* (25). https://doi.org/10.1002/aenm.202200906.

(396) Chu, S.; Cui, Y.; Liu, N. The Path towards Sustainable Energy. *Nature Materials 2017 16:1* **2016**, *16* (1), 16–22. https://doi.org/10.1038/nmat4834.

(397) Dai, L.; Xue, Y.; Qu, L.; Choi, H. J.; Baek, J. B. Metal-Free Catalysts for Oxygen Reduction Reaction. *Chem Rev* **2015**, *115* (11), 4823–4892. https://doi.org/10.1021/CR5003563/ASSET/IMAGES/MEDIUM/CR-2014-003563_0049.GIF.

(398) Debe, M. K. Electrocatalyst Approaches and Challenges for Automotive Fuel Cells. *Nature 2012 486:7401* **2012**, *486* (7401), 43–51. https://doi.org/10.1038/nature11115.

(399) Melchionna, M.; Fornasiero, P.; Prato, M. The Rise of Hydrogen Peroxide as the Main Product by Metal-Free Catalysis in Oxygen Reductions. *Advanced Materials* **2019**, *31* (13), 1802920. https://doi.org/10.1002/ADMA.201802920.

(400) Siahrostami, S.; Verdaguer-Casadevall, A.; Karamad, M.; Deiana, D.; Malacrida, P.; Wickman, B.; Escudero-Escribano, M.; Paoli, E. A.; Frydendal, R.; Hansen, T. W.; Chorkendorff, I.; Stephens, I. E. L.; Rossmeisl, J. Enabling Direct H2O2 Production through Rational Electrocatalyst Design. *Nature Materials 2013 12:12* **2013**, *12* (12), 1137–1143. https://doi.org/10.1038/nmat3795.

(401) Zhao, J.; Fu, C.; Ye, K.; Liang, Z.; Jiang, F.; Shen, S.; Zhao, X.; Ma, L.; Shadike, Z.; Wang, X.; Zhang, J.; Jiang, K. Manipulating the Oxygen Reduction Reaction Pathway on Pt-Coordinated Motifs. *Nature Communications 2022 13:1* **2022**, *13* (1), 1–10. https://doi.org/10.1038/s41467-022-28346-0.

(402) Zhang, L.; Jiang, S.; Ma, W.; Zhou, Z. Oxygen Reduction Reaction on Pt-Based Electrocatalysts: Four-Electron vs. Two-Electron Pathway. *Chinese Journal of Catalysis* **2022**, *43* (6), 1433–1443. https://doi.org/10.1016/S1872-2067(21)63961-X.

(403) Zhang, Y. L.; Goh, K.; Zhao, L.; Sui, X. L.; Gong, X. F.; Cai, J. J.; Zhou, Q. Y.; Zhang, H. Da; Li, L.; Kong, F. R.; Gu, D. M.; Wang, Z. B. Advanced Non-Noble Materials in Bifunctional Catalysts for ORR and OER toward Aqueous Metal–Air Batteries. *Nanoscale* **2020**, *12* (42), 21534–21559. https://doi.org/10.1039/D0NR05511E.

(404) Wang, N.; Ma, S.; Zuo, P.; Duan, J.; Hou, B. Recent Progress of Electrochemical Production of Hydrogen Peroxide by Two-Electron Oxygen Reduction Reaction. *Advanced Science* **2021**, *8* (15), 2100076. https://doi.org/10.1002/ADVS.202100076.

(405) Chang, Q.; Zhang, P.; Mostaghimi, A. H. B.; Zhao, X.; Denny, S. R.; Lee, J. H.; Gao, H.; Zhang, Y.; Xin, H. L.; Siahrostami, S.; Chen, J. G.; Chen, Z. Promoting H2O2 Production via 2-Electron Oxygen Reduction by Coordinating Partially Oxidized Pd with Defect Carbon. *Nature Communications 2020 11:1* **2020**, *11* (1), 1–9. https://doi.org/10.1038/s41467-020-15843-3.

(406) Gao, G.; Tian, Y.; Gong, X.; Pan, Z.; Yang, K.; Zong, B. Advances in the Production Technology of Hydrogen Peroxide. *Chinese Journal of Catalysis* **2020**, *41* (7), 1039–1047. https://doi.org/10.1016/S1872-2067(20)63562-8.

(407) Tang, Q.; Jiang, L.; Liu, J.; Wang, S.; Sun, G. Effect of Surface Manganese Valence of Manganese Oxides on the Activity of the Oxygen Reduction Reaction in Alkaline Media. *ACS Catal* **2014**, *4* (2), 457–463. https://doi.org/10.1021/CS400938S/ASSET/IMAGES/LARGE/CS-2013-00938S_0011.JPEG.

(408) Spendelow, J. S.; Wieckowski, A. Electrocatalysis of Oxygen Reduction and Small Alcohol Oxidation in Alkaline Media. *Physical Chemistry Chemical Physics* **2007**, *9* (21), 2654–2675. https://doi.org/10.1039/B703315J.

(409) Mao, L.; Zhang, D.; Sotomura, T.; Nakatsu, K.; Koshiba, N.; Ohsaka, T. Mechanistic Study of the Reduction of Oxygen in Air Electrode with Manganese Oxides as Electrocatalysts. *Electrochim Acta* **2003**, *48* (8), 1015–1021. https://doi.org/10.1016/S0013-4686(02)00815-0.

(410) Cheng, F.; Chen, J. Metal–Air Batteries: From Oxygen Reduction Electrochemistry to Cathode Catalysts. *Chem Soc Rev* **2012**, *41* (6), 2172–2192. https://doi.org/10.1039/C1CS15228A.

(411) Sun, W.; Hsu, A.; Chen, R. Carbon-Supported Tetragonal MnOOH Catalysts for Oxygen Reduction Reaction in Alkaline Media. *J Power Sources* **2011**, *196* (2), 627–635. https://doi.org/10.1016/J.JPOWSOUR.2010.07.082.

(412) Feng, J.; Liang, Y.; Wang, H.; Li, Y.; Zhang, B.; Zhou, J.; Wang, J.; Regier, T.; Dai, H. Engineering Manganese Oxide/Nanocarbon Hybrid Materials for Oxygen Reduction Electrocatalysis. *Nano Res* **2012**, *5* (10), 718–725. https://doi.org/10.1007/S12274-012-0256-8/METRICS.

(413) Guan, J.; Zhang, Z.; Ji, J.; Dou, M.; Wang, F. Hydrothermal Synthesis of Highly Dispersed Co3O4 Nanoparticles on Biomass-Derived Nitrogen-Doped Hierarchically

Porous Carbon Networks as an Efficient Bifunctional Electrocatalyst for Oxygen Reduction and Evolution Reactions. *ACS Appl Mater Interfaces* **2017**, *9* (36), 30662–30669. https://doi.org/10.1021/ACSAMI.7B08533/ASSET/IMAGES/LARGE/AM-2017-08533T_0005.JPEG.

(414) Hu, C.; Dai, L. Multifunctional Carbon-Based Metal-Free Electrocatalysts for Simultaneous Oxygen Reduction, Oxygen Evolution, and Hydrogen Evolution. *Advanced Materials* **2017**, *29* (9), 1604942. https://doi.org/10.1002/ADMA.201604942.

(415) Ren, M.; Zhang, J.; Zhang, C.; Stanford, M. G.; Chyan, Y.; Yao, Y.; Tour, J. M. Quasi-Solid-State Li-O2 Batteries with Laser-Induced Graphene Cathode Catalysts. *ACS Appl Energy Mater* **2020**, *3* (2), 1702–1709. https://doi.org/10.1021/ACSAEM.9B02182/ASSET/IMAGES/LARGE/AE9B02182_0006.JPEG.

(416) Gao, M.; Dong, X.; Mei, X.; Wang, K.; Wang, W.; Zhu, C.; Duan, W.; Sun, X. Laser Direct Writing of Graphene/MnO-Mn3O4 Doped with Sulfur for High-Performance Microsupercapacitors. *J Energy Storage* **2022**, *49*, 104118. https://doi.org/10.1016/J.EST.2022.104118.

(417) Ju, K.; Miao, Y.; Li, Q.; Yan, Y.; Gao, Y. Laser Direct Writing of MnO2/Carbonized Carboxymethylcellulose-Based Composite as High-Performance Electrodes for Supercapacitors. *ACS Omega* **2023**, *8* (8), 7690–7698. https://doi.org/10.1021/ACSOMEGA.2C07350/SUPPL_FILE/AO2C07350_SI_001.PDF.

(418) Dang, M. N.; Nguyen, T. H.; Nguyen, T. H.; Nguyen, T. Van; Thu, T. V.; Le, H.; Akabori, M.; Ito, N.; Nguyen, H. Y.; Nguyen, H. Y.; Le, T. L.; Le, T. L.; Nguyen, T. H.; Nguyen, V. T.; Phan, N. H.; Phan, N. H. One-Pot Synthesis of Manganese Oxide/Graphene Composites via a Plasma-Enhanced Electrochemical Exfoliation

Process for Supercapacitors. *Nanotechnology* **2020**, *31* (34), 345401. https://doi.org/10.1088/1361-6528/AB8FE5.

(419) Lu, L.; Zhang, D.; Xie, Y.; Wang, W. A Stretchable, High-Voltage and Biobased Microsupercapacitor Using Laser Induced Graphene/MnOx Electrodes on Cotton Cloth. *J Energy Storage* **2022**, *51*, 104458. https://doi.org/10.1016/J.EST.2022.104458.

(420) Niu, S.; Li, S.; Du, Y.; Han, X.; Xu, P. How to Reliably Report the Overpotential of an Electrocatalyst. *ACS Energy Lett* **2020**, *5* (4), 1083–1087. https://doi.org/10.1021/ACSENERGYLETT.0C00321/ASSET/IMAGES/LARGE/NZ0C00321_0005.JPEG.

(421) Zhou, R.; Zheng, Y.; Jaroniec, M.; Qiao, S. Z. Determination of the Electron Transfer Number for the Oxygen Reduction Reaction: From Theory to Experiment. *ACS Catal* **2016**, *6* (7), 4720–4728. https://doi.org/10.1021/ACSCATAL.6B01581/ASSET/IMAGES/LARGE/CS-2016-01581C_0005.JPEG.

(422) Deng, H.; Zhang, C.; Xie, Y.; Tumlin, T.; Giri, L.; Karna, S. P.; Lin, J. Laser Induced MoS 2 /Carbon Hybrids for Hydrogen Evolution Reaction Catalysts. *J Mater Chem A Mater* **2016**, *4* (18), 6824–6830. https://doi.org/10.1039/C5TA09322H.

(423) Panomsuwan, G.; Saito, N.; Ishizaki, T. Nitrogen-Doped Carbon Nanoparticle-Carbon Nanofiber Composite as an Efficient Metal-Free Cathode Catalyst for Oxygen Reduction Reaction. *ACS Appl Mater Interfaces* **2016**, *8* (11), 6962–6971. https://doi.org/10.1021/ACSAMI.5B10493/ASSET/IMAGES/LARGE/AM-2015-10493R_0006.JPEG.

(424) Zhang, Y.; Han, T.; Fang, J.; Xu, P.; Li, X.; Xu, J.; Liu, C. C. Integrated Pt 2 Ni Alloy@Pt Core–Shell Nanoarchitectures with High Electrocatalytic Activity for Oxygen Reduction Reaction. *J Mater Chem A Mater* **2014**, *2* (29), 11400–11407. https://doi.org/10.1039/C4TA00731J.

(425) Wang, S.; Iyyamperumal, E.; Roy, A.; Xue, Y.; Yu, D.; Dai, L. Vertically Aligned BCN Nanotubes as Efficient Metal-Free Electrocatalysts for the Oxygen Reduction Reaction: A Synergetic Effect by Co-Doping with Boron and Nitrogen. *Angewandte Chemie International Edition* **2011**, *50* (49), 11756–11760. https://doi.org/10.1002/ANIE.201105204.

(426) D’Amico, F.; Musso, M. E.; Berger, R. J. F.; Cefarin, N.; Birarda, G.; Tondi, G.; Bertoldo Menezes, D.; Reyer, A.; Scarabattoli, L.; Sepperer, T.; Schnabel, T.; Vaccari, L. Chemical Constitution of Polyfurfuryl Alcohol Investigated by FTIR and Resonant Raman Spectroscopy. *Spectrochim Acta A Mol Biomol Spectrosc* **2021**, *262*, 120090. https://doi.org/10.1016/J.SAA.2021.120090.

(427) Burket, C. L.; Rajagopalan, R.; Marencic, A. P.; Dronvajjala, K.; Foley, H. C. Genesis of Porosity in Polyfurfuryl Alcohol Derived Nanoporous Carbon. *Carbon N Y* **2006**, *44* (14), 2957–2963. https://doi.org/10.1016/J.CARBON.2006.05.029.

(428) Meng, L.; Turner, A. P. F.; Mak, W. C. Conducting Polymer-Reinforced Laser-Irradiated Graphene as a Heterostructured 3D Transducer for Flexible Skin Patch Biosensors. *ACS Appl Mater Interfaces* **2021**, *13* (45), 54456–54465. https://doi.org/10.1021/ACSAMI.1C13164/ASSET/IMAGES/LARGE/AM1C13164_0006.JPEG.

(429) Wahab, H.; Jain, V.; Tyrrell, A. S.; Seas, M. A.; Kotthoff, L.; Johnson, P. A. Machine-Learning-Assisted Fabrication: Bayesian Optimization of Laser-Induced Graphene Patterning Using in-Situ Raman Analysis. *Carbon N Y* **2020**, *167*, 609–619. https://doi.org/10.1016/J.CARBON.2020.05.087.

(430) Biswal, A.; Tripathy, B. C.; Sanjay, K.; Subbaiah, T.; Minakshi, M. Electrolytic Manganese Dioxide (EMD): A Perspective on Worldwide Production, Reserves and Its Role in Electrochemistry. *RSC Adv* **2015**, *5* (72), 58255–58283. https://doi.org/10.1039/C5RA05892A.

(431) Hatakeyama, T.; Okamoto, N. L.; Ichitsubo, T. Thermal Stability of MnO2 Polymorphs. *J Solid State Chem* **2022**, *305*, 122683. https://doi.org/10.1016/J.JSSC.2021.122683.

(432) Dasappa, S.; Camacho, J. Formation of Nanocrystalline Manganese Oxide in Flames: Oxide Phase Governed by Classical Nucleation and Size-Dependent Equilibria. *CrystEngComm* **2020**, *22* (33), 5509–5521. https://doi.org/10.1039/D0CE00734J.

(433) Cheraghi, A.; Yoozbashizadeh, H.; Safarian, J. Gaseous Reduction of Manganese Ores: A Review and Theoretical Insight. *https://doi.org/10.1080/08827508.2019.1604523* **2019**, *41* (3), 198–215. https://doi.org/10.1080/08827508.2019.1604523.

(434) Darul, J.; Lathe, C.; Piszora, P. Mn3O4 under High Pressure and Temperature: Thermal Stability, Polymorphism, and Elastic Properties. *Journal of Physical Chemistry C* **2013**, *117* (45), 23487–23494. https://doi.org/10.1021/JP404852J/SUPPL_FILE/JP404852J_SI_001.PDF.

(435) Darul, J.; Lathe, C.; Piszora, P. Mn3O4 under High Pressure and Temperature: Thermal Stability, Polymorphism, and Elastic Properties. *Journal of Physical Chemistry C* **2013**, *117* (45), 23487–23494. https://doi.org/10.1021/JP404852J/SUPPL_FILE/JP404852J_SI_001.PDF.

(436) Joo, S. W.; Cheney, M. A.; Bhowmik, P. K.; Moriuchi, S.; Villalobos, M.; Qian, S. The Effect of Stirring on the Morphology of Birnessite Nanoparticles. *J Nanomater* **2008**, *2008* (1). https://doi.org/10.1155/2008/168716.

(437) Jian, G.; Xu, Y.; Lai, L. C.; Wang, C.; Zachariah, M. R. Mn3O4 Hollow Spheres for Lithium-Ion Batteries with High Rate and Capacity. *J Mater Chem A Mater* **2014**, *2* (13), 4627–4632. https://doi.org/10.1039/C4TA00207E.

(438) Tinsley, D. M.; Sharp, J. H. Thermal Analysis of Manganese Dioxide in Controlled Atmospheres. *Journal of Thermal Analysis* **1971**, *3* (1), 43–48. https://doi.org/10.1007/BF01911769/METRICS.

(439) Feng, X.; Cox, D. F. Oxidation of MnO(100) and NaMnO2 Formation: Characterization of Mn2+ and Mn3+ Surfaces via XPS and Water TPD. *Surf Sci* **2018**, *675*, 47–53. https://doi.org/10.1016/J.SUSC.2018.04.022.

(440) Li, M.; Lei, W.; Yu, Y.; Yang, W.; Li, J.; Chen, D.; Xu, S.; Feng, M.; Li, H. High-Performance Asymmetric Supercapacitors Based on Monodisperse MnO Nanocrystals with High Energy Densities. *Nanoscale* **2018**, *10* (34), 15926–15931. https://doi.org/10.1039/C8NR04541K.

(441) Liu, H.; Liu, Q.; Wang, Y.; Wang, Y.; Chou, S.; Hu, Z.; Zhang, Z. Bifunctional Carbon-Based Cathode Catalysts for Zinc-Air Battery: A Review. *Chinese Chemical Letters* **2022**, *33* (2), 683–692. https://doi.org/10.1016/J.CCLET.2021.07.038.

(442) Qin, Y.; Ou, Z.; Xu, C.; Zhang, Z.; Yi, J.; Jiang, Y.; Wu, J.; Guo, C.; Si, Y.; Zhao, T. Progress of Carbon-Based Electrocatalysts for Flexible Zinc-Air Batteries in the Past 5 Years: Recent Strategies for Design, Synthesis and Performance Optimization. *Nanoscale Res Lett* **2021**, *16* (1), 1–13. https://doi.org/10.1186/S11671-021-03548-5/FIGURES/3.

(443) Wang, Q.; Guesmi, H.; Tingry, S.; Cornu, D.; Holade, Y.; Minteer, S. D. Unveiling the Pitfalls of Comparing Oxygen Reduction Reaction Kinetic Data for Pd-Based Electrocatalysts without the Experimental Conditions of the Current-Potential Curves. *ACS Energy Lett* **2022**, *7* (3), 952–957. https://doi.org/10.1021/ACSENERGYLETT.2C00181/ASSET/IMAGES/LARGE/NZ2C00181_0005.JPEG.

(444) Cheng, F.; Su, Y.; Liang, J.; Tao, Z.; Chen, J. MnO2-Based Nanostructures as Catalysts for Electrochemical Oxygen Reduction in Alkaline Media. *Chemistry of Materials* **2010**, *22* (3), 898–905. https://doi.org/10.1021/CM901698S/ASSET/IMAGES/LARGE/CM-2009-01698S_0010.JPEG.

(445) Zhong, X.; Oubla, M.; Wang, X.; Huang, Y.; Zeng, H.; Wang, S.; Liu, K.; Zhou, J.; He, L.; Zhong, H.; Alonso-Vante, N.; Wang, C. W.; Wu, W. Bin; Lin, H. J.; Chen, C. Te; Hu, Z.; Huang, Y.; Ma, J. Boosting Oxygen Reduction Activity and Enhancing Stability through Structural Transformation of Layered Lithium Manganese Oxide. *Nature Communications 2021 12:1* **2021**, *12* (1), 1–12. https://doi.org/10.1038/s41467-021-23430-3.

(446) Xiao, X.; Fang, Z.; Yu, D. Boosting Oxygen Reduction Performance of Manganese Oxide in Alkaline Media by Three-Dimensional Highly Ordered Conductive Porous Framework. *Front Mater* **2019**, *6*, 219. https://doi.org/10.3389/FMATS.2019.00219/BIBTEX.

(447) Sheng, Z. H.; Shao, L.; Chen, J. J.; Bao, W. J.; Wang, F. Bin; Xia, X. H. Catalyst-Free Synthesis of Nitrogen-Doped Graphene via Thermal Annealing Graphite Oxide with Melamine and Its Excellent Electrocatalysis. *ACS Nano* **2011**, *5* (6), 4350–4358. https://doi.org/10.1021/NN103584T/SUPPL_FILE/NN103584T_SI_001.PDF.

(448) Hamal, K.; May, J.; Koirala, D.; Zhu, H.; Kabir, H.; Echeverria, E.; McIlroy, D. N.; Nicholas, N.; Cheng, I. F. Highly Stable, Low-Cost Metal-Free Oxygen Reduction Reaction Electrocatalyst Based on Nitrogen-Doped Pseudo-Graphite. *Energy and Fuels* **2021**, *35* (12), 10146–10155. https://doi.org/10.1021/ACS.ENERGYFUELS.1C00658/ASSET/IMAGES/LARGE/EF1C00658_0007.JPEG.

(449) Hosseini-Benhangi, P.; Garcia-Contreras, M. A.; Alfantazi, A.; Gyenge, E. L. Method for Enhancing the Bifunctional Activity and Durability of Oxygen Electrodes with Mixed Oxide Electrocatalysts: Potential Driven Intercalation of Potassium. *J Electrochem Soc* **2015**, *162* (12), F1356–F1366. https://doi.org/10.1149/2.0561512JES/XML.

(450) Zhang, Y. C.; Ullah, S.; Zhang, R.; Pan, L.; Zhang, X.; Zou, J. J. Manipulating Electronic Delocalization of Mn3O4 by Manganese Defects for Oxygen Reduction

Reaction. *Appl Catal B* **2020**, *277*, 119247. https://doi.org/10.1016/J.APCATB.2020.119247.

(451) Hao, J.; Liu, Y.; Shen, H.; Li, W.; Li, J.; Li, Y.; Chen, Q. Effect of Nickel-Ion Doping in MnO2 Nanoneedles as Electrocatalyst for the Oxygen Reduction Reaction. *Journal of Materials Science: Materials in Electronics* **2016**, *27* (6), 6598–6605. https://doi.org/10.1007/S10854-016-4606-2/FIGURES/8.

(452) Cao, Y. L.; Yang, H. X.; Ai, X. P.; Xiao, L. F. The Mechanism of Oxygen Reduction on MnO2-Catalyzed Air Cathode in Alkaline Solution. *Journal of Electroanalytical Chemistry* **2003**, *557*, 127–134. https://doi.org/10.1016/S0022-0728(03)00355-3.

(453) Chai, H.; Xu, J.; Han, Ji.; Su, Y.; Sun, Z.; Jia, D.; Zhou, W. Facile Synthesis of Mn3O4-RGO Hybrid Materials for the High-Performance Electrocatalytic Reduction of Oxygen. *J Colloid Interface Sci* **2017**, *488*, 251–257. https://doi.org/10.1016/J.JCIS.2016.10.049.

(454) Ahmad Shah, S. S.; Najam, T.; Cheng, C.; Chen, S.; Xiang, R.; Peng, L.; Lu, L.; Ding, W.; Wei, Z. Design and Synthesis of Conductive Carbon Polyhedrons Enriched with Mn-Oxide Active-Centres for Oxygen Reduction Reaction. *Electrochim Acta* **2018**, *272*, 169–175. https://doi.org/10.1016/J.ELECTACTA.2018.04.008.

(455) Roche, I.; Chaînet, E.; Chatenet, M.; Vondrák, J. Carbon-Supported Manganese Oxide Nanoparticles as Electrocatalysts for the Oxygen Reduction Reaction (ORR) in Alkaline Medium: Physical Characterizations and ORR Mechanism. *Journal of Physical Chemistry C* **2007**, *111* (3), 1434–1443. https://doi.org/10.1021/JP0647986/ASSET/IMAGES/MEDIUM/JP0647986E00031.GIF.

(456) Lee, J. S.; Park, G. S.; Lee, H. Il; Kim, S. T.; Cao, R.; Liu, M.; Cho, J. Ketjenblack Carbon Supported Amorphous Manganese Oxides Nanowires as Highly Efficient Electrocatalyst for Oxygen Reduction Reaction in Alkaline Solutions. *Nano Lett* **2011**,

11 (12), 5362–5366. https://doi.org/10.1021/NL2029078/SUPPL_FILE/NL2029078_SI_001.PDF.

(457) Cheng, H.; Xu, K.; Xing, L.; Liu, S.; Gong, Y.; Gu, L.; Zhang, L.; Wu, C. Manganous Oxide Nanoparticles Encapsulated in Few-Layer Carbon as an Efficient Electrocatalyst for Oxygen Reduction in Alkaline Media. *J Mater Chem A Mater* **2016**, *4* (30), 11775–11781. https://doi.org/10.1039/C6TA02846B.

(458) Li, P. C.; Hu, C. C.; Lee, T. C.; Chang, W. S.; Wang, T. H. Synthesis and Characterization of Carbon Black/Manganese Oxide Air Cathodes for Zinc-Air Batteries. *J Power Sources* **2014**, *269*, 88–97. https://doi.org/10.1016/J.JPOWSOUR.2014.06.108.

(459) Cheng, R.; Yang, J.; Jiang, M.; Dong, A.; Guo, M.; Zhang, J.; Sun, B.; Fu, C. Hierarchical Porous Manganese- and Nitrogen-Codoped Carbon Nanosheets Derived from Surface Modified Biomass as Efficient Oxygen Reduction Catalysts for Al-Air Batteries. *J Electrochem Soc* **2020**, *167* (11), 110552. https://doi.org/10.1149/1945-7111/ABA5DA.

(460) Panganoron, H. O.; Pascasio, J. D. A.; Esparcia, E. A.; Del Rosario, J. A. D.; Ocon, J. D. Hydrothermally Carbonized Waste Biomass as Electrocatalyst Support for α-MnO2 in Oxygen Reduction Reaction. *Catalysts 2020, Vol. 10, Page 177* **2020**, *10* (2), 177. https://doi.org/10.3390/CATAL10020177.

(461) Li, Y.; Lu, J. Metal-Air Batteries: Will They Be the Future Electrochemical Energy Storage Device of Choice? *ACS Energy Lett* **2017**, *2* (6), 1370–1377. https://doi.org/10.1021/ACSENERGYLETT.7B00119/ASSET/IMAGES/LARGE/NZ-2017-00119S_0005.JPEG.

(462) Zhang, T.; Zhang, S.; Cao, S.; Yao, Q.; Lee, J. Y. Bridging the Energy Efficiency Gap between Quasi-Neutral and Alkaline Rechargeable Zinc-Air Batteries by an Efficient Hybrid Battery Design. *Energy Storage Mater* **2020**, *33*, 181–187. https://doi.org/10.1016/J.ENSM.2020.08.019.

---

(463) Spendelow, J. S.; Wieckowski, A. Electrocatalysis of Oxygen Reduction and Small Alcohol Oxidation in Alkaline Media. *Physical Chemistry Chemical Physics* **2007**, *9* (21), 2654–2675. https://doi.org/10.1039/B703315J.

(464) Piwowarczyk, J.; Jedrzejewski, R.; Moszyński, D.; Kwiatkowski, K.; Niemczyk, A.; Baranowska, J. XPS and FTIR Studies of Polytetrafluoroethylene Thin Films Obtained by Physical Methods. *Polymers 2019, Vol. 11, Page 1629* **2019**, *11* (10), 1629. https://doi.org/10.3390/POLYM11101629.

(465) Liang, R. Q.; Su, X. B.; Wu, Q. C.; Fang, F. Study of the Surface-Modified Teflon/Ceramics Complex Material Treated by Microwave Plasma with XPS Analysis. *Surf Coat Technol* **2000**, *131* (1–3), 294–299. https://doi.org/10.1016/S0257-8972(00)00795-7.

(466) Xiaoqing Huang; Zipeng Zhao; Liang Cao; Yu Chen; Enbo Zhu; Zhaoyang Lin; Mufan Li; Aiming Yan; Alex Zettl; Morris Wang; Xiangfeng Duan; Tim Mueller; Yu Huang. High-Performance Transition Metal–Doped Pt3Ni Octahedra for Oxygen Reduction Reaction. *Science (1979)* **2015**, *348* (6240), 1226–1230. https://doi.org/10.1126/science.aaa2951.

(467) Dai, L.; Xue, Y.; Qu, L.; Choi, H. J.; Baek, J. B. Metal-Free Catalysts for Oxygen Reduction Reaction. *Chemical Reviews*. American Chemical Society June 10, 2015, pp 4823–4892. https://doi.org/10.1021/cr5003563.

(468) Shao, M.; Chang, Q.; Dodelet, J. P.; Chenitz, R. Recent Advances in Electrocatalysts for Oxygen Reduction Reaction. *Chemical Reviews*. American Chemical Society March 23, 2016, pp 3594–3657. https://doi.org/10.1021/acs.chemrev.5b00462.

(469) Nie, Y.; Li, L.; Wei, Z. Recent Advancements in Pt and Pt-Free Catalysts for Oxygen Reduction Reaction. *Chemical Society Reviews*. Royal Society of Chemistry April 21, 2015, pp 2168–2201. https://doi.org/10.1039/c4cs00484a.

(470) Wu, Z.; Song, M.; Wang, J.; Liu, X. Recent Progress in Nitrogen-Doped Metal-Free Electrocatalysts for Oxygen Reduction Reaction. *Catalysts*. MDPI May 1, 2018. https://doi.org/10.3390/catal8050196.

(471) Masa, J.; Xia, W.; Muhler, M.; Schuhmann, W. Über Die Rolle von Metallen in Elektrokatalysatoren Auf Basis von Stickstoffdotiertem Kohlenstoff Für Die Sauerstoffreduktion. *Angewandte Chemie* **2015**, *127* (35), 10240–10259. https://doi.org/10.1002/ange.201500569.

(472) Takeyasu, K.; Furukawa, M.; Shimoyama, Y.; Singh, S. K.; Nakamura, J. Role of Pyridinic Nitrogen in the Mechanism of the Oxygen Reduction Reaction on Carbon Electrocatalysts. *Angewandte Chemie - International Edition* **2021**, *60* (10), 5121–5124. https://doi.org/10.1002/anie.202014323.

(473) Lv, Q.; Si, W.; He, J.; Sun, L.; Zhang, C.; Wang, N.; Yang, Z.; Li, X.; Wang, X.; Deng, W.; Long, Y.; Huang, C.; Li, Y. Selectively Nitrogen-Doped Carbon Materials as Superior Metal-Free Catalysts for Oxygen Reduction. *Nat Commun* **2018**, *9* (1). https://doi.org/10.1038/s41467-018-05878-y.

(474) Qu, L.; Liu, Y.; Baek, J. B.; Dai, L. Nitrogen-Doped Graphene as Efficient Metal-Free Electrocatalyst for Oxygen Reduction in Fuel Cells. *ACS Nano* **2010**, *4* (3), 1321–1326. https://doi.org/10.1021/nn901850u.

(475) Wang, Z.; Jia, R.; Zheng, J.; Zhao, J.; Li, L.; Song, J.; Zhu, Z. Nitrogen-Promoted Self-Assembly of N-Doped Carbon Nanotubes and Their Intrinsic Catalysis for Oxygen Reduction in Fuel Cells. *ACS Nano* **2011**, *5* (3), 1677–1684. https://doi.org/10.1021/nn1030127.

(476) Tang, Y.; Allen, B. L.; Kauffman, D. R.; Star, A. Electrocatalytic Activity of Nitrogen-Doped Carbon Nanotube Cups. *J Am Chem Soc* **2009**, *131* (37), 13200–13201. https://doi.org/10.1021/ja904595t.

(477) Yadav, R. M.; Wu, J.; Kochandra, R.; Ma, L.; Tiwary, C. S.; Ge, L.; Ye, G.; Vajtai, R.; Lou, J.; Ajayan, P. M. Carbon Nitrogen Nanotubes as Efficient Bifunctional

Electrocatalysts for Oxygen Reduction and Evolution Reactions. *ACS Appl Mater Interfaces* **2015**, *7* (22), 11991–12000. https://doi.org/10.1021/acsami.5b02032.

(478) Lin, Z.; Song, M. K.; Ding, Y.; Liu, Y.; Liu, M.; Wong, C. P. Facile Preparation of Nitrogen-Doped Graphene as a Metal-Free Catalyst for Oxygen Reduction Reaction. *Physical Chemistry Chemical Physics* **2012**, *14* (10), 3381–3387. https://doi.org/10.1039/c2cp00032f.

(479) Zhang, C.; Hao, R.; Liao, H.; Hou, Y. Synthesis of Amino-Functionalized Graphene as Metal-Free Catalyst and Exploration of the Roles of Various Nitrogen States in Oxygen Reduction Reaction. *Nano Energy* **2013**, *2* (1), 88–97. https://doi.org/10.1016/j.nanoen.2012.07.021.

(480) Liu, R.; Liu, H.; Li, Y.; Yi, Y.; Shang, X.; Zhang, S.; Yu, X.; Zhang, S.; Cao, H.; Zhang, G. Nitrogen-Doped Graphdiyne as a Metal-Free Catalyst for High-Performance Oxygen Reduction Reactions. *Nanoscale* **2014**, *6* (19), 11336–11343. https://doi.org/10.1039/c4nr03185g.

(481) Yang, L.; Zeng, X.; Wang, W.; Cao, D. Recent Progress in MOF-Derived, Heteroatom-Doped Porous Carbons as Highly Efficient Electrocatalysts for Oxygen Reduction Reaction in Fuel Cells. *Adv Funct Mater* **2018**, *28* (7). https://doi.org/10.1002/adfm.201704537.

(482) Fu, S.; Zhu, C.; Song, J.; Du, D.; Lin, Y. Metal-Organic Framework-Derived Non-Precious Metal Nanocatalysts for Oxygen Reduction Reaction. *Advanced Energy Materials*. Wiley-VCH Verlag October 11, 2017. https://doi.org/10.1002/aenm.201700363.

(483) Faisal, S. N.; Haque, E.; Noorbehesht, N.; Zhang, W.; Harris, A. T.; Church, T. L.; Minett, A. I. Pyridinic and Graphitic Nitrogen-Rich Graphene for High-Performance Supercapacitors and Metal-Free Bifunctional Electrocatalysts for ORR and OER. *RSC Adv* **2017**, *7* (29), 17950–17958. https://doi.org/10.1039/c7ra01355h.

---

(484) Rybarczyk, M. K.; Lieder, M.; Jablonska, M. N-Doped Mesoporous Carbon Nanosheets Obtained by Pyrolysis of a Chitosan-Melamine Mixture for the Oxygen Reduction Reaction in Alkaline Media. *RSC Adv* **2015**, *5* (56), 44969–44977. https://doi.org/10.1039/c5ra05725f.

(485) Sheng, Z. H.; Shao, L.; Chen, J. J.; Bao, W. J.; Wang, F. Bin; Xia, X. H. Catalyst-Free Synthesis of Nitrogen-Doped Graphene via Thermal Annealing Graphite Oxide with Melamine and Its Excellent Electrocatalysis. *ACS Nano* **2011**, *5* (6), 4350–4358. https://doi.org/10.1021/nn103584t.

(486) Zhou, T.; Zhou, Y.; Ma, R.; Zhou, Z.; Liu, G.; Liu, Q.; Zhu, Y.; Wang, J. Nitrogen-Doped Hollow Mesoporous Carbon Spheres as a Highly Active and Stable Metal-Free Electrocatalyst for Oxygen Reduction. *Carbon N Y* **2017**, *114*, 177–186. https://doi.org/10.1016/j.carbon.2016.12.011.

(487) Unni, S. M.; Bhange, S. N.; Illathvalappil, R.; Mutneja, N.; Patil, K. R.; Kurungot, S. Nitrogen-Induced Surface Area and Conductivity Modulation of Carbon Nanohorn and Its Function as an Efficient Metal-Free Oxygen Reduction Electrocatalyst for Anion-Exchange Membrane Fuel Cells. *Small* **2015**, *11* (3), 352–362. https://doi.org/10.1002/smll.201303892.

(488) Lin, Z.; Waller, G.; Liu, Y.; Liu, M.; Wong, C. P. Facile Synthesis of Nitrogen-Doped Graphene via Pyrolysis of Graphene Oxide and Urea, and Its Electrocatalytic Activity toward the Oxygen-Reduction Reaction. *Adv Energy Mater* **2012**, *2* (7), 884–888. https://doi.org/10.1002/aenm.201200038.

(489) Li, X.; Fang, Y.; Zhao, S.; Wu, J.; Li, F.; Tian, M.; Long, X.; Jin, J.; Ma, J. Nitrogen-Doped Mesoporous Carbon Nanosheet/Carbon Nanotube Hybrids as Metal-Free Bi-Functional Electrocatalysts for Water Oxidation and Oxygen Reduction. *J Mater Chem A Mater* **2016**, *4* (34), 13133–13141. https://doi.org/10.1039/c6ta04187f.

(490) Beckert, M.; Menzel, M.; Tölle, F. J.; Bruchmann, B.; Mülhaupt, R. Nitrogenated Graphene and Carbon Nanomaterials by Carbonization of Polyfurfuryl Alcohol in the

Presence of Urea and Dicyandiamide. *Green Chemistry* **2015**, *17* (2), 1032–1037. https://doi.org/10.1039/c4gc01676a.

(491) Lin, Z.; Waller, G. H.; Liu, Y.; Liu, M.; Wong, C. ping. 3D Nitrogen-Doped Graphene Prepared by Pyrolysis of Graphene Oxide with Polypyrrole for Electrocatalysis of Oxygen Reduction Reaction. *Nano Energy* **2013**, *2* (2), 241–248. https://doi.org/10.1016/j.nanoen.2012.09.002.

(492) Zhang, X.; Zhang, X.; Zhao, S.; Wang, Y. Q.; Lin, X.; Tian, Z. Q.; Shen, P. K.; Jiang, S. P. Precursor Modulated Active Sites of Nitrogen Doped Graphene-Based Carbon Catalysts via One-Step Pyrolysis Method for the Enhanced Oxygen Reduction Reaction. *Electrochim Acta* **2021**, *370*. https://doi.org/10.1016/j.electacta.2021.137712.

(493) Li, Y.; Li, T.; Yao, M.; Liu, S. Metal-Free Nitrogen-Doped Hollow Carbon Spheres Synthesized by Thermal Treatment of Poly(o-Phenylenediamine) for Oxygen Reduction Reaction in Direct Methanol Fuel Cell Applications. *J Mater Chem* **2012**, *22* (21), 10911–10917. https://doi.org/10.1039/c2jm30781b.

(494) Conder, J.; Vaulot, C.; Marino, C.; Villevieille, C.; Ghimbeu, C. M. Chitin and Chitosan - Structurally Related Precursors of Dissimilar Hard Carbons for Na-Ion Battery. *ACS Appl Energy Mater* **2019**, *2* (7), 4841–4852. https://doi.org/10.1021/acsaem.9b00545.

(495) Hammi, N.; Chen, S.; Dumeignil, F.; Royer, S.; El Kadib, A. Chitosan as a Sustainable Precursor for Nitrogen-Containing Carbon Nanomaterials: Synthesis and Uses. *Materials Today Sustainability*. Elsevier Ltd December 1, 2020. https://doi.org/10.1016/j.mtsust.2020.100053.

(496) Khan, A.; Goepel, M.; Colmenares, J. C.; Gläser, R. Chitosan-Based N-Doped Carbon Materials for Electrocatalytic and Photocatalytic Applications. *ACS Sustain Chem Eng* **2020**, *8* (12), 4708–4727. https://doi.org/10.1021/acssuschemeng.9b07522.

(497) Guo, D.; Wei, H.; Chen, X.; Liu, M.; Ding, F.; Yang, Z.; Yang, Y.; Wang, S.; Yang, K.; Huang, S. 3D Hierarchical Nitrogen-Doped Carbon Nanoflower Derived from

Chitosan for Efficient Electrocatalytic Oxygen Reduction and High Performance Lithium-Sulfur Batteries. *J Mater Chem A Mater* **2017**, *5* (34), 18193–18206. https://doi.org/10.1039/c7ta04728b.

(498) Liu, G.; Liu, Z.; Li, J.; Zeng, M.; Li, Z.; He, L.; Li, F. Chitosan/Phytic Acid Hydrogel as a Platform for Facile Synthesis of Heteroatom-Doped Porous Carbon Frameworks for Electrocatalytic Oxygen Reduction. *Carbon N Y* **2018**, *137*, 68–77. https://doi.org/10.1016/j.carbon.2018.05.027.

(499) Kumar, S.; Gonen, S.; Friedman, A.; Elbaz, L.; Nessim, G. D. Doping and Reduction of Graphene Oxide Using Chitosan-Derived Volatile N-Heterocyclic Compounds for Metal-Free Oxygen Reduction Reaction. *Carbon N Y* **2017**, *120*, 419–426. https://doi.org/10.1016/j.carbon.2017.05.071.

(500) Qiao, Y.; Kong, F.; Zhang, C.; Li, R.; Kong, A.; Shan, Y. Highly Efficient Oxygen Electrode Catalyst Derived from Chitosan Biomass by Molten Salt Pyrolysis for Zinc-Air Battery. *Electrochim Acta* **2020**, *339*. https://doi.org/10.1016/j.electacta.2020.135923.

(501) Charkhi, A.; Kazemian, H.; Kazemeini, M. Optimized Experimental Design for Natural Clinoptilolite Zeolite Ball Milling to Produce Nano Powders. *Powder Technol* **2010**, *203* (2), 389–396. https://doi.org/10.1016/J.POWTEC.2010.05.034.

(502) Zhou, X.; Dai, Z.; Bao, J.; Guo, Y. G. Wet Milled Synthesis of an Sb/MWCNT Nanocomposite for Improved Sodium Storage. *J Mater Chem A Mater* **2013**, *1* (44), 13727–13731. https://doi.org/10.1039/C3TA13438E.

(503) Stolle, A.; Szuppa, T.; Leonhardt, S. E. S.; Ondruschka, B. Ball Milling in Organic Synthesis: Solutions and Challenges. *Chem Soc Rev* **2011**, *40* (5), 2317–2329. https://doi.org/10.1039/C0CS00195C.

(504) Janot, R.; Guérard, D. Ball-Milling in Liquid Media: Applications to the Preparation of Anodic Materials for Lithium-Ion Batteries. *Prog Mater Sci* **2005**, *50* (1), 1–92. https://doi.org/10.1016/S0079-6425(03)00050-1.

(505) Suryanarayana, C. Mechanical Alloying and Milling. *Prog Mater Sci* **2001**, *46* (1–2), 1–184. https://doi.org/10.1016/S0079-6425(99)00010-9.

(506) Zhang, W.; Zhang, J.; Jiang, Q.; Xia, W. Physicochemical and Structural Characteristics of Chitosan Nanopowders Prepared by Ultrafine Milling. *Carbohydr Polym* **2012**, *87* (1), 309–313. https://doi.org/10.1016/J.CARBPOL.2011.07.057.

(507) Ye, R.; James, D. K.; Tour, J. M. Laser-Induced Graphene: From Discovery to Translation. *Advanced Materials*. Wiley-VCH Verlag January 4, 2019. https://doi.org/10.1002/adma.201803621.

(508) Ren, M.; Zhang, J.; Tour, J. M. Laser-Induced Graphene Hybrid Catalysts for Rechargeable Zn-Air Batteries. *ACS Appl Energy Mater* **2019**, *2* (2), 1460–1468. https://doi.org/10.1021/acsaem.8b02011.

(509) Sun, X.; Liu, X.; Li, F. Sulfur-Doped Laser-Induced Graphene Derived from Polyethersulfone and Lignin Hybrid for All-Solid-State Supercapacitor. *Appl Surf Sci* **2021**, *551*, 149438. https://doi.org/10.1016/J.APSUSC.2021.149438.

(510) Li, C.; Xiong, J.; Zheng, C.; Zhao, J. Screen-Printing Preparation of High-Performance Nonenzymatic Glucose Sensors Based on Co3O4Nanoparticles-Embedded N-Doped Laser-Induced Graphene. *ACS Appl Nano Mater* **2022**, *5* (11), 16655–16663. https://doi.org/10.1021/ACSANM.2C03694/ASSET/IMAGES/LARGE/AN2C03694_0006.JPEG.

(511) Zhao, J.; Wang, S.; Gao, L.; Zhang, D.; Guo, Y.; Xu, R. NiO Nanoparticles Anchored on N-Doped Laser-Induced Graphene for Flexible Planar Micro-Supercapacitors. *ACS Appl Nano Mater* **2022**, *5* (8), 11314–11323. https://doi.org/10.1021/ACSANM.2C02434/ASSET/IMAGES/LARGE/AN2C02434_0007.JPEG.

(512) Wan, Z.; Umer, M.; Lobino, M.; Thiel, D.; Nguyen, N. T.; Trinchi, A.; Shiddiky, M. J. A.; Gao, Y.; Li, Q. Laser Induced Self-N-Doped Porous Graphene as an

Electrochemical Biosensor for Femtomolar MiRNA Detection. *Carbon N Y* **2020**, *163*, 385–394. https://doi.org/10.1016/J.CARBON.2020.03.043.

(513) Peng, Z.; Ye, R.; Mann, J. A.; Zakhidov, D.; Li, Y.; Smalley, P. R.; Lin, J.; Tour, J. M. Flexible Boron-Doped Laser-Induced Graphene Microsupercapacitors. *ACS Nano* **2015**, *9* (6), 5868–5875. https://doi.org/10.1021/ACSNANO.5B00436/SUPPL_FILE/NN5B00436_SI_001.PDF.

(514) Khandelwal, M.; Tran, C. Van; Lee, J.; In, J. Bin. Nitrogen and Boron Co-Doped Densified Laser-Induced Graphene for Supercapacitor Applications. *Chemical Engineering Journal* **2022**, *428*, 131119. https://doi.org/10.1016/J.CEJ.2021.131119.

(515) Shuai Han; Cui Liu; Nian Li; Shudong Zhang; Yanping Song; Liqing Chen; Min Xi; Xinling Yu; Wenbo Wang; Mingguang Kong; Zhenyang Wang. One-Step Fabrication of Nitrogen-Doped Laser-Induced Graphene Derived from Melamine/Polyimide for Enhanced Flexible Supercapacitors. *CrystEngComm* **2022**, *24* (10), 1866–1876. https://doi.org/10.1039/D1CE01608C.

(516) Kim, K. Y.; Choi, H.; Tran, C. Van; In, J. Bin. Simultaneous Densification and Nitrogen Doping of Laser-Induced Graphene by Duplicated Pyrolysis for Supercapacitor Applications. *J Power Sources* **2019**, *441*, 227199. https://doi.org/10.1016/J.JPOWSOUR.2019.227199.

(517) Erra, P.; Molina, R.; Jocic, D.; Julia, M. R.; Cuesta, A.; Tascon, J. M. D. Shrinkage Properties of Wool Treated with Low Temperature Plasma and Chitosan Biopolymer. *Textile Research Journal* **1999**, *69* (11), 811–815. https://doi.org/10.1177/004051759906901103.

(518) Shih, C. Y.; Huang, K. S. Synthesis of a Polyurethane–Chitosan Blended Polymer and a Compound Process for Shrink-Proof and Antimicrobial Woolen Fabrics. *J Appl Polym Sci* **2003**, *88* (9), 2356–2363. https://doi.org/10.1002/APP.11802.

(519) Ssekatawa, K.; Byarugaba, D. K.; Wampande, E. M.; Moja, T. N.; Nxumalo, E.; Maaza, M.; Sackey, J.; Ejobi, F.; Kirabira, J. B. Isolation and Characterization of Chitosan from Ugandan Edible Mushrooms, Nile Perch Scales and Banana Weevils for Biomedical Applications. *Sci Rep* **2021**, *11* (1), 4116. https://doi.org/10.1038/S41598-021-81880-7.

(520) Chen, S.; Bi, J.; Zhao, Y.; Yang, L.; Zhang, C.; Ma, Y.; Wu, Q.; Wang, X.; Hu, Z. Nitrogen-Doped Carbon Nanocages as Efficient Metal-Free Electrocatalysts for Oxygen Reduction Reaction. *Advanced Materials* **2012**, *24* (41), 5593–5597. https://doi.org/10.1002/ADMA.201202424.

(521) Li, Y.; Shen, J.; Li, J.; Sun, X.; Shen, J.; Han, W.; Wang, L. A Protic Salt-Derived Porous Carbon for Efficient Capacitive Deionization: Balance between Porous Structure and Chemical Composition. *Carbon N Y* **2017**, *116*, 21–32. https://doi.org/10.1016/J.CARBON.2017.01.084.

(522) Guo, J.; Zhang, S.; Zheng, M.; Tang, J.; Liu, L.; Chen, J.; Wang, X. Graphitic-N-Rich N-Doped Graphene as a High Performance Catalyst for Oxygen Reduction Reaction in Alkaline Solution. *Int J Hydrogen Energy* **2020**, *45* (56), 32402–32412. https://doi.org/10.1016/J.IJHYDENE.2020.08.210.

(523) Kakaei, K.; Ghadimi, G. A Green Method for Nitrogen-Doped Graphene and Its Application for Oxygen Reduction Reaction in Alkaline Media. *Materials Technology* **2021**, *36* (1), 46–53. https://doi.org/10.1080/10667857.2020.1724692.

(524) Ou, C.; Chen, H.; Wang, H.; Liao, Y.; Li, R.; Liu, H. A Novel in Situ Synthesis of Nitrogen-Doped Graphene with Excellent Electrocatalytic Performance for Oxygen Reduction Reaction. *Electrochim Acta* **2021**, *380*, 138256. https://doi.org/10.1016/J.ELECTACTA.2021.138256.

(525) Lemes, G.; Sebastián, D.; Pastor, E.; Lázaro, M. J. N-Doped Graphene Catalysts with High Nitrogen Concentration for the Oxygen Reduction Reaction. *J Power Sources* **2019**, *438*, 227036. https://doi.org/10.1016/J.JPOWSOUR.2019.227036.

---

(526) Chen, X.; Liang, Y.; Wan, L.; Xie, Z.; Easton, C. D.; Bourgeois, L.; Wang, Z.; Bao, Q.; Zhu, Y.; Tao, S.; Wang, H. Construction of Porous N-Doped Graphene Layer for Efficient Oxygen Reduction Reaction. *Chem Eng Sci* **2019**, *194*, 36–44. https://doi.org/10.1016/J.CES.2018.04.004.